

Simulation, Reconstruction, and Design Optimization for the PANDA Barrel DIRC

Dissertation
zur Erlangung des Doktorgrades
der Naturwissenschaften

vorgelegt beim Fachbereich Physik
der Johann Wolfgang Goethe-Universität
in Frankfurt am Main

von

Maria Patsyuk
aus Alma-Ata

Frankfurt am Main (2014)
D(30)

vom Fachbereich Physik der
Johann Wolfgang Goethe-Universität als Dissertation angenommen.

Dekan: Prof. Dr. Joachim Stroth

Gutachter : Prof. Dr. Klaus Peters

Prof. Dr. Wolfgang Kühn

Datum der Disputation:

Abstract

The PANDA experiment at FAIR will study fundamental questions of strong interaction with high precision. Efficient particle identification for a wide momentum range and the full solid angle is required for successful reconstruction of the benchmark channels of the broad PANDA physics program. For this purpose a compact ring imaging Cherenkov detector is being developed for the barrel region of the PANDA detector. The concept and the baseline design of the PANDA Barrel DIRC were inspired by the BABAR DIRC and improved with important modifications, like fast photon timing, a compact expansion volume, and focusing optics.

The required detector resolution was defined based on the PANDA PID specifications using the phase space distributions of the final state kaons produced in selected benchmark channels. To optimize the PANDA Barrel DIRC design in terms of performance and cost the baseline detector geometry and a number of design options were implemented in the simulation. The key options include the radiator dimensions, two types of expansion volume shapes, and a variety of focusing systems. The performance of the detector designs was quantified in terms of single photon Cherenkov angle resolution and photon yield. It was found that the number of radiators can be reduced by about 40% without loss in performance. A compound spherical lens without air gap was found to be a promising focusing system. An optimized Barrel DIRC design meeting the PID requirements includes three radiator bars per flat section, the compound lens without air gap, a compact prism-shaped EV, and a total of 192 Microchannel-Plate PMTs as photosensors. The number of electronic channels can be halved without loss in performance by combining two neighbouring pixels. For such a detector design the total cost will be significantly reduced compared to the baseline version while still meeting or exceeding the PANDA PID performance goals.

Contents

1	Introduction	5
2	The PANDA Experiment	7
2.1	Motivation	7
2.2	Accelerator Facility	10
2.3	The PANDA Detector	11
3	The PANDA Barrel DIRC	17
3.1	Introduction to Cherenkov Counters	17
3.2	The Baseline Design	27
3.3	Performance Requirements	28
4	Detector Design Optimization	41
4.1	Parameter Space	41
4.2	Detailed Detector Simulation	45
4.3	Reconstruction Method	56
4.4	The Figures of Merit	61
4.5	Focusing	67
4.6	Radiator Dimensions	81
4.7	Parameters of the Photon Camera	86
4.8	Reconstruction Bias	94
4.9	Conclusions	95
5	Summary and Outlook	99
6	Ausführliche Zusammenfassung	101
	Appendices	113

A Other Results	113
------------------------	------------

Chapter 1

Introduction

Modern particle physics is in general consistently described by the Standard Model. It incorporates three out of four fundamental interactions, which are mediated by specific boson particles between quarks and leptons, the building blocks of matter. The Standard Model is currently one of the most powerful and precise theories. The recent discovery of one of its crucial elements – the Higgs boson – was an impressive verification of this fact. Though the Standard Model successfully describes and predicts many of the phenomena in particle physics, there are lots of puzzling questions, which cannot be answered intrinsically within this theory. For example, the entirety of hadronic states, which started to grow really fast in the late decades of the last century, now contains so many exceptions from the established ordering scheme, that new studies on hadron spectroscopy aiming to refine this aspect are required. Exotic objects, like glueballs (consisting of only gluons) and hybrids (hadrons with gluonic excitation), that are not forbidden by the theory, should be observable at GeV energies, but until now have not been unambiguously identified. They are expected to have low production cross sections and reveal themselves in thorough analysis of the data from special experiments dedicated to accurate studies of hadron properties at medium energies.

One of these experiments will be PANDA, which stands for AntiProton ANnihilation in DArmstadt. It will be located at the future Facility for Antiproton and Ion Research (Germany). It will use an antiproton beam and a nuclear target to investigate the nature of strong interaction. The emphasis of the PANDA detector is the precise measurements of all kinds of final state particles produced in the broad range of reactions, which requires excellent particle identification (PID). The description of the PANDA subdetectors contributing to the global PID, and the explanation of the methods they use, is given in Chapter 2. Some benchmark channels, such as open charm decays, require excellent separation between kaons and pions. Three Cherenkov¹ detectors are foreseen for hadron identification at PANDA. One of them is the PANDA Barrel DIRC [1], which is going to distinguish between pions and kaons up to particle momenta of 3.5 GeV/ c .

¹The international standard ISO9 assumes the correct transliteration of the Russian name as “Čerenkov”, but I prefer to write “Cherenkov” which is the accepted spelling in HEP literature.

The PANDA Barrel DIRC was motivated by the *BABAR* DIRC, which has operated successfully for about ten years at the PEP-II facility at SLAC. The state-of-the-art technology of photodetectors allow significant improvement in the performance of the modern DIRCs with respect to the *BABAR* experience: faster response and smaller size allow more compact detector geometry and possibility to use the detector information online. To benefit from this, the PANDA Barrel DIRC has the following crucial improvements compared to its predecessor: fast timing, compact expansion volume, and focusing optics.

The general PANDA PID requirement is to achieve at least 3σ separation between kaons and pions in the momentum range between $0.5 \text{ GeV}/c$ and $3.5 \text{ GeV}/c$. This requirement sets the limit for the PANDA Barrel DIRC resolution. In order to determine the acceptable upper limit for the detector resolution the phase space distributions of the final state kaons produced in a number of benchmark reactions were studied. The details of the PANDA Barrel DIRC design and the analysis of the required performance can be found in Chapter 3. The limit for the detector resolution as a function of the track polar angle was then used to evaluate the performance of different detector designs.

In order to find the best design for the PANDA Barrel DIRC in terms of its performance and cost, a number of parameters were optimized and different design options were tested. This thesis focuses on the detailed simulation of the PANDA Barrel DIRC, which is an essential part of the R&D process, together with prototype tests in particle beams. The Barrel DIRC software, which is a part of the full PANDA simulation, includes different design options and allows quantitative comparison of their performances. The influence of the design options and parameters, including the focusing system and the shape of radiators and the expansion volume, on the detector performance were systematically studied using the detailed detector simulation. The photon yield, N_γ , the single photon Cherenkov angle resolution (SPR) and the detector resolution under assumption of perfect reconstruction of the momentum direction $\sigma_0 = \text{SPR}/\sqrt{N_\gamma}$ are chosen to be the figures of merit, as these values, unlike efficiency and misidentification, can be and were measured in test beam campaigns. Since the SPR, the number of detected photons, and, therefore, σ_0 vary across the detector phase space, the results for a given geometry are depicted with two-dimensional diagrams. The behaviour of N_γ , SPR and σ_0 over the track polar angle allow simple comparison between different designs and easy evaluation of the design quality. The details of the simulation, reconstruction, as well as the method to quantify the particular detector performance are presented in Chapter 4.

The discussion of the optimal PANDA Barrel DIRC design as well as the outlook is set out in Chapter 5.

Chapter 2

The PANDA Experiment

PANDA is one of the future experiments at the FAIR facility in Darmstadt, which is currently under construction as an extension of the existing GSI complex. PANDA is a fixed-target experiment, which will use a circulating beam of antiprotons colliding with a target consisting of hydrogen or heavier material. The high luminosity of up to $L = 2 \cdot 10^{32} \text{ s}^{-1} \text{ cm}^{-2}$ achieved by the fixed-target design, makes it possible to reach high statistics of rare events. Due to the annihilation process of a proton and antiproton, the full center-of-mass energy becomes available for the production of hadrons with mass up to charmonium. This enables the detailed studies in this particular energy region making the hadron spectroscopy one of the main topics of the broad PANDA physics program [2]. A few main aspects are set out in the next section followed by the brief description of the accelerator facility and PANDA detector.

2.1 Motivation

On the way towards understanding the most elementary bricks of matter and their interaction (more information about the fundamentals can be found in Ref. [3]) the experiments with accelerated particles were very useful. Indeed, they provided us with such amazing discoveries in recent years, like W^\pm and Z^0 bosons [4, 5] (LEP facility) – intermediators of weak interaction, the top quark [6] (TEVATRON) - the heaviest observed particle, beauty baryons and the long searched-for Higgs boson [7, 8] (LHC facility). The milestone observations of the main fundamental bricks of the Standard Model prove its validity and power, whereas the hadrons are characterized by a number of most effective models covering usually only a part of the hadronic states. Non of these models describes all the discovered strongly bound states in a consistent way. To complete the theoretical description of hadrons, eliminate contradictions, and inspire future breakthroughs, the masses and widths of strongly bound states should be carefully measured. A significant number of experiments focused on hadron spectroscopy, but only a few used antiprotons at medium energies. In this sense PANDA has a distinctive advantage compared to other experiments.

In the recent studies of electron-positron reactions the initial state for hadron production is (in leading order) restricted to the quantum numbers of a virtual photon ($J^{PC} = 1^{--}$), which limits the access to characteristics of other spin states. In case of antiproton-proton-annihilations all conventional quantum number combinations for directly formed states are allowed, mesonic states with so called “exotic” quantum numbers ($J^{PC} = 0^{--}, 0^{+-}, 1^{-+}, 2^{+-}, \dots$) can be observed in production. The lower density of states as well as more narrow resonances in the charmonium mass region makes the interpretation and comparison of results with other experiments easier.

Colliding protons with antiprotons at GeV energies gives an opportunity to produce heavy quarks (c), which then hadronize with open or hidden heavy flavour or undergo other decays. The available mass of the produced particles is limited to $2.3 - 5.5 \text{ GeV}/c^2$ according to the corresponding $p\bar{p}$ center-of-mass energy. The following kinds of particles are expected to be produced:

- Charmonia ($c\bar{c}$ states) and open charm mesons, produced above the $D\bar{D}$ -threshold ¹ of $3.73 \text{ GeV}/c^2$
- Baryons with charmed or strange quarks
- Systems consisting of more than three quarks (tetraquarks, di-mesons, pentaquarks...), gluonic hadron systems like glueballs (objects made of gluons), and hybrids (hadrons with gluonic excitations), which can have quantum numbers not accessible by a simple $q\bar{q}$ state
- Hypernuclei, where one or two of the nucleons are substituted by strange particles like Λ

Hypernuclei become observable in the late stage of the experiment with a special detector setup (for more detail see Ref. [2]).

The final state particles will be measured by the PANDA detector, which allows extraordinary accuracy for hadron interaction studies at GeV energies (see Ref. [2] for detail). Careful studies of the underlying physics will enrich the knowledge about the nature of strong interaction and refine the Standard Model. For example, the discrepancy between theoretical predictions and experimental observations in hadron sector has to be clarified. Concerning open-charm mesons, theory and experiment are in agreement about light states, but the recently discovered heavier ones are difficult to interpret (see Fig. 2.1a). In the charmonium sector there is also a number of charmonium-like candidates, many of which do not really fit into the current theoretical picture. Above the $D\bar{D}$ threshold for $m > 3.73 \text{ GeV}/c^2$ the charmonium spectrum is generally poorly known. The recently discovered X, Y, Z states are shown in Fig. 2.1b together with the established charmonium spectrum. The nature of many of these states is not understood. They are assigned to charmonia based

¹The region below the $D\bar{D}$ -threshold was studied using $p\bar{p}$ collisions at the E835 experiment at Fermilab. Due to the high statistics and precision PANDA will be able to perform more accurate measurements than the E835 experiment.

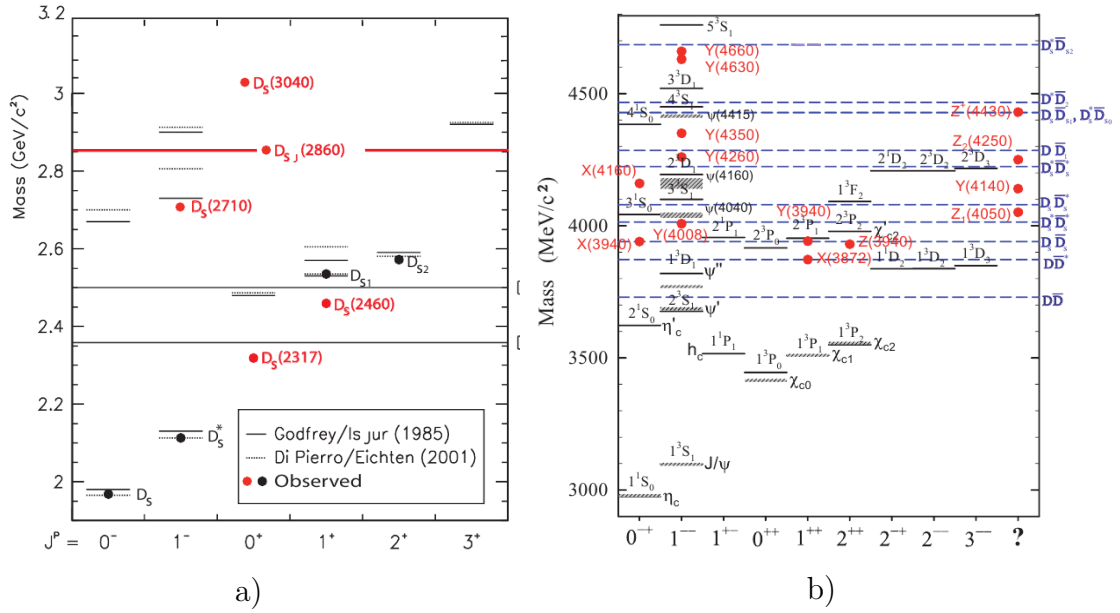


Figure 2.1: a) The spectrum of D_s mesons. Lines represent the theoretical predictions and points the experimentally measured values (black points refer to well established measured states, red ones to newly discovered ones). b) The spectrum of charmonia. Solid lines correspond to the theoretical predictions according to the constituent quark model, the shaded lines are the observed conventional charmonium states. The horizontal dashed lines correspond to various thresholds. The red dots show the newly discovered charmonium-like states placed in the column of the most probable spin assignment (Figure taken from Ref. [9]).

on their spin parity and their predominant decay via J/ψ or ψ' [9]. PANDA will be able to precisely measure key properties like, e.g., the width and line shapes of some of these states and thereby significantly contribute to the knowledge about their nature.

The rare channels of interest have usually kaons in the signal, which have to be filtered out of an enormous amount of background, mostly consisting of pions.

a)

$$p\bar{p} \rightarrow \psi(3770) \rightarrow D^+D^- \rightarrow K^-\pi^+\pi^+ + c.c.$$

$$p\bar{p} \rightarrow \psi(4040) \rightarrow D^{*+}D^{*-} \rightarrow D^0\pi^+\bar{D}^0\pi^-, D^0 \rightarrow K^-\pi^+(\pi^-\pi^+)$$

b)

$$p\bar{p} \rightarrow D_{s0}^*(2317)^+ D_{s0}^*(2317)^- \rightarrow D_s^+ \pi_0 D_s^- \pi_0 \rightarrow K^- K^+ \pi^+ \gamma \gamma + c.c.$$

$$p\bar{p} \rightarrow D_{s1}(2460)^+ D_{s1}(2460)^- \rightarrow D_s^+ \gamma D_s^- \gamma \rightarrow K^- K^+ \pi^+ \gamma + c.c.$$

Figure 2.2: Example reactions of charmonia production (a) and D_{sJ} -meson decays (b).

High quality PID information helps to sort out the background and make the signal measurable. Besides that some benchmark reactions have both pions and kaons in their final state (see 2.2). Good vertex recognition and excellent particle identification system for charged kaons from very low energies up to 3.5 GeV is essential to reconstruct the final states of many benchmark reactions successfully. Tackling that issue requires, amongst others, good kaon identification and high efficiency for open-charm final states.

2.2 Accelerator Facility

The accelerator facility FAIR is an international project, which is being built near GSI (Darmstadt) and is expected to start operating in 2018. The schematic of the facility is shown in Fig. 2.3. The existing GSI accelerators UNILAC and SIS18, together with the proton LINAC will provide the injection into the double ring synchrotron SIS100/300 with circumference of 1100 m. The antiprotons required for PANDA are going to be produced by protons colliding with a target made of nickel, iridium or copper [11]. The energy of the protons just before the collision will be 29 GeV, which allows effective collection of produced antiprotons and moderate magnetic rigidity to transport them with initial antiproton energies of about 3 GeV. The generated antiprotons will be selected using mass spectrometry and finally col-

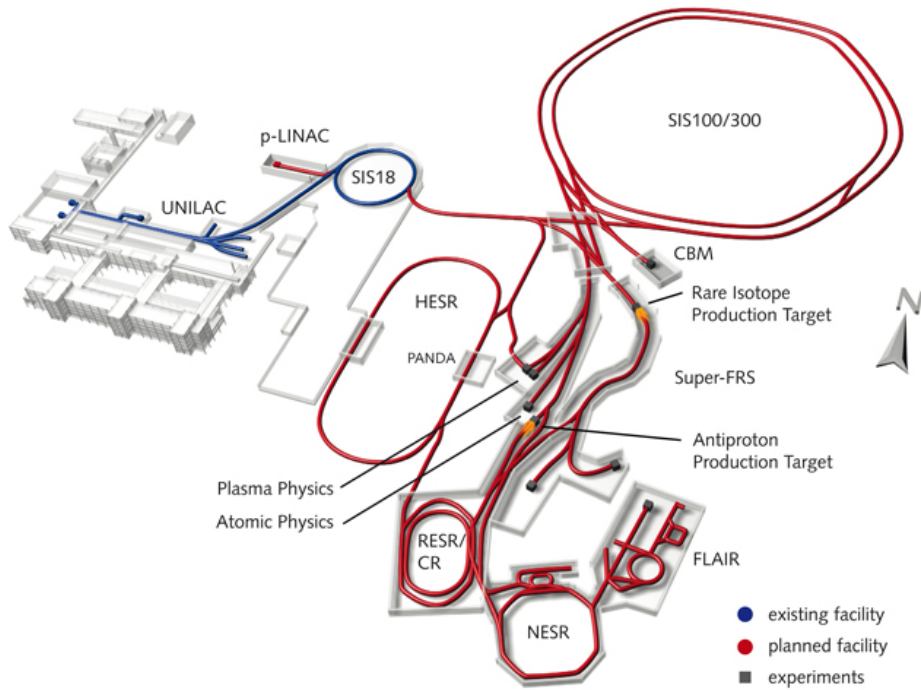


Figure 2.3: Accelerator facility schematic. The existing part of GSI is shown on the left, the existing accelerators are marked in blue, the elements of the future FAIR complex in red (Figure from Ref. [10]).

lected in the HESR (High Energy Storage Ring), where they can be accelerated or decelerated to any particular momentum between $1.5 \text{ GeV}/c$ and $15 \text{ GeV}/c$, and collide with the target inside the PANDA detector. The two possible implementations for the hydrogen target are: the cluster-jet target, which is formed by a jet of hydrogen clusters, and the pellet target, formed by a stream of frozen spherical hydrogen micro-pellets.

There are two operation modes of the HESR storage ring [2]. One is the high resolution mode, where the luminosity of the antiprotons will be about $L = 2 \cdot 10^{31} \text{ cm}^{-2} \text{ s}^{-1}$ and the momentum resolution $\Delta p/p$ will be less than $4 \cdot 10^{-5}$. This allows fine scanning in a particular energy range to precisely determine widths and line shapes of resonances ($\Delta E = O(50) \text{ keV}$). The high luminosity mode, providing luminosity of up to $2 \cdot 10^{32} \text{ cm}^{-2} \text{ s}^{-1}$ with a slightly worse momentum resolution of $\Delta p/p \approx 10^{-4}$, is foreseen to collect larger data samples or rare signals.

2.3 The PANDA Detector

The PANDA detector is a complex structure consisting of a number of subdetectors operating together, like most of the particle detectors for high energy experiments. The subdetectors are arranged in a sequence of layers, so that the particles propagating from the collision point outwards are getting detected and measured. Each subdetector is designed to measure a specific set of particle properties. The PANDA detector is described in detail in Ref. [12]. To register all the particles produced in collisions of the antiproton beam with the target, there are two main detector segments covering different parts of the solid angle: the Forward Spectrometer, accepting particles with polar angles below 5° , and the Target Spectrometer surrounding the Interaction Point (IP). The barrel-shaped components of the Target Spectrometer have polar angle acceptance in the range between 22° and 150° , whereas the corresponding end-caps complement it for steep polar angles ($\sim 5^\circ - 22^\circ$). Fig. 2.4 gives an overview of the detector components of the Target Spectrometer.

All subdetectors are in a magnetic field in order to bend the tracks of charged particles for momentum and charge determination. In the Target Spectrometer the magnetic field is provided by a superconducting solenoid coil [14] with an inner radius of 90 cm and a length of 2.8 m. The field homogeneity is foreseen to be better than 2% over the volume of the vertex detector and central tracker.

Efficient identification of charged hadrons and leptons plays an important role for PANDA and should be provided in a wide momentum range from $200 \text{ MeV}/c$ up to approximately $10 \text{ GeV}/c$ [2]. To achieve this goal the contributions of different subsystems are taken into account. The identification of stable particles can be done either by evaluating the signals from detectors sensible only to a particular species (e.g. muon systems, calorimeters), or by determining their mass. The most frequently appearing charged particles are pions, protons and kaons. They will be registered in the PANDA detector by the following signals: energy deposit

The three prominent effects of these particle species in the PANDA detector sys-

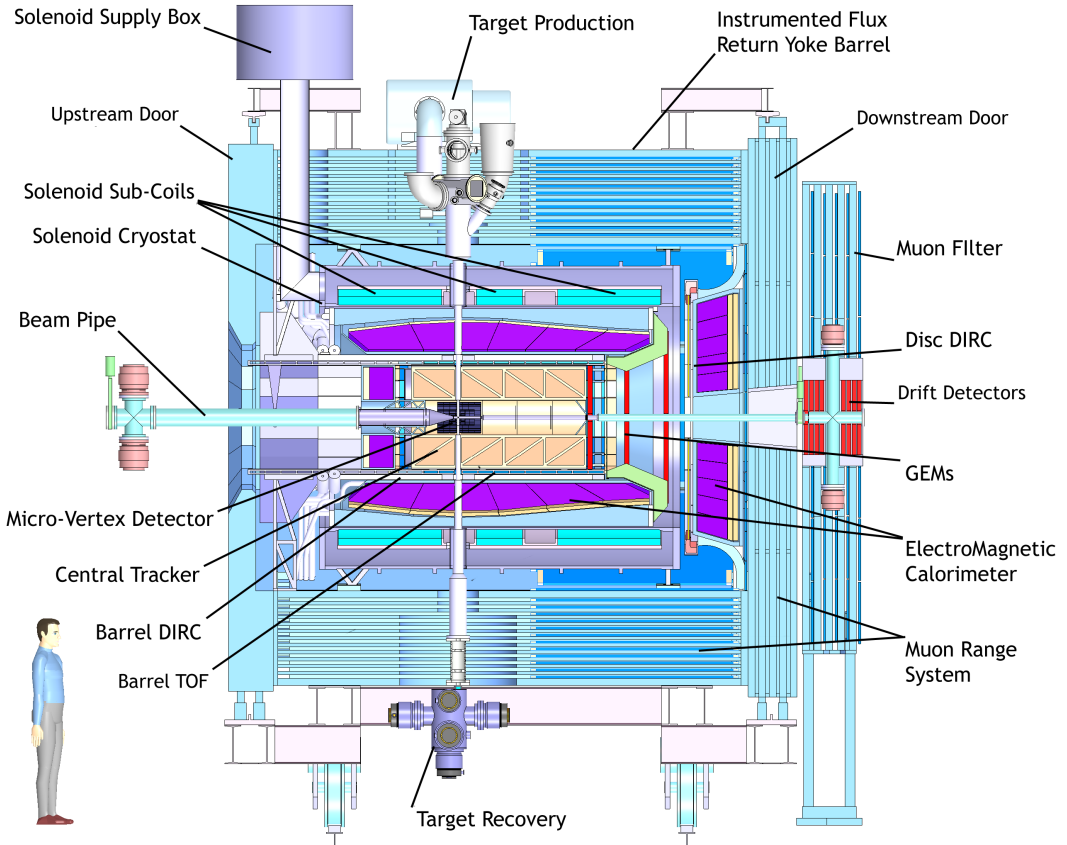


Figure 2.4: Side view of the PANDA Target Spectrometer. Figure from [13].

tem are: energy deposit in the tracking system, signal from the Cherenkov detectors, and timing signal from the time-of-flight device [15].

The subdetectors of the Target Spectrometer contributing to the global PID are briefly described in the next sections. The pictures of the PANDA subsystems were created from Ref. [16].

Charged Particle Tracking

The tracking chambers define the particle momentum based on the curvature of the track in the magnetic field. Energy loss measurements provide useful information for the distinction between the different particle types with momenta below 1 GeV/c . In addition charged kaons may be identified in a high-resolution tracking system using their characteristic “kink” topology, e.g., $K^\pm \rightarrow \mu^\pm \nu_\mu$ (64%) and $K^\pm \rightarrow \pi^\pm \pi^0$ (21%) [15]. The kinematics of such a topology allows the separation of kaon decays from the main source of background kinks coming from charged pion decays [17].

In the Target Spectrometer there will be two tracking systems. The innermost Micro-Vertex Detector (MVD) [18] is designed to reconstruct secondary vertices close to the interaction point (see Fig. 2.5). It has the length of 420 mm and the

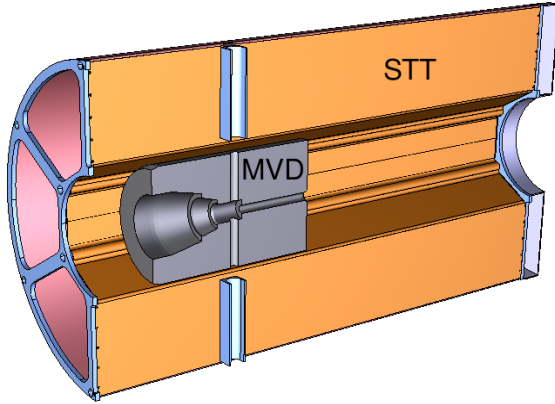


Figure 2.5: Mechanical drawing of the tracking detectors located in the PANDA Target Spectrometer and covering the polar angle range $\theta_{tr} > 22^\circ$. Figure from Ref. [16].

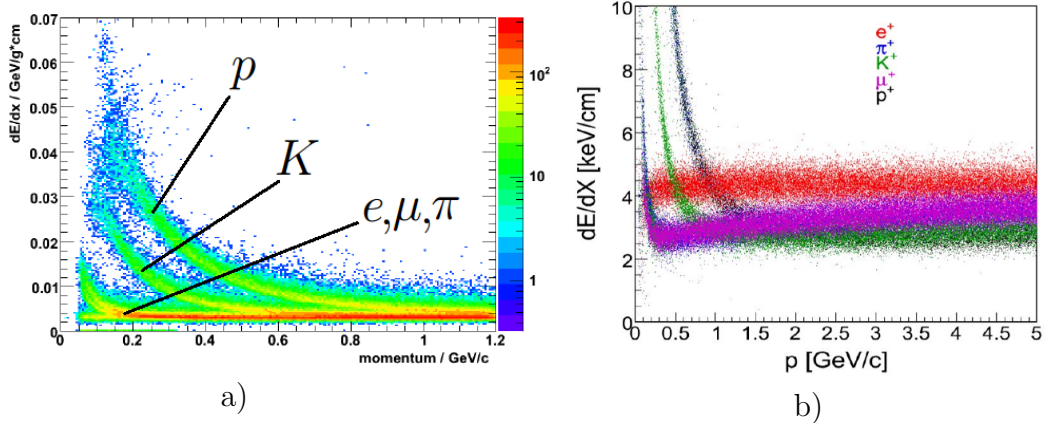


Figure 2.6: Energy loss (dE/dx) as a function of particle momentum obtained with the MVD (a) and the STT (b). Figures from Ref. [2]).

outer diameter of 15 cm covering the polar angle range between 3° and 150° . The first layer of sensors is located at the radius of 2.2 cm around the beam pipe. The MVD provides precise 3D hit information by collecting signals from radiation hard silicon pixels and strips. It is able to separate different particle species according to the accurate measurement of the energy loss and the particle momentum [2]. The energy loss per unit length in MVD as a function of particle momentum is shown for different particle species in Fig. 2.6a. The MVD will be able to contribute to the separation of low momentum protons from other species. Kaons can be distinguished up to ≈ 600 MeV/c from pions, muons and electrons. The latter three species can not be further separated [19].

The Straw Tube Tracker [20] (Fig. 2.5) consists of aluminized mylar tubes with 1 cm in diameter, so called straws, which are arranged in planar layers mounted in a hexagonal shape around the MVD. In total there are 4200 straws around the beam pipe at radial distances between 15 cm and 42 cm with the polar angle acceptance

between 10° and 140° . The PID performance of the STT is illustrated in Fig. 2.6b. The STT is efficient for kaon identification below the Cherenkov threshold. For higher momenta the STT signals from different particle species overlap, and no clear PID information can be obtained.

Particle Identification Systems

Cherenkov Detectors

The main subsystems of the Target Spectrometer dedicated to hadron PID are the two Cherenkov imaging detectors [21]: the Barrel DIRC and the Disc DIRC [22, 23], that will separate kaons from pions in the momentum range above $0.5 \text{ GeV}/c$. They are shown in Fig. 2.7. The Barrel DIRC, being the subject of this thesis, is described in detail in the next chapters. Both detectors are based on the same DIRC (Detection of Internally Reflected Cherenkov light) principle. They occupy an extremely small space and introduce only a small material budget, which makes it possible to use a smaller electromagnetic calorimeter and magnet for the PANDA detector.

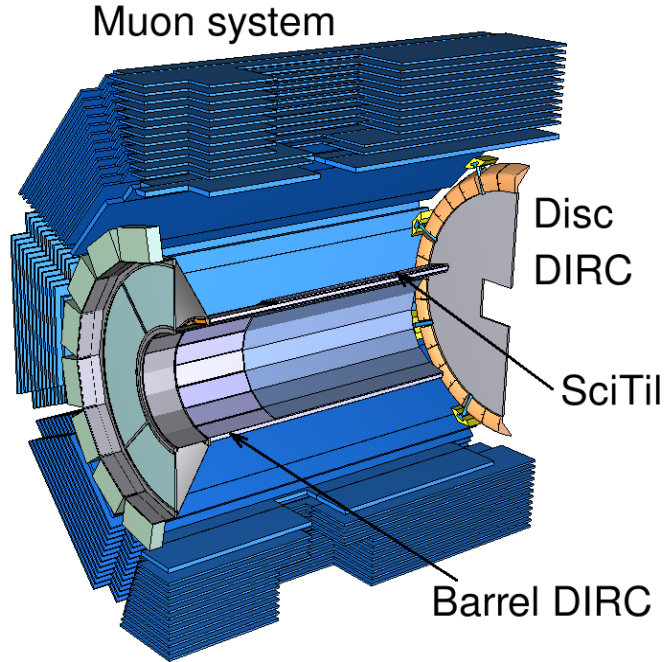


Figure 2.7: Mechanical drawing of the PANDA Target Spectrometer subsystems dedicated to PID. Figure from Ref. [16].

Time-of-Flight Detectors

The Scintillation Tiles hodoscope (SciTil) is mounted between the Barrel DIRC and the Electromagnetic Calorimeter (EMC). It is a thin barrel made of $3 \times 3 \times 0.5 \text{ cm}^3$

scintillating tiles. The system will be read out by $3 \times 3 \text{ mm}^2$ Silicon Photomultiplier Tubes (SiPMs). The SciTil has a low material budget, it will provide fast timing at the order of $\Delta t = 100 \text{ ps}$ and the separation between K and π in the momentum range $0.4 - 0.7 \text{ GeV}/c$ [19]. This detector will also allow detection of γ -conversions inside the Barrel DIRC radiators.

Muon Detectors

The PANDA Muon System [24] illustrated in Fig. 2.7 is based on the range system technique to register muons in a laminated iron absorber. The muon detectors in the barrel region are integrated into the solenoid, so that the absorbing iron layers are alternating with detecting Mini Drift Tubes (MDTs), which provide two-coordinate readout of the track information. There are 13 sensitive layers, each 3 cm thick. Such a laminated iron-detector structure may also serve as a coarse hadron calorimeter, being able to distinguish pions from muons, identify antiprotons, neutrons and anti-neutrons.

Electromagnetic Calorimetry

In general, calorimeters detect neutral and charged particles, measure their kinetic energy and determine whether electromagnetic or hadronic interaction took place.

In the target spectrometer there are a Barrel EMC and two End-caps EMCs covering a wide energy range between a few MeV and several GeV [25] (see Fig. 2.8a). The Barrel EMC (see Fig. 2.8a) occupies the radial space between 57 and 94 cm and covers the polar angle range from 22° to 140° . The forward end-cap located at the distance of 205 cm downstream from the collision point has a diameter of

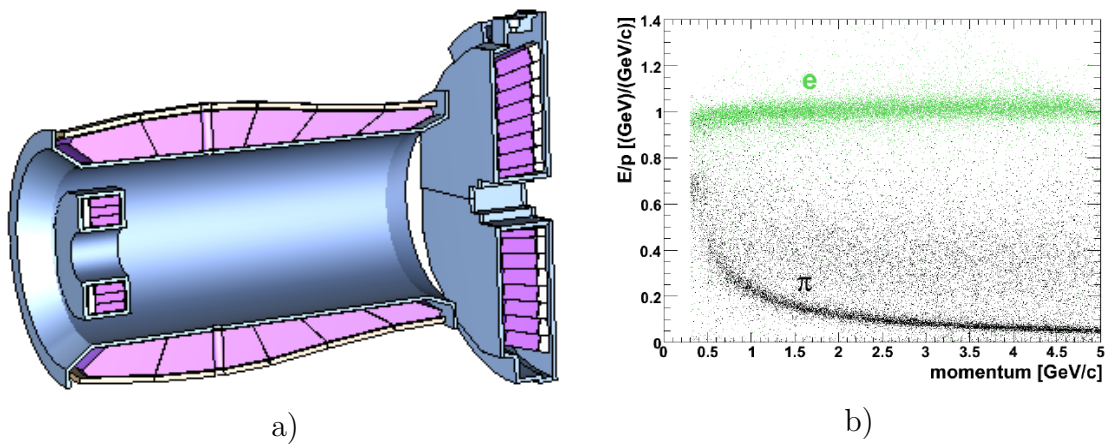


Figure 2.8: a) Mechanical drawing of the electromagnetic calorimeters in the barrel region at PANDA (figure from Ref. [16]), b) E/p ratio as a function of track momentum for electrons (green) and pions (black) in the momentum range from 0.3 up to 5 GeV/c obtained with EMC [2].

2 m. The backward calorimeter disc located at the distance of 55 cm upstream from the IP has a diameter of 0.8 m. The electromagnetic showers are created in fast scintillating crystals ($\Delta t < 20$ ns) made of lead-tungstate with dimensions of about $2 \times 2 \times 20$ cm³. There are about 15.5 thousands of such crystals in total. The contribution of EMC to the global PID in terms of separation between pions and electrons is illustrated in Fig. 2.8b. The expected energy resolution is less than 1%.

Chapter 3

The PANDA Barrel DIRC

This chapter starts with the basic principles of the Cherenkov effect and its application in the field of particle identification (PID). Then an overview of general PID detector types based on the Cherenkov principle is presented. The main focus is put on the PANDA Barrel DIRC, starting with its baseline design, which is quite similar to the *BABAR* DIRC. Different terms contributing to the detector resolution are discussed in detail, followed by the study of the required PANDA Barrel DIRC resolution, focusing on the positive kaon identification and illustrating the results with a number of benchmark channels. The limitation for the minimal PANDA Barrel DIRC detector resolution to achieve the envisaged PID quality are formulated for further use in the performance studies. Finally, the method to reconstruct the Cherenkov angle and obtain the detector resolution is described in detail.

3.1 Introduction to Cherenkov Counters

Cherenkov Effect

If a particle is moving through a medium with velocity greater than the speed of light in that medium $c_n = c/n(\lambda)$ (c – speed of light in vacuum, $n(\lambda)$ – refractive index of the medium) it emits Cherenkov radiation. The Nobel Prize in 1958 [26] was awarded jointly to P.A. Cherenkov, who studied and first described the effect, and I.M. Frank and I.Y. Tamm, who proposed the theoretical explanation. The Cherenkov radiation in isotropic media is emitted on a cone surface. The cone opening angle θ_C can be calculated as

$$\cos \theta_C = \frac{1}{\beta n(\lambda)}. \quad (3.1)$$

The main properties of the Cherenkov effect can be summarized in the following way [27]:

1. The effect takes place in a given medium (with refractive index $n(\lambda)$) only

when the velocity of the particle β is above the threshold: $\beta = \frac{v}{c} \geq 1/n(\lambda)$.

2. The opening angle of the Cherenkov cone (θ_C) increases with the particle velocity β from zero to the maximum value: $\lim_{\beta \rightarrow 1} \theta_C = \arccos(1/n(\lambda))$.
3. The wavelength spectrum of Cherenkov photons is continuous and drops proportionally to $1/\lambda^2$ with increasing wavelength.
4. Cherenkov light is emitted promptly, unlike scintillation.

Chromatic Dispersion

In a general case, the refractive index of the medium varies with the photon wavelength $n = n(\lambda)$. This effect is called chromatic dispersion and illustrated in Fig. 3.1 for some materials typically used in Cherenkov detectors.

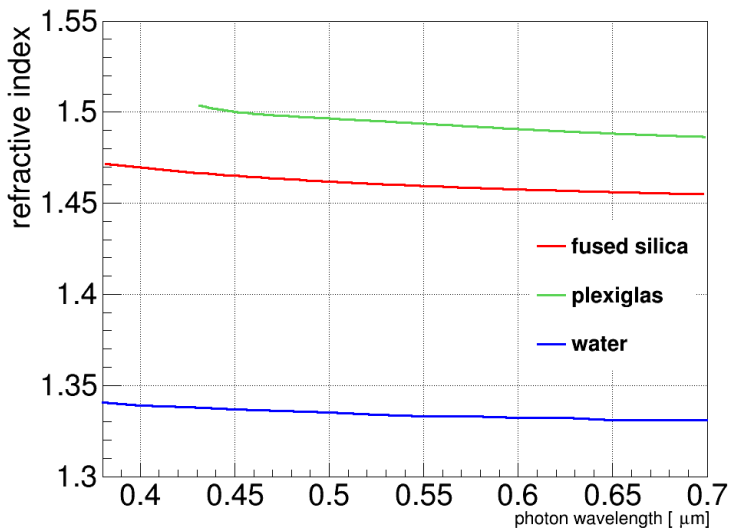


Figure 3.1: Refractive index as a function of the wavelength for different radiator materials [28].

In a transparent optical medium the refractive index $n(\lambda)$ is defined as ratio $n(\lambda) = c/v(\lambda)$, where c is the speed of light in vacuum and $v(\lambda)$ is the phase velocity of light in that medium. Cherenkov photon propagation occurs with the group velocity u [29], since in dispersive media energy propagates at the group velocity. The relation between u and v is

$$u = v \left(1 + \frac{\lambda}{n} \frac{\partial n}{\partial \lambda}\right). \quad (3.2)$$

For media with constant refractive index ($dn/d\lambda = 0$), such as vacuum, the group velocity equals the phase velocity. In most transparent media at optical frequencies the refractive index slightly changes with the wavelength, which means, that the

group and phase velocities of light in dispersive media take different values (see Fig. 3.2, bottom plot).

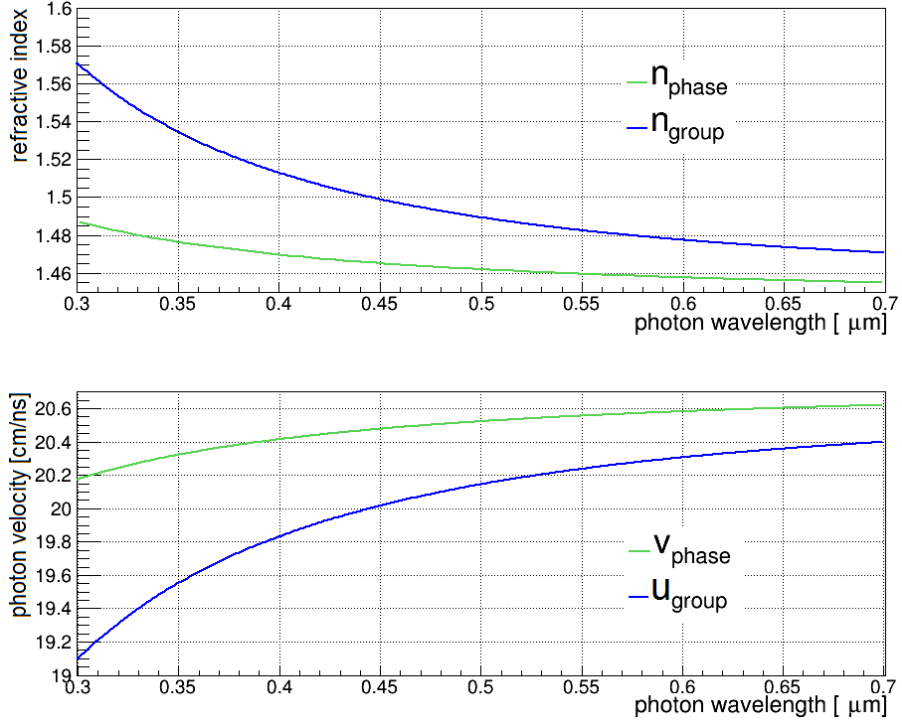


Figure 3.2: Phase and group refractive indices and velocities for photons in synthetic fused silica.

The group refractive index, defined as $n_{\text{group}} = c/u$, can be obtained from Eq. 3.2 using error propagation (illustrated in Fig. 3.2 in the upper plot):

$$n_{\text{group}} = \frac{c}{u} = n - \lambda \frac{\partial n}{\partial \lambda}. \quad (3.3)$$

Intensity of the Cherenkov Light

The intensity of Cherenkov light has been firstly calculated by I. E. Tamm and I. M. Frank [30]. The ratio between the number of emitted photons N_γ , the wavelength λ , and the path length x is the following:

$$\frac{d^2 N_\gamma}{dx d\lambda} = \frac{2\pi\alpha z^2}{\lambda^2} \left(1 - \frac{1}{\beta^2 n^2(\lambda)}\right) = \frac{2\pi\alpha z^2}{\lambda^2} \sin^2(\theta_C(\lambda)), \quad (3.4)$$

where α is the fine-structure constant, z is the charge of the particle in units of the elementary charge, β is the particle velocity, $n(\lambda)$ is the refractive index of the medium, and θ_C the Cherenkov angle. The larger the particle velocity is, the more Cherenkov photons are produced along its track. The number of produced photons drops quadratically with increasing wavelength: $N_\gamma \sim 1/\lambda^2$. Cherenkov effect is a rather weak source of light, which can be seen in the formula above for $\theta_C \rightarrow 0$.

The number of photons in the optical range (λ between 400 nm and 700 nm) for a particle with charge $z = 1$ in a medium with $n(\lambda) \approx \text{const}$ can be approximated by the expression [27]:

$$\frac{dN_\gamma}{dx} = \frac{490}{[\text{cm}]} \sin^2(\theta_C). \quad (3.5)$$

Cherenkov Counters

Cherenkov counters identify charged particles by correlating the information about the particle direction with the Cherenkov specific observables, e.g. the number of observed photon and the Cherenkov angle. Generally, such detectors contain two main elements: radiators through which charged particles pass and where Cherenkov photons are produced (a transparent dielectric medium), and photodetectors where the photons are measured. The optical system consisting of lenses and mirrors can be used to ensure optimal light collection and improve the imaging. The momentum range, where a Cherenkov counter operates, depends on the radiator material. Cherenkov light properties for different typical radiator materials are listed in Tab. 3.1. The refractive index should ensure separable detector signals for particle species of interest in the whole momentum acceptance from the threshold to the highest anticipated value. The thickness of the radiator is adjusted to assure a sufficient number of photoelectrons for the given momentum range [15]. As Cherenkov radiation is rather weak source of photons, the light transmission, collection and detection must be as efficient as possible. This puts limitations on the choice of photosensors and radiator dimensions.

Radiator type	θ_C for $\beta = 1$ [mrad]	Cherenkov threshold [GeV/c]	N_γ/cm for $\beta = 1$, $\lambda(400, 700)$ [nm]
Plexiglas (PMMA)	841	$p(K): 0.44, p(\pi): 0.121$	272
Fused silica (SiO_2)	823	$p(K): 0.46, p(\pi): 0.125$	263
H_2O	728	$p(K): 0.55, p(\pi): 0.15$	217
Aerogel (Si_xO_y)	309	$p(K): 1.54, p(\pi): 0.42$	45
C_5F_{12} gas at 1 bar	58.3	$p(K): 8.47, p(\pi): 2.33$	1.7

Table 3.1: Properties of the Cherenkov light produced in different radiator materials.

Depending on the particular information used, there is a number of ways to

perform PID with Cherenkov counters. The simplest version is a threshold detector, which exploits the fact, that the light emission starts at a certain velocity in an adjusted radiator material. There out of two (or more) particle species with the same momentum the heaviest one is below the Cherenkov threshold and does not emit photons. One example of a threshold counter is the Belle Aerogel detector [31]. More sophisticated differential detectors use the information about the Cherenkov angle of interest. They sort out particles in a narrow velocity interval with given Cherenkov angle.

A more advanced concept is a Ring Imaging Cherenkov Detector (RICH) [32]. It makes full use of the Cherenkov information by reconstructing the Cherenkov angle and the number of detected photoelectrons. The hit pattern on the detection plane usually has a circular shape. The ring is reconstructed by determination of the coordinates of the center and the radius, which is analytically related to the Cherenkov emission angle. This, in combination with the charged particle momentum, makes possible determination of the species. An example of a RICH detector is the LHCb RICH [33]. Figure 3.3a shows the relation between the Cherenkov angle and the momentum for different particle species and three values of the refractive index corresponding to the three radiator materials used in the LHCb RICH setup. In Fig. 3.3b the Cherenkov angles for $e/\mu/\pi/K/p$ are shown as a function of momentum for the PANDA Barrel DIRC.

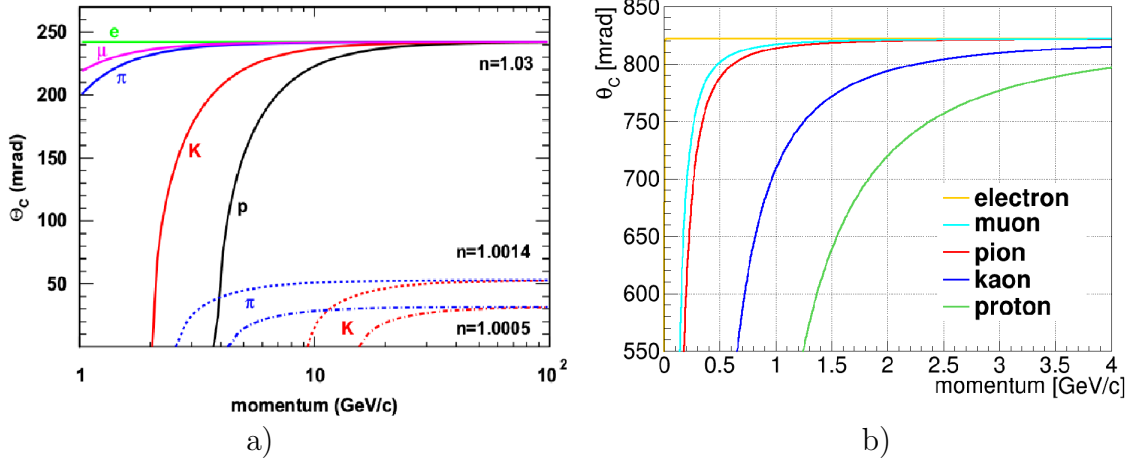


Figure 3.3: Cherenkov angles as a function of momentum for different particle species: a) for the three radiator materials with refractive indices n of the LHCb RICH setup [15], b) for the fused silica radiators of the PANDA Barrel DIRC.

Solid radiators match the momentum region interesting for experiments at intermediate and high energies, such as PANDA, and ensure emission of a sufficiently large number of Cherenkov photons already in a thin layer (~ 1 cm, see Tab. 3.1). This allows creating an extremely compact detector, if the readout module is located outside of the particle flux. The idea to use the radiators as light guides to transport Cherenkov photons towards the photosensors [34] is the basic DIRC (Detection of Internally Reflected Cherenkov light) idea. The parallel highly polished sides of the radiator with rectangular cross section conserve the information about the

Cherenkov angle during photon transport via total internal reflection. The resulting DIRC hit pattern is not a ring (like it is for RICH), but rather an overlapped conic section (its shape depends on the particular detector geometry). Usually, the reconstruction procedure for a DIRC transforms the hit pattern into Cherenkov space or time space, which is a different approach from RICH technique.

The principle of DIRC is illustrated in Fig. 3.4. A charged particle traversing a radiator with velocity β emits Cherenkov photons on a cone. For particles with $\beta \approx 1$ there are always some photons fulfilling the total internal reflection condition in the radiator ($\alpha_{critical} < \arcsin(n_3/n_1)$, for fused silica $\alpha_{critical} = 42.9^\circ$) [34]. The trapped photons are transported to either radiator end, one of which is equipped with a mirror to reflect photons back towards the readout end. After exiting the radiator into an expansion volume the photons are imaged in three dimensions with an array of sensors. The position (x, y) and the arrival time t of the detected photon are the input for the reconstruction, which either determines the Cherenkov angle or uses likelihood functions to perform PID. A detailed discussion on the DIRC concept can be found in Ref. [35, 36].

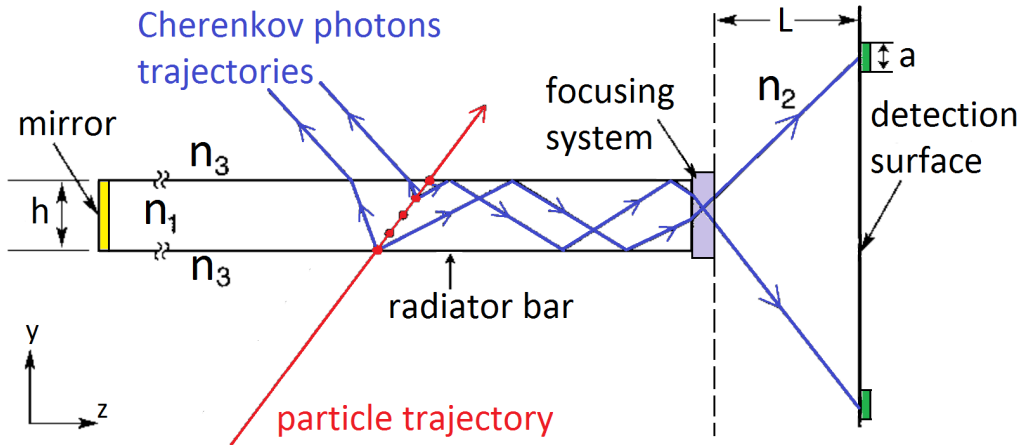


Figure 3.4: Schematic of the DIRC principle. The different media of the radiator, expansion volume, and environment have refractive indices n_1 , n_2 , and n_3 . Some important values, as the radiator bar aperture h , distance between the radiator bar and the detection plane L , and pixel size a , are labelled.

The *BABAR* DIRC

The first version of the novel Cherenkov imaging detector based on the DIRC principle was used in the *BABAR* experiment at SLAC. It showed stable and reliable operation during more than eight years of data taking from 1999 until 2008. This detector performed K/π separation in the wide momentum range from the pion Cherenkov threshold up to $4.2 \text{ GeV}/c$ and could operate at four times the design luminosity after installation of a new readout system and shielding. The original quality of the polished radiator bar surfaces remained unchanged throughout the

whole period of detector operation [37]. The details of the DIRC operational experience can be found in Ref. [38]. This successful application inspired development of other DIRCs, one of which is the PANDA Barrel DIRC. It is important to discuss the functionality of the *BABAR* DIRC geometry elements and the detector performance. The concept of imaging of Cherenkov photons used in *BABAR* DIRC is illustrated in Fig. 3.5.

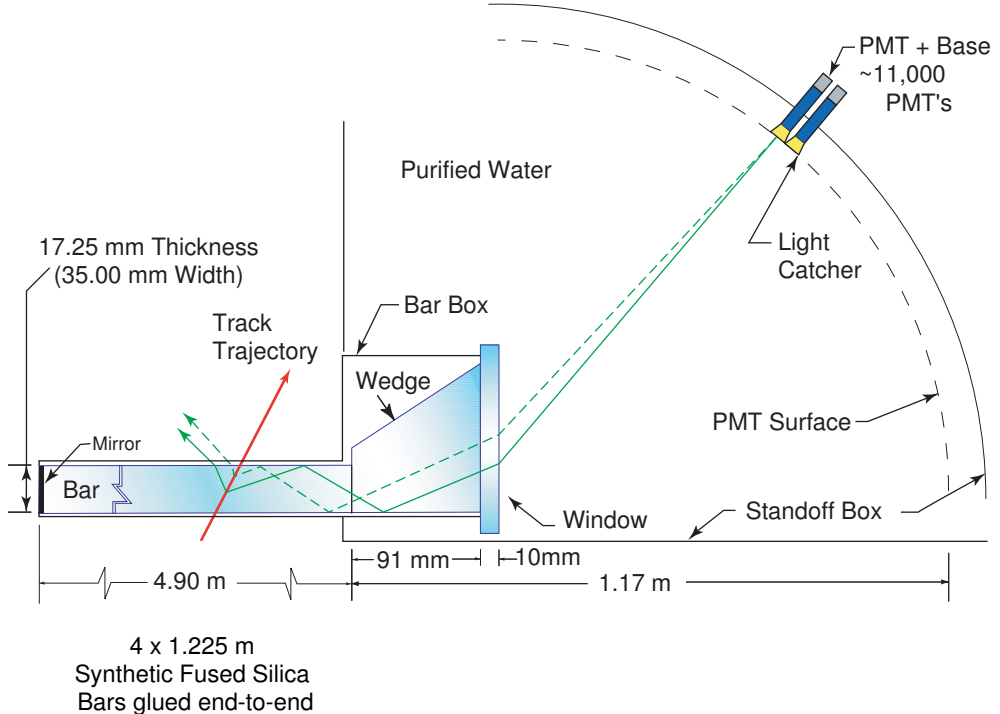


Figure 3.5: Schematic of the imaging principle used in the *BABAR* DIRC. Figure from Ref. [38].

The radiator bars forming the barrel were assembled from four 1.225 m pieces of synthetic fused silica glued end-to-end¹ and had a cross section of $3.5 \times 1.75 \text{ cm}^2$. A fused silica prism was placed between each radiator bar and the window to the expansion volume (EV). It reduced the required photosensitive area and at the same time improved the angular resolution. The photons reflected off the slightly tilted upwards bottom side (by 6 mrad) ended up approximately on top of those not undergoing any reflections inside the wedge. The EV of the *BABAR* DIRC detector was a single volume for the whole barrel, filled with purified water, which was a reasonable choice due to its high refractive index (see Fig. 3.1), modest cost and large absorption length in the wavelength range of detectable Cherenkov light. Since the *BABAR* DIRC had enough space to place a large EV, it could afford to use simple “pinhole” focusing of Cherenkov photons onto the detection surface, located at a distance of $L \sim 1.2 \text{ m}$ from the bar ends. In this method the principle of the pinhole camera was used: all photons enter the EV in approximately the same point. Therefore, the uncertainty of the photon direction inside the EV, which defines the

¹A bar length of 1.225 m was the easily obtainable for the industry with sufficiently high quality.

error on the reconstructed single photon Cherenkov angle, is independent of a precise track location inside the radiator, but is a function of the effective size of the pixel a . Figure 3.6 illustrates the effective pixel size seen from the middle of the radiator bar end. The *BABAR* DIRC had an approximately toroidal detection surface, so that all Photomultiplier tubes had roughly the same effective size. The corresponding error of the single photon Cherenkov angle due to the pixel size $\sigma_{\theta_{C,det}}$ can be written as

$$\sigma_{\theta_{C,det}}^2 = \frac{a^2/12}{L^2}, \quad (3.6)$$

The effective size of the radiator bar end seen from the pixel should be taken into account in the similar way. This leads to the following focusing error $\sigma_{\theta_{C,foc}}$

$$\sigma_{\theta_{C,foc}}^2 = \frac{h^2/12}{L^2}, \quad (3.7)$$

where h is the effective size of the radiator bar aperture (see Fig. 3.6). Considering the diameter of one PMT to be 2.8 cm, the resulting uncertainty of the single photon Cherenkov angle due to the design of the photon camera can be estimated as

$$\sqrt{\sigma_{\theta_{C,det}}^2 + \sigma_{\theta_{C,foc}}^2} \approx 7\text{mrad.} \quad (3.8)$$

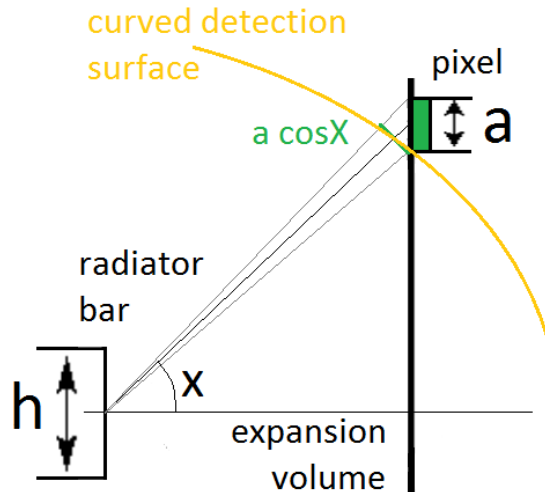


Figure 3.6: Schematic illustrating how the effective pixel size depends on its location and on the shape of the detection surface. The marked pixel with the size a located on the flat vertical surface has effective size of $a \cdot \cos X$, where X is the angle between the bar axis and the direction to the pixel from the center of the bar end. A special curved detection surface (shown in yellow) can keep the effective size of each pixel approximately the same. This was used in *BABAR* DIRC.

Cherenkov photons have path length of some meters, and can undergo up to hundreds of reflections inside the thin radiator before being detected. This puts

strict requirements on the surface finish, edge sharpness and geometrical precision to conserve the Cherenkov angle information. The non-flatness of the radiator bar surfaces and non-perpendicularity of its faces cause the Cherenkov angle information to be distorted at every internal reflection. The non-squareness of the radiator bar has a tight tolerance of less than 0.25 mrad, and each bar surface was required to be flat within 0.1 mm [39]. The chamfer of the radiator are unavoidable, which means that all the photons that hit it either loose the Cherenkov information or get lost from the radiator. The uncertainty of the single photon Cherenkov angle due to imperfect radiator bar shape $\sigma_{\theta_C,bar}$ is about 2 – 3 mrad.

The error of the Cherenkov angle due to the chromatic dispersion can be written as

$$\sigma_{\theta_C,chrom} = \frac{1}{\tan \theta_C} \frac{dn}{n}. \quad (3.9)$$

Thus, the chromatic dispersion contribution depends on the radiator dispersion averaged over the response of the photodetector. For a DIRC with a fused silica radiator and bialkali photocathodes, this averaged value of dn/n is 5.8 mrad, so that $\sigma_{\theta_C,chrom} = 5.4$ mrad for a $\beta = 1$ particle [34]. Taking into account also the systematic error occurring due to neglecting the curvature of the charged particle track inside the radiator $\sigma_{\theta_C,sys}$, the uncertainty of the single photon Cherenkov angle can be calculated as

$$\sigma_{\theta_C}^2 = \sigma_{\theta_C,det}^2 + \sigma_{\theta_C,foc}^2 + \sigma_{\theta_C,chrom}^2 + \sigma_{\theta_C,sys}^2 + \sigma_{\theta_C,bar}^2. \quad (3.10)$$

The measured single photon Cherenkov angle resolution (SPR) for the *BABAR* DIRC was 9.6 mrad. It is illustrated in Fig. 3.7a by the difference between the measured Cherenkov angle for single photons and expected Cherenkov angle for the charged particle ($\Delta\theta_C$). The resolution on the Cherenkov angle of the particle $\sigma_{\theta_C,track}$ depends on the single photon Cherenkov angle resolution as

$$\sigma_{\theta_C,track}^2 = \sigma_{corr}^2 + \left(\frac{\sigma_{\theta_C}}{\sqrt{N_\gamma}} \right)^2 = \sigma_{corr}^2 + \sigma_0^2, \quad (3.11)$$

where σ_{corr} includes a number of correlated uncertainties, e.g., errors coming from the resolution of the tracking system $\sigma_{tracking}$, multiple scattering, and misalignment of the system. The correlated term σ_{corr} was at the level of 1.5 – 2 mrad for high momentum particles. The second term σ_0 can effectively be influenced by the detector design. N_γ is the number of detected Cherenkov photons per track. The Cherenkov angle resolution for a track σ_{θ_C} was measured to be 2.4 mrad (see Fig. 3.7b), which is within 10% of the design.

The average number of observed photons as a function of the track polar angle is shown in Fig. 3.7c. The *BABAR* DIRC was measuring between 20 and 60 photons per charged particle. The “W”-like shape of this distribution being typical for barrel-shaped DIRCs with IP lying inside can be understood from the detector geometry.

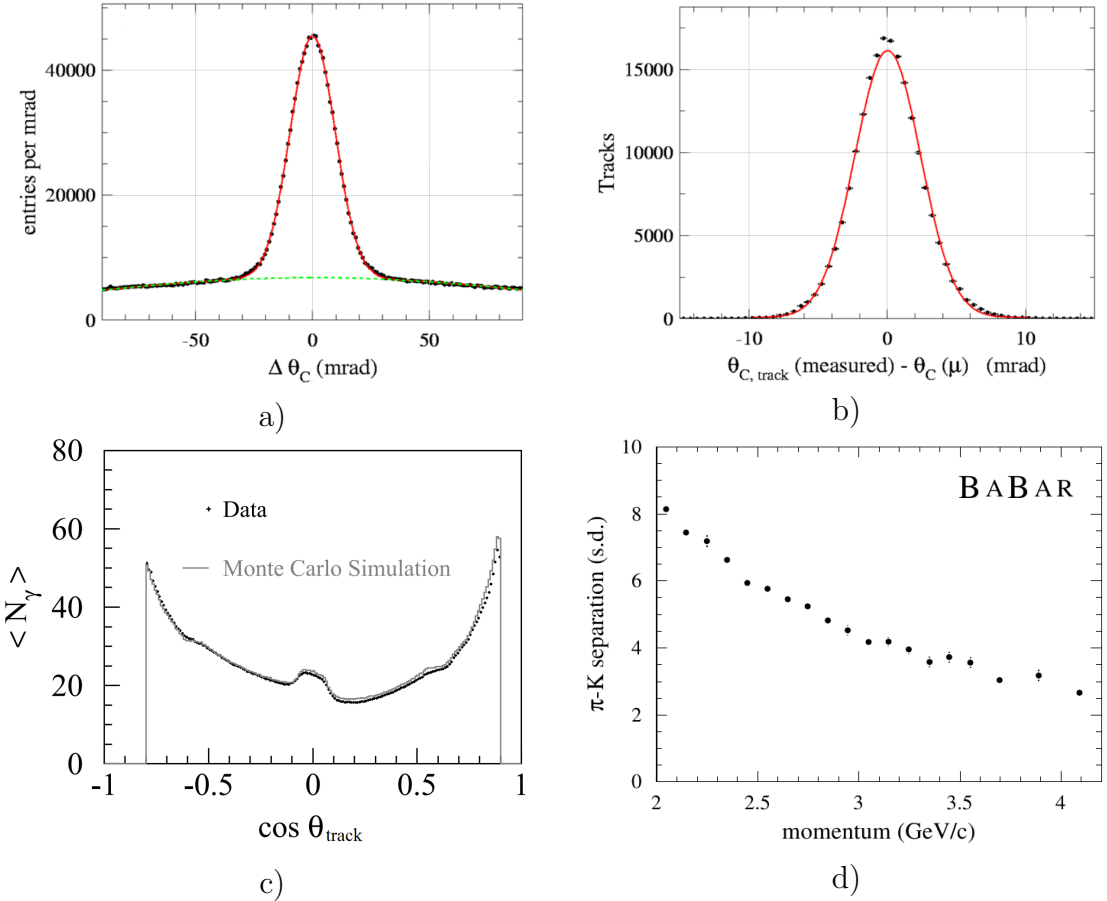


Figure 3.7: Performance delivered by the *BABAR* DIRC including a) the difference between the measured single photon Cherenkov angle and the expected Cherenkov angle for the charged particle, b) the distribution of the difference between the measured and expected Cherenkov angles per track, c) the average number of detected photons versus track polar angle for reconstructed tracks in di-muon events compared with Monte Carlo simulation [38], and d) the separation between pions and kaons as a function of the charged particle momentum (the data is extracted from $D^0 \rightarrow K^- \pi^+$ decays [40]).

The photon yield is proportional to the length of the particle trajectory inside the radiator bar (see Eq. 3.4), which is the smallest at perpendicular incidence and increases towards the end of the bars. In addition, the fraction of photons trapped by total internal reflection generally rises with larger values of $|\cos \theta|$, except close to 90° where a fraction of both forward- and backward-going photons can be trapped, leading to an enhancement of trapping efficiency². There are more photons in the backward direction than forward due to their shorter path length to the photon detector.

In case of Gaussian distributions, the resolution of the Cherenkov angle for a

²For particles with low momentum this effect can be the opposite when the Cherenkov angle is small, so that the generated photons do not satisfy the total internal condition.

track $\sigma_{\theta_C,track}$ defines the separation power of the DIRC. Figure 3.7d illustrates the separation power defined as the distance between two detector signals described with single Gaussians divided by the average sigma. In reality the distributions have non-gaussian tails, which should be taken into account for calculation of efficiencies and mis-identifications.

3.2 The Baseline Design

Reference [1] contains the detailed design description of the PANDA Barrel DIRC, which is located between the Straw Tubes Tracker (STT) and the Scintillation Tiles hodoscope (SciTil) and covers the polar angle range of $22^\circ - 140^\circ$. The average radius of the barrel is 47.6 cm. The radiator bars are grouped into 16 flat sections. Each of these contains five fused silica bars optically isolated by a 0.2 mm air gap. The container for each section is made of 0.5 mm thick carbon fibre. There are gaps of about 1.5 cm between neighbouring sections. In the baseline design (see Fig. 3.8) the fused silica bars have dimensions of $17 \times 35 \times 2400$ mm³. Each bar is composed of two sub-bars, each 1200 mm in length, which are optically coupled by a glue. The readout end of the bar is pointing upstream the antiproton beam. The downstream bar end is equipped with a mirror to reflect photons towards the expansion volume. A fused silica window attached to the backward end of the bar box makes each unit hermetic. The EV is a single vessel filled with mineral oil matching the refractive index of fused silica. The relatively small depth of the EV of $d = 30$ cm makes

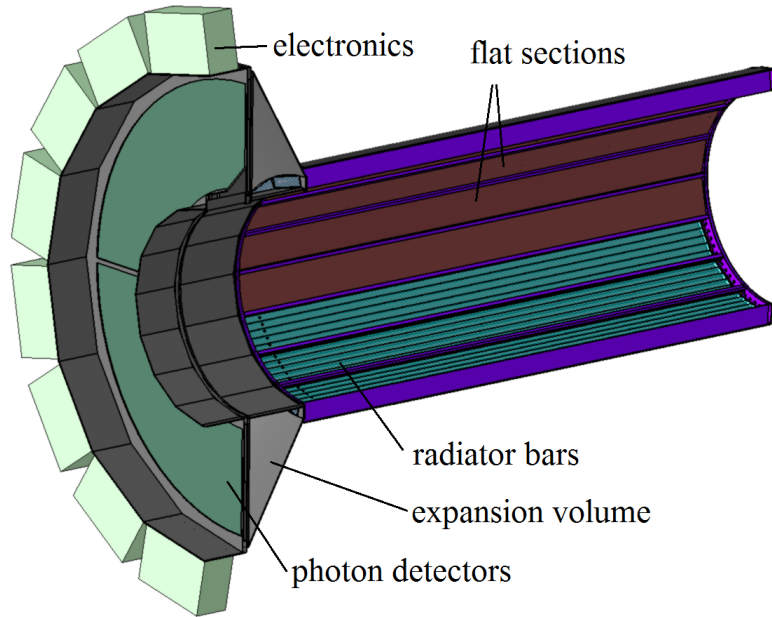


Figure 3.8: Mechanical drawing of the PANDA Barrel DIRC, including support structure for the bar boxes, expansion volume and electronics. The fused silica bars are visible inside three of the bar boxes.

essential the use of a focusing system, implemented by a lens between the radiator bar and the EV.

The photosensors for the PANDA Barrel DIRC were chosen to be Micro-Channel Plate Photomultiplier Tubes (MCP-PMTs). The working principle is illustrated in Fig. 3.9a. An electron from the photocathode created by the photoelectric effect is accelerated in the gap between the cathode and MCP plates, enters the glass capillary (= micro channel) of the first MCP plate, and creates a number of secondary electrons by hitting the channel wall. The avalanche develops while electrons propagate through the channels. Finally, the electron cloud enters the gap between the plate and the anode and drifts in the high voltage to the anode pad, where the electrons are detected. If the size of the electron cloud drifting from the microchannel plate to the anode pads is larger than the gap between adjacent pixels, the charge cloud can induce signals in several pixels at the same time. This effect, called charge sharing, is implemented in the simulation of the photosensors.

The array of MCP-PMTs is located on the upstream side of the expansion volume. This kind of photon detector is able to efficiently detect photons in the visible and near-UV range.³. Furthermore, MCP-PMTs are able to operate in the 1 T magnetic field and are sufficiently radiation hard to sustain $\approx 1 \text{ C/cm}^2$ per year [41]. A photo of the PHOTONIS [42] tube, being a photosensor candidate for the PANDA Barrel DIRC, is shown in Fig. 3.9b. The tube is square with dimensions of $59 \times 59 \text{ mm}^2$, the sensitive area has size of $53 \times 53 \text{ mm}^2$. The anode of the MCP-PMT is divided into 8×8 pixels, each of size $6.5 \times 6.5 \text{ mm}^2$. The photocathode is made of a bialkali-material.



Figure 3.9: a) Working principle of the MCP-PMT. Figure from [43], modified.
 b) Photo of the PHOTONIS XP85012 Planacon MCP-PMT [42].

3.3 Performance Requirements

The general requirement for the PANDA Barrel DIRC is to achieve at least three Standard Deviation (SD) separation between K and π in the momentum range

³According to the Frank-Tamm equation (Eq. 3.4), most photons are emitted with small wavelengths, but they are not transported to the PD due to the properties of the optical joints. The available optical glues are not transparent for photons with small wavelengths (see Fig. 4.6).

up to $3.5 \text{ GeV}/c$, corresponding to 91% efficiency at a 5% misidentification level for one-sided integrals. This means that the total detector resolution should be at most 1/3 of the difference in Cherenkov angle between pions and kaons in the given momentum range. The detector resolution for the PANDA Barrel DIRC can be calculated in the same way as for the *BABAR* DIRC.

PANDA is a fixed target experiment, where the final state particles are distributed non-uniformly in the phase space. Reaction products are boosted forwards, and the higher the momentum of the anti-proton beam particles, the larger the boost. Examples of the correlation of momentum and polar angle of final state kaons and pions for different benchmark channels are shown in Fig. 3.10.

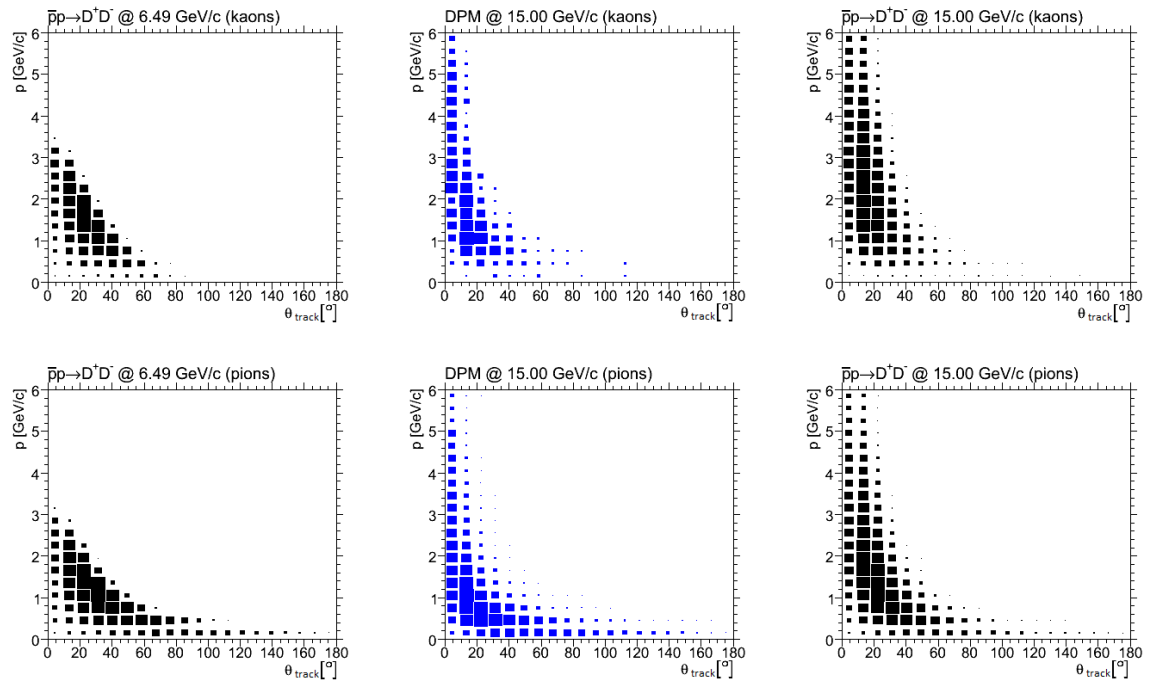


Figure 3.10: Phase space distributions (momentum p vs. track polar angle θ_{track}) for kaons (upper row) and pions (bottom row) coming from D^+D^- decay (signal channel, shown in black) or inelastic $p\bar{p}$ scattering (background distributions created with the DPM event generator [44]), shown in blue). Figures from [19].

The PANDA experiment has a very broad physics program. Therefore, it is at present very difficult to define a specific reaction (for each beam energy), which would provide the most challenging PID conditions. Instead, there is a variety of different channels of scientific interest with a number of potential background reactions (see Ref. [19] for detail), and the PID-devoted detectors should provide sufficiently good PID for all of them at the same time. Usually kaons in the final state correspond to the signal, whereas most of the pions originate from background reactions. The following study of the required Barrel DIRC resolution uses a set of benchmark channels and focuses on positive kaon identification under assumption of Gaussian distributions. The final state kaons are assumed to be identified independently of the other particle hypotheses and particle flux.

Selected benchmark reactions

Most of the reactions at intermediate beam momenta, listed in Ref. [19], do not have kaons with high momenta in their final states. The cumulative phase space plot for some of those channels (listed in Tab. 3.2), where a substantial part of the kaons actually fall into the Barrel DIRC acceptance, is shown in Fig. 3.11a. According to this figure, all final state kaons have momenta below 3.5 GeV/ c . Considering the benchmark channels for PANDA from Ref. [19], one can see that the majority of the reactions with kaons in their final states satisfy the criterion “ $p(K) < 3.5$ GeV/ c ” in the whole acceptance region (in terms of polar angle) of the Barrel DIRC.

Reaction	Decay chain	$p(\bar{p})$ [GeV/ c]
$p\bar{p} \rightarrow K^+K^-2\pi^+2\pi^-$		6.57
$p\bar{p} \rightarrow D^+D^-$		6.57
$p\bar{p} \rightarrow D^{*+}D^{*-}$	$D^{*+} \rightarrow D^0\pi^+$ (67%), $D^{*-} \rightarrow \bar{D}^0\pi^-$ (67%), $D^{*+} \rightarrow D^+\pi^0$ (33%), $D^{*-} \rightarrow \bar{D}^-\pi^0$ (33%)	7.7
$p\bar{p} \rightarrow h_c \rightarrow \eta_c\gamma$	$\eta_c \rightarrow K^{*0}\bar{K}^{*0}$	5.6
$p\bar{p} \rightarrow \Lambda_c^+\Lambda_c^-$	$\Lambda_c^+ \rightarrow pK^-\pi^+$, $\Lambda_c^- \rightarrow \bar{p}K^+\pi^-$	10
$p\bar{p} \rightarrow \phi\phi$		10
$p\bar{p} \rightarrow K^+K^-\gamma$		10
$p\bar{p} \rightarrow \tilde{\eta}_{c1}\eta$	$\tilde{\eta}_{c1} \rightarrow D^0\bar{D}^{*0}$, $\eta \rightarrow \gamma\gamma$, $D^0 \rightarrow K^-\pi^+\pi^0$, $D^{*0} \rightarrow \bar{D}^0\pi^0$, $\bar{D}^0 \rightarrow K^+\pi^-\pi^0$ + c.c.	15

Table 3.2: List of reactions that produce final state kaons with intermediate momenta in the Barrel DIRC acceptance. $\tilde{\eta}_{c1}$ is a predicted charmonium hybrid state [13]. Standard decays are listed in Tab. 3.3.

$D^+ \rightarrow K^-\pi^+\pi^+$	$D^0 \rightarrow K^-\pi^+$	$K^{*0} \rightarrow K^+\pi^-$	$\phi \rightarrow K^+K^-$
$D^- \rightarrow K^+\pi^-\pi^-$	$\bar{D}^0 \rightarrow K^+\pi^-$	$\bar{K}^{*0} \rightarrow K^-\pi^+$	

Table 3.3: Standard decay channels used in reactions listed in Tab. 3.2 and Tab. 3.4.

Nevertheless, some open charm decays at the highest antiproton beam momentum produce kaons with momenta significantly higher than 3.5 GeV/ c . Those reactions are listed in Tab. 3.4. The corresponding cumulative phase space plot, shown in Fig. 3.11b, illustrates that a considerable fraction of kaons with momenta up to 6 GeV/ c end up in the Barrel DIRC acceptance.

Reaction	Decay chain	$p(\bar{p})$ [GeV/c]
$p\bar{p} \rightarrow \tilde{\eta}_{c1}\eta$	$\tilde{\eta}_{c1} \rightarrow D^0\bar{D}^{*0}$, $\eta \rightarrow \gamma\gamma$, $D^0 \rightarrow K^-\pi^-\pi^+\pi^+$, $\bar{D}^{*0} \rightarrow \bar{D}^0\pi^0$	15
$p\bar{p} \rightarrow D^0\bar{D}^0\gamma$		15
$p\bar{p} \rightarrow D^+D^-\gamma$		15
$p\bar{p} \rightarrow D_s^+D_s^-\gamma$	$D_s^+ \rightarrow \phi\pi^+$ (50%), $D_s^- \rightarrow \phi\pi^-$ (50%), $D_s^+ \rightarrow \bar{K}^{*0}K^+$ (50%), $D_s^- \rightarrow K^{*0}K^-$ (50%),	15
$p\bar{p} \rightarrow D^{*0}\bar{D}^{*0}\gamma$	$D^{*0} \rightarrow D^0\pi^0$, $\bar{D}^{*0} \rightarrow \bar{D}^0\pi^0$,	15
$p\bar{p} \rightarrow D^{*+}D^{*-}\gamma$	$D^{*+} \rightarrow D^0\pi^+$ (67%), $D^{*-} \rightarrow \bar{D}^0\pi^-$ (67%), $D^{*+} \rightarrow D^+\pi^0$ (33%), $D^{*-} \rightarrow D^-\pi^0$ (33%),	15
$p\bar{p} \rightarrow \phi\phi$		15
$p\bar{p} \rightarrow D^{*0}\bar{D}^{*0}$	$D^{*0} \rightarrow D^0\pi^0$, $\bar{D}^{*0} \rightarrow \bar{D}^0\pi^0$	15
$p\bar{p} \rightarrow D_s^+\bar{D}_s^-$	$D_s^+ \rightarrow \phi\pi^+$ (50%), $D_s^- \rightarrow \phi\pi^-$ (50%), $D_s^+ \rightarrow \bar{K}^{*0}K^+$ (50%), $D_s^- \rightarrow K^{*0}K^-$ (50%),	15
$p\bar{p} \rightarrow D^+D^-$		15
$p\bar{p} \rightarrow D^0\bar{D}^0$		15

Table 3.4: List of reactions that produce final state kaons with high momenta in the Barrel DIRC acceptance. $\tilde{\eta}_{c1}$ is a predicted charmonium hybrid state [13]. Standard decays are listed in Tab. 3.3.

Regarding the current state-of-the-art technology, PANDA-specific geometrical conditions and reasonable budget, it probably will be impossible to build a DIRC detector able to separate kaons from pions up to 6 GeV/c. However, optimizing the design could make it possible to shift the upper momentum limit corresponding to 3 SD kaon/pion separation from 3.5 to approximately 4 GeV/c. In that case kaons with momenta above 4 GeV/c will also end up in the Barrel DIRC acceptance. They would not be identified as efficiently as less energetic kaons. The fraction of the final state kaons with momenta below a particular threshold is shown in Fig. 3.12. For example, for the channel $p\bar{p} \rightarrow D^0\bar{D}^0$ at $p(\bar{p}) = 15$ GeV/c (the lowermost green line), which produces the most energetic kaons, 18% of them have momentum above 3.5 GeV/c.

In that case energetic kaons from some reactions will also end up in the Barrel DIRC acceptance, for which the PID would not work as effectively as for the other

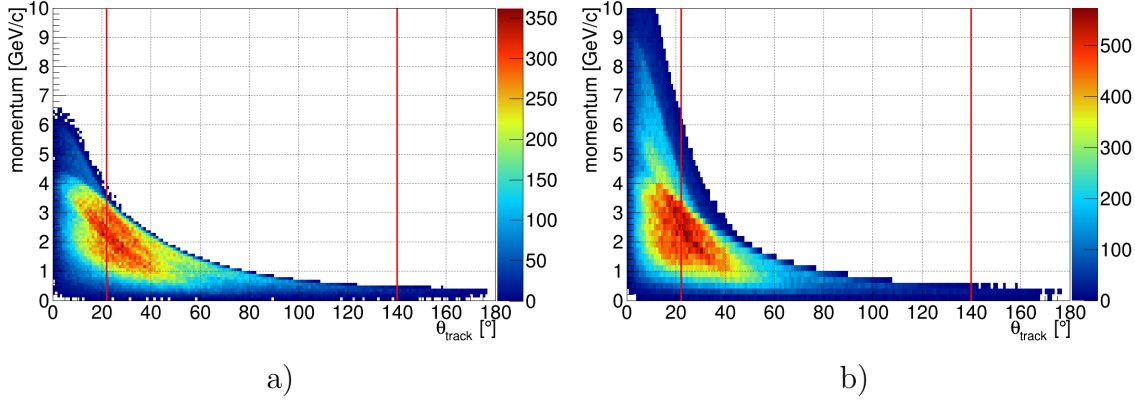


Figure 3.11: Phase space occupancy of the final state kaons coming from the reactions listed in Tab. 3.2 (a) and Tab. 3.4 (b). All channels are taken with equal weights. The red lines show the limiting polar angle of the Barrel DIRC acceptance.

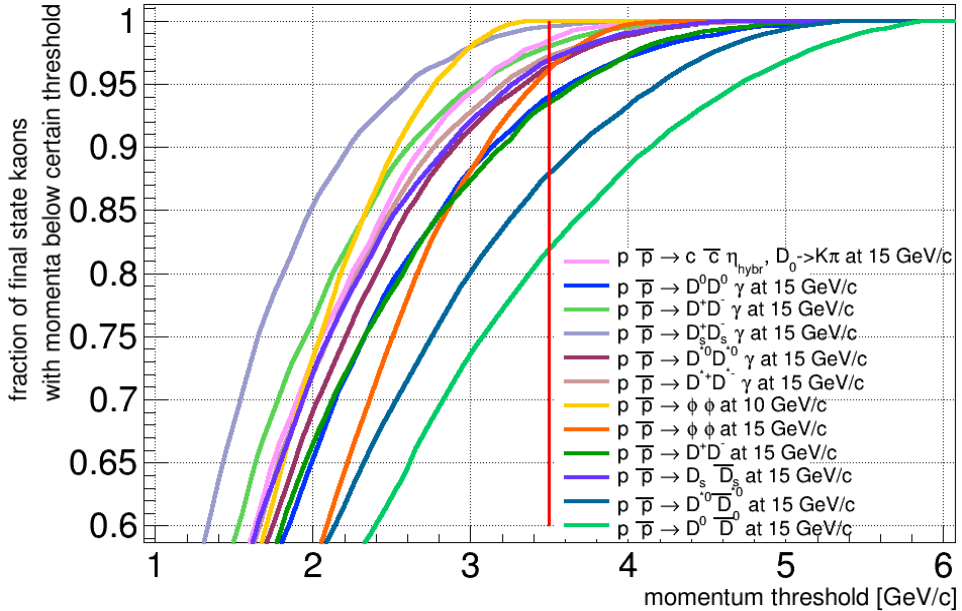


Figure 3.12: Fraction of kaons with momenta below a certain threshold as a function of this threshold.

less energetic channels. The fraction of the final state kaons with momenta below a particular threshold is shown in Fig. 3.12. For example, for the channel $p\bar{p} \rightarrow D^0 \bar{D}^0$ at $p(\bar{p}) = 15$ GeV/c (the lowermost green line), which produces the most energetic kaons, 18% of them have momentum above 3.5 GeV/c. It is important to study the impact of the kaon efficiency loss on the kaons phase space distributions, as the smoothness of such distributions is of particular importance for certain physics analyses.

Analysis of selected channels

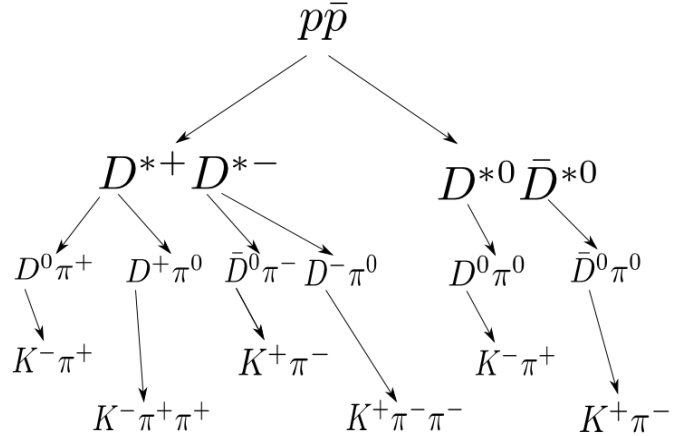


Figure 3.13: Decay chain of the D^* mesons.

Decays of D^* mesons at the maximum antiproton beam momentum of 15 GeV/c are instructive examples to study the impact of kaon efficiency on the phase space distributions. The considered scheme of the simulated decay is shown in Fig. 3.13, where exactly two kaons are produced in the final state of each individual decay chain. Figure 3.14 shows the momentum distributions for D and D^* , Fig. 3.15 the corresponding invariant mass spectra of the D^* mesons.

Different colors reflect four different cases:

- Red – both kaons in the final state are in the Barrel DIRC angular acceptance
- Blue – both of these kaons have momenta lower than 3.5 GeV/c
- Magenta – one kaon has a momentum below, the other one above 3.5 GeV/c
- Green – both kaons have momenta higher than 3.5 GeV/c

Obviously the shape of the blue distributions do not exhibit any holes or cuts, therefore, it can be anticipated that, even if kaons with momenta above 3.5 GeV/c will not at all be identified⁴ the shapes of simple phase space plots are generally conserved.

A more sophisticated approach to examine the non-uniformity of the phase-space occupancy of three-body decays is given by a Dalitz plot⁵ study. In cases where the particles were simulated following simple phase-space kinematics, the area of the Dalitz plot is uniformly filled.

The uniformity has been studied e.g., for decays $D^+ \rightarrow K^-\pi^+\pi^+$, where the phase-space distributions are determined for the following cases:

⁴This case is more severe than the reality, because kaons with momenta above 3.5 GeV/c might still be identified with separation lower than three SD.

⁵A Dalitz plot represents m_{12}^2 vs m_{13}^2 for three body decays $M \rightarrow m_1 m_2 m_3$.

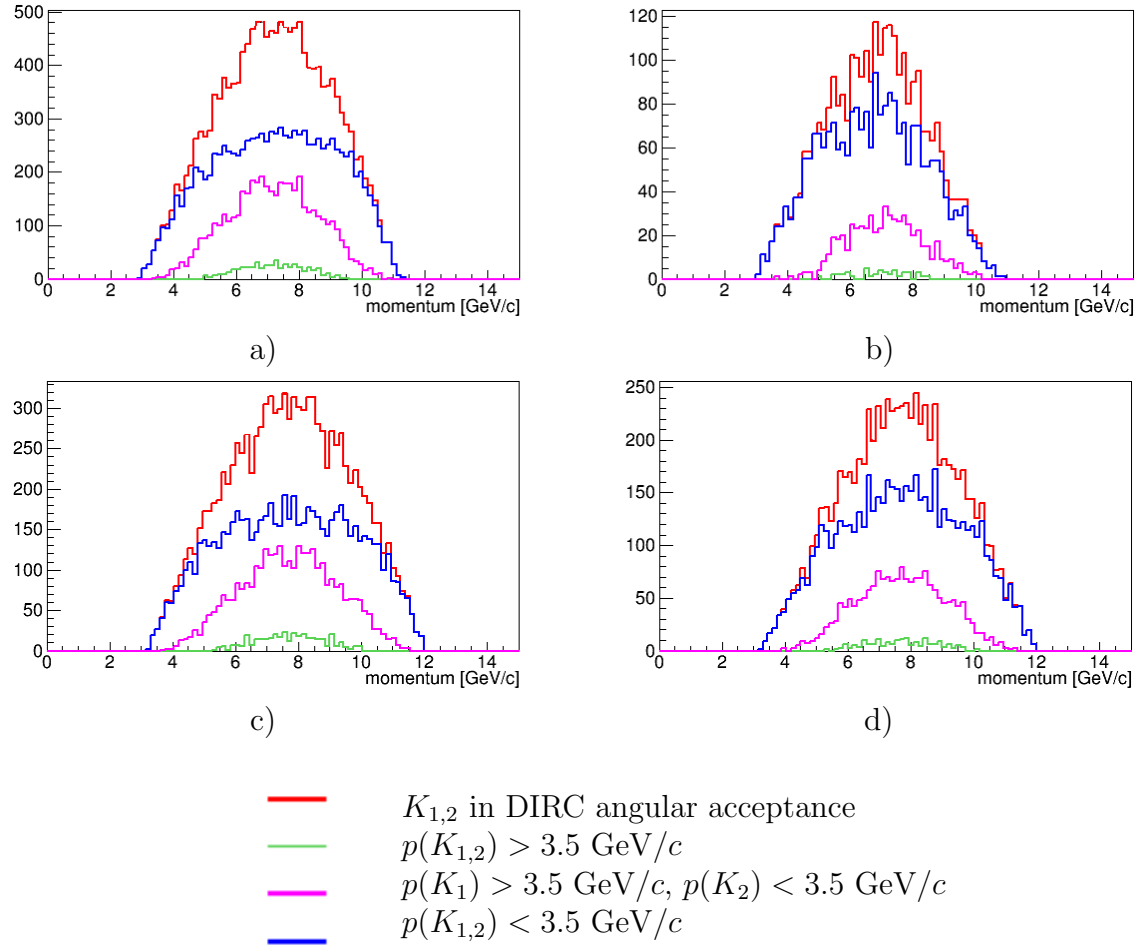


Figure 3.14: Momentum spectrum for D^0 (a), D^\pm (b), D^{*0} (c), and $D^{*\pm}$ (d) mesons produced in the decay chains shown in Fig. 3.13. The color code corresponds to the listed four different cases.

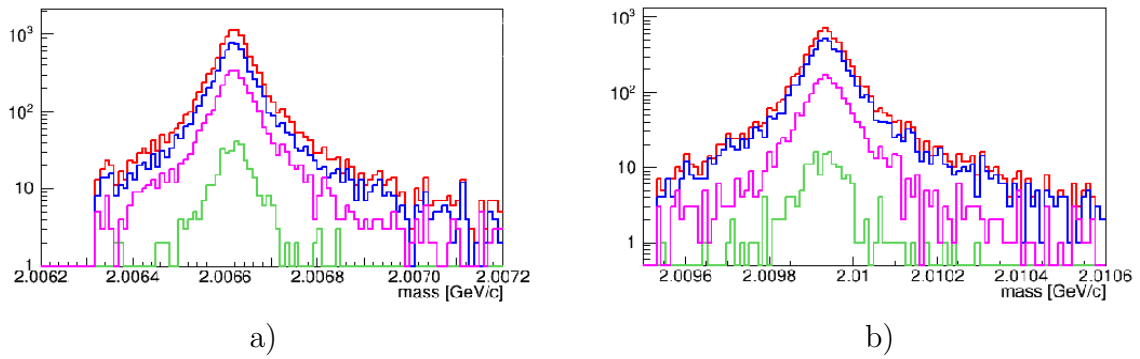


Figure 3.15: Invariant mass spectrum for D^{*0} (a) and for the $D^{*\pm}$ (b) produced in the decay chains shown in Fig. 3.13. Coloring as in Fig. 3.14.

1. Only kaons in the Barrel DIRC acceptance with momenta below $3.5 \text{ GeV}/c$ are considered.

2. All the kaons ending up in the Barrel DIRC acceptance are taken into account.

The ratio of these two distributions represents the efficiency as a function of the two-dimensional phase space, which is shown in Fig. 3.16. In case when only kaons with momenta below 3.5 GeV/c could be identified in the Barrel DIRC, the shape of the two-dimensional phase space distribution is slightly distorted. The resulting Dalitz plot is nevertheless sufficiently smooth and close to one, which allows correction for the kaon efficiency in the future physics analysis of the PANDA data.

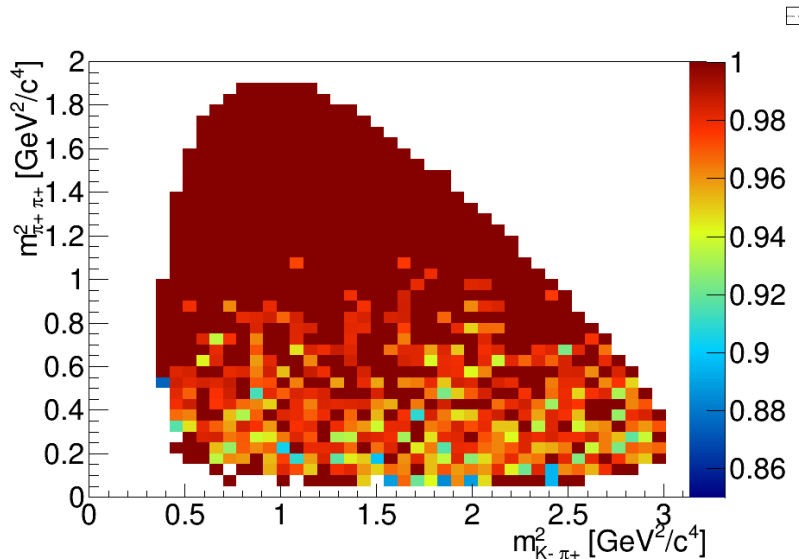


Figure 3.16: Phase space dependent efficiency distribution of D^\pm mesons originating in the decay 3.13 for the kaon momentum acceptance limit of 3.5 GeV/c .

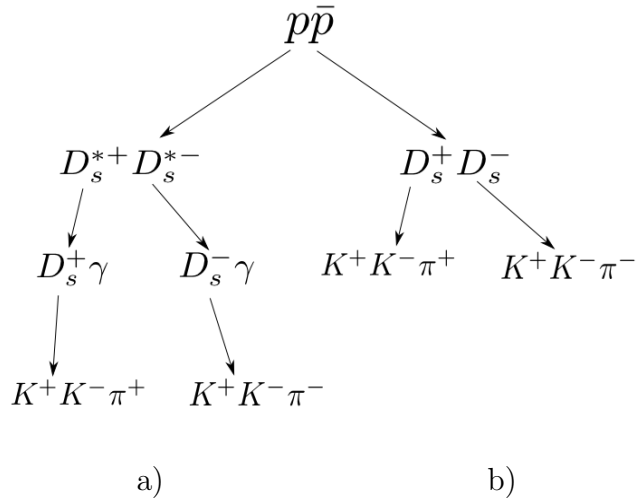


Figure 3.17: Decay chain of the D_s mesons.

Decays of $D_s^{*\pm}$ and D_s^\pm mesons (shown in Fig. 3.17) also provide prominent amount of highly energetic kaons ending up in the Barrel DIRC acceptance. Here all the possible decay chains under consideration lead to three particles in the final state, which makes possible studying of the corresponding Dalitz plots. The same method as above has been applied to derive the corresponding efficiency distributions for the D_s mesons, which are shown in Fig. 3.18.

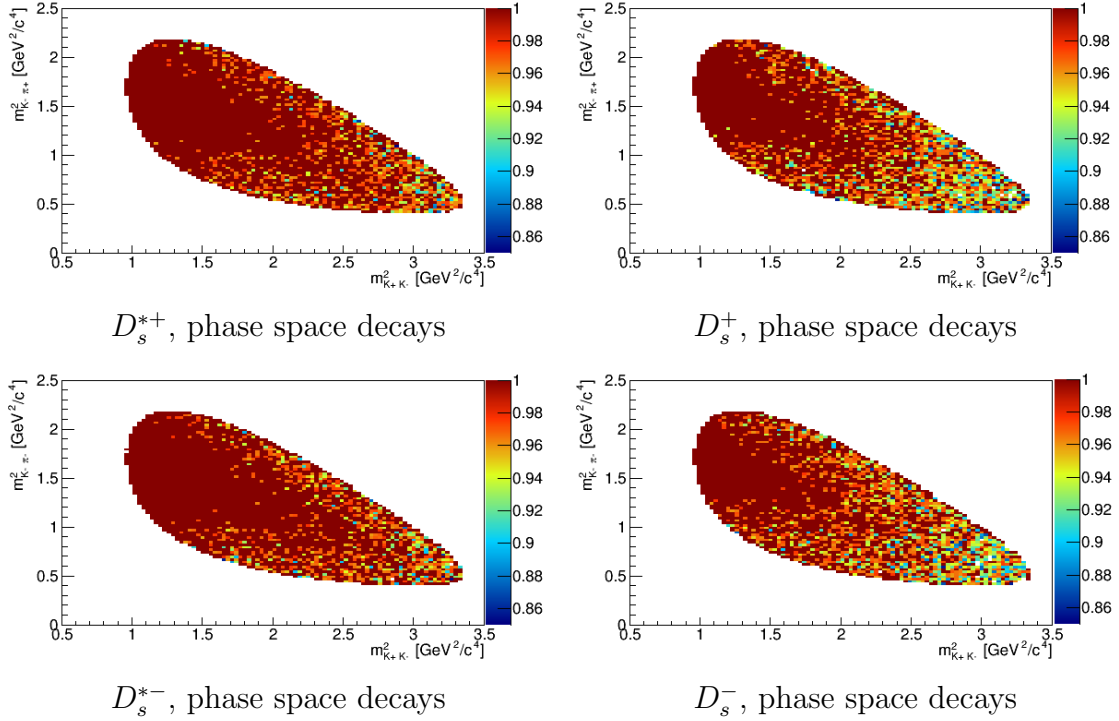


Figure 3.18: Phase space dependent efficiency distributions of D_s mesons from decays 3.17a (on the left) and 3.17b (on the right) for the kaon momentum acceptance limit of 3.5 GeV/c .

The effect in both cases is at the order of some percent. Again, the shape of the kaon phase space plots is affected by the upper momentum limit of the 3σ -interval, but the distributions look smooth. The undistorted shape of the phase space distributions is an important characteristic, which allows implementation of corrections for the future physics analysis.

The absolute majority of the final state kaons produced in a wide range of the PANDA benchmark reactions have momenta below 3.5 GeV/c . This means, that the general PID requirement ensures efficient separation of kaons from background pions in almost all cases. However, there are channels with highly energetic kaons in the final states, e.g. decays of D and D_s mesons. For these reactions the relevant distributions of mass and momenta, and Dalitz plots were studied. The worst case scenario was considered, when kaons with momenta above 3.5 GeV/c are not identified at all. The shape of phase space distributions is not dramatically distorted and the reconstruction efficiencies for D and D_s mesons are smoothly distributed.

This means, that such channels can be analysed using efficiency corrections. The possibility to extend the upper momentum limit by about $0.5 \text{ GeV}/c$ would result in a gain for the physics analysis.

Limit for the detector resolution

The phase space distributions of the final state kaons and pions (Fig. 3.10) demonstrate that large particle momenta clearly correlate with small values of polar angles, whereas for large values of polar angles the maximum available kaon momentum drops significantly. Figure 3.19a represents a cumulative phase space distribution of the final state kaons produced in open charm decays with the beam momentum of $p = 15 \text{ GeV}/c$. The color scale indicates the occupancy. The high momentum region ($p = 3.5 \text{ GeV}/c$), where $\theta_C(\pi) - \theta_C(K) \approx 8.5 \text{ mrad}$ (see Fig. 3.3) is the most challenging for the PANDA Barrel DIRC. Assuming a Gaussian shape of the reconstructed Cherenkov angle distributions and the required separation of three sigma, the corresponding required Cherenkov angle resolution for a track $\sigma_{\theta_C,track}$ is about 2.8 mrad. The difference in Cherenkov angle between kaons and pions increases rapidly with decreasing momentum, so that for less energetic particles the same separation can be achieved with worse detector resolution. For example, for kaons with $\theta_{track} = 90^\circ$ the PID requirement effectively softens to three SD up to $1 \text{ GeV}/c$, since there are no kaons at 90° with $p > 1 \text{ GeV}/c$. In order to construct the functional dependency $p_{max}(\theta_{track})$ from the cumulative distribution shown in Fig. 3.19a, the following procedure is applied: as long as there are kaons with momentum higher than $3.5 \text{ GeV}/c$, the maximum kaon momentum accepted by the Barrel DIRC is assumed to stay constant at the level $3.5 \text{ GeV}/c$, otherwise the maximum kaon momentum envelopes the upper edge of the cumulative kaon phase space distribution. The green line in Fig. 3.19a illustrates the empirically obtained relation between the maximum kaon momentum and the track polar angle. Figure 3.19b shows the resulting upper limit for the acceptable Cherenkov angle resolution per track

$$\max \sigma_{\theta_C}(\theta_{track}) = \frac{1}{3} \cdot (\theta_{C,K}(p_{max}, \theta_{track}) - \theta_{C,\pi}(p_{max}, \theta_{track})). \quad (3.12)$$

The empirically obtained required detector resolution is based on the difference in Cherenkov angles between kaons and pions and is conservatively driven by the maximum kaon momentum. In the polar angle range below $\theta_{track} \approx 35^\circ$ the required detector resolution stays constant at the level of 3 mrad, then it rises steeply with the increasing track polar angle. This function used as a performance figure of merit limits the obtained detector resolution below $\approx 35^\circ$, whereas for the large polar angles the limitation is very soft and does not require any optimization of the detector geometry.

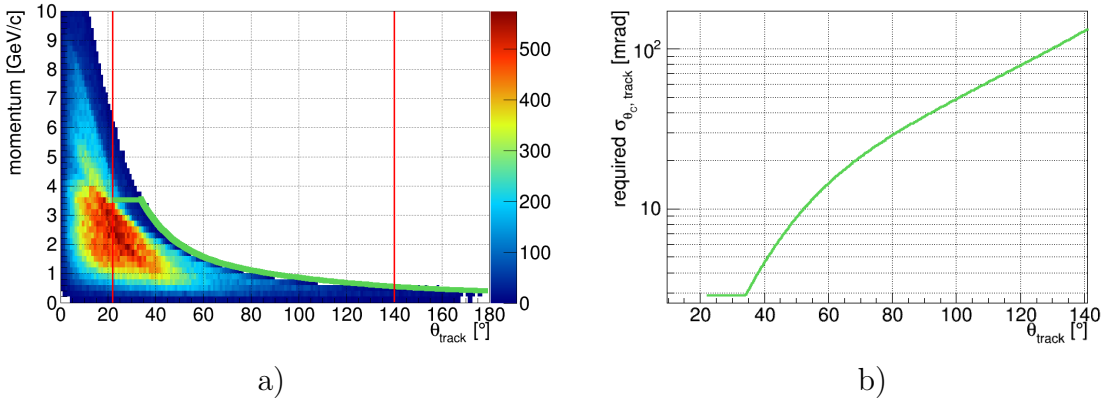


Figure 3.19: a) Cumulative phase space occupancy for the final state kaons coming from open charm decays for beam momentum $p = 15 \text{ GeV}/c$. The maximum kaon momentum (and thus, the effective momentum requirement for the separation) as a function of the polar angle is empirically defined and shown as a green line. Red lines mark the angular acceptance of the PANDA Barrel DIRC. b) Required PANDA Barrel DIRC resolution, obtained using the maximum kaon momentum as a function of the track polar angle θ_{track} .

Contribution from Tracking Detectors

The charged particle direction, provided by the tracking system, is an input parameter for the DIRC. The error on the charged particle direction is described by the angular tracking resolution $\sigma_{tracking}$. In the total PANDA Barrel DIRC detector resolution (see Eq. 3.11) $\sigma_{tracking}$ is included in σ_{corr} .

Fig. 3.20 represents the tracking resolution including the multiple scattering effects [45]. It was calculated using single track MC events. The kaons were generated at the IP with momenta varying from 0.5 to $5 \text{ GeV}/c$ with the step of $0.5 \text{ GeV}/c$. The reconstructed tracks were propagated to the Barrel DIRC radiators. There the reconstructed kaon direction compared to the MC true one provided the basis for the represented $\sigma_{tracking}$.

The tracking resolution was transformed into a function $\sigma_{corr}(\theta_{track})$ by evaluating $\sigma_{corr}(p)$ (shown in Fig. 3.20) for each polar angle at a such momentum value, where Eq. 3.11 takes the maximum value. The first term σ_{corr} decreases with increasing momentum, and the behaviour of σ_0 is the opposite. A closer look at a few selected points in phase space revealed that the contribution from the tracking resolution does not dominate the performance of the PANDA Barrel DIRC for any design. Given the tracking resolution in Fig. 3.20, the most challenging region is always that with high momenta. This can be illustrated using Eq. 3.11 and the main constraint on the total detector resolution under requirement of three SD separation: $\Delta\theta_C/3 \geq \sigma_{\theta_C, track}$. The upper limit for σ_0 can then be expressed as

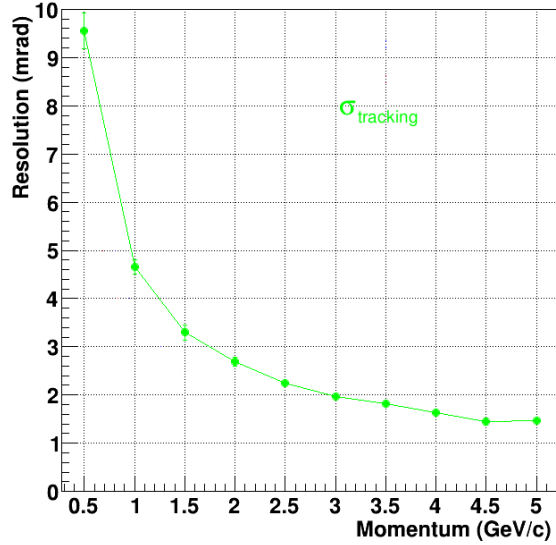


Figure 3.20: Angular tracking resolution calculated at the Barrel DIRC radius [45].

$$\sigma_0 < \sqrt{\frac{\Delta\theta_C^2(p)}{9} - \sigma_{corr}^2(p)} = w(p). \quad (3.13)$$

The function $w(p)$ is shown in Fig. 3.21. The limit for $\sigma_0(p)$ is a continuous function, which decreases with momentum and does not have any local minima. Therefore, the most challenging case is always connected with the maximum momentum accessible for a particular value of the polar angle and thus, the difference in Cherenkov angle between species of interest and not the tracking resolution. Therefore, the relevant kaon momentum for calculating the tracking resolution is the envelope of the phase space distribution from Fig. 3.19a. The resulting $\sigma_{tracking}(\theta_{track})$ is shown in Fig. 3.22 as the blue line.

Cherenkov angle resolution per track

While $\sigma_{tracking}$ is an external quantity for the PANDA Barrel DIRC, the second term σ_0 in the total detector resolution $\sigma_{\theta_C,track}$ (see Eq. 3.11) reflects the performance of the PANDA Barrel DIRC. Taking into account the upper limit for the required PANDA Barrel DIRC resolution σ_0 , shown in Fig. 3.19b and the estimated tracking resolution, the upper limit for the required σ_0 as a function of the track polar angle can be estimated as

$$\sigma_0 < \frac{\sigma_{\theta_C}}{\sqrt{N_\gamma}} = \sqrt{\sigma_{\theta_C,track}^2 - \sigma_{corr}^2}. \quad (3.14)$$

Assuming $\sigma_{corr} = \sigma_{tracking}$ we get

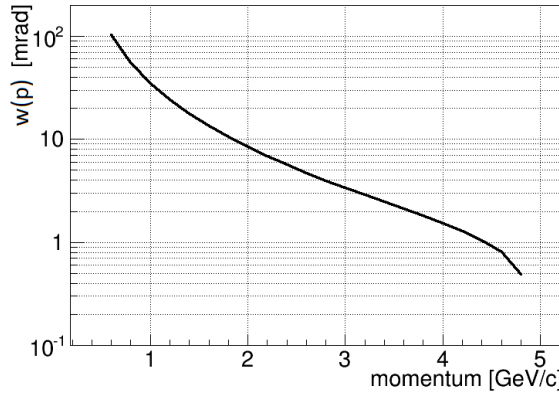


Figure 3.21: The required upper limit for the PANDA Barrel DIRC resolution σ_0 as a function of charged particle momentum p assuming three SD separation between kaons and pions and tracking resolution from Fig. 3.20.

$$\sigma_0 < \sqrt{\sigma_{\theta_C,track}^2 - \sigma_{tracking}^2}. \quad (3.15)$$

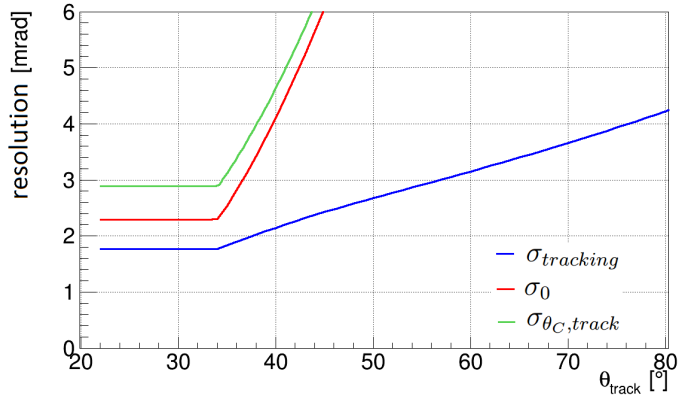


Figure 3.22: The tracking resolution $\sigma_{tracking}$ (blue), the upper limits for the required PANDA Barrel DIRC resolution $\sigma_{\theta_C,track}$ (green) and for σ_0 (red) as functions of the track polar angle θ_{track} .

The upper limit for the required $\sigma_0(\theta_{track})$ is shown in Fig. 3.22 as the red line. For the polar angles up to 33° the PANDA Barrel DIRC has to achieve $\sigma_0 = 2.15$ mrad to meet the PID goal. The relation between $\max \sigma_0$ and θ_{track} is used as a figure of merit for evaluation of different design options: in case when the simulated $\sigma_0(\theta_{track})$ points are located under the red line, the design satisfies the PANDA PID requirement. The evaluation of different PANDA Barrel DIRC designs are presented in Chapter 4.

Chapter 4

Detector Design Optimization

The concept and the baseline design of the PANDA Barrel DIRC were described in detail in the previous chapter. The baseline design of the PANDA Barrel DIRC is based on the *BABAR* DIRC, however, there are a number of alternative design elements and tunable parameters. The optimization of the final detector design aims to reduce the total detector cost keeping the performance sufficient for the PANDA PID requirement. The key aspect of the optimization study is the detailed detector simulation. It includes the complex geometry of the Barrel DIRC optical elements. The detector signal was reconstructed using a geometric algorithm similar to the one used for *BABAR* DIRC. The results of the performance evaluation studies helped to decide on the most optimal design for the PANDA Barrel DIRC.

4.1 Parameter Space

The technology of the DIRC counters is quite new, as the pioneer in this field and the only operating detector the *BABAR* DIRC was proposed in 1992. There are currently several large projects around the world developing DIRC counters for accelerator experiments. All of the DIRCs for large accelerator experiments are being designed to distinguish between kaons, pions and/or protons in a momentum range from the Cherenkov threshold up to ≈ 4 GeV/c and are using solid radiators. Although many of the current barrel DIRC projects inherit the main geometry features from the *BABAR* DIRC (and even some parts of the detector itself), there is no doubt that the necessary improvements, which are essential for the future experiments, require a significant departure from the *BABAR* system, demanding extensive R&D. The challenges include the design of a more compact EV and sophisticated focusing elements. Modern pixel PDs (MCP-PMT or SiPM), which have emerged more than a decade later than the design of the *BABAR* DIRC was developed, can substantially improve the performance of DIRCs due to their small size and fast response. The presence of the magnetic field in the area of PDs may challenge the detector development. The main DIRC devices can be grouped into two categories based on their shape: barrel (*BABAR* DIRC, Belle II [43, 46], FDIRC for Super B [47, 48], PANDA Barrel DIRC), and end-caps (PANDA Disc DIRC [22],

TORCH for LHCb [49–51], WASA@COSY DIRC [52–55]).

The PANDA Barrel DIRC inherits from the *BABAR* DIRC the general layout of the main functional elements. However, the baseline design requires optimization of the wide range of geometric parameters and the choice between some alternative detector components. This improvement has a goal of achieving possibly lower detector cost keeping the sufficient performance. Therefore, it makes sense to prioritize the design elements according to their value. The main cost driver is the fabrication of radiators, in particular the total number of polished surfaces [56]. The second important criterion is the number of photosensors used. The other parameters have lower priority in terms of the total cost, but they also were investigated carefully, since many parameters correlate with each other and their particular combination results into a specific detector performance. The particular design parameters and options studied in this thesis are presented in Tab. 4.1 and discussed below. The set of the optimal values describes the most suitable PANDA Barrel DIRC design.

Radiator dimensions	Focusing	EV parameters
width [cm]: 3.2, 4.0, 5.3 thickness [cm]: 1.0, 1.7, 2.0	with/without air gap N components: 1, 2, 3 cylindrical, spherical, asymmetric	type: tank, prism opening angle [°]: 36, 42, 48 offset range [cm]: downward (0, 5), upward (0, 10) tilt of the PD plane [°]: 10, 20, 30 EV depth [cm]: 30, 35 combined pixels of the PD

Table 4.1: Overview of the studied parameter values and design options.

The use of fewer radiators with fixed dimensions of the bar box ultimately leads to a single radiator plate filling each section, which is obviously the most favourable solution in terms of cost and construction. Such radiators are going to be used by Belle II DIRCs. This option requires an alternative likelihood-based reconstruction approach, which does not reconstruct the Cherenkov angle itself, but is focused on the differences in hit patterns for different particle species. A version of the PANDA Barrel DIRC design with wide radiator plates (one per bar box) instead of narrow bars is being investigated as well [57] and will not be discussed any further here. The studied options for the radiator width are the baseline 5.3 cm, corresponding to five bars per bar box, 4.0 cm, and 3.2 cm (four and three radiators per section). For these cases the geometric reconstruction approach, discussed further, can be applied. Another radiator dimension is the thickness. Thinner bars reduce the Barrel DIRC material budget and improve the pinhole focusing on the cost of the

photon yield. Thicker radiators ensure more detected photons and are more likely to require a focusing system. The thickness of the DIRC bars is naturally limited by the production possibility and the available space inside the PANDA detector. For the study the variation of the radiator thickness in the range between 1.0 cm and 2.0 cm was considered.



Figure 4.1: Photo of a fused silica prism used as an EV in the test beam.

The optimization of the total number of photosensors is strongly coupled to the type of the EV. The shape and the material of the expansion volume influence the total detector cost and the number of photosensors used. An alternative compact prism-shaped expansion volume for each bar box is shown in Fig. 4.1. Most future DIRCs tend to use a compact fused silica EV for each section of the barrel (FDIRC, Belle II). This option was not yet proved to work under real experimental conditions, but is expected to perform well, as was shown in prototype tests. The PANDA Barrel DIRC geometries with the tank and prism-shaped EVs are shown in Fig. 4.4a,b. The whole detector requires 16 prisms and 240 photosensors, which results in a lower total detector cost than the baseline option with the oil tank and 282 MCP-PMTs. Another important advantage of prisms is that they are easier to assemble and align, as the alignment of each bar box with the corresponding prism EV becomes independent of the rest of the barrel. Figure 4.2 shows one section of the barrel with the compact EV in simulation. In turn, the baseline single vessel EV has some crucial disadvantages. The quite large amount of oil filling the tank EV requires a complicated infrastructure (e.g. pumps), which makes it difficult to maintain such an EV during the periods of detector operation. The inner sides of the EV have to be mirrored to reflect Cherenkov photons so that they end up on the photosensors. The procedure of mirroring and keeping the high mirror quality during the whole detector life is complicated in case, when the mirror is located in oil.

The particular shape of the prism should be tailored according to the focusing system and available space. Figure 4.3 illustrates the tunable parameters of the photon camera, which are the upward and the downward steps, the opening angle, the depth, and the tilt/shape of the detection surface. The steps of the EV are the vertical distances between the radiator bar sides and the edges of the prism (see Fig. 4.3). The values between 0 cm and 10 cm were considered for the upper step, and between 0 cm and 5 cm for the downward step. The opening angle of the

EV is defined by the EV depth and the number of MCP-PMT rows located on the detection surface. The baseline depth of the EV is 30 cm. Given this, three values of the EV opening angle were taken into account, corresponding to four ($\alpha_4 = 36^\circ$), five (baseline, $\alpha_5 = 42^\circ$), and six ($\alpha_6 = 48^\circ$) horizontal rows of MCP-PMTs. The larger distance between the radiators and photosensors ensures better performance, but the space limitations inside the PANDA detector do not allow significantly deeper EV. The affordable EV depths of 35 and 40 cm were chosen for the test. The detection plane in the baseline design is perpendicular to the symmetry axis of the barrel. The values of 10° , 20° , and 30° for the tilt of the detection plane towards the radiators were taken into account in the study.

The size parameters including the bar thickness, step sizes, vertical lens size, were varied within the baseline design bar box dimensions to see if a good design can be found without the need to redesign the mechanical structures.

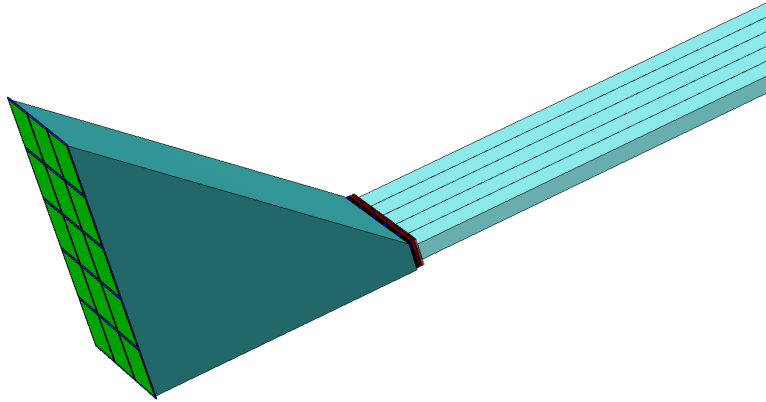


Figure 4.2: The fused silica prism-shaped EV with attached radiators and photosensors comprising one section of the barrel.

An important parameter for the PANDA Barrel DIRC is the total number of channels used for the readout system. The baseline version has square pixels, but they could be also rectangular, when two neighbouring pixels are combined together. This would lead to the reduced by half number of channels.

A key design element dramatically influencing the detector performance is the focusing system. In order to find a sufficient focusing system, the detector performance was studied for layouts with lenses of different complexity, starting from a simple one-component focusing lens with an air gap. A special asymmetric type of lens was studied as well. In total eight lens configurations were implemented and tested in the simulation.

These were the major design options considered for the simulation tests and implemented in the detailed detector simulation. The particular combinations of various geometric parameters are described along with the results.

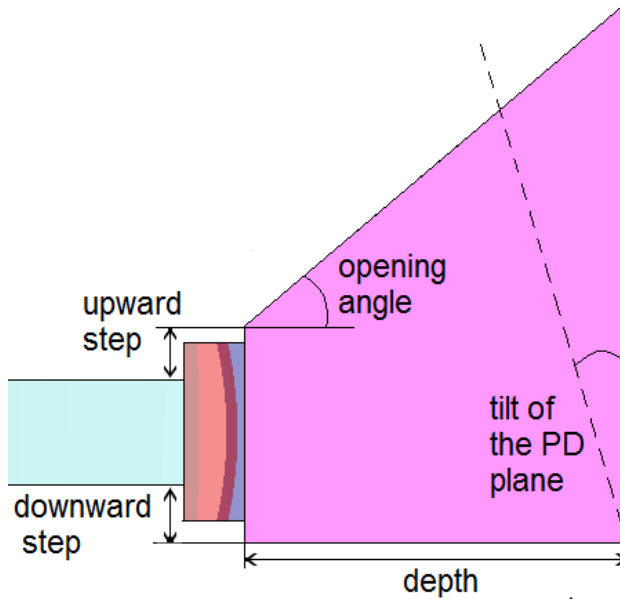


Figure 4.3: Illustration of the parameters of the photon camera, that were tuned to achieve the optimal performance. The schematic is not to scale.

4.2 Detailed Detector Simulation

The simulation of the PANDA Barrel DIRC is a part of the global simulation chain of the PANDA detector. Refinement of the Barrel DIRC model itself includes a detailed description of the photon production and propagation processes, comparison of the simulation results with the test beam data and with the prototype simulation using the ray-tracing software DrcProp [58]. The high optical quality of single elements for the DIRC detectors makes them expensive and, hence, not easy affordable for laboratory testing. Therefore, simulation results are important when making decisions about the geometry of single detector elements as well as for the whole detector.

The software for the detailed simulation of the whole PANDA detector and its response is based on Geant and ROOT [59]. PandaRoot [60–62]) is still under development and thus is being constantly modified. The revision used in this thesis is 23427. For simulation of the interactions of elementary particles with the matter they are passing through, PandaRoot uses Geant, which is the standard transport engine of the HEP community. This program has two versions: Geant3 and Geant4 [63, 64], which deliver compatible results in most of the cases. The concept of Virtual Monte Carlo (VMC) [65] provides a fixed interface to transparently use different models for particle transport with exactly the same code and the same geometry definition. Comparing the results for Geant3 and Geant4 helped to figure out the following problems:

1. The photon group velocity in Geant3 used to be wrong (it was fixed in the version v1.15).

2. The large difference in photon yield between Geant3 and Geant4 was (partly) caused by some bugs in VMC (patched in the version 2.14a, which works with Geant4 9.6.p01)¹.

The software versions used for this thesis are: ROOT 5.34, VMC 2.11 and Geant4.9.4 patch 01 (18 February 2011).

The full simulation of the PANDA detector includes the physical reactions of the particles penetrating its components and the generated detector response. This complex process for any sub-detector consists of a few main stages. First the physics reaction is created with an event generator. Then the generated particles are propagated through the detector volumes. The interactions with the materials are simulated by the chosen transport model. The relevant interactions of particles with sensitive elements are processed into detector-specific data, where relevant resolution effects are also emulated. At the digitization stage the format of the simulated data imitates the real signal of a particular detector, so that the reconstruction can consistently be performed on both kinds of data (real and MC) without any changes in the software. In the following sections the detailed description of the PANDA Barrel DIRC simulation chain is presented.

Simulation Stage

A detector in simulation is defined by the geometry description and the functionality of the sensitive elements. Each simulated sub-detector can be either activated or put into the setup as passive material.

The baseline PANDA Barrel DIRC design is shown in Fig. 4.4a and described in detail in Sec. 3.2. The detector geometry is an important part of the detector simulation. It should resemble all main features of the detector and contain all the elements responsible for the detector response. At the same time it should be simple and contain as few geometrical constituents as possible to keep the simulation fast. Each volume is defined by its shape and material. The general physical properties of the media (such as density, atomic weights, atomic numbers etc.) are used by the transport engine to simulate interactions of the particles with detector materials (e.g., Bremsstrahlung, ionization, production of secondary particles). If a material has, in addition, Cherenkov properties, then a particle can emit Cherenkov photons inside this material. The expectation value of the number of Cherenkov photons emitted per unit of trajectory dN/dx is calculated according to the Frank-Tamm equation (3.4). During the propagation process of a charged particle inside a volume consisting of a material with Cherenkov properties the number of photons produced within each step is generated according to a Poisson distribution with the mean of $\langle n \rangle = L_{\text{step}} \cdot dN/dx$. After the photons are produced they are propagated individually

¹Special settings for Geant4 adjusted the number of Cherenkov photons at the production stage, so that it was the same in Geant4 and Geant3. Currently there is still some remaining difference at 10% level in the number of detected photons between the two versions. This effect is related to the absorption of Cherenkov photons in the materials of photosensors.

through the detector materials. The particles are transported inside the detector volume by the Monte Carlo engine in an iterative process to discrete positions with a certain step size. At each of these positions a detector-specific routine is called by the transport software in order to process the simulated information inside its sensitive volumes. There, the current particle state (e.g. momentum, type, and mother-daughter relation) and the relevant processes during the current step (e.g. reflection, refraction) are available.

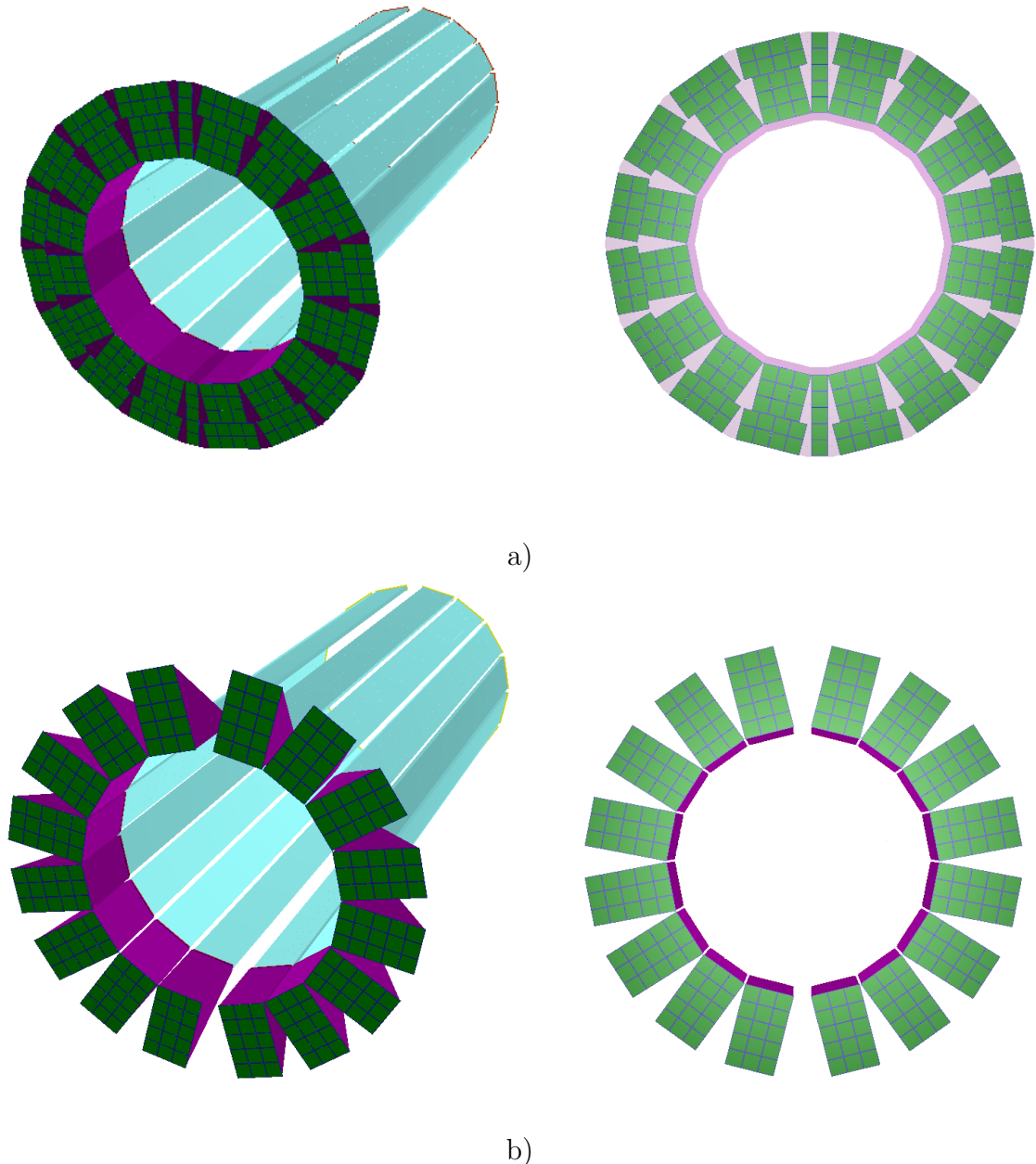


Figure 4.4: The PANDA Barrel DIRC in simulation and the layout of the photosensors on the PD plane: a) the baseline design with the tank EV, b) the design with the alternative compact prism-shaped EV.

The most important issue for the PANDA Barrel DIRC simulation is the realistic transport of Cherenkov photons through the optical elements of the detector from production to detection. Out of about 260 photons produced per cm along the charged particle track inside the radiator (according to Eq. 3.5) only about 20 are expected to be detected for some track configurations. Typical photon energies are at the order of few eV. For proper estimation of the detector performance it is very important to predict realistic photon yields. The majority of the emitted photons is lost during the propagation through the detector. The schematic of the functional optical elements in the yz projection, illustrating different materials, used in the PANDA Barrel DIRC simulation, is shown in Fig. 4.5. The physical processes in the materials are simulated by Geant based on the main Cherenkov properties. Figure 4.6 illustrates the wavelength dependent attenuation lengths and refractive indices based on the experimental data. The materials coupling together the elements of the detector optical system can introduce additional photon losses due to the poor Cherenkov properties. In the simulation the sub-bars are glued with $d_{\text{glue}} = 50 \mu\text{m}$ thick layer of the optical glue Epotek [66]. To couple together the bar box, EV, and MCP-PMTs the optical grease EJ-550 [67] was used. The layer with $d_{\text{EVgrease}} = 15 \mu\text{m}$ thickness was introduced between the bar box window and the EV, and that of $d_{\text{MCPgrease}} = 500 \mu\text{m}$ thickness between the EV and photosensors.

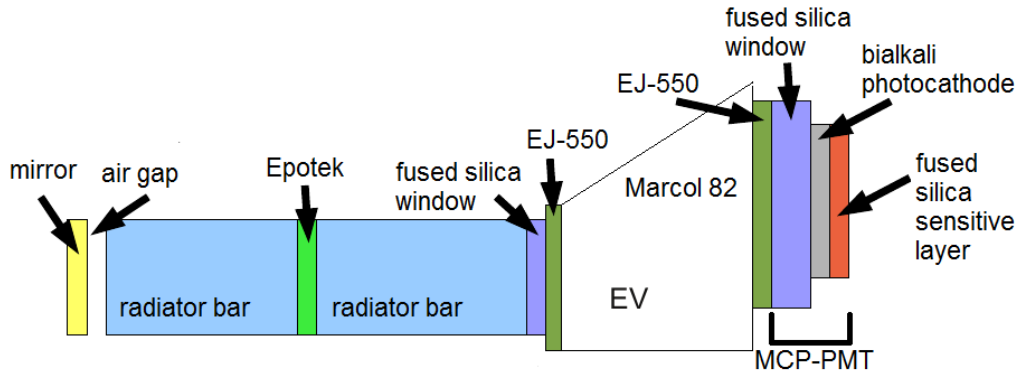


Figure 4.5: Schematic of one bar box in yz projection for the simplified case without focusing, which illustrates the materials used for the detector simulation.

The processes of total internal reflection, chromatic dispersion, transmission, and absorption of Cherenkov photons inside the optical elements of the PANDA Barrel DIRC are treated by Geant.

When a simulated Cherenkov photon passes from one medium to another, the particular photon behaviour depends on the propagation algorithm² as well as on the properties of the two media, and the border properties. Although it was possible to run the detector simulation software with both Geant3 and Geant4, the latter was chosen to be the propagation engine for the studies performed here. It provides

²In Geant4, as soon as a photon comes across a border between two volumes, it makes a virtual step into the next volume and then back “probing” the material properties, and in Geant3 this does not happen.

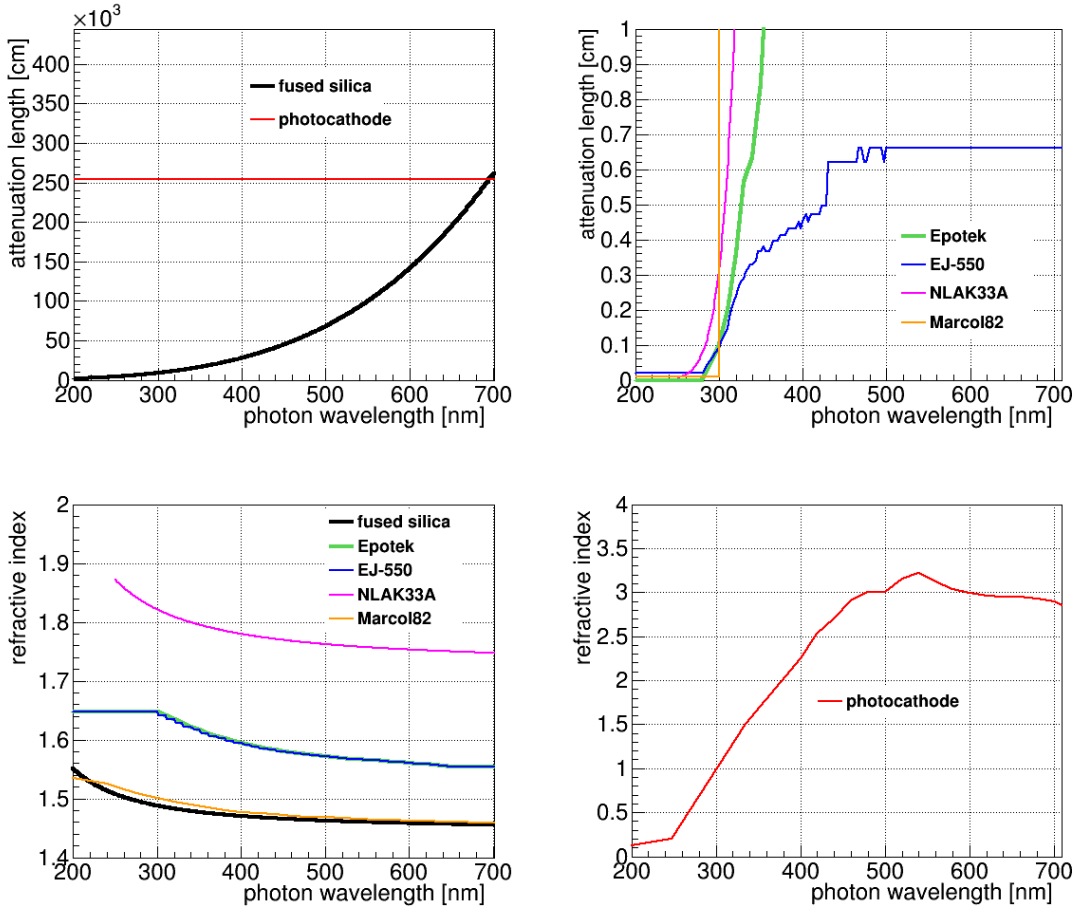


Figure 4.6: The wavelength-dependent attenuation lengths and refractive indices of the materials used in the PANDA Barrel DIRC simulation.

definition of optical surfaces between volumes with different properties (such as reflectivity or roughness), whereas in Geant3 the surfaces of the volumes are always ideal and photon reflection/refraction on the border happens based only on the Cherenkov properties of the two materials. The functionality of optical surfaces allows more realistic description of the detector: photons can be reflected on the borders between materials even if one of them does not have Cherenkov properties (such as the flat mirror at the bar end).

The Cherenkov photons trapped inside the radiator due to total internal reflection effect get reflected off the radiator sides. Due to surface roughness photons can get scattered to a random direction or escape from the radiator. The probability P for a single reflection on the radiator side depends on the photon wavelength λ , incident angle of the photon α , refractive index n , and the surface roughness r . According to the scalar theory [68]

$$P \approx 1 - \left(\frac{4\pi \cdot r \cdot \cos(\alpha) \cdot n(\lambda)}{\lambda} \right)^2, r \ll \lambda. \quad (4.1)$$

$P(\lambda, \alpha)$ is illustrated in Fig. 4.7. The surface finish is expected to be similar to that of *BABAR* radiators, which was $r \approx 5 \text{ \AA}$ [39]. Cherenkov photons usually undergo $N = \mathcal{O}(10) - \mathcal{O}(100)$ internal reflections inside long radiators. The probability to survive the transportation through the whole radiator can be calculated as $P_{total} = P^N$. In the simulation the radiator sides are perfectly polished, therefore the transport efficiency was implemented in the hit-processing function and calculated for each single photon at the production stage. The number of reflections N was calculated based on the initial photon direction with respect to the radiator sides. Fig. 4.8 illustrates the impact of the transport efficiency on the photon yield for the whole range of the track polar angles θ_{track} . At steep polar angles the effect is about 25 – 30%, whereas in the middle it is as large as 40%. This correlates with the Cherenkov cone orientation inside the radiator: for the track polar angles around 90° the Cherenkov cone is oriented upwards, and photons have more reflections on the radiator sides than in cases, when the charged particle went shallowly through the bar.

For those photons reaching the flat mirror attached to the upstream radiator end the probability to be reflected back is implemented according to the experimental data shown in Fig. 4.9a.

The photon sensors are represented in the simulation as a set of functional layers (see Fig. 4.5). The propagation of Cherenkov photons through them is handled by Geant. The detection efficiency was applied additionally. It consists of the following terms:

1. The collection efficiency – corresponds to the probability for a photoelectron to enter a microchannel, which is driven by the open area fraction of the microchannel plate (for Planacon MCP-PMT it is typically 0.65 [69])
2. The quantum efficiency – corresponds to the probability for a photon to create a photoelectron. For the bialkali photocathode the relation between the quantum efficiency and the photon wavelength is shown in Fig. 4.9b.

The packing fraction, which is the fraction of the detection surface covered with photosensitive material, is influenced by the width of the MCP-PMT case, the thickness of the support structure holding the array of MCP-PMTs together, and by the arrangement of the MCP-PMTs on the PD surface. An example of the layout of photosensors for the tank expansion volume is shown in Fig. 4.4b on the right. Here 282 MCP-PMTs are used leading to the packing efficiency of around 72%. The gaps between the neighbouring pixels cause a photon loss of approximately 4%. For the prism expansion volumes, shown in Fig. 4.4b, the packing efficiency is around 81%, including the gaps between the pixels. To save processing time the detector efficiency is applied at the photon production stage.

The deterioration effects caused by imperfections of the physical shape of the radiators are not taken into account, since the production specifications for the *PANDA* Barrel DIRC radiators are not yet known. The radiator bars in the detector simulation are perfect parallelepipeds, unlike in reality. Therefore, the systematic

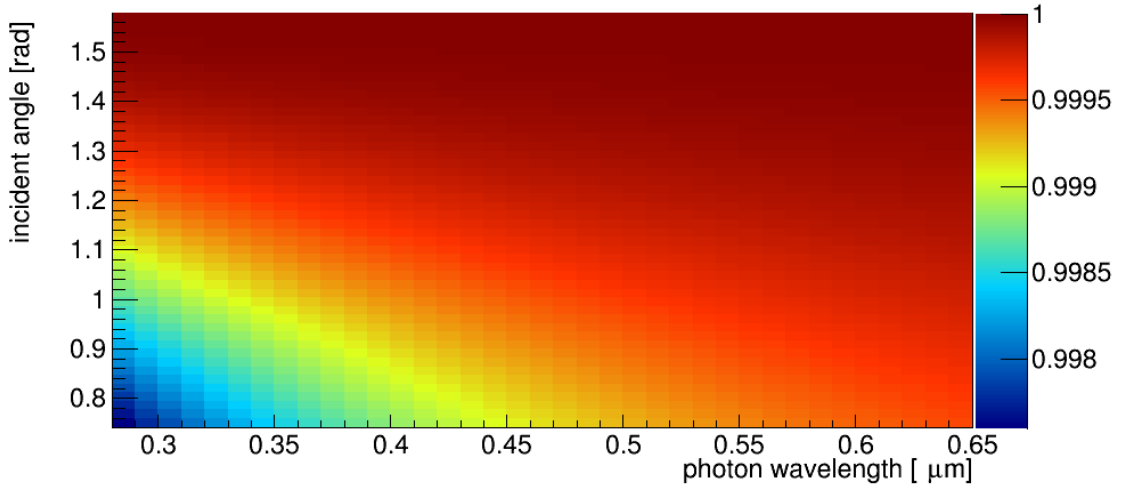


Figure 4.7: Reflection coefficient P as a function of the wavelength and incident angle of the photon.

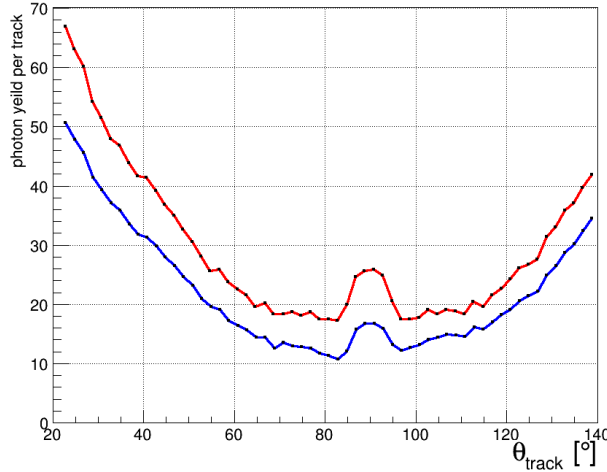


Figure 4.8: Difference in photon yield for the PANDA Barrel DIRC for the case when no transport efficiency is applied (red) and when it is taken into account (blue).

smearing of the photon direction at every reflection inside the real radiator, which introduces an additional error to the reconstructed photon direction and therefore, to the obtained Cherenkov angle, is not taken into account for this thesis.

Fig. 4.10 illustrates photon losses at different stages inside the PANDA Barrel DIRC detector as a function of the photon wavelength. The spectrum of photons generated by Geant (dark blue) is cut for $\lambda < 120$ nm due to the limit in the Cherenkov properties table. Those photons that satisfy the total internal reflection condition contribute to the violet spectrum. The Cherenkov photons trapped inside

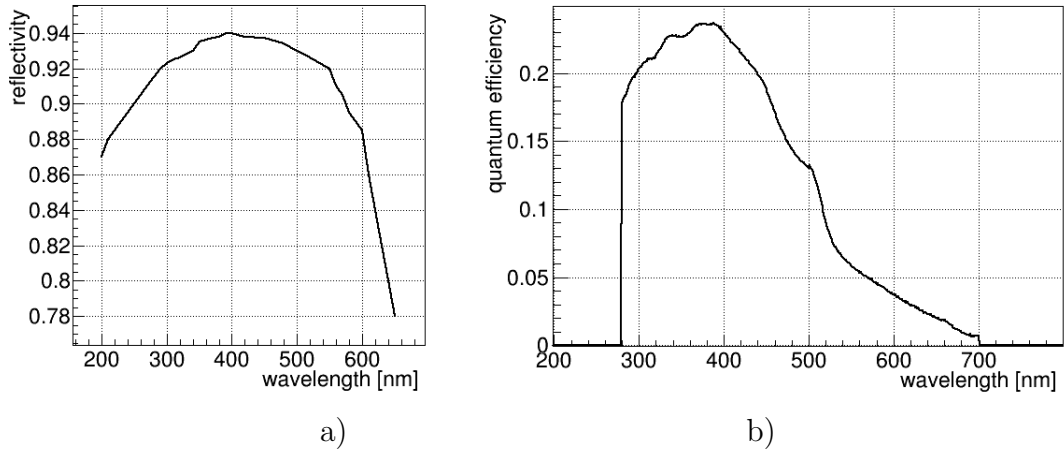


Figure 4.9: a) Mirror reflectivity [39], b) the quantum efficiency of the PD [72].

the radiator propagate towards the flat mirror attached to the end of the bar. The blue spectrum illustrates the fraction of them successfully reflected on the flat mirror or on the air gap between the mirror and the bar. The teal spectrum represents the impact of transporting the photons through the whole radiator. The optical glue that couples together two sub-bars is nontransparent below $\lambda = 280$ nm [39], which causes the sharp acceptance cut in the cyan spectrum. The green spectrum reflects the fraction of photons that passed the lens and entered the expansion volume, which is filled with a mineral oil. The absorption length of the Marcol 82 oil [70] is quite short (see Fig. 4.6) leading to the yellow spectrum. The photons reached the photocathode are shown in the orange spectrum. The final spectrum of detected photons is represented in red.

Kaleidoscopic Effect

The so-called “kaleidoscopic effect” is an optics phenomenon taking place in long radiators with rectangular cross section, where photons undergo many reflections while transportation. If Cherenkov photons are transported through a DIRC bar and projected onto a distant screen, the picture of the cone gets folded, which does not happen in the case, when the photons do not experience any reflections on the way from the production point to the imaging plane. The distortion of the resulting pattern happens because different parts of the cone experience different numbers of reflections on the radiator sides. The conic sections corresponding to the groups of photons having the same reflections get displaced from the ideal curve. The distance between them and the ideal curve corresponds to the thickness and the width of the radiator. This effect was studied in detail for FDIRC [71].

The gradual decrease of the resolution and formation of kaleidoscopic patterns is shown in Fig. 4.11. To simulate the kaleidoscopic effect Cherenkov photons were generated in a single point towards the readout end of the bar. The distance between the origin and the read out end of the bar is labelled on the plots as Δz . Photon

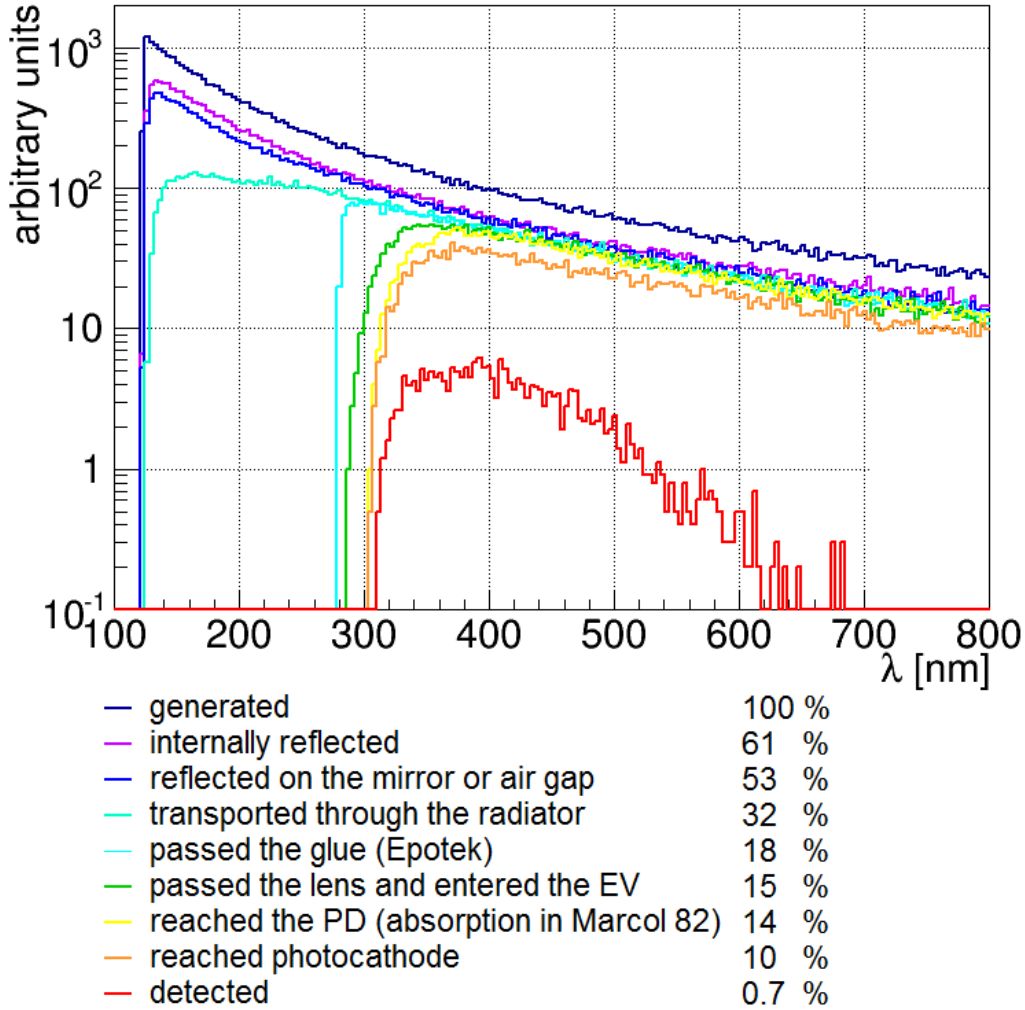


Figure 4.10: The photon wavelength spectra for 3 GeV/c forward going muons, measured at different stages of photon propagation inside the detector. The plot illustrates the gradual decrease in the number of Cherenkov photons from the production to the detection. Each spectrum results from the previous one. Percentages are given with respect to the dark blue spectrum (100%).

directions formed one half of a cone with the opening angle of 45° for the case illustrated in Fig. 4.11a and 30° for the case shown in Fig. 4.11b. When no focusing was used, the natural thickness of the image when photons did not have reflections on the radiator sides is defined by the spread in the photon wavelength (see upper left plot in Fig. 4.11a, where $\Delta z = 0$). Moving the photon origin deeper inside the radiator bar (corresponding to $\Delta z > 0$) and making the photons reflect off the radiator sides, the resolution of the projected picture gets uniformly worse, ring segments get displaced with respect to the ideal line, but stay parallel to it. For the case when a lens is attached to the read out end of the radiator bar (Fig. 4.11b), the ring segments get additionally rotated with respect to the ideal line. This effect increases while going from the middle of the picture towards the outer parts, where

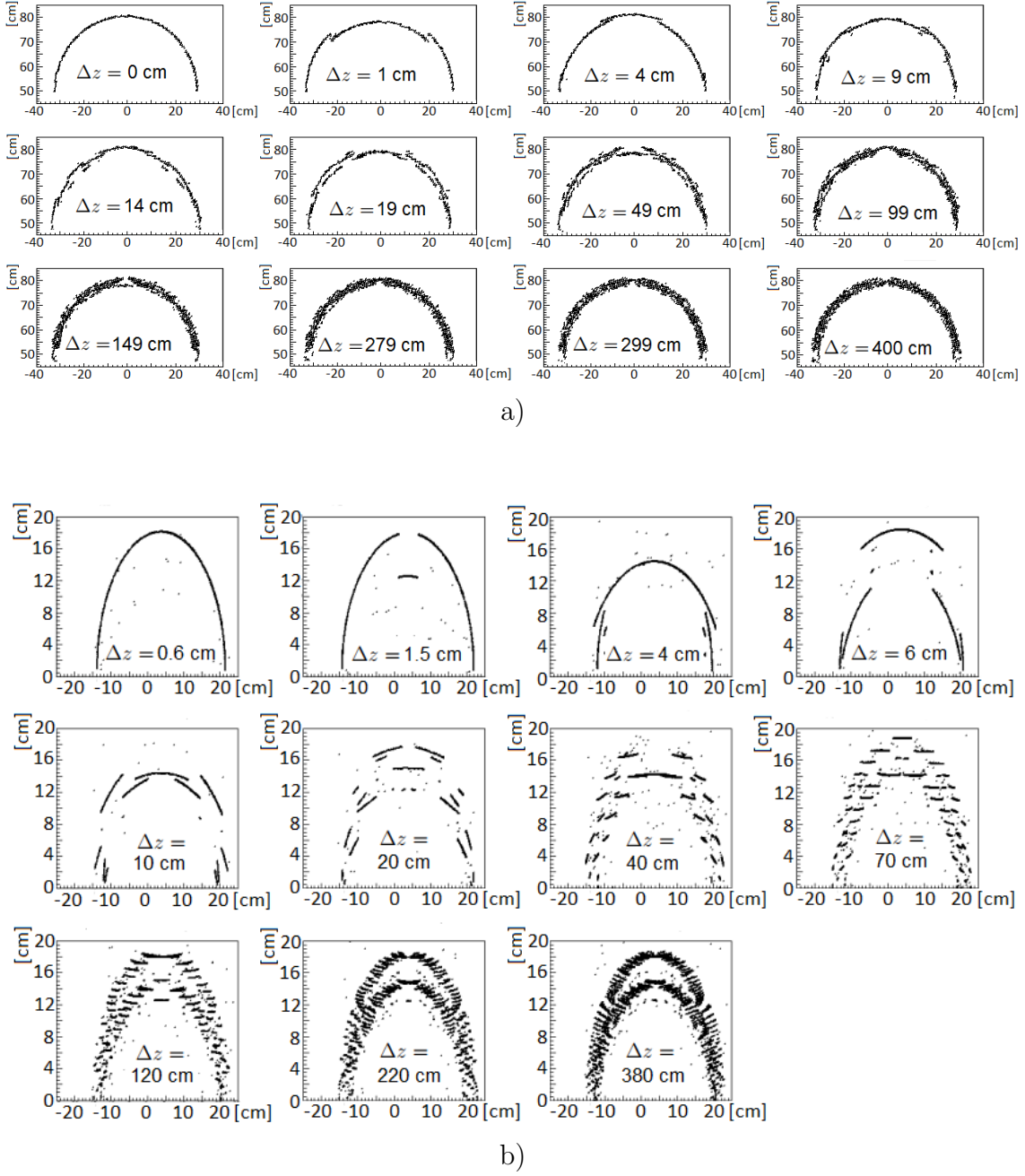


Figure 4.11: Photon locations for different distances between the Cherenkov cone origin and the radiator read out end Δz illustrating the kaleidoscopic effect: a) setup without lens – the hit pattern gets thicker with increasing Δz , b) setup with a lens – individual ring segments are almost perpendicular to the initial arch at large Δz , which is most prominent towards the wings of the hit pattern. The double ring structure is caused by an additional reflection on the wall located in the expansion region perpendicularly to the screen.

the ring segments stay almost perpendicular to the original position. This effect is

consistently reproduced in all simulations independently of the lens geometry used. It influences the total detector resolution – the impact of the kaleidoscopic effect can not be eliminated by using lenses or other focusing systems.

Digitization Stage

The digitization process, being the emulation of the detector response, starts at the level of the PD. As soon as a photon reaches the sensitive layer of the PD it stops and creates a data object, containing the position and time. The digitized information is created on the next stage based on these data.

The digitization stage transforms the MC objects into the digitized data comparable to the signal from the real detector. For the PANDA Barrel DIRC the raw detector information consists of the unique references of the pixels being hit and the corresponding hit times. The actual spatial positions of the hit pixels are determined via a lookup table. Since the readout system for the PANDA Barrel DIRC is not yet finalized, the pixels in the simulation are globally enumerated for simplicity. The digitization stage (see Fig. 4.12) was created in the course of this thesis and simulates the detector specific phenomena, such as charge sharing, dark noise, and timing resolution.

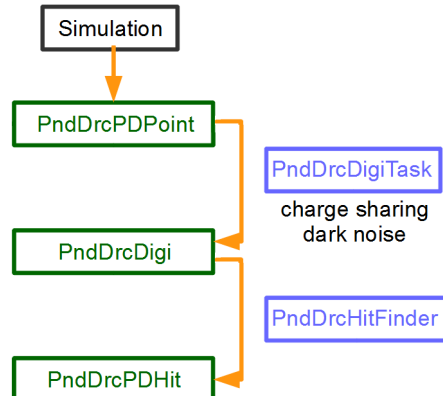


Figure 4.12: Simulation scheme of the PANDA Barrel DIRC response.

The charge sharing effect is characterized by the probability to induce a signal in the neighbouring pixels given the position of the photon hit. This value depends on the size of the charge cloud with respect to the pixel dimensions. Figure 4.13 illustrates the measured anode signal as a function of the light pulse position on the sensitive surface of a MCP-PMT [41]. The upper edge of each signal distribution was fit with the error function representing the integral of a Gaussian distribution. The obtained Gaussian $\sigma = 1$ mm was used as the charged sharing characteristic in the simulation. Ultimately the charge sharing effect can improve the detector performance. Applying the center of gravity method to the pixels, which share the charge cloud, makes it possible to obtain subpixel resolution.

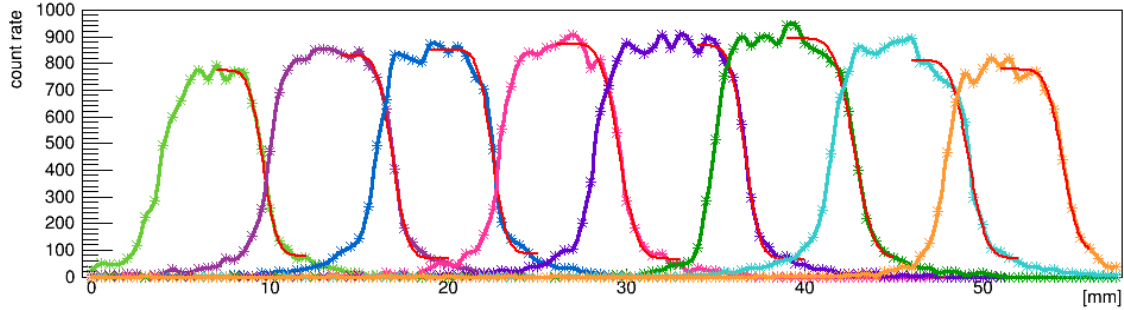


Figure 4.13: Detector response for different pixels (shown in different colors) as a function of the light source position. The data is measured for the fourth row of a PHOTONIS XP85012 MCP-PMT. Figure from Ref. [41]. The red lines show the Gaussian error function fit to the right edge of the signal distributions.

The charge sharing effect is significant for the prototype tests, whereas for the conditions of the PANDA experiment its influence is expected to be rather modest. The charge cloud drifting from the micro-channel tubes towards the anode pads does not expand much in the magnetic field, which will be the case at PANDA. When the external magnetic field lines are approximately parallel to the electric field lines inside the MCP, the electrons in the cloud follow the spiral trajectories aligned to the magnetic field, which diminishes the effect of electron repulsion inside the cloud. The charge sharing effect was implemented in the simulation as an optional feature.

The average value of the dark noise for the photosensors is estimated to be 1 kHz/pixel [72]. The maximum average PANDA event rate at design luminosity is about 20 MHz. Therefore, the probability for a given pixel to have a dark noise count in an individual event is $\sim 5 \cdot 10^{-5}$. There are about 15000 pixels, which means that in each event there is on average one pixel with dark noise for the whole PD surface. The dark count rate of 1 pixel per event will be resolved using the timing information in reconstruction. In the case of the lower event rate of below 1 MHz (during the starting phase of the experiment) the dark noise stays at the same level, as the duration of one event for the DIRC depends on the time of Cherenkov photon propagation through the detector optical system and not on the event rate. For the study presented in this thesis the effect of dark noise is not taken into account.

To make the ideal MC time of the photon detection look more like the detector signal it is smeared according to a Gaussian distribution with $\sigma = 100$ ps, which is based on the photodetector resolution, and digitized with granularity of 1 ps.

4.3 Reconstruction Method

Figure 4.14 illustrates the creation of the detector response in the PANDA Barrel DIRC. The charged particle, shown in gray, traverses one of the radiators, creating Cherenkov photons (orange). They are transported to the photodetectors, where a

small fraction of the initially created photons is detected. The typical hit pattern has the shape of a conic section in the case of the tank EV and a more complicated hit pattern in the case of the prism EV. The color scale from blue (low values) to red (high values) illustrates the photosensors occupancy. The detector raw data includes the pixel number and timing information for each detected photon. Combined with the particle momentum, provided by the tracking system, this information allows the reconstruction of the Cherenkov angle for each charged particle. This value is the basis for extraction of the PID information. Ultimately, each reconstructed charged particle candidate gets a set of probabilities, one for each particle hypothesis. The reconstruction algorithm for the Cherenkov angle, which is going to be used in the PANDA Barrel DIRC, depends on the final detector design, but in any case it should be fast enough to be usable by the online event filtering process.

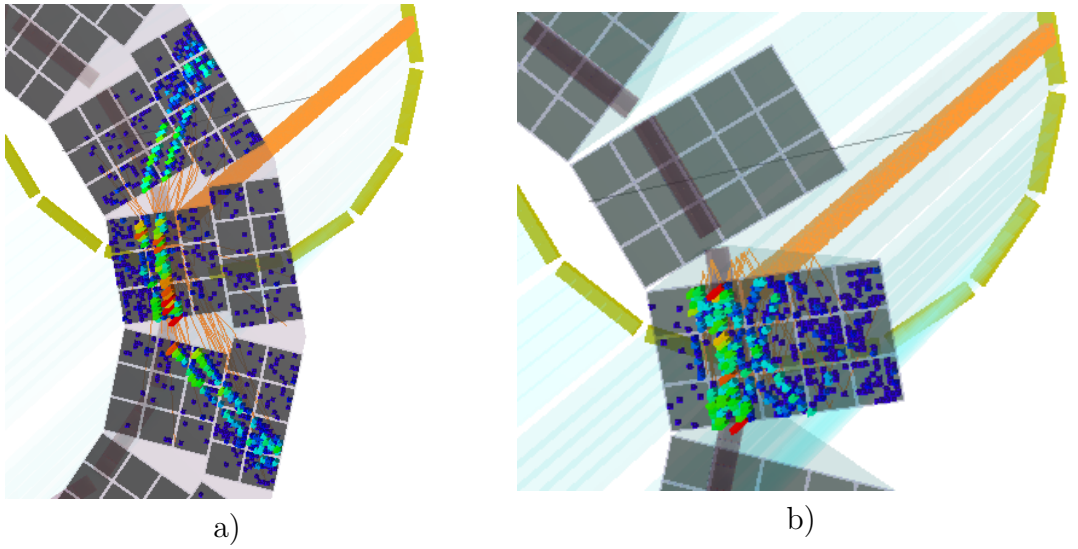


Figure 4.14: Typical hit pattern of the PANDA Barrel DIRC for the baseline design with the tank (a) and prism (b) types of EV. The charged particle (gray) hits the radiator producing Cherenkov photons (orange). The photons are guided all the way through the optical system to the photon detectors and form a hit pattern. The color scale represents the cumulative occupancy. Here the hit patterns from 100 muon tracks with the same direction were superimposed. The blue color corresponds to low, the red to high values.

The reconstruction procedure used for the performance evaluation studies is based on the *BABAR* DIRC geometric approach. In this method, illustrated in Fig. 4.15, the Cherenkov angle is reconstructed individually for every detected photon based on the directions of the charged particle and the photon. The location of the charged particle track is identified by the tracking system. The photon direction is estimated using the spatial positions of the radiator bar, where the photon was produced, and that of the pixel, where the photon was detected.

The described reconstruction method works much faster than others, like Hough-transformation [73] or ray-tracing. This is because the mean photon direction for each pixel on the photodetection surface depends only on the detector geometry

and can be simulated in advance and stored in a special map called “look-up table”. Figure 4.16 illustrates the reconstruction procedure. A three-dimensional photon direction vector \vec{k} is defined pointing from the center of the bar end to the center of the pixel. For an event with some particle type, momentum and location (see Fig. 4.16a), each detected photon yields a set of solutions for the initial photon direction \vec{k}_{init} (see Fig. 4.16b). Together with the track direction, each \vec{k}_{init} gives one hypothesis for the reconstructed Cherenkov angle of the photon (see Fig. 4.16c). Among these solutions there is always the correct one entering the signal peak in the distribution. Going through all the hit pixels for the particle track and collecting the reconstructed Cherenkov angles in a histogram gives a distribution peaking at the expected value of the Cherenkov angle. When the expectation, calculated based on the charged particle momentum and the mean refractive index of fused silica, is subtracted, the resulting distribution peaks at zero (see Fig. 4.16d). The width of the obtained distribution represents the single photon Cherenkov angle resolution (SPR).

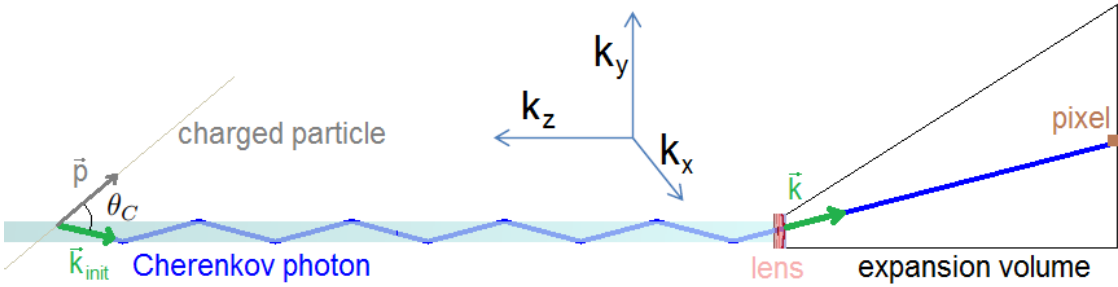


Figure 4.15: Schematic of the reconstruction concept, with one example Cherenkov photon emitted by a charged particle. The photon direction vector \vec{k} is an estimator of the initial photon direction \vec{k}_{init} and is used to reconstruct θ_C . The depicted bar coordinate system is used to describe the photon transportation.

Ambiguities of the Photon Direction

The photon propagation vector at the production point \vec{k}_{init} , in combination with the particle direction, defines the Cherenkov angle θ_C (see Fig. 4.15). During the transport to the PDs a photon experiences reflections inside the optical system of the detector, which changes the propagation vector while preserving the magnitude. In the coordinate system defined by the main axes of the radiator bar (shown in Fig. 4.15) each reflection corresponds to the flip of the sign in the corresponding component of the vector $\vec{k} = (k_x, k_y, k_z)$. Given the initial direction \vec{k}_{init} , the photon propagation vector can have one of the eight possible directions, defined as different combinations of two possibilities for each component: left/right for k_x , up/down for k_y and forward/backward for k_z . The possible photon directions are called “bar ambiguities” ($N_{amb\ BAR} = 8$), as the particular sign combination of the \vec{k}_{init}

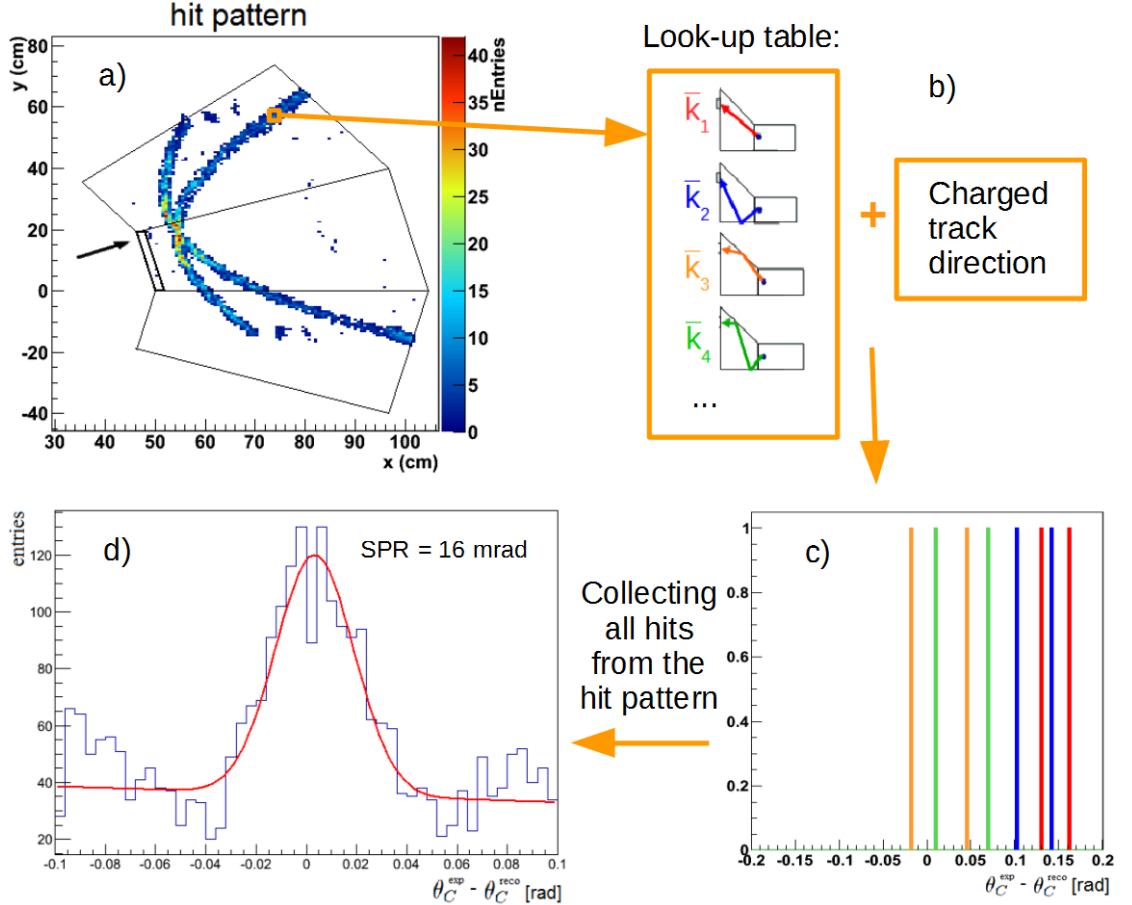


Figure 4.16: Schematic of the Cherenkov angle reconstruction procedure. The occupancy plot (a) and the distribution (d) correspond to 50 pion tracks with the momentum of $3 \text{ GeV}/c$ and direction ($\theta_{\text{track}} = 70^\circ, \varphi_{\text{track}} = 10.8^\circ$) in a simplified detector geometry without focusing. The possible photon directions for a given pixel are obtained from the look-up table (b). Four possible photon trajectories inside the EV are shown in different colors. The Cherenkov angle is computed for each trajectory by combining \vec{k}_i with the charged track direction. The difference between the reconstructed and expected Cherenkov angles for a single pixel and four types of trajectories is shown in (c). There are two entries of each color in the distribution due to the ambiguities of the photon direction discussed in the text. Collecting the differences between the reconstructed and expected Cherenkov angles for all detected photons in a histogram results in a distribution peaking at zero (d). The peak was fitted with a Gaussian function, which provided $\sigma_{\theta_C} \approx 16 \text{ mrad}$. The value is consistent with the expected SPR of 18 mrad estimated based on Eq. 3.10.

components can not be resolved in the reconstruction.

The photons may be reflected on the sides of the EV, therefore there is a number of unique ways to propagate from the radiator bar end to the pixel. Each photon

path inside the EV, called “EV ambiguity” (see Fig. 4.17a), corresponds to some initial photon direction \vec{k}_{init} and leads to a different reconstructed Cherenkov angle. The number of EV ambiguities varies depending on the pixel location and the shape of the EV. In the tank EV photons can be reflected on the inner and/or outer surfaces (see Fig. 4.17a). In the prism EV reflections on the parallel sides have to be taken into account as well. The simulation studies revealed that the total number of EV ambiguities accounting for more than 99% of photons for the tank expansion volume is $N_{amb\ EV}^{99}(\text{tank}) = 24$, and for the prism expansion volume $N_{amb\ EV}^{99}(\text{prism}) = 44$ for all studied values of the EV opening angle. These numbers include up to three photon reflections for the tank EV and up to four reflections for the prism EV. The following letters denote the main types of photon reflections inside the EV: “D” corresponds to no reflections in the EV (direct photons); “U” stands for the reflection on the outer (upper) surface of the vessel; “B” on the inner (bottom) surface; “L” and “R” mean reflections on the left and right sides of the prism. Each EV ambiguity is characterized by a particular sequence of reflections. The chain of letters in the name of an ambiguity denotes this sequence moving from the bar end towards the PD plane. Figure 4.17b shows a photon with four reflections inside the prism EV and the corresponding EV ambiguity. Since the photon reflections inside the EV can not be described by a sign flip in a component of the propagation vector \vec{k} , the correspondence between the pixel location and possible photon directions at the exit of the radiator bar were saved into a look-up table.

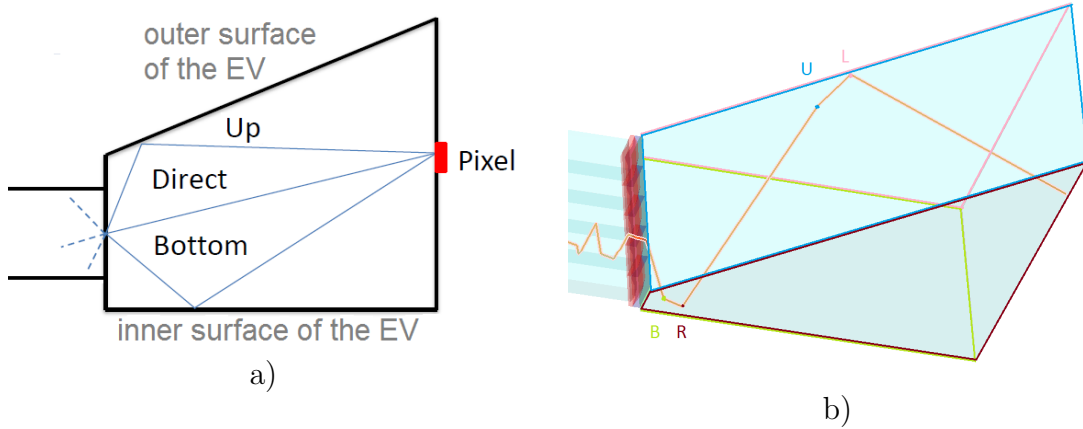


Figure 4.17: a) A two-dimensional schematic of possible photon paths inside the EV to reach a given pixel. b) The chronological sequence of photon reflections on the sides of the prism EV defines the EV ambiguity, which is “BRUL” for the given photon.

One entry of a look-up table contains the pixel number and $N_{amb\ EV}$ vectors containing the photon direction at the radiator exit, \vec{k}_i , and the time of propagation through the focusing system and EV, t_i , for each EV ambiguity. If a particular EV ambiguity does not take place for the pixel, the corresponding entry is zero.

To create a look-up table, single photons were simulated to originate from the center of the readout end of the radiator bar, uniformly illuminating the whole PD

plane³. In total $4 \cdot 10^6$ photons were produced in order to create a look-up table for a particular detector geometry. All the generated photons have the same wavelength of 400 nm ($E_\gamma \approx 3$ eV), since the path from the bar center to the pixel is independent of the photon wavelength, except for the chromatic effects in the focusing system. These effects are negligible for the resulting look-up table. Photons being absorbed or reflected off the curved lens surface were ignored. The detection efficiency was switched off as well. All the photons ending up in a particular pixel were collected and grouped according to different EV ambiguities. For each group the average initial photon direction $\bar{k}_i = (k_{x,i}, k_{y,i}, k_{z,i})$ and the mean time t_i were saved into the corresponding entry of the look-up table.

The look-up table provides a collection of possible vectors \vec{k} , corresponding to different EV ambiguities, for every detected photon coming from a charged particle. To obtain all the possible initial photon directions the bar ambiguities have been taken into account by considering all sign combinations of the vector components $(k_{x,i}, k_{y,i}, k_{z,i})$. The maximum number of possible solutions for the photon initial direction is then $N_{amb\ EV} \times N_{amb\ BAR}$.

The total number of solutions for the photon initial direction can be reduced by excluding non-physical photon paths. First, the total internal reflection condition inside the radiator bar is checked, than the difference between the real and reconstructed arrival times. If the difference is larger than 10 ns, the corresponding solution is rejected. The reconstructed photon propagation time consists of two parts:

- The time inside the radiator – calculated using the velocity and path (z -coordinate of the photon production point and the angle between the photon direction and the z -axis).
- The time inside the EV – provided by the look-up table.

According to the chromatic dispersion photons with different wavelengths have different velocities. Since the wavelength of each single photon is not accessible for the reconstruction, the photon propagation time can only be reconstructed using the same mean wavelength for all the photons. The most probable value for the spectrum of detected photons is 400 nm (see Fig. 4.10) for both expansion volume configurations, which corresponds to the mean group velocity of 19.83 cm/ns (see Fig. 3.2).

4.4 The Figures of Merit

A figure of merit is needed to compare the performance of different PANDA Barrel DIRC designs. It needs to be simple enough to provide clear conclusions, measurable

³For the look-up table the photons were generated only with $k_z < 0$, since those with $k_z > 0$, that went all the way through the radiator bar and back, have the same EV ambiguities.

with prototypes in test beam experiments, and offer the possibility to relate to the general PANDA PID requirement and the performance reached in *BABAR*. The chosen quantities are the photon yield, N_γ , and the single photon Cherenkov angle resolution, σ_{θ_C} . These two quantities can be directly compared to the performance of the *BABAR* DIRC.

The DIRC-only resolution, given by $\sigma_0^2 = \sigma_{\theta_C}^2/N_\gamma$, allows simple evaluation of the performance with respect to the PANDA PID requirement (as described in Sec. 3.3). To illustrate the method and the behaviour of these quantities over the detector phase space simplified design without focusing system, where the radiators were directly attached to the expansion volume (EV), was studied first.

For this purpose reactions with single relativistic particles originating at the interaction point (IP) were simulated on a grid across polar and azimuthal angles of the charged particle ($\theta_{track}, \varphi_{track}$) covering one bar box. As particle type muons were chosen, as they separate pure DIRC effects from electromagnetic and hadronic interactions and decays. The grid was set up in such a way that all the tracks traversed the full thickness of the radiators creating a maximal number of Cherenkov photons inside. The solenoid magnetic field $B = 2$ T was switched on, therefore the muon transverse momentum rather than the total one was fixed to $p_T = 3$ GeV/c to keep $\varphi_{track} = \text{const}$ for all values of θ_{track} . The step size of the grid was chosen to be 1° for both polar and azimuthal angles. For each grid point 400 muons were generated.

The photons produced by tracks with the same direction were collected and reconstructed together using the method described in Section 4.3. The average photon yield and SPR were determined for a given position in the phase space. These two values combined delivered the DIRC-only resolution σ_0 according to Eq. 3.11. The resulting two-dimensional distributions are shown in Fig. 4.18a. The maps represent the number of detected photons N_γ (upper plot), σ_{θ_C} (middle plot), and σ_0 (bottom plot) as functions of the polar (θ_{track}) and azimuthal (φ_{track}) angles within one bar box. Black lines mark single radiators. Figure 4.18b shows the same distributions projected on the polar angle axis. One-dimensional distributions allow easier comparison of the photon yield, σ_{θ_C} , and σ_0 for different detector designs. The blue shaded area around $N_\gamma(\theta_{track})$ in Fig. 4.18b represents the σ of the Gaussian fit to the number of photons for a given slice in the track polar angle. It reflects the variation of the photon yield over the azimuthal angle, as well as the statistical fluctuations. The uncertainty of $\sigma_{\theta_C}(\theta_{track})$ is defined as the root-mean-square of the projection of each θ_{track} slice in the corresponding two-dimensional distribution. Each θ_{track} bin contains specific variations of SPR over ϕ_{track} , which contributed to the root-mean-square. Therefore, the shaded area around each SPR point reflects also the systematic error due to dependence of SPR on ϕ_{track} . The error on $\sigma_0(\theta_{track})$ was calculated using the following error propagation:

$$\frac{\Delta\sigma_0}{\sigma_0} = \sqrt{\left(\frac{\Delta\sigma_{\theta_C}}{\sqrt{N_\gamma}}\right)^2 + \left(\sigma_{\theta_C} \cdot \Delta\left(\frac{1}{\sqrt{N_\gamma}}\right)\right)^2}. \quad (4.2)$$

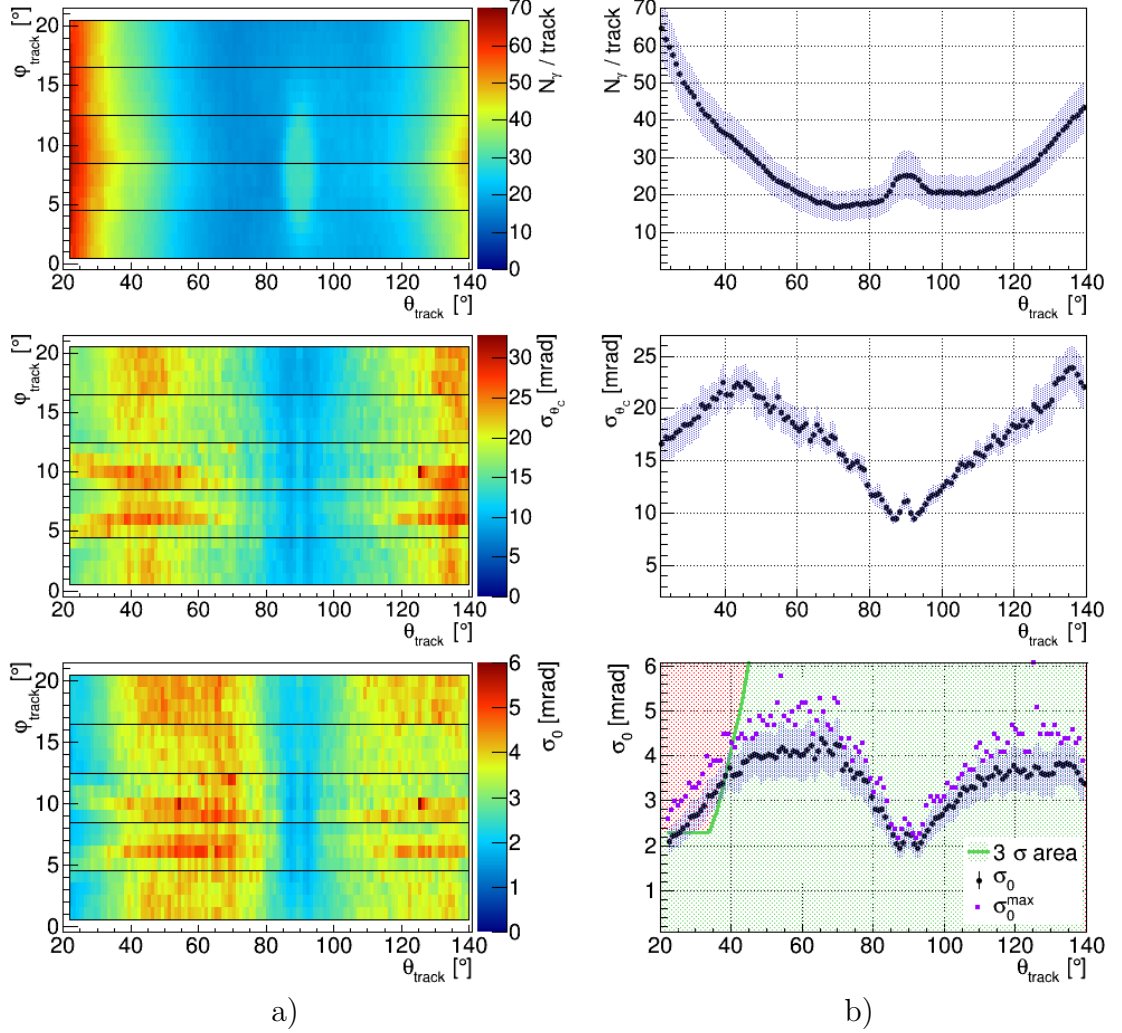


Figure 4.18: Simplified geometry, tank EV. The figures of merit: photon yield (upper row), SPR (middle row), and σ_0 (bottom row) as functions of the track polar and azimuthal angles (a) and only of the track polar angle (b). The area in the one-dimensional distribution of $\sigma_0(\theta_{track})$, where the PID requirement is fulfilled, is shaded in green. The blue uncertainty bands are described in the text.

The distribution of the photon yield over the detector phase space (see the upper plot in Fig. 4.18a) depends mainly on the track polar angle θ_{track} . The largest number of photons is detected for the steep forward and backward angles, where the muon paths inside the radiator are the longest. The number of detected photons per track gradually drops towards the middle of the distribution with a bump at around $\theta_{track} = 90^\circ$, where both backward and forward going photons contribute to the signal. For the simplified design studied here the photon yield is between 17 and 65 photons per track. The relation between the number of detected photons per charged particle track, N_γ , and the track polar angle, θ_{track} , has for DIRCs the characteristic “W-like” structure (compare to *BABAR* DIRC in Fig. 3.7d).

The shape of the SPR distribution has prominent structures in both θ_{track} and

φ_{track} . The improvement of the SPR from 23 mrad at around $\theta_{track} \approx 40^\circ$ towards 10 mrad at $\theta_{track} \approx 90^\circ$ can be explained by the corresponding variations in the hit pattern location. For the steep going particles the hit pattern is located at a smaller radius than for tracks that hit the radiator bar almost perpendicularly (see Fig. 4.19). The location of the hit pattern defines the effective size of the pixel seen from the radiator bar end and that of the radiator bar aperture seen from the pixel. The contributions to the SPR from pixel size ($\sigma_{\theta_{C,det}}$) and focusing ($\sigma_{\theta_{C,foc}}$) for different radial pixel positions in the middle part of the hit pattern are illustrated in Fig. 4.20. Both of these values decrease for charged particles hitting the radiator bar with steeper angles. The focusing error, $\sigma_{\theta_{C,foc}}$, has a larger impact than sensor, $\sigma_{\theta_{C,det}}$, for the non-focusing detector design. The deterioration of the two-dimensional SPR distribution at $\varphi \sim 6^\circ$ and $\varphi \sim 10^\circ$ is caused by the relative orientation of the Cherenkov cone and the radiator bar. Due to the magnetic field the muons hit the bar box perpendicularly in the xy plane at $\varphi_{track} \sim 8^\circ$. The symmetric orientation of the cone relative to the long sides of the radiator leads to the degeneration of the left-right ambiguities, as the Cherenkov photons are reflected off the opposite radiator sides at the same incident angle. The slightly asymmetric orientation of the cone inside the bar leads to solutions that differ only very little from the correct ones. That results in a widening of the single photon Cherenkov angle distribution, which is characterized by SPR, and an increase in the combinatoric background around it. The structures represented in the two-dimensional distributions of the number of detected photons and SPR are visible in σ_0 as well.

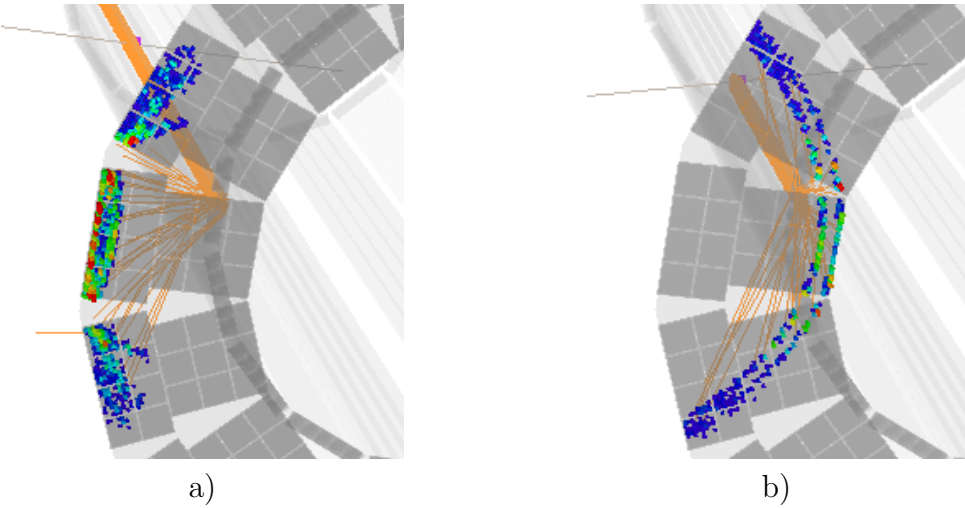


Figure 4.19: Location of the hit pattern for charged particles with different polar angles: a) $\theta_{track} = 90^\circ$, b) $\theta_{track} = 130^\circ$. The magnetic field was switched off for this simulation, as it does not influence the radial location of the hit pattern on the detection surface.

For convenient evaluation and comparison of the various detector designs the figure of merit should be as simple and informative as possible. It was shown that for the simplified design the variation of the photon yield over the detector phase space is a factor of about 2.6, whereas the maximal variation in the SPR can be as large as a factor of 1.5. The ratio $\sigma_{\theta_C}/\sqrt{N_\gamma}$ does not stay constant either. Therefore,

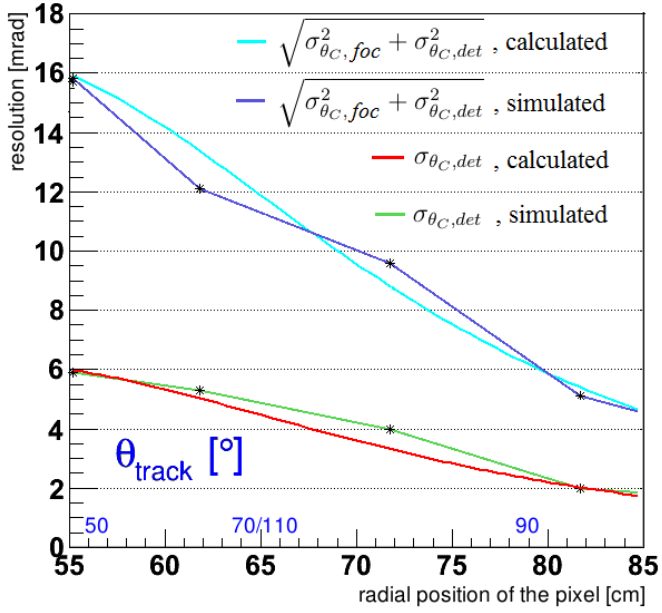


Figure 4.20: The dependency of the imaging and focusing components of SPR ($\sigma_{\theta_C, img}$ and $\sigma_{\theta_C, det}$) on the radial position of the hit pixel for the simplified design without focusing optics. The plot illustrates the impact of the effective size of the pixel and that of the radiator bar aperture for the radial area of the PD plane right in front of the radiator bar end. The cyan and red lines correspond to $\sqrt{\sigma_{\theta_C, foc}^2 + \sigma_{\theta_C, det}^2}$ and $\sigma_{\theta_C, det}$ calculated based on the geometrical approach. The obtained with the simulation values are represented in dark blue and green respectively. The blue text shows approximate radial locations of the hit patterns for different track polar angles.

the simplified design cannot be characterized by three numbers corresponding to the photon yield, SPR, and σ_0 without taking the differential behaviour into account. The two-dimensional distributions illustrating N_γ and σ_{θ_C} as functions of the track polar and azimuthal angles are a reasonable way to represent the important details of the performance of the particular detector design. The one-dimensional distribution of the above mentioned quantities illustrate the main features and allow fast judgement if a particular design meets the PANDA PID requirement.

The SPR and N_γ values for each pixel of a two-dimensional distribution are based on 400 muon tracks with the same direction. Therefore, the corresponding statistical error is 5%. Another source of statistical error is the bin size of the single photon Cherenkov angle distribution (Fig. 4.16d); this contribution is at the order of 0.03%. To extract the SPR this distribution was fitted with a sum of a Gaussian function and a straight line. The fit represents the shape of the distribution correctly in almost all cases due to its smoothness and sufficient statistics. The corresponding statistical error due to the fit function is estimated to be less than 1%. The total statistical error for each point of two-dimensional distributions is less than 6%, and

for one-dimensional plots below 2%.

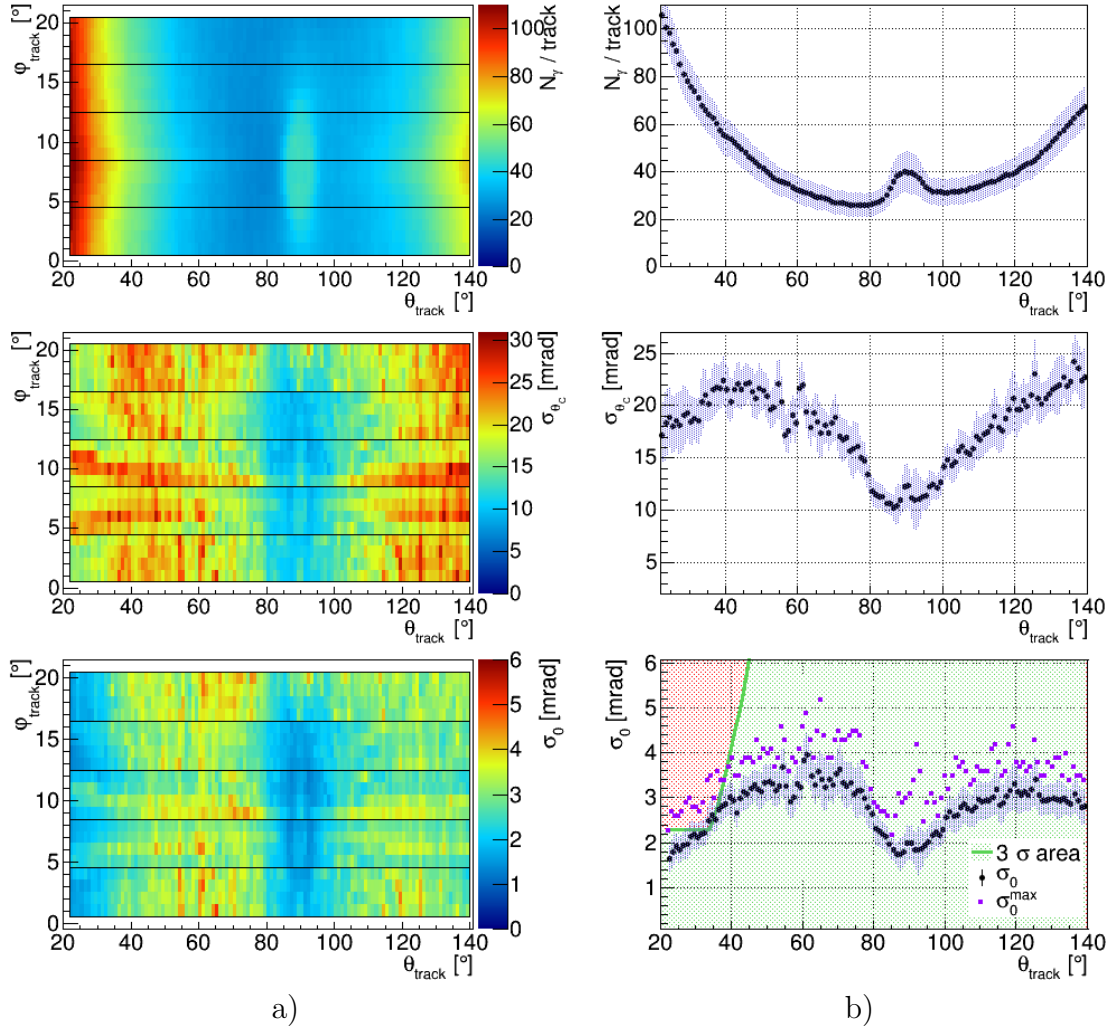


Figure 4.21: Simplified geometry, prism EV. For description of the plots see Fig. 4.18.

The Cherenkov angle resolution per track based on the average value of the SPR (shown as σ_0 in Fig. 4.18b in the bottom plot) helps to estimate the performance of a particular design. Superimposed is the required PANDA Barrel DIRC-only resolution σ_0 (shown in Fig. 3.22) marked as a green line. The area below it is shaded in green indicating the fulfillment of the PID requirement. The red area corresponds to the cases when $\sigma_0(\theta_{track})$ does not meet the PANDA PID requirements. A design of the PANDA Barrel DIRC meeting the PID requirement is characterized by the $\sigma_0(\theta_{track})$ distribution lying completely in the green area well below the green line.

It is important to make sure that for all track configurations the PID requirement is fulfilled. The distribution of $\sigma_0(\theta_{track})$ is based on the averaged value for each φ_{track} , therefore, not accounting for systematic deterioration of the detector resolution caused by the ambiguities. To take into account the largest value of σ_0 in

each slice of θ_{track} , the $\sigma_0^{max}(\theta_{track})$ should be considered⁴. The violet points in the bottom plot in Fig. 4.18b represent $\sigma_0^{max}(\theta_{track})$. For the simplified detector design σ_0^{max} , as well as σ_0 , lie partially in the red area.

One of the key design options is the compact prism-shaped EV. Figure 4.21 illustrates the performance for the simplified detector design, when the radiator bars were directly attached to the prism-shaped EV. The reconstruction in this case has to deal with more possible solutions for the Cherenkov angle due to larger number of EV ambiguities. This leads to higher background for some track directions. The simplified design with the prism EV showed a slightly better overall performance (see Fig. 4.21). The reason is that synthetic fused silica provides higher photon yield (between 26 and 106 photons per track) than mineral oil, due to better transmission. The SPR has similar behaviour as the design with the tank EV. The Cherenkov angle resolution per track is still not sufficient to meet the PANDA PID requirement.

The simplified detector design illustrated the minimal performance capabilities of the PANDA Barrel DIRC and the applicability of the *BABAR*-like reconstruction approach. Taking this design as a starting point, the detector performance can be significantly improved by the use of proper focusing optics. This option can almost eliminate σ_{foc} from the SPR (see Eq. 3.10) at the price of a reduction in the number of detected photons. The crucial σ_{foc} is also influenced by the radiator dimensions in case when no focusing is used as long as the described reconstruction method is applicable for such radiators. The results of both design improvements are summarized in the following sections. Table 4.2 lists all the combinations of parameters and design options that were tested and evaluated in the simulation with references to the plots illustrating the corresponding figures of merit.

4.5 Focusing

The use of a focusing system is essential for the Barrel DIRC to satisfy the PANDA PID requirements. A focusing system can be a focusing mirror or a combination of lenses. Mirrors can be mounted inside the expansion volume, as proposed for FDIRC for the SuperB experiment. In this case the photon trajectories are folded inside the EV. This option is not feasible for the PANDA Barrel DIRC due to the lack of space in the area of the EV. Alternatively, a focusing mirror can be mounted on the downstream radiator bar end instead of a flat mirror. The obvious disadvantage of such a solution is that only the forward going photons will be focused, whereas the photons that do not hit the mirror remain unfocused. Taking into account the phase space distribution of the charged particles in the final state of interesting channels, it might be enough to focus only photons coming from more energetic particles, primarily producing photons going forward, where the difference in Cherenkov angles between pions and kaons is the smallest (for more detail about the phase space distributions of the final state particles see Sec. 3.3). A spherical mirror attached to

⁴The variation in the photon yield has a minor influence on the σ_0^{max} . Therefore, the maximal value of $\sigma_0(\theta_{track})$ is assumed to depend mostly on $\sigma_{\theta_C}^{max}(\theta_{track})$.

Design options		Tank EV	Fig.	Prism EV	Fig.
Simplified design		no lens	4.18	no lens	4.21
Spherical lenses		L1SG	A.1	L2SG	A.3
		L2SG	A.2		
		L2S	4.27		
		L3S	4.30	L3S	A.10
Cylindrical lenses		L2C	4.27	L3C	A.11
		L3C	4.32		
1/2 of spherical lenses		L1SGA	A.4	L2SA	A.7
		L2SA	A.6		
1/2 of cylindrical lenses		L2CA	A.8	L2CA	A.9
		L3CA	4.38	L3CA	A.12
Bar thickness [cm]	1	no lens	4.39	–	
		L3S	A.23	–	
Bar width	5.2 cm (3 bars)	no lens	A.22	–	
		L3C	A.21	–	
		L3S	A.20	–	
	4 cm (4 bars)	no lens	A.19	–	
		L3C	A.18	–	
		L3S	A.17	–	
Combined pixels (c.p.) $6.5 \times 13 \text{ mm}^2$		no lens	A.13	no lens	A.14
		L3S	A.15	L3S	A.16
EV angle [°]	36	L3S	A.26	L3S	A.27
				L3S+c.p.	4.41
EV depth [cm]	48	L3S	A.28	L3S	A.29
	35	L3S	A.30	–	
	40	L3S	A.31	–	
EV downward step		no lens	4.42a	no lens	4.42c
		L3S	4.42b	L3S	4.42d
EV upward step		no lens	4.43a	no lens	4.43c
		L3S	4.43b	L3S	4.43d
Tilted PD plane [°] + EV depth 35 cm	10	–		L3S	A.32
	20			L3S	4.44
	30			L3S	A.33

Table 4.2: Table of possible combinations of design options for the Barrel DIRC. The opening angle of the EV of $\alpha_4 = 36^\circ$ corresponds to 4 radial rows of MCP-PMTs, and the EV opening angle of $\alpha_6 = 48^\circ$ to 6 rows.

the radiator is used in the Belle II DIRC. Figure 4.22 illustrates the focusing mirror implemented in the simulation of the PANDA Barrel DIRC. The performance of such a mirror was found to be not sufficient: the focused photons after propagation through the radiator bar to the photosensors got defocused, so that the resulting hit pattern looked smeared similarly to the kaleidoscopic effect [74]. Therefore, possible designs with the focusing mirror were not evaluated. The overview of the evaluated lens systems and their characteristics is set out below. Table 4.3 gives an overview of the basic lens configurations used in the simulation, and Tab. 4.4 explains the notations used for different lens systems.

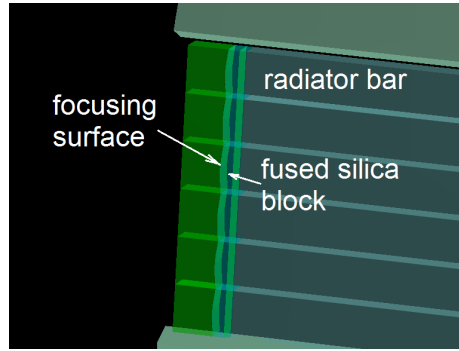


Figure 4.22: Focusing mirrors attached to the forward ends of the bars.

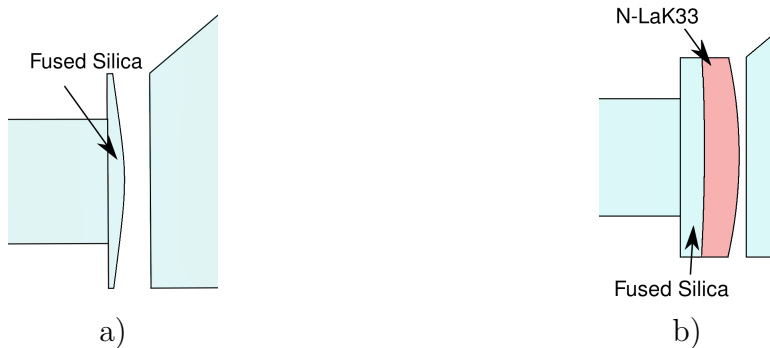


Figure 4.23: Schematic side view of the lens systems with an air gap placed between the readout bar end and the EV. a) one-component lens L1SG, b) two-component lens L2SG.

Initially, a single plano-convex fused silica lens, shown in Fig. 4.23a, was proposed to reduce σ_{foc} and improve the detector performance. It enclosed an air gap between the curved surface and EV. A single thin lens has a parabolic focal surface. Additionally, such a lens has different focal lengths for photons of different wavelengths due to chromatic aberrations. Since the PD surface of the PANDA Barrel DIRC is flat, a single lens will not be able to deliver a sharp image over the whole area of the PDs. To make the focal surface flatter and ensure a sufficiently focused image on the whole area of the PDs, a combination of at least one focusing and one defocusing lenses fulfilling the Petzval condition [75] has to be used. The air gap separates the convex surface of this lens system from the EV. The optimization of

Notation	Components	Curvature radius [cm]	Thickness [cm]	Number of components	Number of curved surfaces
L1SG	FS / air	10	0.5	1	1
L2SG	FS / N-LaK33 / air	75.18/17.95	1	2	2
L2S	N-LaK33 / FS	7.35	0.5	2	1
L3S	FS / N-LaK33 / FS	30/7	1	3	2

Table 4.3: Parameters for different lenses. The materials are listed starting from the component which is the closest to the radiator bar, the radii values correspond to this sequence. “FS” stands for “fused silica”. In the lens notations the number corresponds to the number of components, the letter “S” stands for “spherical”, “G” means “air gap”.

lens / $\frac{1}{2}$ lens (A)		
	spherical (S)	cylindrical (C)
1 component, air gap	L1SG / L1SGA	—
2 component, air gap	L2SG / —	—
2 component, non-air-gap	L2S / L2SA	L2C / L2CA
3 component, non-air-gap	L3S / —	L3C / L3CA

Table 4.4: The studied lens configurations. The number in the notation corresponds to the number of components. The letter “S” stands for “spherical”, “C” for cylindrical, “G” means “air gap”, and “A” “asymmetric”.

a two-component lens system was done [76] using the Optical Software Zemax [77]. Figure 4.23b shows the two-component lens with an air gap L2SG attached to the radiator bar end in front of the EV. The materials for the lens system are synthetic fused silica and N-LaK33, the latter being an optical glass from the lanthanum crown group. N-LaK33 is one of few materials which have a refractive index higher than that of synthetic fused silica $n(\text{N-LaK33}) \approx 1.8$ and are transparent in the optical region. To sustain the conditions of the PANDA experiment, this material has to

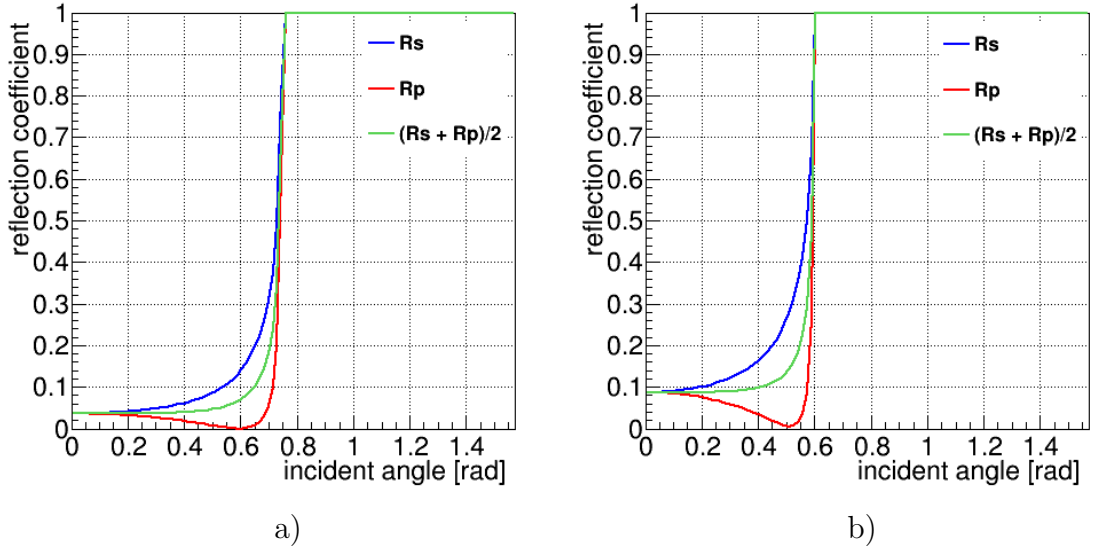


Figure 4.24: Fresnel reflection coefficients for photons propagating from fused silica into air (a) and for photons going from fused silica through N-LaK33 into air (b).

be sufficiently radiation hard, which is to be investigated. The refractive index and attenuation length of N-LaK33 are shown in Fig. 4.6. A crucial disadvantage of the lens systems with an air gap is the fact that many photons are trapped inside the radiator bar due to total internal reflection at the air gap (see the Fresnel reflection coefficients for the interface between fused silica and air and for two interfaces between fused silica, N-LaK33, and air in Fig. 4.24). Figure 4.25 shows the photon yield as a function of the track polar angle for two types of the EV and three focusing options. For $\theta_{track} < 80^\circ$ and $\theta_{track} > 100^\circ$ the number of detected photons for the lens with an air gap L2SG stays above 8 photons per track for both types of the EV, which is ≈ 2.5 times as low for as for the simplified design without focusing, where the radiator bars are directly attached to the EV. For the cases when the track crosses the radiator bar almost perpendicularly the non-focusing design delivers 27 photons per track with the tank EV and 40 photons per track with the prism EV. The setup with the lens without air gap L3S provides 17 and 22 photons per track correspondingly for the same charged particle direction. However, the design with the lens with an air gap L2SG shows a serious drop of the photon yield to about 3 – 4 per track for track polar angles $\theta_{track} \approx 90^\circ$, which is unacceptably small for reconstruction robustness. The minimal sufficient number of detected photons is estimated to be 5 [38], therefore, the setups with an air gap were ruled out as possible options.

To provide a higher photon yield, a lens system without air gap was developed. The focusing in this case is based on the difference in the refractive indices between N-LaK33 and fused silica. There are two basic lens configurations without air gap available in the simulation: a two-component and a three-component system. The first one, labelled as L2S, consists of a plano-convex lens made of N-LaK33 and

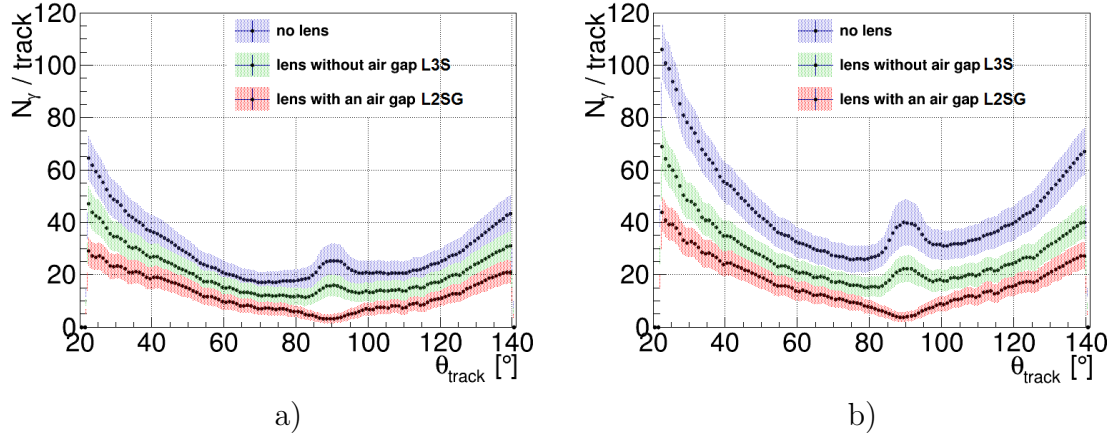


Figure 4.25: Photon yield as a function of the track polar angle for the tank (a) and prism (b) types of the EV.

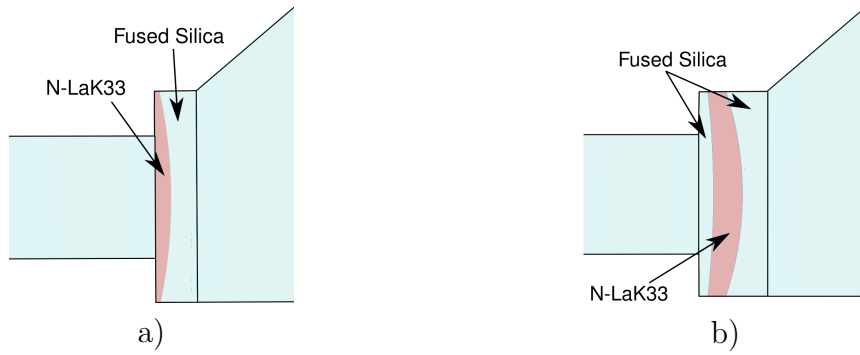


Figure 4.26: Schematic side view of the lens systems without air gap placed between the readout bar end and the EV. a) two-component lens L2S, b) three-component lens L3S.

a concave-plano fused silica lens (see Fig. 4.26a). The two-component system is intrinsically a N-LaK33 lens located in the fused silica environment and, therefore, it has a parabolic focal surface. The two-component lens without air gap was fabricated by industry and tested in 2012 with particle beams at CERN [78]. The three-component lens system consists of a plano-convex and a concave-plano fused silica lens with a concave-convex lens made of N-LaK33 in between (see Fig. 4.26b). It has two curved surfaces and was labelled L3S. All lenses implemented in the simulation are larger in diameter than the aperture of the radiator bar end ($h = 1.7$ cm) in order to minimize the photon losses from reflections on the sides of the lens system. Since the sides of the lens can most likely not be polished to the same quality as the radiator sides, the direction of the photons reflected off them gets smeared. Therefore, such photons contribute to the background rather than the signal. In case when the lens is aligned with the radiator bar sides, the fraction of photons hitting the sides can be as large as 20% for $\theta_{track} \sim 90^\circ$. For the 2 cm high lens this number drops to about 5%. The higher the lens, the smaller the loss, with 2 cm being the maximum height allowed by the baseline version of the bar box. For the performance evaluation studies the side surfaces of the lens were set as absorbent.

Both lens systems without air gap provide more than 10 photons per track with either EV (see Fig. 4.25), which is sufficient for the reconstruction.

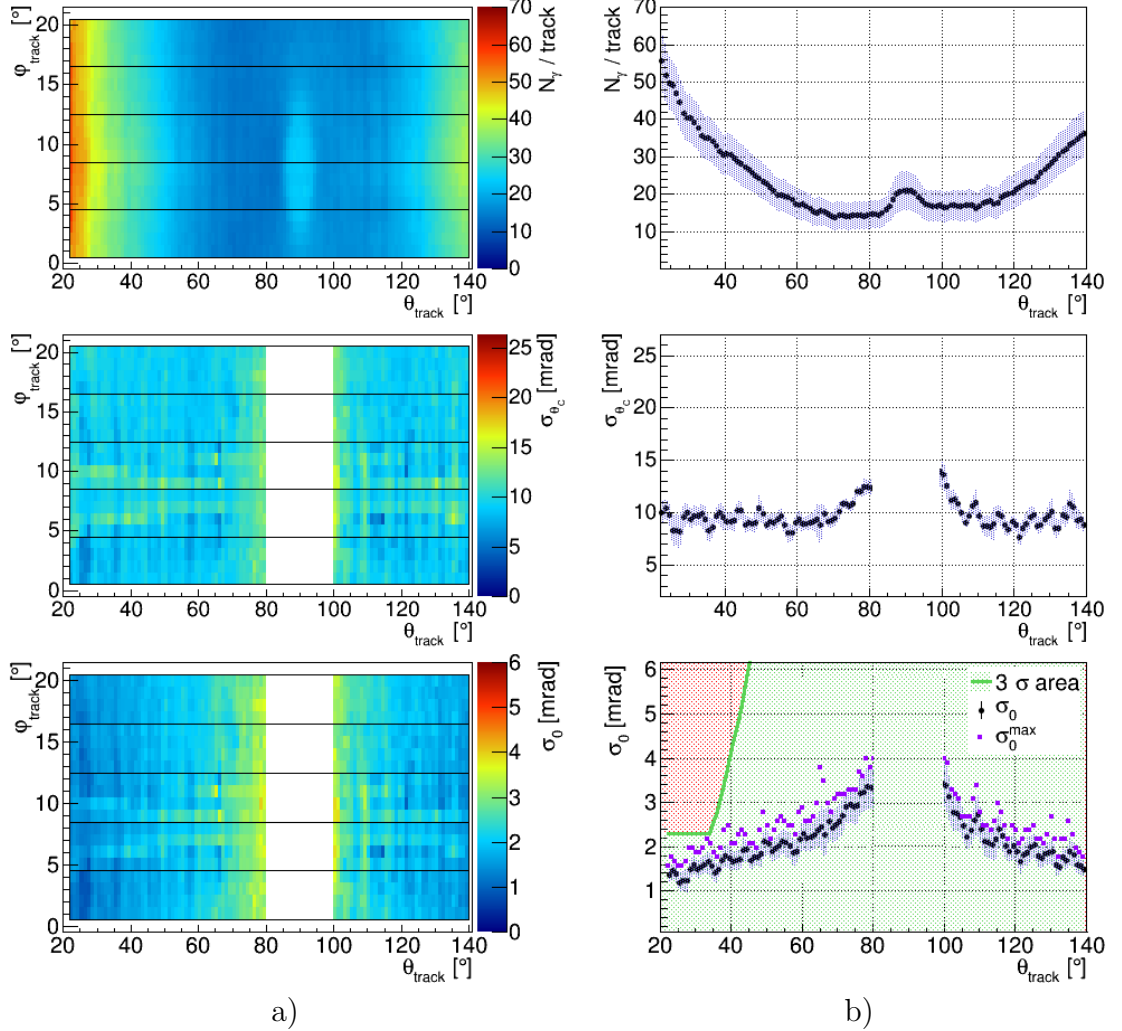


Figure 4.27: Tank EV, two-component lens without air gap L2S. For description of the plots see Fig. 4.18.

The two- and three-component lenses without air gap ensure enough detected photons, therefore, they were thoroughly tested with both kinds of EV. First, consider the imaging properties of a simpler two-component lens. The results for the design with the tank EV and the lens L2S are shown in Fig. 4.27. The SPR improved from 18–23 mrad down to 10 mrad for steep forward and backward angles compared to the simplified design. In the range between $\theta_{track} \sim 80^\circ$ and $\theta_{track} \sim 100^\circ$ the used reconstruction method does not provide reliable values for the SPR. The particular shape of the distribution of $(\theta_C^{reco} - \theta_C^{exp})(\theta_{track})$ for $\theta_{track} = 130^\circ$ and $\theta_{track} = 87^\circ$ are shown in Fig. 4.28. The width of the fitted distribution corresponds to the extracted SPR. For $\theta_{track} = 130^\circ$ the fit represents the SPR correctly. For $\theta_{track} = 87^\circ$ the distribution is broad due to combinatorial background. Here, the shape of $\theta_C^{reco} - \theta_C^{exp}$ distribution can not be described with a single Gaussian, therefore, the extracted value does not represent the SPR correctly. This effect is caused by the poor imaging

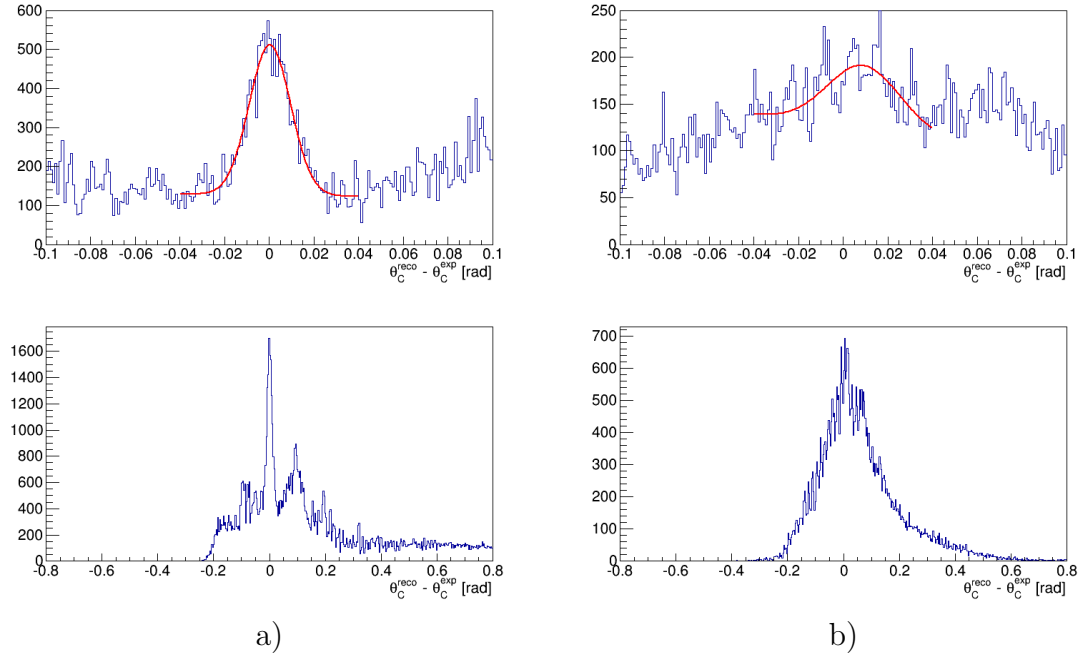


Figure 4.28: Distributions of $\theta_C^{reco} - \theta_C^{exp}$ for the design with the tank EV and lens L2S for different track directions: a) $\theta_{track} = 130^\circ$, $\varphi_{track} = 2^\circ$; b) $\theta_{track} = 87^\circ$, $\varphi_{track} = 2^\circ$. The upper plot shows the zoomed in middle part of the bottom one. The fit is represented by a sum of a Gaussian function and straight line. The extracted value of SPR for the case (a) is 7 mrad. The distribution in the case (b) does not represent SPR correctly.

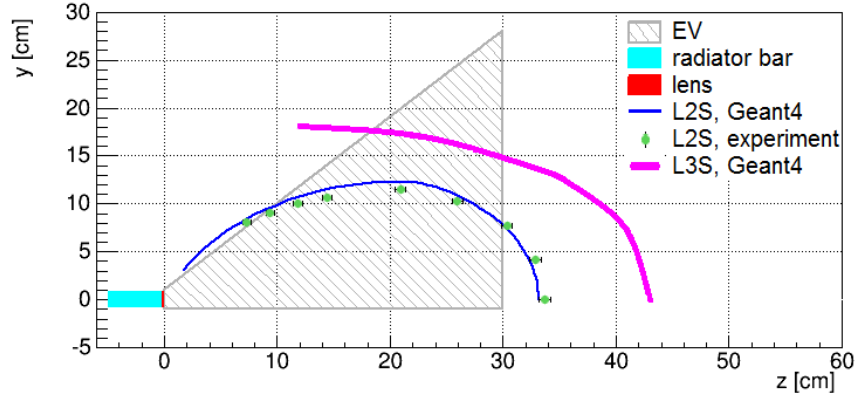


Figure 4.29: The shape of the focal surface in the yz -plane for the two-component lens without air gap (L2S) obtained in the simulation (blue line) and measured in the lab (green points). The magenta points correspond to the shape of the focal surface of the three-component lens without air gap (L3S). The grey prism depicts the baseline expansion volume.

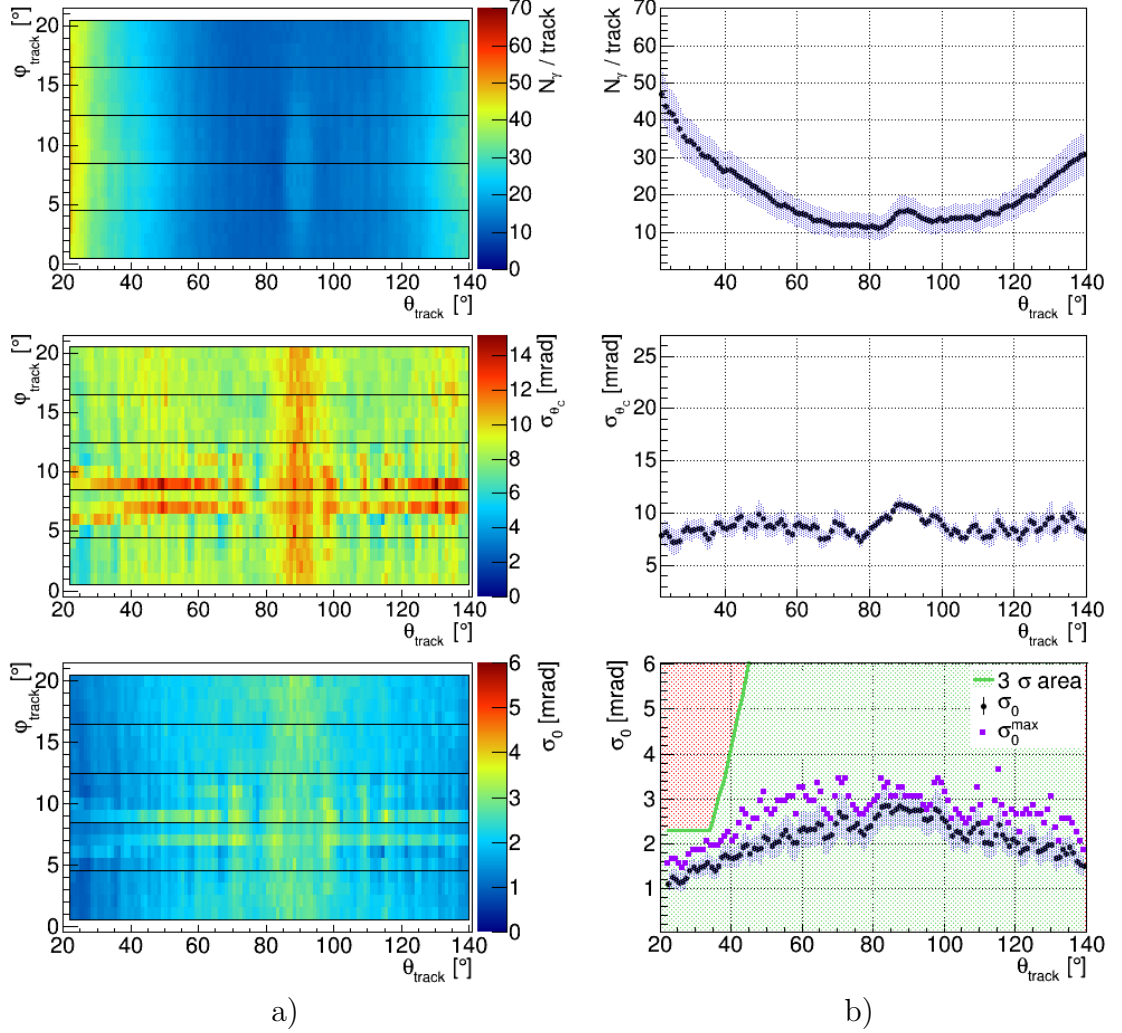


Figure 4.30: Tank EV, three-component lens without air gap L3S. For description of the plots see Fig. 4.18.

properties of the lens L2S. The focal surface of this lens is strongly curved, which was confirmed by laboratory tests [78] and Geant simulation. The shape of the focal surface in the yz plane in the bar coordinate system is shown in Fig. 4.29. The photons with steep angles in the EV are poorly focused, since the focal point for them lies too far in front of the detection plane. Therefore, the solutions of the photon direction for such photons result in the Cherenkov angle values, which do not form a prominent peak but rather contribute to the background. However, the SPR values in the range $(80^\circ, 100^\circ)$ are expected to be as large as $25 - 30$ mrad, which leads to σ_0 to be around 6 mrad. Since this value lies in the green area, the considered design is sufficiently good, although not easily quantified.

Although the focal surface in the yz plane for the three-component spherical lens without air gap lens L3S, illustrated in Fig. 4.29, is not flat, it has better imaging properties on the whole PD plane and especially on the outer part, corresponding to the track polar angles around 90° . For the detector design with the tank EV and the lens L3S the two-dimensional distribution of the SPR stays almost flat at

the level of $8 - 11$ mrad (see Fig. 4.30). The photon yield of $12 - 48$ photons per track is slightly lower compared to $14 - 56$ for the two-component lens. The higher photon loss is caused by an additional interface, which traps some photons inside the radiator due to the total internal reflection effect. The overall performance of the detector design with the tank EV and the lens L3S is better than that for the two-component lens without air gap. The same is true for the lenses with the air gap: the two-component lens L2SG performs better than the single lens L1SG. The performance of the design with the three-component lens L3S and the tank EV meets the PANDA PID requirement, as the σ_0 distribution lies well below the 3σ line in the green area. The same is true for the design, where the lens L3S is used with the prism EV (see Fig. A.10). The configurations with the lens L3S and either of the EV are considered as the baseline design for further optimization.

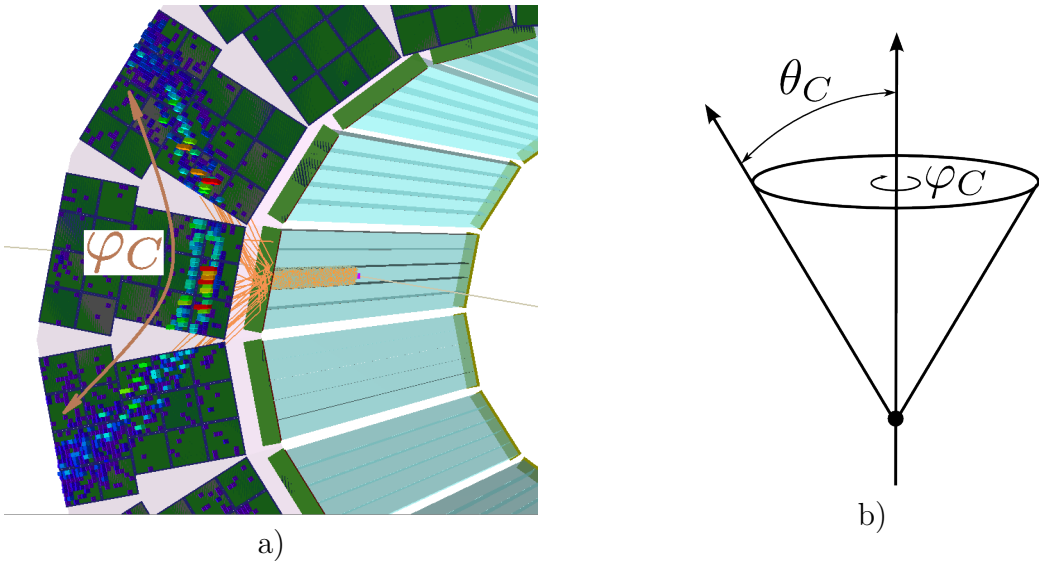


Figure 4.31: a) The Cherenkov angle φ_C illustrated for a typical Barrel DIRC hit pattern. The Cherenkov θ_C angle corresponds to the radial location of the hit pattern on the PD plane; b) schematic of the Cherenkov coordinate system including the Cherenkov φ_C - and θ_C -angles.

Each of the four basic lens configurations, listed in Tab. 4.3, is available in the simulation in cylindrical and in spherical shape. A cylindrical lens is a single object for one bar box, whereas spherical lenses are attached individually to the readout end of each radiator bar. The cylindrical lens focuses only in the y -direction of the bar coordinate system. Due to the specific orientation of the hit patterns in the Barrel DIRC, shown in Fig. 4.31a, focusing along the y axis is more important than along the x axis. The hit pattern is extended along the x axis, therefore uncertainty in this direction leads to a much smaller distortion than the error in y direction, where the hit pattern is thin (see Fig. 4.31b). The difference in the performance of spherical and cylindrical lenses was studied based on the three-component lens without air gap (L3S), as it has the best imaging properties among the available lens types. The figure of merit for the detector design with the tank EV and the cylindrical lens L3C is shown in Fig. 4.32. The photon yield for the

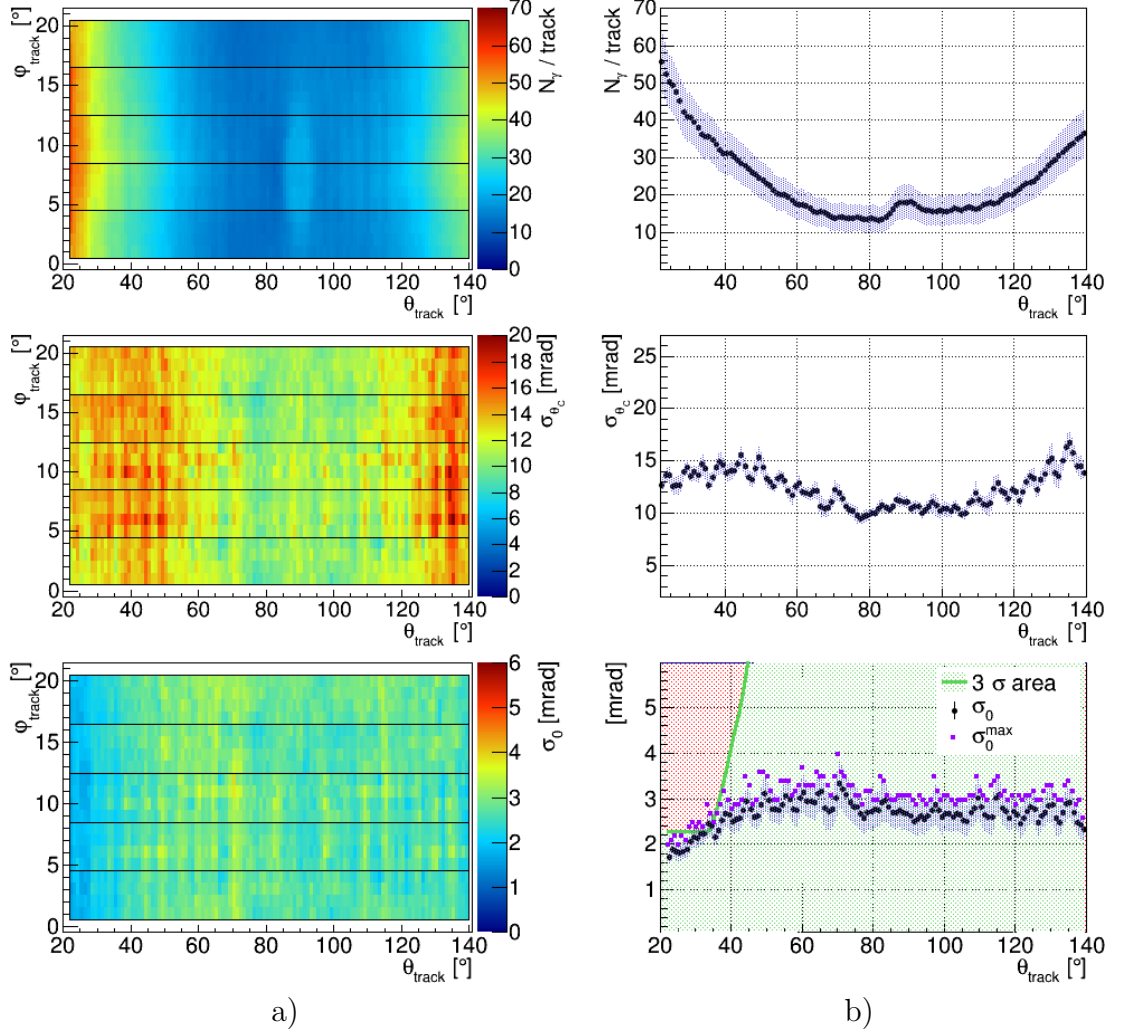


Figure 4.32: Tank EV, lens L3C. For description of the plots see Fig. 4.18.

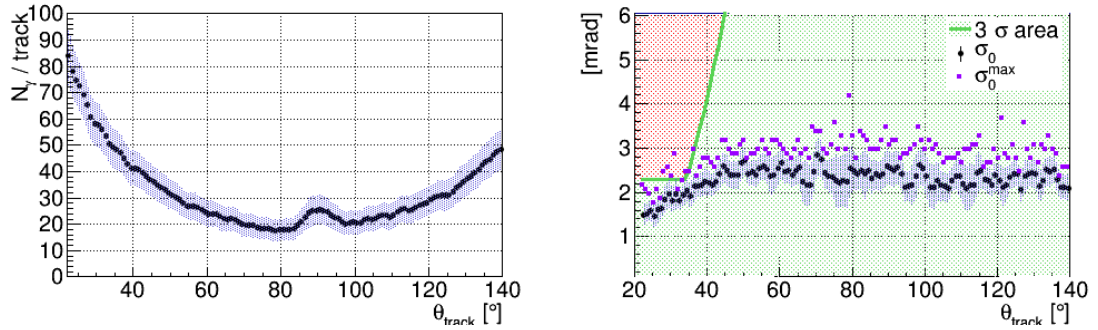


Figure 4.33: The number of detected photon per track and σ_0 as functions of the track polar angle θ_{track} for the design containing the prism EV and the lens L3C.

cylindrical lens L3C is about 20% higher than for the corresponding spherical lens L3S, since there are less side area, where photons can be lost. On the other hand,

the cylindrical lens has a larger variation of the SPR and σ_0 over the polar angle range (see Fig. 4.32). In case when a cylindrical lens was used the SPR was about 40% worse for steep forward and backward going particles compared to the spherical one. Figure 4.33 illustrates the photon yield and σ_0 for the design containing the lens L3C and compact prism-shaped EV. The designs with the cylindrical lens L3C meet the general PID requirement. Since several points in the azimuthal angle are outside of the nominal PID requirement range, these designs are not favoured.

The performance of the designs with different focusing systems is summarized in Tab. 4.5 for the prism EV and in Tab. 4.6 for the tank EV. The first column shows different values of the radiator thickness (discussed in the next section). The second column lists the focusing options used. The key quantities for each design are represented in other columns. They are the number of detected Cherenkov photons per track (N_γ), the single photon Cherenkov angle resolution (SPR), and the DIRC-only Cherenkov angle resolution per track (σ_0). The minimal and maximal values of σ_0 in the whole range of available track polar angles, and in particular for the region between 22° and 37° are given in the last two columns. This shows the variation of σ_0 over the detector acceptance and draws attention to the most challenging interval in polar angles with the tightest requirement on the detector resolution. The table cells marked with an asterisk indicate the designs, which were evaluated not in the whole range of the track polar angles. For these designs the geometric reconstruction method does not provide the correct SPR value in the area around $\theta_{track} = 90^\circ$ similarly to the described above case with the lens L2S. The values of σ_0 for these designs correspond to the evaluated range of the track polar angles.

Asymmetric Lens

Figure 4.34 illustrates the concept of the asymmetric lens, which was proposed [79] to avoid two parallel curves of the hit pattern (see e.g. Fig. 4.19b). The asymmetric lens is the upper part of the full convex lens cut horizontally in the middle (see Fig. 4.35). In case when a full lens is used (see Fig. 4.34a), the parallel rays directed towards the inner surface of the EV are focused in a different point than those directed upwards in the bar CS, which results in the double structure of the hit pattern. The distance between the images of the direct and reflected photons corresponds to the aperture of the radiator bar and can be increased with help of the downward step of the expansion volume (see Fig. 4.3). When the parallel hit patterns are overlapping the distribution of the reconstructed single photon Cherenkov angle gets wider and less prominent due to increased background. This leads to worse detector performance. In case when the asymmetric lens is used (see Fig. 4.34b), the virtual picture completes up the lens to a full one and doubles the radiator bar thickness. The parallel rays reflected off the inner surface of the EV are focused in the same point with those directed upwards. In this case the hit pattern is a single conic section. The use of the asymmetric lens does not require the bottom step of the EV. The size of the asymmetric lens corresponds to the cross section of the radiator bar. The bottom side of the asymmetric lens (where the full lens was cut) has to be aligned with the radiator bottom side. The expansion volume should be

Prism EV					
Bar thickness	Focusing	N_γ	SPR	σ_0 [mrad]	σ_0 [mrad] for $\theta_{track} \in (22^\circ, 37^\circ)$
1.7	no	26 – 106	10 – 24	1.6 – 4.0	1.6 – 2.7
	L2SG	4 – 44	7 – 19	1. – 9.	1.1 – 1.9
	L3C	18 – 85	9 – 16	1.4 – 3.0	1.4 – 2.1
	L3S	15 – 70	7 – 13	1.0 – 2.8	1.0 – 1.6
	L2CA	20 – 100	13 – 23	2.0 – 5.0 *	2.0 – 2.5 *
	L2SA	20 – 90	9 – 25	1.5 – 6.5 *	1.5 – 1.8 *
	L3CA	19 – 86	12 – 23	1.6 – 5.5	1.6 – 2.4

Table 4.5: Performance of the designs with different lenses and prism EV. The table cells shaded in red indicate insufficient values for one of the performance parameters. The green-shaded table cells correspond to the detector designs meeting the PANDA PID requirement. Asterisk indicates the designs evaluated only for steep forward and backward track polar angles.

aligned with the bottom side of the lens. In order for this concept to work the lens bottom side should be polished. For the purpose of the simulation the sides of the asymmetric lens were set as ideally reflecting.

Different asymmetric lenses (see Tab. 4.4) were tested in the simulation. The asymmetric lenses without air gap and with one curved surface, L2SA and L2CA, failed to place the two parallel hit patterns on top of each other for the full range of polar angles. Figure 4.37 shows the photon yield and σ_0 depending on the track polar angle for the design with the tank EV and the lens L2SA. In case of not fully overlapping images for track polar angle ranges ($70^\circ, 110^\circ$) the distributions of the difference between the reconstructed and expected Cherenkov angles for each track direction was broad as shows in Fig. 4.36b. In this case the fit with a single Gaussian did not represent the SPR correctly, therefore, the range of the track polar angles between 70° and 110° was not evaluated for the designs with either type of the EV. However, the SPR values in this range for lenses L2SA and L2CA and both types of the EV is expected to be at the order of 25 – 30 mrad with leading to σ_0 of approximately 6 – 7 mrad, which lies in the green area. Therefore, the two-component asymmetric lenses without air gap used with tank and prism types

Tank EV					
Bar thickness [cm]	Focusing	N_γ	SPR	σ_0 [mrad]	σ_0 [mrad] for $\theta_{track} \in (22^\circ, 37^\circ)$
1	no lens	9 – 37	7 – 17	2.0 – 4.5	2.4 – 3.5
	L3S	5 – 27	7 – 9	1.2 – 3.5	1.4 – 2.1
1.7	no lens	17 – 65	10 – 23	2.0 – 4.5	2.0 – 3.3
	L1SG	4 – 34	9 – 19	1.7 – 9.1	1.6 – 2.2
	L2SG	3 – 29	7 – 16	1.2 – 9.1	1.2 – 2.0
	L2C	16 – 62	10 – 19	1.7 – 4.1	1.6 – 2.4
	L2S	14 – 56	8 – 17	1.1 – 4.0 *	1.1 – 1.8 *
	L3C	15 – 56	9 – 16	0.8 – 3.4	1.7 – 2.3
	L3S	12 – 48	8 – 11	1.0 – 2.8	1.1 – 1.7
	L1SGA	4 – 36	10 – 25	2.1 – 9 *	2.1 – 3.8 *
	L2SA	15 – 60	10 – 18	1.5 – 4.9 *	1.5 – 2.0 *
2	L2CA	16 – 62	12 – 20	2.0 – 5.5 *	2.0 – 2.6 *
	L3CA	15 – 58	12 – 21	1.8 – 4.8	1.8 – 3.0
	no lens	19 – 75	10 – 26	2.0 – 4.8	2.2 – 3.5
	L3S	12 – 54	7 – 12	1.0 – 2.9	1.0 – 1.7

Table 4.6: Performance of the simplified design with different thicknesses of the radiator bars, basic lens configurations, and tank EV. The table cells shaded in red indicate insufficient values for one of the performance parameters. The green-shaded table cells correspond to the detector designs meeting the PANDA PID requirement. Asterisk indicates the designs evaluated only for steep forward and backward track polar angles.

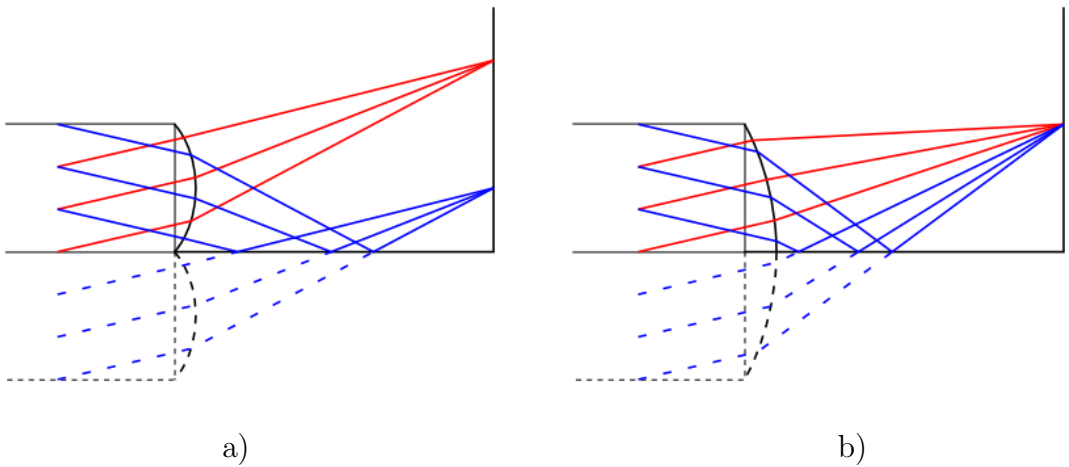


Figure 4.34: Schematic illustrating formation of the hit pattern for a full lens (a) and an asymmetric lens (b).

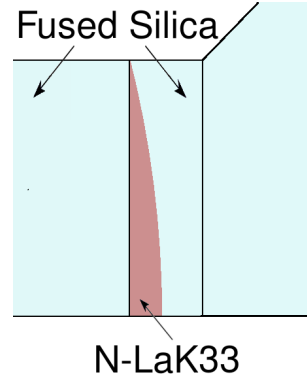


Figure 4.35: The asymmetric implementation of the two-component lens L2SA and its alignment with the bar and the EV.

of the EV deliver performance meeting the PID requirement.

Figure 4.38 shows the figures of merit for the design with the tank EV and the asymmetric implementation of the three-component cylindrical lens without air gap L3CA. The resulting SPR is around 30% worse, than for the case with the symmetrical lens of the same configuration (L3C), shown in Fig. 4.32. Despite the partial compensation by providing about 20% more photons due to the reflecting sides, the overall performance of the design with the lens L3CA is, nevertheless, not sufficient to satisfy the PANDA PID requirement.

4.6 Radiator Dimensions

The length of the radiator is defined by the barrel radius and the required polar angle acceptance of the PANDA Barrel DIRC and, thus, has a fixed value. In contrast, the

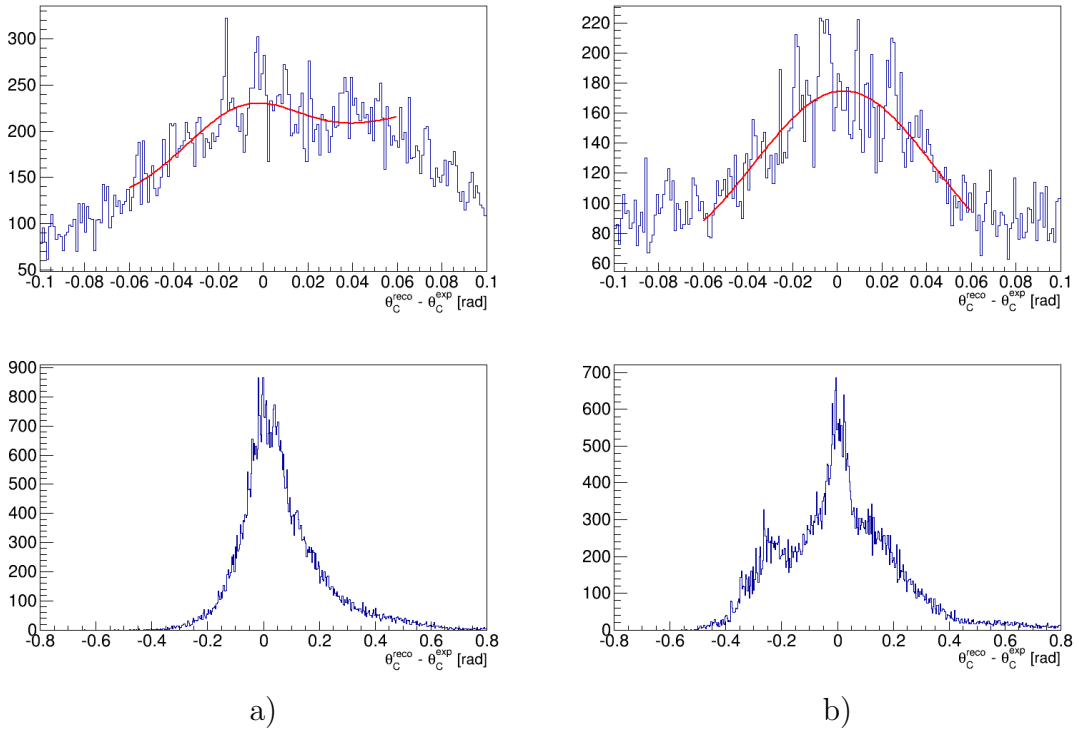


Figure 4.36: Distributions of $\theta_C^{reco} - \theta_C^{exp}$ for the design with the tank EV and lens L2CA for different track directions: a) $\theta_{track} = 88^\circ$, $\varphi_{track} = 3^\circ$; b) $\theta_{track} = 97^\circ$, $\varphi_{track} = 2^\circ$. The upper plot shows the zoomed in middle part of the bottom one. The fit is represented by a sum of a Gaussian function and straight line. The extracted values of SPR are 24 mrad for the case (a) and 40 mrad for (b). The distributions do not represent SPR correctly.

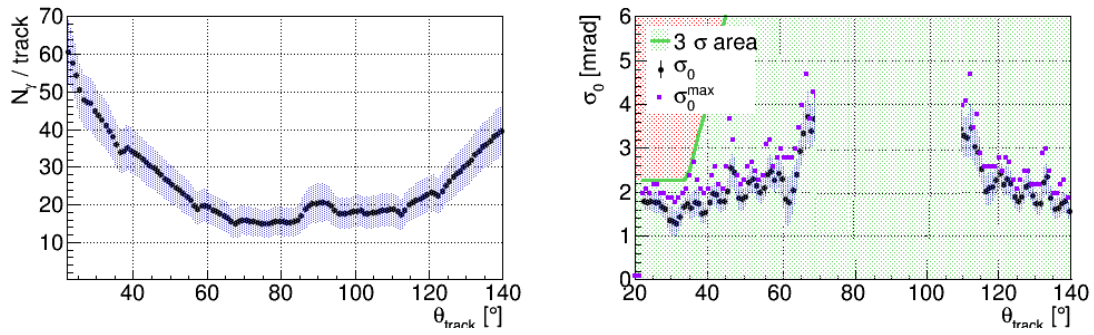


Figure 4.37: The photon yield and σ_0 as functions of the track polar angle θ_{track} for the design with the tank EV and the asymmetric lens L2SA.

width and thickness of the radiator bars are, to a certain degree, tunable parameters. As it turns out, their variations can influence the detector performance significantly.

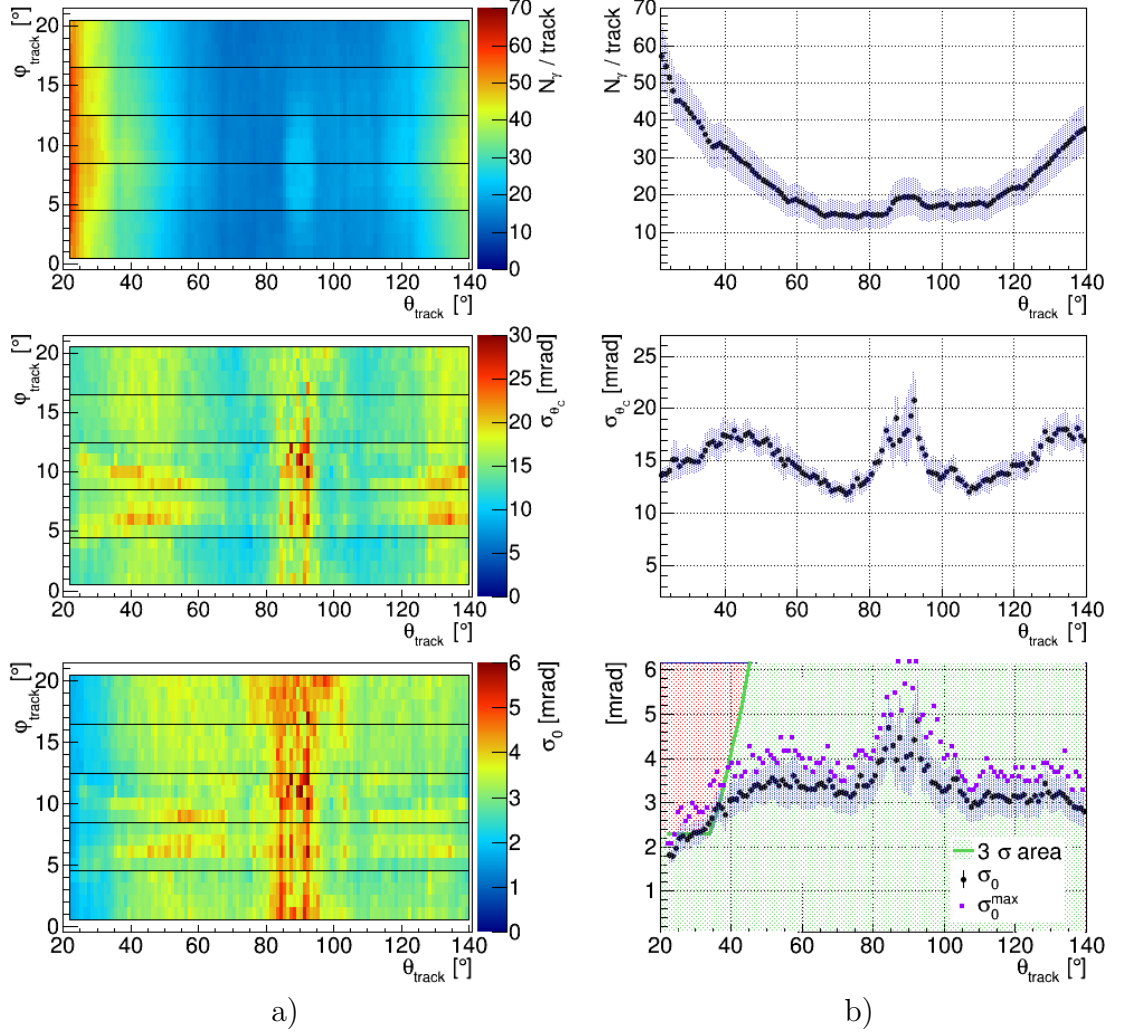


Figure 4.38: Tank EV, lens L3CA. For description of the plots see Fig. 4.18.

Bar Thickness

The radiator thickness, which is measured along the y axis in the bar CS, affects the length of the charged particle trajectory inside the radiator and, therefore, the photon yield. Thicker radiators ensure more detected photons, which leads to a more robust detector performance. Since the PANDA Barrel DIRC is located inside the electromagnetic calorimeter, the material budget of the radiators should be kept as low as possible compromising the stable detector performance. The boundary conditions for the radiator thickness value are the detector geometry, possibility of industrial fabrication, and the experience of the successfully operating DIRC counter. Based on the experience of the optical industry the minimum thickness of 10 mm is required for the standard fabrication of radiator bars [56]. The groups of Belle II and Disc DRC have decided on the radiator thickness of 2.0 cm. The baseline radiator thickness value for the PANDA Barrel DIRC (1.7 cm) is based on the *BABAR* DIRC specifications of 1.725 cm [39]. Since this number is a priori not the only possible or best value, the variation of the radiator thickness in the range

between 1 cm and 2 cm and the influence on the detector performance were studied in detail. The range of examined values was chosen around the baseline thickness to fit in the baseline mechanical structures.

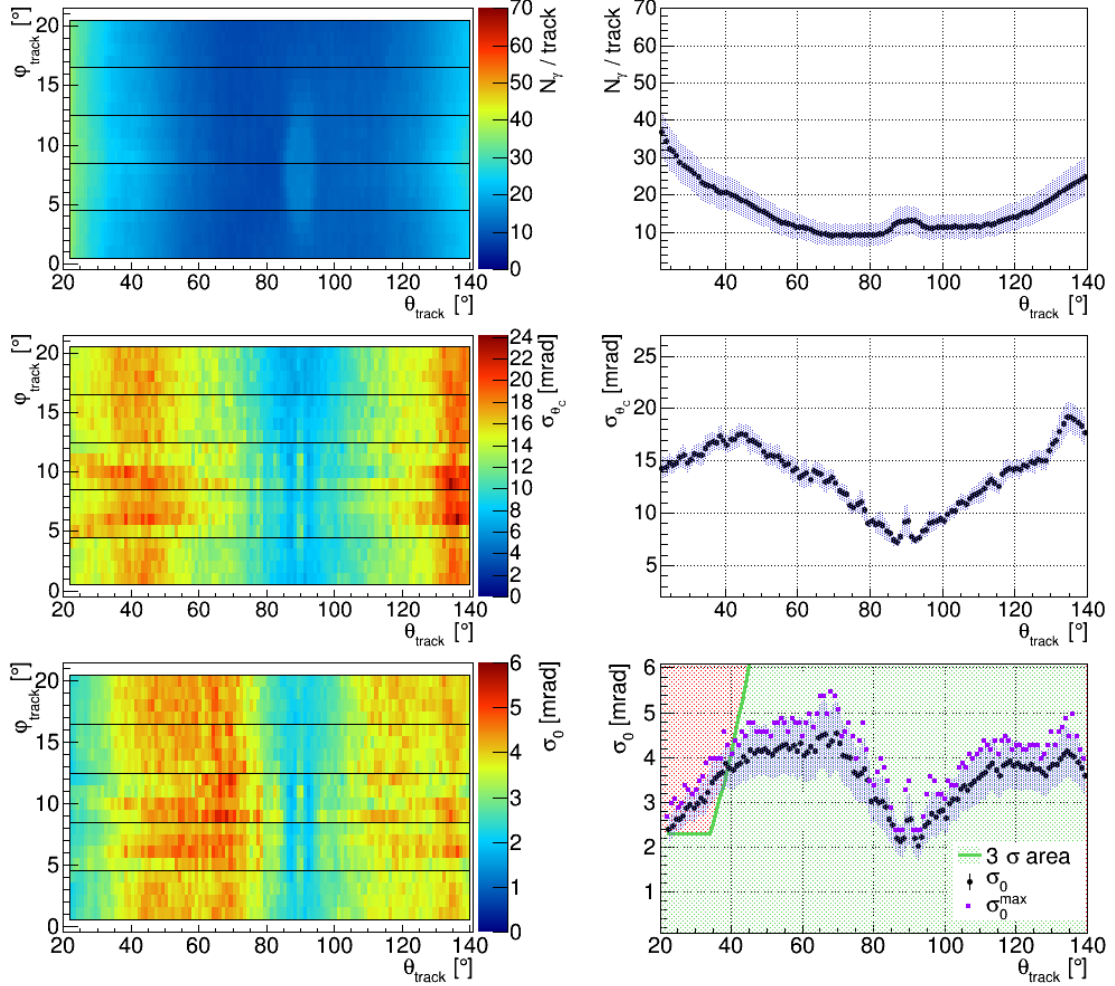


Figure 4.39: Simplified geometry without focusing, tank EV, bar thickness 1 cm. For description of the plots see Fig. 4.18.

The performance of different designs with the tank EV and radiator thickness of 1cm, 1.7 cm and 2 cm is summarized in Tab. 4.6. The detector performance for the simplified design with tank EV and 1 cm thick bars is shown in Fig. 4.39. This setup does not have focusing system, therefore the bar thickness impacts the detector resolution as $\sigma_{\theta_C, foc}$ in Eq. 3.11. The SPR improves to 7 – 17 mrad compared to that of 10 – 23 mrad for 1.7 cm thick radiators, keeping the same behaviour over the polar angle range. The number of generated photons inside the thin fused silica layer linearly depends on the radiator thickness and thus is 1.7 times smaller than for the design with the baseline radiator thickness, which results in the decreased photon yield between 9 and 37 photons per track. However, the resulting distribution of σ_0 cuts the red area even more than for the simplified design with the baseline bar thickness. This indicates that the reduced photon yield can not be compensated by the improved SPR and a focusing system is necessary even for thinner bars. In

the case when the detector design includes thinner radiators and a focusing system, the photon yield is further reduced due to the photon losses on the lens. For the case with 1 cm thick bars and the lens L3S only 5 photons were detected for some track configurations (for details see App. A), which is not sufficient for a robust reconstruction. Therefore, the detector geometry with the thinner bars and focusing does not satisfy the PID requirement.

Thicker bars ensure larger photon yield and make the $\sigma_{\theta_C, foc}$ term larger when no focusing is used. The maximum bar thickness of 2 cm was evaluated both with no focusing and with the lens L3S. The photon yield increased by 18% compared to the baseline design. The SPR distributions did not change significantly. The overall performance for the non-focusing design with the bar thickness of 1.7 cm differs insignificantly from the one with 2 cm thick bars. Variation of the radiator thickness for designs without focusing did not provide the performance satisfying the PANDA PID requirement in any case studied. The variations of the performance between detector geometries with the lens L3S and different bar thickness are negligible. Therefore, taking into account the requirements from the EMC, the baseline radiator thickness of 1.7 cm is optimal.

Bar Width

The width of one bar box is fixed by the radius of the barrel ($R = 47.6$ cm) and the number of its flat segments ($N_{sec} = 16$), while the bar width defines the total number of radiators used in the barrel. This number has the major influence on the total cost, which is mainly driven by the number of polished surfaces [56]. The baseline design envisages five bars per bar box each 3.2 cm wide. When using a reconstruction method being similar to the *BABAR* approach [38], the bar width influences the precision of the reconstructed Cherenkov angle: the wider the bar, the worse the resolution. However, the use of a spherical lens can eliminate this effect to some extent.

Detector designs with three and four bars per bar box, corresponding to the radiator width of 5.3 cm and 4 cm respectively, were tested in three configurations: without focusing, and with the cylindrical or spherical three-component lens without air gap (L3C or L3S). The results of the design evaluations can be found in App. A and are summarized in Tab. 4.7. The variation over the polar angle range, as well as the average value of the SPR increases with increasing bar width when no focusing or the cylindrical lens were used, but stays almost constant when using the spherical lens L3S. The spherical lens makes the resolution term $\sigma_{\theta_C, foc}$ negligible, therefore, the obtained results are almost the same for different radiator widths.

The photon yield shows a weak dependency on the bar width: with wider bars photons have fewer reflections during transportation and, therefore, a higher probability to reach the EV. The gain in the photon yield when going from 5 to 4 bars and from 4 to 3, is about 1.5% for the case when either no focusing or a cylindrical lens was used, and about 4% in case of the lens L3S. The overall performance of the detector designs with the compound spherical lens without air gap and 4 or 3

number of bars in bar box	bar width [cm]	focusing	N_γ	SPR	σ_0 [mrad]	σ_0 [mrad] for $\theta_{track} \in (22^\circ, 37^\circ)$
5	3.2	no lens	18 – 65	10 – 23	2.0 – 4.5	2.0 – 3.3
		L3C	14 – 56	10 – 16	1.8 – 3.3	1.7 – 2.4
		L3S	12 – 48	8 – 11	1.0 – 2.8	1.1 – 1.7
4	4	no lens	18 – 66	10 – 25	2.0 – 4.8	2.2 – 3.5
		L3C	14 – 57	10 – 17	1.9 – 3.7	1.9 – 2.8
		L3S	12 – 50	8 – 12	1.0 – 2.9	1.0 – 1.6
3	5.3	no lens	18 – 68	11 – 28	2.1 – 5.6	2.7 – 4.2
		L3C	14 – 58	10 – 23	2.3 – 4.5	2.5 – 3.6
		L3S	13 – 52	8 – 12	1.0 – 2.9	1.0 – 1.4

Table 4.7: Performance of the designs with the tank EV, different radiator bar width, and three focusing options. The table cells indicating insufficient values for one of the performance parameters are shaded in red. The green-shaded table cells correspond to the detector designs meeting the general PID requirement.

radiator bars in each bar box meets the PANDA PID requirements.

4.7 Parameters of the Photon Camera

Shape of the Expansion Volume (EV)

In the baseline design the EV of the PANDA Barrel DIRC is a single tank for the whole barrel with a polygonal cross section (see Fig. 4.40a). It has 16 flat segments at the inner radius with the width corresponding to that of the bar box, and two smaller sections at the top and bottom, matching the shape of the barrel. The tank expansion volume is going to be filled with a mineral oil, which has the refractive index approximately matching that of synthetic fused silica. The EV side equipped with photosensors is perpendicular to the axis of the barrel. Figure 4.40b illustrates

an alternative EV design, where MCP-PMTs are located on a curved surface. This ensures a better imaging on the whole detection surface in case when the focal surface is curved. However, such a shape is difficult and expensive to fabricate and, therefore, not likely to be produced.

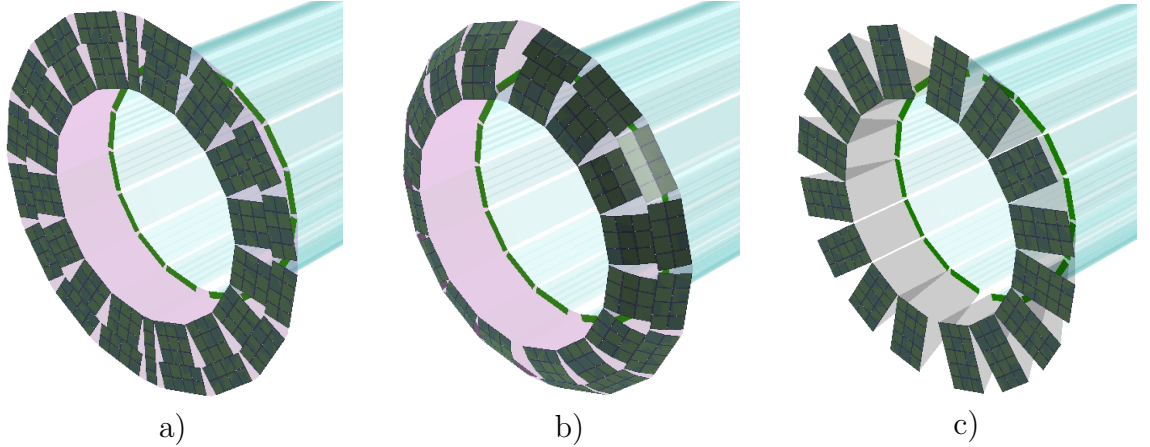


Figure 4.40: Expansion volume shapes: a) tank, b) tank with curved PD surface, c) prisms.

An alternative compact fused silica prism-shaped EV is shown in Fig. 4.40c. Figures 4.18 and 4.21 allow comparison of the detector performance for the simplified design and both EV shapes. The main difference is in the photon yield (see Fig. 4.25), since fused silica has better transmission properties than mineral oil. The parallel sides of the prism cause extra photon reflections during reconstruction, which leads to an increased background and worsens the apparent detector resolution for some track configurations. That does not happen in case of the tank EV. The compact EV with depth of 30 cm, width of 17 cm, and opening angle of 30° was tested during the 2012 test beam campaign. In spite of the increased background the SPR value could be extracted for a number of track configurations (for details see [78]). An alternative PANDA Barrel DIRC design including wide plates was tested in particle beams in 2014 with the compact EV [57] of the same dimensions with the opening angle of 45°.

EV Opening Angle

The opening angle of the EV (see Fig. 4.3) together with the depth of the EV determines the size of the PD plane. The whole detection plane has to be covered with photosensors to allow coverage of the track polar angles between 22° and 140°. Therefore, the opening angle of the EV affects the total number of photosensors used for the full detector. On the other hand, the variation of the EV opening angle leads to a change in the ratio between different EV ambiguities. Larger values make the EV ambiguities with more reflections (especially with “U”-reflection) less probable, opposite to the smaller values of the EV opening angle. According to simulation studies, the variation of the EV opening angle between $\alpha_4 = 36^\circ$ and $\alpha_6 = 48^\circ$ does

not introduce new photon paths, which were not accounted for in the baseline set of $N_{amb\,EV}$ EV ambiguities.

The designs with tank and prism types of EV were tested together with the lens L3S and with four or six radial rows of MCP-PMTs corresponding to an EV opening angle of α_4 and α_6 . Both configurations did not show a significant difference compared to the baseline performance with five radial rows ($\alpha_5 = 42^\circ$) of photon detectors (see Tab. 4.8 and Tab. 4.9). This means, that the total number of MCP-PMTs can be reduced by 20% without measurable performance loss.

EV parameter	focusing	N_γ	SPR	σ_0 [mrad]	σ_0 [mrad] for $\theta_{track} \in (22^\circ, 37^\circ)$
EV depth 35 cm	L3S	10 – 45	7 – 10	1.1 – 3.0	1.2 – 1.7
EV depth 40 cm		10 – 45	7 – 10	1.1 – 3.0	1.1 – 1.7
EV angle 48°		10 – 47	7 – 11	1.1 – 2.9	1.1 – 1.6
EV angle 36°		12 – 48	7 – 12	1.1 – 3.5	1.1 – 1.6
combined pixels		12 – 48	8 – 11	1.1 – 3.0	1.1 – 1.6
shifted MCPs		11 – 46	8 – 11	1.1 – 3.0	1.1 – 1.7

Table 4.8: Performance of the designs with the lens L3S and different parameters of the tank EV. The green-shaded table cells correspond to the detector designs meeting the general PID requirement.

Asymmetric Pixels

Asymmetric pixels can be used to reduce the number of electronic channels. Standard MCP-PMTs, which are likely to be used for the PANDA Barrel DIRC, have 8×8 square pixels with the size of $6.5 \times 6.5 \text{ mm}^2$ each. Reading out neighbouring pixels in pairs leads to 4×8 pixels with size of $13 \times 6.5 \text{ mm}^2$ on each MCP-PMT and reduces the total number of the electronic channels by half. The orientation of the usual DIRC hit pattern shown in Fig. 4.31b indicates, that for the θ_C reconstruction a good resolution $\sigma_{\theta_{C,det}}$ in the radial direction is more important than in the azimuthal direction. Therefore, the pixels can be rectangular with the long side oriented along the x axis of the bar CS. This option is being considered by the Super B (pixel size $3 \times 12 \text{ mm}^2$) and LHCb ($0.41 \times 6.5 \text{ mm}^2$) groups. The performance of the design with the lens L3S, four radial rows of photosensors, and rectangular pixels, shown in Fig. 4.41, differs negligibly from that of the same configuration

parameter	focusing	N_γ	SPR	σ_0 [mrad]	σ_0 [mrad] for $\theta_{track} \in (22^\circ, 37^\circ)$
combined pixels	no lens L3S	25 – 110	10 – 23	1.6 – 3.8	1.6 – 2.7
combined pixels		15 – 70	8 – 12	1.0 – 2.5	1.1 – 1.5
EV angle 48°		15 – 70	8 – 12	1.0 – 2.5	1.1 – 1.5
EV angle 36°		15 – 70	8 – 12	1.0 – 2.9	1.1 – 1.5
EV angle 36°, combined pixels		16 – 70	7 – 13	1.0 – 2.9	1.1 – 1.6
EV depth 35 cm, PD tilt 10°		15 – 69	8 – 13	1.0 – 2.9	1.1 – 1.4
EV depth 35 cm, PD tilt 20°		15 – 69	7 – 12	1.0 – 2.8	1.1 – 1.4
EV depth 35 cm, PD tilt 30°		15 – 69	7 – 12	1.0 – 2.8	1.1 – 1.4

Table 4.9: Performance of the designs with the lens L3S and different parameters of the prism EV. The green-shaded table cells correspond to the detector designs meeting the general PID requirement.

with the square pixels (see Fig. A.27). This result shows that the number of pixels (electronic channels) can be halved without loss of performance.

EV Depth

The depth of the EV influences the amount of the fused silica used for the prism and, therefore, the detector cost. On the other hand, deeper EV improves σ_{foc} and σ_{det} terms of the detector resolution. Cherenkov photons are usually reflected only a few times inside the expansion volume (EV) before getting detected. The larger the depth of the EV, the more EV ambiguities have to be taken into account for the geometric reconstruction algorithm. The simulation studies revealed, that the increased EV depth of 40 cm does not add new EV ambiguities compared to the baseline detector setup. Therefore, the set of N_{ambEV}^{99} is sufficient for event reconstruction in this case.

The depth of the EV is constrained by the space required for the front end electronics and, therefore, can only be changed over a small range. The maximum values for the EV depth according to the mechanical design are approximately 35 – 40 cm. The values of 35 and 40 cm were chosen to be tested together with the lens L3S (see the shape and the location of the focal surface of the lens L3S in Fig. 4.29). Since

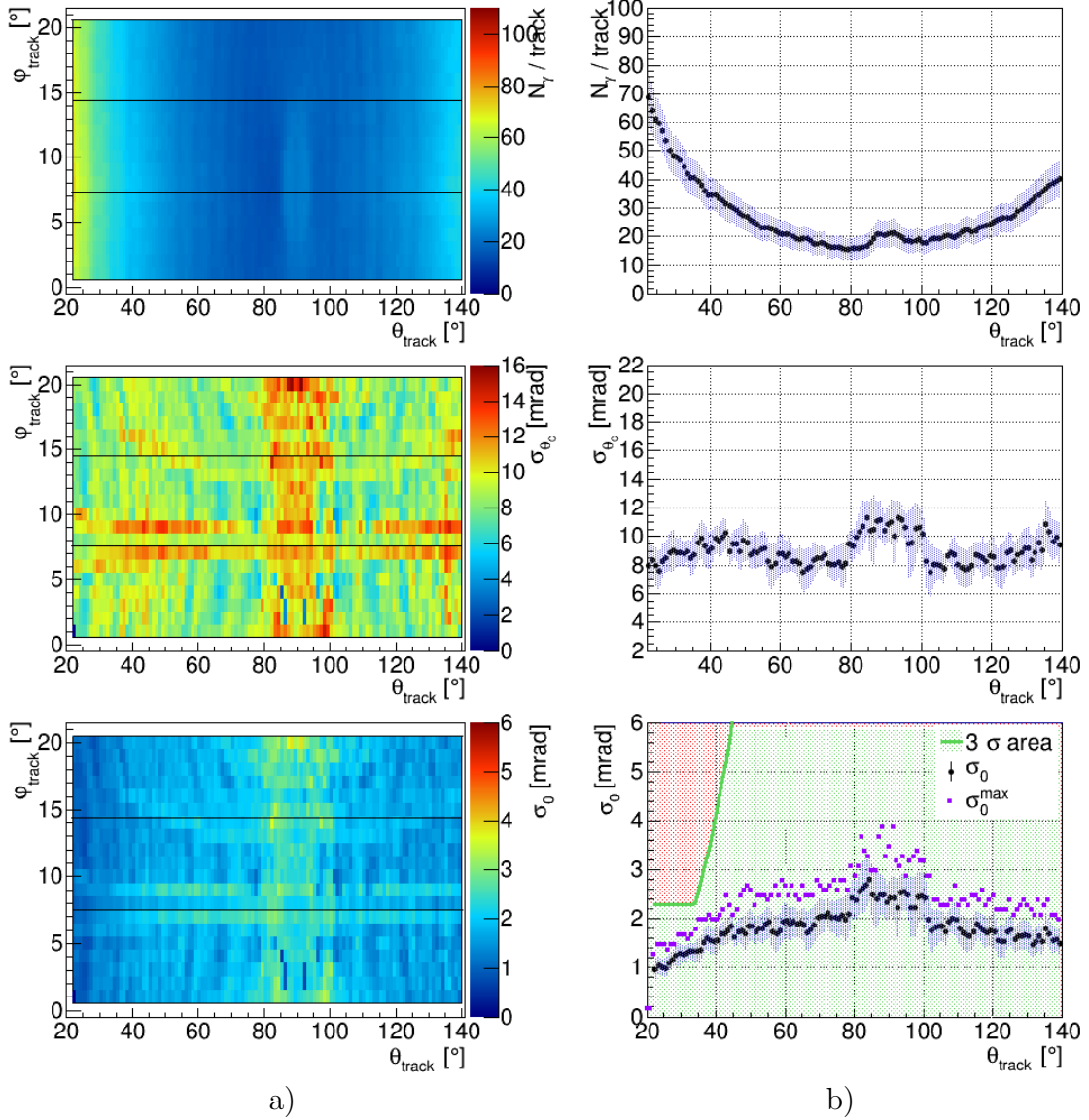


Figure 4.41: Prism EV with four radial rows of photosensors, the pixels on the PD combined in pairs, and lens L3S. For description of the plots see Fig. 4.18.

larger EV depth is favourable, smaller values, for which the resolution deteriorates, were not considered. A deeper tank EV increases the photon losses due to absorption in mineral oil, which results in a slightly dropping photon yield of the order of 3%. On the other hand, the effective pixel size gets smaller, which leads to an improved SPR, as summarized in Tab. 4.8. The overall performance changed too little to motivate a modification of the EV depth, though.

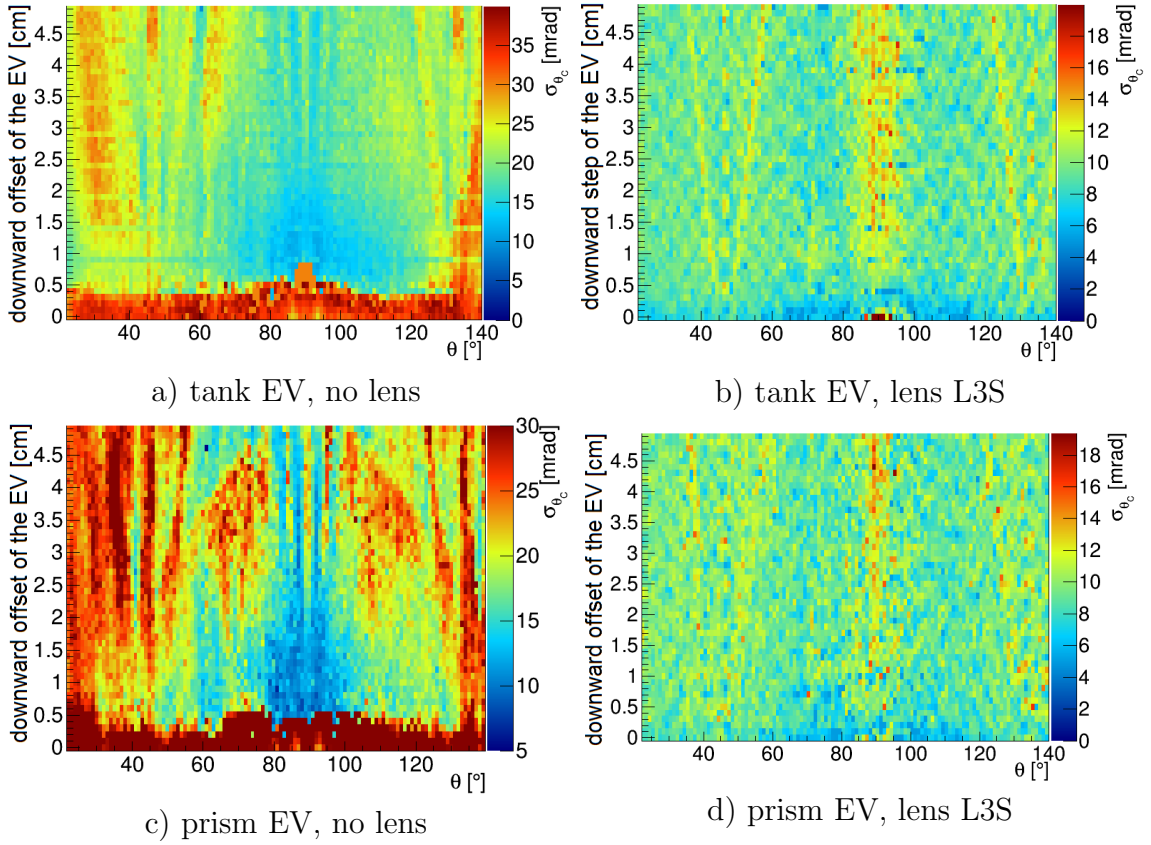


Figure 4.42: SPR as a function of the track polar angle θ_{track} and the value of the EV downward step for different designs.

EV Offsets

The upper and downward offsets of the EV (see Fig. 4.3) have little impact on the performance. These parameters mainly affect the number of Cherenkov photons reflected off the outer and inner surfaces of the EV. This influences the contribution from the EV ambiguities with many reflections. The downward step is responsible for the increasing optical separation of the two parallel hit patterns (in case when no asymmetric lens is used).

To study the influence of the downward and upward offsets on the detector performance the single muon events were used. The charged particles were hitting the middle bar of the bar box, so that $\sigma_{\theta_C}(\theta_{track})$ can be calculated for each value of the offset. The influence of the downward step in the range between 0 cm and 5 cm on the SPR was studied for the simplified design without focusing and for the lens L3S (see Fig. 4.42). If the lens was used, the value of the downward EV offset did not influence the SPR. For the non-focusing geometry the offset of at least 0.5 cm is necessary to optically separate the parallel hit patterns. The SPR as a function of the track polar angle depending on the upper offset of the EV in the range (0, 10) cm is represented in Fig. 4.43. The shape of $\sigma_{\theta_C}(\theta_{track})$ for each value of the upper offset for the design with the lens L3S (Fig. 4.43a,c) is quite uniform,

which corresponds to the figure of merit of the designs with the baseline value of the upper offset (see Fig. 4.30 for the tank EV and Fig A.10 for the prism EV). The same is true for the non-focusing designs (Fig. 4.43b,d): the improvement of the SPR around $\theta_{track} \approx 90^\circ$ is visible on the figure of merit for the simplified designs without focusing (see Fig. 4.18 for the tank and Fig. 4.21 for the prism EVs). The value of the upper step does not influence the SPR.

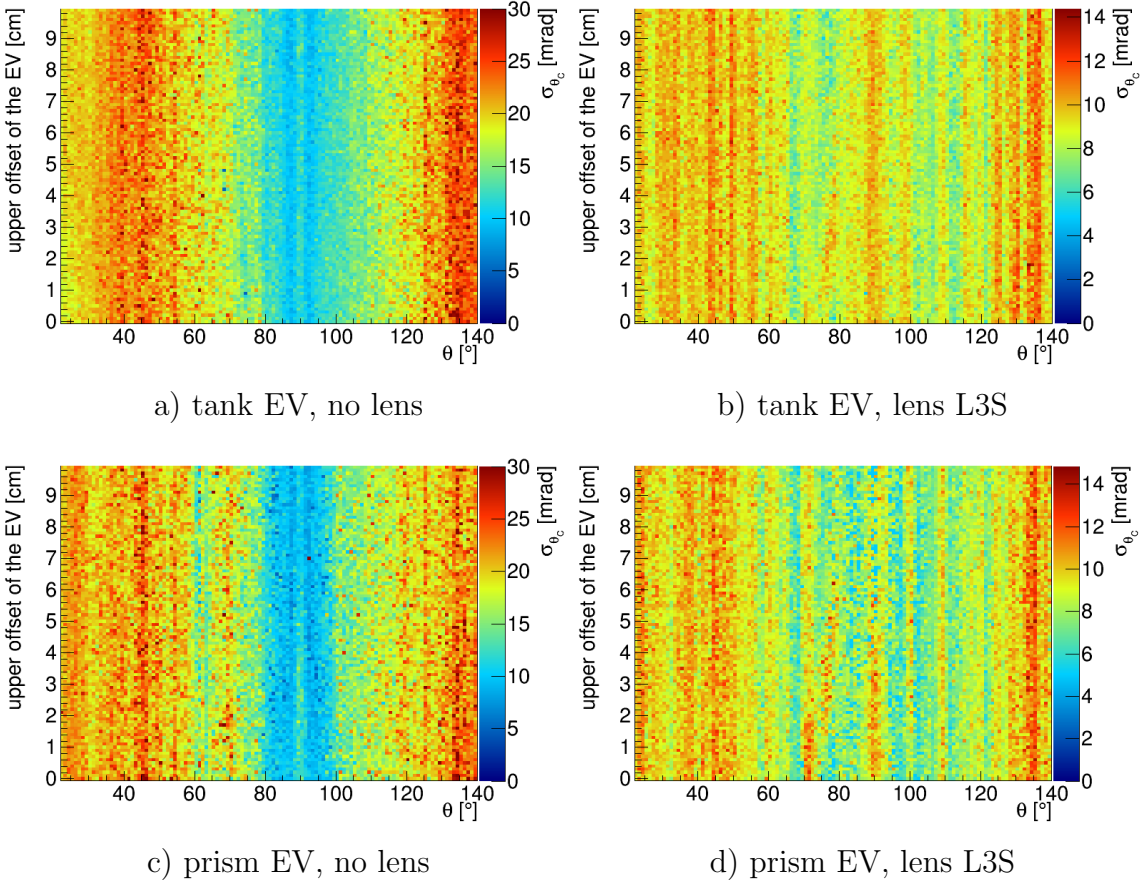


Figure 4.43: SPR as a function of the track polar angle θ_{track} and the value of the EV upper step for different designs.

Tilt of the PD Plane

The tilt of the PD plane optimizes the location of the detection plane with respect to the curved focal surface of the lens. The designs with the prism EV, lens L3S and PD tilt of 10° , 20° and 30° degrees were tested in the simulation. Figure 4.44 illustrates the figures of merit for the case of PD tilt of 20° . The photon yield is between 16 and 68 photons per track. The values of SPR are between 7 mrad and 13 mrad leading to the σ_0 values in the range (1; 3.7) mrad. The σ_0 distribution lies completely in the green area, which means that the design with the lens L3S and tilted by 20° PD plane meets the PID requirement. The performance of the designs

without tilt (see Fig. A.10 for the baseline EV depth) and with the tilt of 10° , 20° , and 30° turned out to be almost identical, which leads to the conclusion, that the tilt of the PD does not help to optimize the shape of the focal plane for the lens L3S.

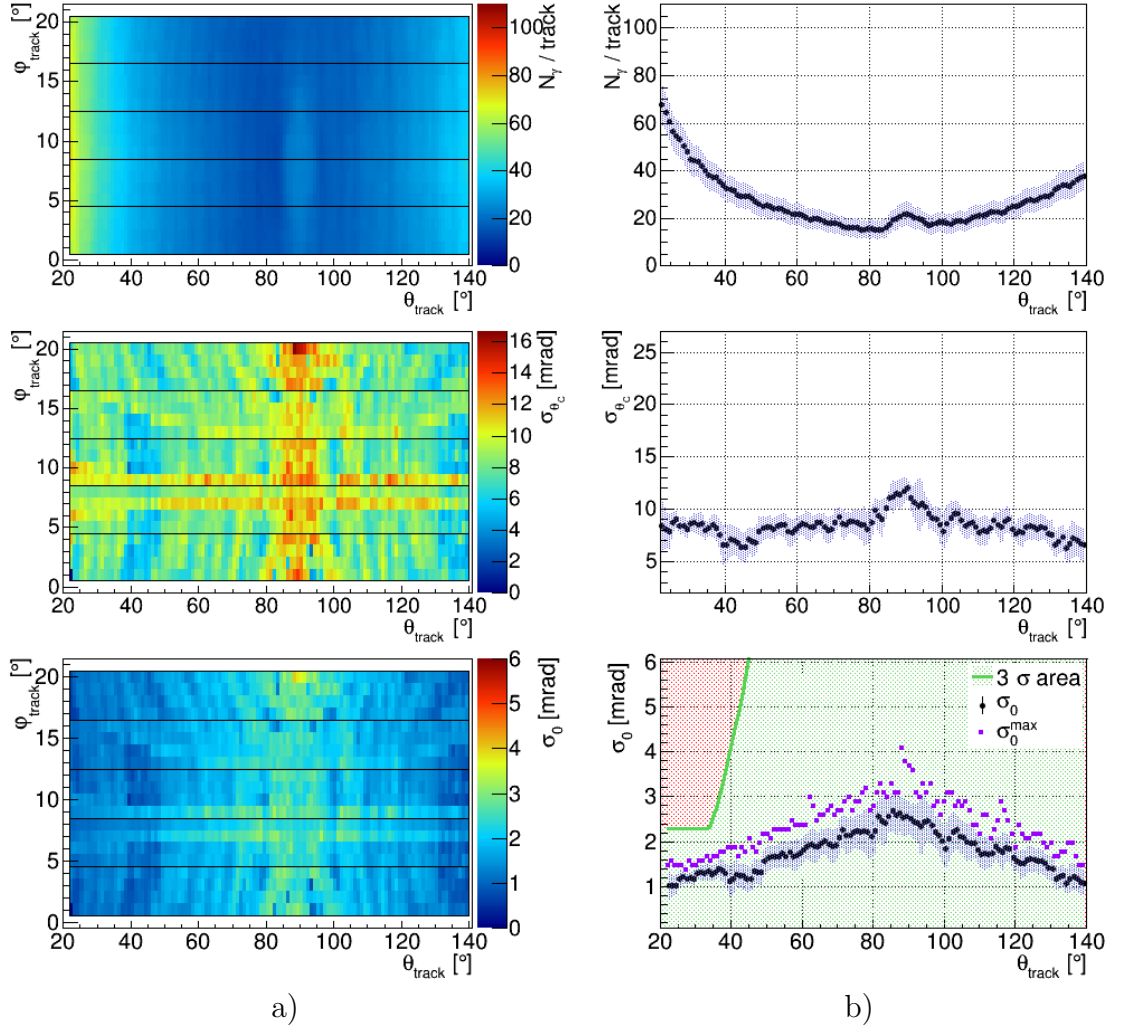


Figure 4.44: Prism EV with depth of 35 cm, lens L3S, the tilt of the PD plane is 20° . For description of the plots see Fig. 4.18.

Shifted MCP-PMTs

A shift of neighbouring radial columns of MCP-PMTs in half a pixel size shown in Fig. 4.45 helps to avoid long gaps between the photosensors, although it introduces additional spaces not covered by photon sensors at the inner and middle radii of the PD plane. Since the fraction of photons that hit these gaps is quite low, the improvement over the usual PD configuration is expected to be minor. This modification was inspired by the prototype studies of the WASA@COSY DIRC [54]. The performance of the geometry with tank EV, lens L3S and shifted columns of MCPs

is even slightly worse compared to the one with the baseline layout of photosensors (see Tab. 4.8). The number of detected photons stayed almost the same. Therefore, that long gaps between the rows of photosensors in the baseline layout do not noticeably influence the performance of the PANDA Barrel DIRC.



Figure 4.45: Schematic layout of the PD plane covered with MCP-PMTs when the neighbouring radial columns of MCPs are shifted with respect to each other in half of the pixel size.

4.8 Reconstruction Bias

The mean value of the difference between the reconstructed and expected Cherenkov angles $\langle \theta_C^{reco} - \theta_C^{exp} \rangle$ is an important parameter of the reconstruction, which influences the extraction of PID information. The identification of charged particles is based on likelihoods, which are in the simplest case the function of the reconstructed Cherenkov angle. In the high momentum region, where the difference in Cherenkov angles between kaons and pions is about 8.5 mrad the deviation of θ_C^{reco} from the expected value by 1 mrad impacts on the PID output and may lead to a wrong conclusion about the particle specie. In practice, the bias of the difference between the reconstructed and expected Cherenkov angles can be moderated by alignment procedure similar to the one described in [38].

For the geometric reconstruction the bias of the difference between the reconstructed and expected Cherenkov angles $\langle \theta_C^{reco} - \theta_C^{exp} \rangle$ is primarily caused by the ambiguities of the photon direction. The behaviour of $\langle \theta_C^{reco} - \theta_C^{exp} \rangle$ depends on the particular geometry used and does not vary with the track azimuthal angle φ_{track} , as illustrated in Fig. 4.46 for the tank and prism types of the EV and both focusing and non-focusing options. Figure 4.47 reveals the bias depending on the track polar angle. Here, the plots were obtained by projecting the two-dimensional distributions on the polar angle axis. The blue shaded area represents the root-mean-square of each θ_{track} bin. For the simplified design without focusing (Fig. 4.47a,b) the mean value stays almost constant over the full polar angle range, but have fluctuations with a larger spread in the case of the prism EV compared to the tank EV. When

a lens is used, the mean value varies over the track polar angle range with a maximum bias at $\theta_{track} = 90^\circ$. For the cylindrical lens, the values of $\langle \theta_C^{reco} - \theta_C^{exp} \rangle(\theta_{track})$ are less biased, than for the spherical lens (see Fig. 4.47c,d). The spread of the $\langle \theta_C^{reco} - \theta_C^{exp} \rangle(\theta_{track})$ distribution increases with the width of the bar when no focusing is used (compare Fig. 4.47a and f). The same tendency, but less pronounced was present, when a cylindrical or spherical lens was used (compare Fig. 4.47d and e). The designs without focusing, illustrated in Fig. 4.47a,b,f, are characterized by a strongly fluctuating mean value of the difference between the reconstructed and expected Cherenkov angles. Since the final detector design needs focusing, the relevant $\theta_{track}^{reco} - \theta_{track}^{exp}(\theta_{track})$ illustrated in Fig. 4.47c,d,e is quite stable. Although a quite significant dependency of the reconstruction bias on the track polar angle is visible, it most likely does not affect the extraction of the single photon Cherenkov angle resolution.

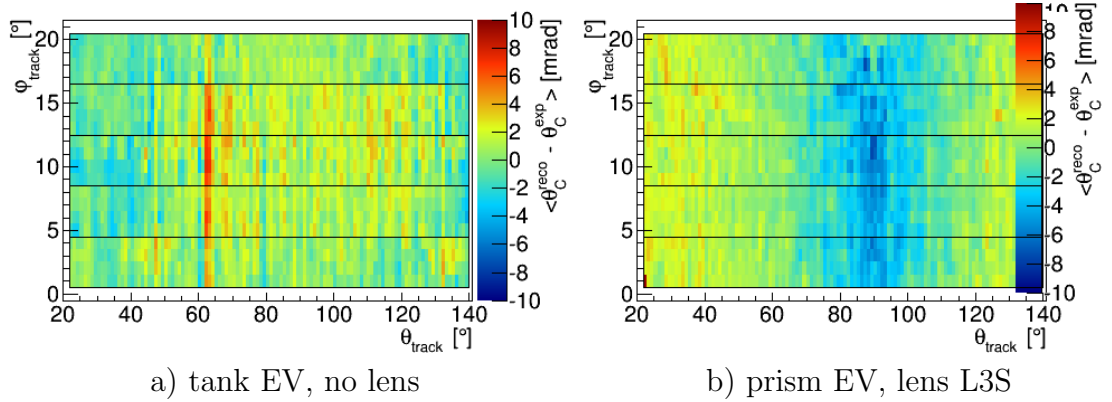


Figure 4.46: Mean value of the difference between the reconstructed and expected Cherenkov angles $\langle \theta_C^{reco} - \theta_C^{exp} \rangle$ (reconstruction bias) as a function of the polar and azimuthal angles of the charged particle for two design options.

4.9 Conclusions

The studies of the optimization of the PANDA Barrel DIRC design options and parameters were prioritized according to their impact on the detector cost and performance. The main cost drivers are the number of radiator pieces and the total number of photosensors. Most of the design options were tested with two types of expansion volumes (EV): the baseline single tank filled with mineral oil and the compact prism-shaped EVs made of synthetic fused silica. The design options influencing the performance the most and having a significant impact on the detector cost are the different focusing systems and the radiator dimensions.

It was demonstrated that a focusing system is essential to meet the PANDA PID requirement. The evaluation of the detector design with a standard lens revealed that it meets the performance requirement for most of the polar angle range. However, the air gap causes unacceptably low photon yield for track angles close

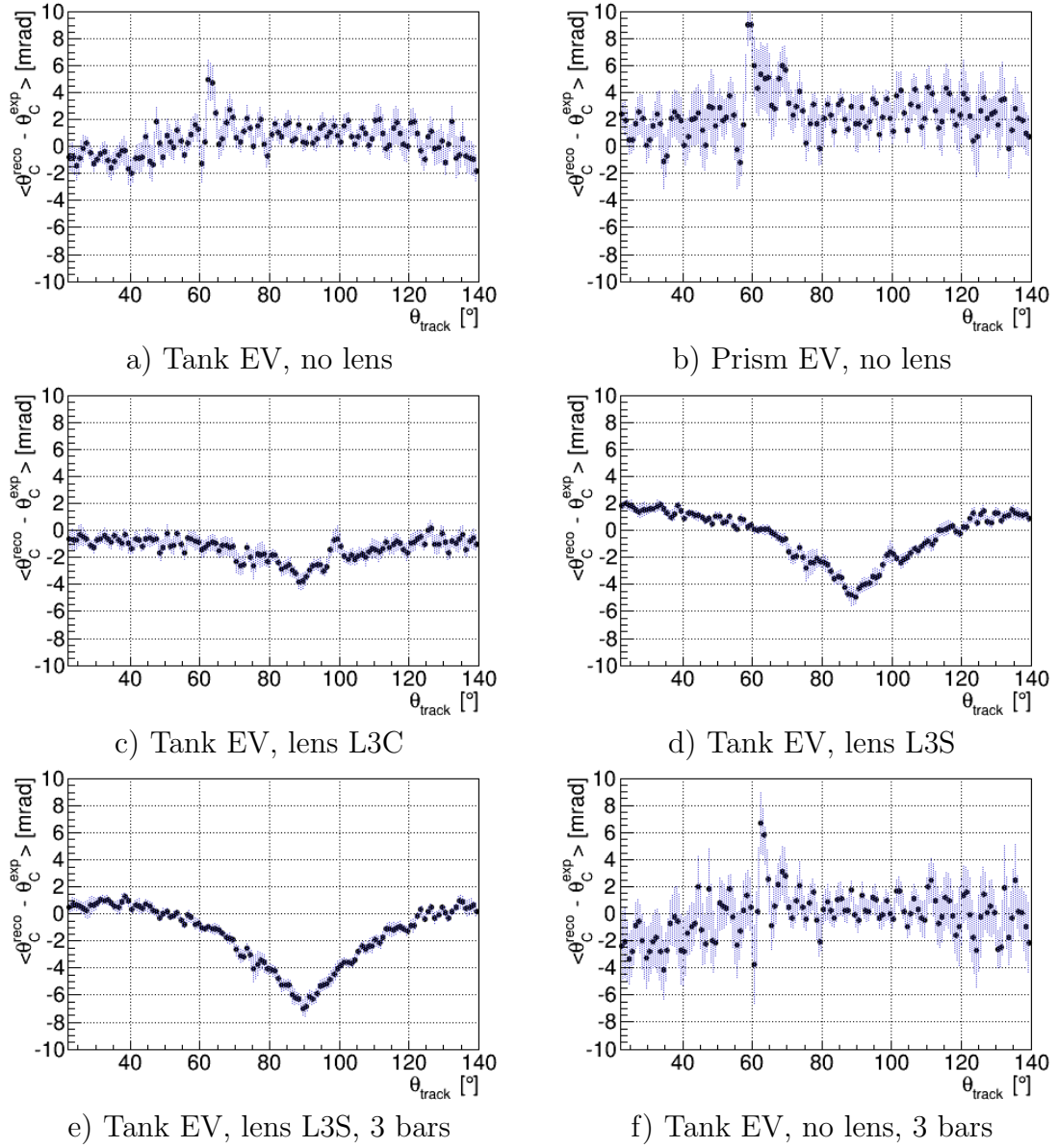


Figure 4.47: Mean value of the difference between the reconstructed and expected Cherenkov angles $\langle \theta_C^{\text{reco}} - \theta_C^{\text{exp}} \rangle$ (reconstruction bias) as a function of the polar angle of the charged particle for different design options.

to perpendicular incidence. The same problem exists for a more sophisticated two-component lens with an air gap. To solve this problem, lenses without an air gap were developed. Among those lenses the spherical two-component lens (L2S) provides good focusing quality and meets the PID requirement. However, since it has a parabolic focal surface, the imaging was not equally good across the photodetection plane. This lead to complicated distributions of the figures of merit. The spherical three-component lens without air gap (L3S) was proven to be a promising option for the PANDA Barrel DIRC with good focusing properties and a sufficient number of detected photons for the whole range of the track polar angles. All the available

lenses were implemented in spherical and cylindrical shape. The designs with the cylindrical two- and three-component lenses without air gap meet the PID requirement. A special asymmetric lens configuration failed to provide the performance meeting the PANDA PID requirement.

The evaluation of the baseline detector design, comprising the tank expansion volume, the compound lens without air gap, and five radiator bars in each bar box, confirmed that this design is capable of reaching the required performance. The same design with the prism-shaped EV also meets the PID requirement. However, further studies revealed that some design modifications improve the total detector cost with little or no loss in performance. One example is the number of radiators, which can be reduced by 40%. The corresponding design has three wide bars (with width of 5.2 cm) for each flat section of the barrel. The radiator thickness was varied in the range between 1 cm, which is the minimal value for industrial fabrication of the radiators, to 2 cm, which still fits with the baseline mechanical structures. The performance of the designs with the modified radiator thickness showed no improvement compared to the baseline value of 1.7 cm. The fused silica prism-shaped expansion volume improves the photon yield compared to the oil-filled vessel and requires fewer photosensors to be used (240 MCP-PMTs compared to 282 for the tank EV). The baseline dimensions of the prism are: a width of 17 cm, depth of 30 cm, and opening angle of 42°, which corresponds to 3 × 5 MCP-PMTs covering the prism backplane. The detector performance for the opening angle values of 48° and 36°, corresponding to 6 and 4 rows of photosensors respectively, did not show major differences. This means that the number of MCP-PMTs can be reduced by 20% with no loss in performance. The baseline depth of the EV is the maximum available given the space limitations inside the PANDA detector. However, a slightly deeper EV can be accommodated, if it shows a better performance. Smaller values of the EV depth lead to deterioration of the detector resolution, therefore, were not tested. The EV depths of 35 cm and 40 cm were evaluated in the simulation and showed no improvement. The upward and downward steps of the EV have a very little impact on the detector performance. The minimal value of the downward step of 0.5 cm is required when the geometric reconstruction method is used. The tilt of the photodetection plane did not influence the detector performance much, therefore, is not needed. The number of channels can be reduced using rectangular pixels, which are the square pixels of MCP-PMTs used in pairs.

Chapter 5

Summary and Outlook

A compact Cherenkov counter based on the DIRC principle will be used in the PANDA detector for hadronic particle identification (PID) in the barrel region. The baseline design of the PANDA Barrel DIRC is based on the successful *BABAR* DIRC. An extensive R&D process, including the simulation and prototype tests in particle beams, is being carried out to optimize the PANDA Barrel DIRC design in terms of performance and cost. First, the general PANDA PID requirement of more than three standard deviations separation between kaons and pions in the momentum range up to 3.5 GeV/c was adapted to the Barrel DIRC and transformed into the DIRC-only detector resolution. The detailed detector simulation allows testing of different design options and optimize their parameters before fabricating those elements for prototype tests. A geometric reconstruction procedure based on the one used for the *BABAR* DIRC, was applied to obtain the Cherenkov angle and the corresponding single photon Cherenkov angle resolution σ_{θ_C} . Combined with the photon yield N_γ , it results in the DIRC-only Cherenkov angle resolution for a track $\sigma_0 = \sigma_{\theta_C}/N_\gamma$. These three values are the figure of merit for a particular detector design.

The main cost drivers are the number of radiator pieces and the total number of the photosensors. Most of the design options were tested with two types of expansion volumes (EV): the baseline single tank filled with mineral oil and the compact prism-shaped EVs made of synthetic fused silica. The comprehensive parameter space investigated in the simulation included the variation of the radiator shape in both width and thickness, different lens configurations, and various parameters of the expansion volume and photodetectors.

It was demonstrated that a focusing system is essential to meet the PID requirement. The compound lens without air gap was proven to be a promising option for the PANDA Barrel DIRC. The evaluation of the baseline detector design comprising the tank expansion volume, the compound spherical lens without air gap, and five radiator bars in each bar box confirmed, that it is capable of reaching the required performance. However, the total detector cost can be reduced while keeping the performance at the same level, if some design modifications are made. The number of radiators can be reduced by 40% with no loss in performance by increasing the

width of the bars. The fused silica prism-shaped expansion volumes improves the photon yield compared to the oil-filled vessel and requires fewer photosensors. The number of MCP-PMTs can be further reduced by shrinking the opening angle of the expansion volume.

The most promising cost-effective detector design that meets the PID requirement includes

- Three bars in each bar box;
- The three-component spherical lens without air gap;
- The prism-shaped fused silica EV with opening angle of 38° ;
- 192 MCP-PMTs (3×4 MCP-PMT for each 16 prism EV);

The number of channels in this option can be halved by combining the neighbouring pixels. This detector design has 40% fewer radiators and 31% fewer MCP-PMTs, which leads to a significant cost reduction compared to the baseline design. The remaining questions are oriented towards the possible use of a single wide radiator plate in each bar box instead of narrow bars, which further reduces the radiator fabrication cost, and towards further optimization of the lens system. These issues are currently under investigation and will be the focus of the test beam campaign in 2015, which will form the basis for the technical design report of the PANDA Barrel DIRC, expected in 2016.

Chapter 6

Ausführliche Zusammenfassung

Das PANDA (antiProton Annihilation in DArmstadt) Experiment wird an der zukünftigen FAIR Facility (Facility for Antiproton and Ion Research) in Darmstadt durchgeführt werden. Zur Messung zentraler Eigenschaften der starken Wechselwirkung werden streureaktionen von Antiprotonen an unterschiedlichen nuklearen Targets untersucht. Bei wesentlichen Anforderungen an den PANDA Detektor ist in dieser Hinsicht der präzise Nachweis aller Reaktionsprodukte einschließlich der Bestimmung der jeweiligen Teilchenart, welche eine exzellente Teilchenidentifikation (engl. PID, Particle Identification) erfordert. Von besonderer Bedeutung im Charmonium- und Open Charm Bereich ist dabei die Trennung von Kaonen und Pionen mit hoher Güte. Für die Identifikation von Hadronen sind bei PANDA drei Detektoren vorgesehen. Basierend auf dem DIRC (Detection of Internally Reflected Cherenkov light) Prinzip wird gegenwärtig für die Barrel Region ein Cherenkov Zähler entwickelt, der den polaren Winkelbereich von 22° bis 140° abdecken wird und eine Kaon-Pion-Trennung bis zu Teilchenimpulsen von $3.5 \text{ GeV}/c$ erlauben soll.

Der PANDA Barrel DIRC (siehe Abb. 6.1) ist ein kompakter Tscherenkow-Detektor, welcher konzeptionell an den für das *BABAR*-Experiment entwickelten DIRC Detektor angelehnt ist. Dieser war über zehn Jahre lang bei der Beschleuniger-Anlage PEP-II am Stanford Linear Accelerator Center (SLAC) erfolgreich in Betrieb. Die heutzutage zur Verfügung stehende verbesserte Technologie von Photondetektoren erlaubt allerdings signifikante Verbesserungen in der Umsetzung eines modernen DIRCs unter Berücksichtigung der Erfahrungen bei *BABAR*. Damit ist insbesondere eine deutlich schnellere Signalverarbeitung und eine kompaktere Detektorgeometrie durch kleinere Photosensoren gemeint. Um hiervon zu profitieren, gibt es entscheidende Verbesserungen am PANDA Barrel DIRC gegenüber seinem Vorgänger bei *BABAR*: schnelleres Timing, ein kompakteres Expansionvolumen und fokussierende Optik.

Die allgemeine PANDA PID Anforderung ist die Kaon-Pion-Trennung mit einer Güte von mindestens drei Standardabweichungen für Teilchen im Impulsbereich zwischen $0.5 \text{ GeV}/c$ und $3.5 \text{ GeV}/c$. Aus diesem Gütekriterium lässt sich ein entsprechendes Limit für das Auflösungsvermögen des PANDA Barrel DIRC ableiten. Um die akzeptable Obergrenze für die Detektorauflösung zu bestimmen, wird die

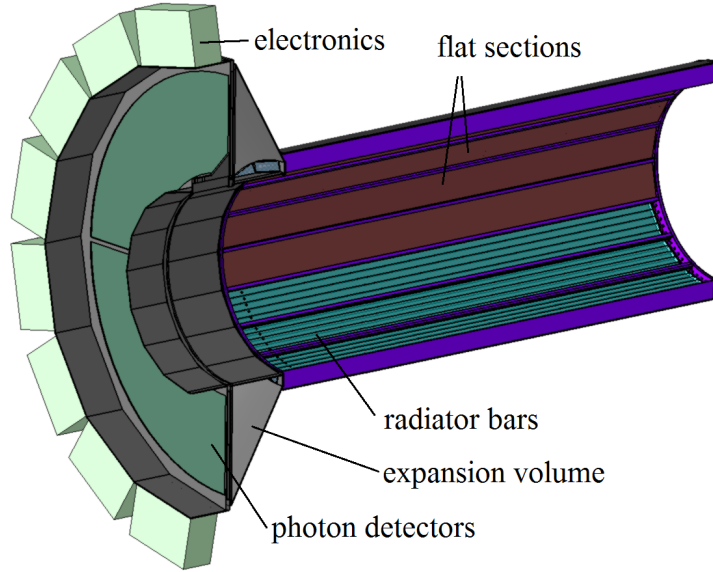


Figure 6.1: Technische Zeichnung des PANDA Barrel DIRC inklusive der tragenden Struktur für die Stabboxen, Expansionsvolumen und Elektronik. Die Quarzstäbe sind in drei der Stabboxen graphisch dargestellt.

Verteilung der Kaonen aus typischen PANDA Signalreaktionen betrachtet. Die kumulative Phasenraumverteilung der Kaonen im Endzustand ist in Abbildung 6.2a gezeigt. Das Limit für die Detektorauflösung als Funktion des Teilchenpolarwinkels (grüne Linie in Abb. 6.2b) wurde dann genutzt um die verschiedenen Detektorkonfigurationen quantitativ zu beurteilen.

Der R&D Prozess umfasst detaillierte Simulationsrechnungen sowie Vermessung von Prototypen mittels Teststrahl. Hierbei soll das Barrel-DIRC Design hinsichtlich des Kosten-Nutzen-Verhältnisses optimiert werden.

Die detaillierte Detektorsimulation ermöglicht das Testen verschiedener Detektorkonfigurationen und die Optimierung ihrer Parameter, bevor die entsprechenden Elemente für Prototyp Tests hergestellt werden. Zur Rekonstruktion des Tscherenkowwinkels und der Bestimmung der damit verknüpften Einzel-Photon-Auflösung (engl. SPR, Single Photon Cherenkov angle Resolution) wurde dieselbe Rekonstruktionsstrategie wie beim *BABAR* DIRC angewandt. Die Photonenausbeute (N_γ), SPR, und die sich heraus ergebende Auflösung des Tscherenkowwinkels für eine Einzelspur $\sigma_0 = SPR/\sqrt{N_\gamma}$ werden als Bewertungsfaktor gewählt, da sich diese Werte im Gegensatz zu den üblichen Kenngrößen wie Effizienz der Klassifikation oder der sog. Mis-ID (fehlerhafte Akzeptanz von Teilchen falschen Typs) gut in Testexperimenten messen lassen. Da die Bewertungsfaktoren über den Detektorphasenraum variieren, werden die Ergebnisse für eine vorgegebene Geometrie als zweidimensionales Diagramm dargestellt. Das Verhalten von N_γ , SPR und σ_0 als Funktion des Teilchenpolarwinkels lässt einen einfachen Vergleich der verschiedenen Designs und eine entsprechende Beurteilung der Designqualität zu.

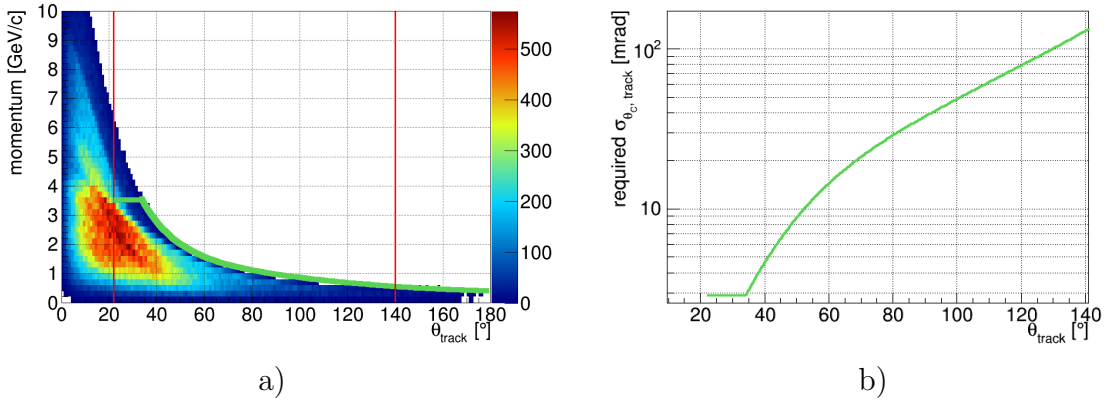


Figure 6.2: a) Kumulative Phasenraumbelegung der Kaonen aus verschiedenen Open Charm Zerfällen bei maximalem Strahlimpuls $p = 15 \text{ GeV}/c$. Der maximale, für die K/π Ternnung relevante Teilchenimpuls ist hier als Funktion des Polarwinkels in grün dargestellt. Die roten Linien markieren den Akzeptanzbereich des PANDA Barrel DIRC. b) Minimal erforderliche Auflösung des Tscherenkovwinkels (grüne Linie), welche sich aus der in (a) gezeigten funktionalen Abhängigkeit ergibt.

Die Studien hinsichtlich der Optimierung des PANDA Barrel DIRC Designs wurden gemäß ihres Einflusses auf die Detektorkosten und -leistung priorisiert. Hauptkostenverursacher sind die Anzahl der Radiatorelemente und die Gesamtanzahl der Photosensoren. Die meisten der Konfigurationen wurde mit zwei Typen des Expansionsvolumens (EV) getestet: dem mit allen Radiatorboxen verbundenen mit Mineralöl gefüllten Tank als Basisoption, und den pro Radiatorbox separierten Prismen aus Quarzglas. Der in der Simulation untersuchte Parameterraum umfasst die Variation der Radiatorform, -breite und -dicke, verschiedene Linsenkonfigurationen, und verschiedenartige Parameter des Expansionsvolumen und der Photodetektoren.

Es konnte im Rahmen dieser Arbeit gezeigt werden, dass für die Erfüllung der PID Anforderungen, ein fokussierendes System erforderlich ist. Die Verbundlinsen ohne Luftspalt erwiesen sich als eine vielversprechende Option für den PANDA Barrel DIRC. Als Grundlage für die Beurteilung der verschiedenen Detektordesigns diente die Basiskonfiguration, charakterisiert durch den Öltank als Expansionsvolumen, die zusammengesetzte Linse ohne Luftspalt und fünf Quarzstäbe pro Box, da diese Konfiguration den Anforderungen der PANDA PID genügt. Jedoch können die Gesamtkosten bei Erhalt ausreichender Leistungsfähigkeit reduziert werden, wenn einige Veränderungen im Design vorgenommen werden. Die Anzahl der Radiatoren kann ohne Verlust der Leistungsfähigkeit durch eine Verbreiterung der Stäbe um 40% reduziert werden. Das kompakte Expansionsvolumen aus Quarz verbessert verglichen mit zu dem Ölbehälter die Photonenausbeute und benötigt weniger Photosensoren. Die Anzahl der Photosensoren (MCP-PMTs) kann darüber hinaus durch einen flacheren Öffnungswinkel des Expansionsvolumen noch weiter reduziert werden.

Das im Rahmen dieser Arbeit ermittelte, optimale Detektorkonfiguration ist durch die Kombination der folgenden Designparameter gegeben:

- Drei stabförmige Radiatorelemente pro Box
- Die Verbundlinse ohne Luftspalt
- Die kompakten Quarz-Prismas als Expansionsvolumina (EV) mit einem Öffnungswinkel von 38°
- 192 MCP-PMTs (3×4 MCP-PMT für jedes der 16 EV).

Darüber hinaus kann die Anzahl der Kanäle durch das Zusammenschalten jeweils zweier benachbarter Pixel halbiert werden. Diese Detektorkonfiguration hat damit 40% weniger Radiatorelemente und 31% weniger MCP-PMTs im Vergleich zur Basiskonfiguration, was zu einer signifikanten Kostenreduktion führt. In Abb. 6.3 sind die verschiedenen Leistungsmerkmale dieser optimalen Konfiguration dargestellt. Eine weiterführende Modifikation im Detektordesign stellt die Verwendung einer einzigen breiten Radiatorenplatte pro Stabbox anstelle der schmalen Stäbe dar, was zu einer zustzlichen Senkung der Herstellungskosten der Radiatorelemente führt, sowie die weitere Optimierung des Linsensystems. Diese Aspekte sind Gegenstand aktueller Studien, deren Resultate Bestandteil des in Arbeit befindlichen Technischen Design Reports über den PANDA Barrel DIRC sein werden. Dieser wird voraussichtlich im Jahr 2016 fertiggestellt sein.

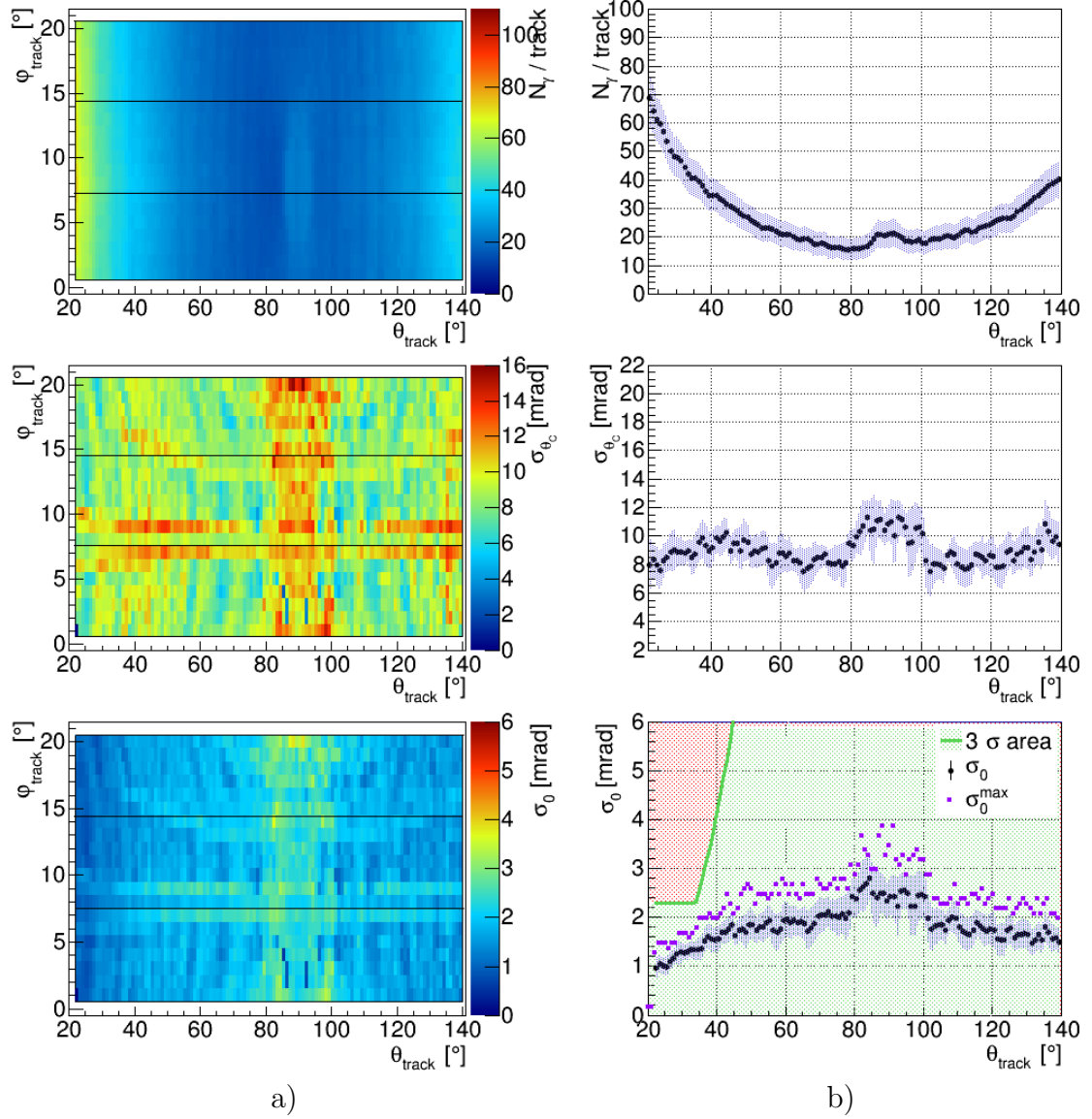


Figure 6.3: Die Leistungsmerkmale der optimierten Detektorkonfiguration (siehe Text): Photonenausbeute: Photonenausbeute (oberste Reihe), SPR (mittlere Reihe), und σ_0 (untere Reihe) als Funktion des Teilchenpolarwinkels und des azimuthalen Winkels (a) und des Teilchenpolarwinkels (b). Der grün markierten Bereich im untersten Diagramm entspricht den Werten der Auflösung $\sigma_0(track)$, welche den PID Anforderungen genügen.

Bibliography

- [1] J. Schwiening. “The barrel DIRC detector for the PANDA experiment at FAIR”. In: *Nucl. Instr. and Meth. A* 639 (2011). Proceedings of the Seventh International Workshop on Ring Imaging Cherenkov Detectors, pp. 315–318.
- [2] PANDA Collaboration et al. “Physics Performance Report for PANDA: Strong Interaction Studies with Antiprotons”. In: *arXiv:0903.3905 [hep-ex]* (Mar. 23, 2009).
- [3] Donald H. Perkins. *Introduction to High Energy Physics*. Addison-Wesley Publishing Company, 1972.
- [4] P. Bagnaia et al. “Evidence for $Z^0 \rightarrow e^+e^-$ at the CERN pp collider”. In: *Phys. Lett. B* 129 (1983), pp. 130–140.
- [5] J. Alitti et al. “A measurement of the W and Z production cross sections and a determination of Γ_w at the CERN $\bar{p}p$ collider”. In: *Phys. Lett. B* 276 (1992), pp. 365–374.
- [6] S. Abachi et al. “Observation of the Top Quark”. In: *Phys. Rev. Lett.* 74 (14 Apr. 1995), pp. 2632–2637.
- [7] G. Aad et al. “Observation of a new particle in the search for the Standard Model Higgs boson with the ATLAS detector at the LHC”. In: *Phys. Lett. B* 716 (2012), pp. 1–29.
- [8] K. Ranjan. “Observation of a new boson at the LHC with the CMS Experiment”. In: *Nuclear Physics B - Proceedings Supplements* 251 (2014), pp. 129–134.
- [9] P. Gianotti. “Results and perspectives in hadron spectroscopy”. In: *Physica Scripta* 2012.T150 (2012), p. 014014.
- [10] <http://www.fair-center.eu/>.
- [11] *Technical Design Report FAIR Antiproton Target and Separator*. Tech. rep. 2008.
- [12] *Technical Progress Report for PANDA*. Tech. rep. 2005.
- [13] PANDA Collaboration. *Physics Performance Report for: PANDA*. Tech. rep. Facility for Antiproton and Ion Research, 2009.
- [14] PANDA Collaboration et al. “Technical Design Report for the PANDA Solenoid and Dipole Spectrometer Magnets”. In: *arXiv:0907.0169 [hep-ex, physics:physics]* (July 1, 2009).

- [15] C. Lippmann. “Particle identification”. In: *Nucl. Instr. and Meth. A* 666 (2012). Advanced Instrumentation, pp. 148–172.
- [16] http://www-panda.gsi.de/html/det/pictures/detector/Panda_1401_1_3D.pdf.
- [17] Camelia Mironov The Star Collaboration. “Studying nuclear matter created in $p + p$, $d + Au$ and $Au + Au$ collisions using charged kaons”. In: *Journal of Physics: Conference Series* 50.1 (2006), p. 311.
- [18] PANDA Collaboration et al. “Technical Design Report for the: PANDA Micro Vertex Detector”. In: *arXiv:1207.6581 [physics]* (July 2012). arXiv: 1207.6581.
- [19] *Particle Identification at PANDA, Report of the PID TAG*. Tech. rep. 2009.
- [20] PANDA Collaboration et al. “Technical Design Report for the: PANDA Straw Tube Tracker”. In: *The European Physical Journal A* 49 (Feb. 2013).
- [21] C. Schwarz et al. “Particle identification for the PANDA detector”. In: *Nucl. Instr. and Meth. A* 639.1 (2011), pp. 169–172.
- [22] O. Merle et al. “Development of an Endcap DIRC for PANDA”. In: *Nucl. Instr. and Meth. A* 766 (2014). RICH2013 Proceedings of the Eighth International Workshop on Ring Imaging Cherenkov Detectors Shonan, Kanagawa, Japan, December 2-6, 2013, pp. 96–100.
- [23] O. Merle, “Design und Entwicklung von DIRC Čerenkov Detektoren für das PANDA Experiment”. PhD thesis. Justus-Liebig-Universität Giessen, 2014.
- [24] *The PANDA Muon System*. Tech. rep. 2011.
- [25] PANDA Collaboration et al. “Technical Design Report for PANDA Electromagnetic Calorimeter (EMC)”. In: *arXiv:0810.1216 [hep-ex, physics:physics]* (Oct. 7, 2008).
- [26] nobelprize.org. *The Nobel Prize in Physics 1958*. nobelprize.org/nobel-prizes/physics/laureates/1958/. 2011.
- [27] K.A. Olive et al. “Review of Particle Physics”. In: *Chin.Phys. C*38 (2014), p. 090001.
- [28] http://refractiveindex.info/?group=GLASSES&material=F_SILICA.
- [29] J. Weber. “Phase, Group, and Signal Velocity”. In: *American Journal of Physics* 22 (1954), pp. 618–620.
- [30] I. Tamm and I. Frank. 1937.
- [31] T. Sumiyoshi et al. “Silica Aerogel Cherenkov Counter for the KEK B-factory Experiment”. In: *Nucl. Instr. and Meth. A* 433 (1999), pp. 385–391.
- [32] J. Seguinot and T. Ypsilantis. “Photo-ionization and Cherenkov ring imaging”. In: *Nucl. Instr. and Meth. A* 142 (1977), pp. 377–391.
- [33] S. Easo. “Overview of LHCb RICH detector development”. In: *Nucl. Instr. and Meth. A* 553 (2005). Proceedings of the fifth International Workshop on Ring Imaging Detectors Fifth International Workshop on Ring Imaging Detectors, pp. 333–338.

[34] P. Coyle et al. “The DIRC counter: A New type of particle identification device for B factories”. In: *Nucl. Instr. and Meth.* A343 (1994), pp. 292–299.

[35] Blair N. Ratcliff. “Imaging rings in Ring Imaging Cherenkov counters”. In: *Nucl. Instr. and Meth.* A502 (2003), pp. 211–221.

[36] T. Kamae et al. “Focusing DIRC: A New compact Cherenkov ring imaging device”. In: *Nucl. Instr. and Meth.* A382 (1996), pp. 430–440.

[37] J. Benitez et al. *Status of the Fast Focusing DIRC (fDIRC)*. 2008.

[38] I. Adam, et al. “The DIRC particle identification system for the BABAR experiment”. In: *Nucl. Instr. and Meth.* A 538 (2005), pp. 281–357.

[39] J. Cohen-Tanugi et al. “Optical properties of the DIRC fused silica Cherenkov radiator”. In: *Nucl. Instr. and Meth.* A 515 (Dec. 11, 2003), pp. 680–700.

[40] BABAR-DIRC collaboration and J. Schwiening. “Construction and performance of the BABAR-DIRC”. In: *Journal of Instrumentation* 4.10 (2009), P10004.

[41] A. Britting. “Analyse und signifikante Verbesserung der Lebensdauer von Microchannel-Plate Photomultipliern hinsichtlich ihrer Applikation für das PANDA-Experiment”. PhD thesis. Friedrich-Alexander-Universität Erlangen-Nürnberg, 2014.

[42] PHOTONIS. 660 Main Street, Sturbridge, MA 01518, USA. <http://www.photonis.com/en/ism/63-planacon.html>.

[43] K. Inami. “TOP counter for particle identification at the Belle II experiment”. In: *Nucl. Instr. and Meth.* A766 (2014). RICH2013 Proceedings of the Eighth International Workshop on Ring Imaging Cherenkov Detectors Shonan, Kanagawa, Japan, December 2-6, 2013, pp. 5–8.

[44] V.V. Uzhinsky A. Galoyan. “New Monte Carlo Implementation of Quark-Gluon-String model of p-bar p-Interactions”. In: *AIP Conf. Proc.* 796 (2005), pp. 79–82.

[45] Private communication - Gianluigi Boca and Susanna Constanza.

[46] M. Starič. “Performance studies of the Belle II TOP counter”. In: *Nucl. Instr. and Meth.* A766 (2014). RICH2013 Proceedings of the Eighth International Workshop on Ring Imaging Cherenkov Detectors Shonan, Kanagawa, Japan, December 2-6, 2013, pp. 237–240.

[47] A. Carbone et al. *SuperB Progress Report: Detector*. 2012.

[48] D.A. Roberts et al. “Results from the FDIRC prototype”. In: *Nucl. Instr. and Meth.* A766 (2014). RICH2013 Proceedings of the Eighth International Workshop on Ring Imaging Cherenkov Detectors Shonan, Kanagawa, Japan, December 2-6, 2013, pp. 114–117.

[49] M.W.U. van Dijk et al. “TORCH - a Cherenkov based time-of-flight detector”. In: *Nucl. Instr. and Meth.* A766 (2014). RICH2013 Proceedings of the Eighth International Workshop on Ring Imaging Cherenkov Detectors Shonan, Kanagawa, Japan, December 2-6, 2013, pp. 118–122.

- [50] The LHCb Collaboration and A Augusto Alves Jr et al. “The LHCb Detector at the LHC”. In: *Journal of Instrumentation* 3.08 (2008), S08005.
- [51] R. Forty M.J. Charles. “TORCH: Time of Flight Identification with Cherenkov Radiation”. In: *Nucl.Instr. and Meth.* A639 (2011), pp. 173–176.
- [52] K. Föhl et al. “The WASA focussing light guide disc DIRC”. In: *Journal of Instrumentation* 7.01 (2012), p. C01002.
- [53] A Zink et al. “The DIRC prototype for the WASA experiment at COSY”. In: *Journal of Instrumentation* 9.04 (2014), p. C04014.
- [54] A. Zink. “Ein DIRC Detektor für das WASA@COSY-Experiment”. PhD thesis. Friedrich-Alexander-Universität Erlangen-Nürnberg, 2014.
- [55] Private communication - Adrian Zink.
- [56] Private communication - Joachim Schwiening.
- [57] M. Zühlsdorf. “Alternative Geometrical Designs for Quartz-based Cherenkov Detectors for the PANDA Barrel DIRC Detector”. In preparation. PhD thesis. Johann Wolfgang Goethe-Universität in Frankfurt am Main, 2015.
- [58] `svn+shn://charme@lx1001.gsi.de/v/charme/svn/drcprop`.
- [59] F. Rademakers R. Brun. “ROOT: An object oriented data analysis framework”. In: *Nucl.Instr. and Meth.* A389 (1997), pp. 81–86.
- [60] S. Spataro. “Simulation and event reconstruction inside the PandaRoot framework”. In: *Journal of Physics: Conference Series* 119.3 (2008), p. 032035.
- [61] F. Uhlig M. Al-Turany. “FairRoot framework”. In: *PoS ACAT08* (2008), p. 048.
- [62] S. Spataro. “Simulation and event reconstruction inside the PandaRoot framework”. In: *J. Phys. Conf. Ser.* 119 (2008), p. 032035.
- [63] J. Allison et al. “Geant4 developments and applications”. In: *Nuclear Science, IEEE Transactions on* 53.1 (Feb. 2006), pp. 270–278.
- [64] S. Agostinelli et al. “Geant4 – a simulation toolkit”. In: *Nucl. Instr. and Meth.* A 506 (2003), pp. 250–303.
- [65] I. Hřivnáčová. “The Geant4 Virtual Monte Carlo”. In: *Journal of Physics: Conference Series* 396.2 (2012), p. 022024.
- [66] Epoxy Technology, Inc. 14 Fortune Drive Billerica, MA 01821.
- [67] Eljen Technology, 1300 W. Broadway Sweetwater, TX79556, USA. <http://www.eljentechnology.com/index.php/products/accessories/93-ej-500>.
- [68] H. Bennet J. Elson and J. Bennet. *Scattering from optical surfaces*. Vol. 7. Applied Optics and Optical Engineering. Academic Press New York, 1979.
- [69] MCP-PMT refractive index courtesy of PHOTONIS France S.A.S.
- [70] ExxonMobil Lubricants & Specialties Europe, Hermeslaan 2, 1831 Machelen, Belgium.

- [71] J. Va’Vra. “Simulation of the focusing DIRC optics with Mathematica”. In: *Nuclear Science Symposium Conference Record, 2008. NSS ’08. IEEE*. Oct. 2008, pp. 2408–2412.
- [72] A. Britting, W. Eyrich, A. Lehmann, F. Uhlig. “Lifetime-issues of MCP-PMTs”. In: *Journal of Instrumentation* 6.10 (2011), p. C10001.
- [73] R. Duda and P. Hart. “Use of the Hough Transformation to Detect Lines and Curves in Pictures”. In: *Communications of the Association Computing Machinery* 15 (1972), pp. 11–15.
- [74] Private communication - Carsten Schwarz.
- [75] M. Katz. *Introduction to Geometrical Optics*. World Scientific Publishing Co. Pte. Ltd., 2002.
- [76] C. Schwarz et al. “Prototyping the {PANDA} Barrel {DIRC}”. In: *Nucl. Instr. and Meth. A* 766 (2014). {RICH2013} Proceedings of the Eighth International Workshop on Ring Imaging Cherenkov Detectors Shonan, Kanagawa, Japan, December 2-6, 2013, pp. 32–35.
- [77] Radian Zemax, 22908 NE Alder Crest Drive, WA 98053 USA. <https://www.radianzemax.com>.
- [78] G. Kalicy. “Development and Test of a Prototype for the PANDA Barrel DIRC Detector at FAIR”. PhD thesis. Johann Wolfgang Goethe-Universität in Frankfurt am Main, 2015.
- [79] Private communication - Klaus Föhl.

BIBLIOGRAPHY

Appendix A

Other Results

Chapter 4 contains figures of merit of the detector performance for a selected number of studied PANDA Barrel DIRC designs. Here the figures of merit for the rest of the studied detector designs listed in Tab. A.1 are present.

The designs containing the lenses with an air gap and one or two curved surfaces, L1SG and L2SG respectively, have the photon yield below 5 photons per track for the polar angles around 90° (see Fig. A.1, Fig. A.2, Fig. A.3). This is too low for the robust reconstruction. The single photon Cherenkov angle resolution (SPR) is better for the lens L2SG (7 – 18 mrad) than for the lens L1SG (8 – 20 mrad). The overall performance for the lenses with an air gap and both EV types is characterized by $\sigma_0(\theta_{track})$ lying completely in the green area, but due to a low photo yield these designs are not acceptable. The asymmetric one-component lens with an air gap L1SGA failed to place the parallel hit patterns on top of each other for the track polar angles around perpendicular incidence and, therefore, did not provide correct estimation of the SPR using the geometric reconstruction method for the polar angle range ($70^\circ, 110^\circ$). The design with the tank EV and the lens L1SGA was not evaluated in this range.

The lenses without air gap were developed to increase the number of detected photons. The design with the tank EV and two-component cylindrical lens without air gap (L2C) meets the performance requirements (see Fig. A.5). The designs containing the asymmetric two-component lenses without air gap in spherical and cylindrical shape, lenses L2SA and L2CA respectively, and either type of the EV (see Fig. A.6, Fig. A.7, Fig. A.8, and Fig. A.9) were evaluated in most of the polar angle range except of the range between 75° and 105° . In that range the ambiguous solutions for the reconstructed Cherenkov angle are distributed broadly around the true value, which deteriorates the peak shape and does not allow to extract the correct SPR value.

The performance of the design with the three-component lens without air gap (L3S) and the prism EV, which meets the performance requirements, is shown in Fig. A.10. In case when the cylindrical lens L3C of the same structure is used (see Fig. A.11), the photon yield increases by approximately 14% due to less side area of the cylindrical lens, where photons get lost. The SPR values deteriorate from

Design options		Tank EV	Fig.	Prism EV	Fig.
Spherical lenses		L1SG L2SG	A.1 A.2	L2SG L3S	A.3 A.10
Cylindrical lenses		L3C		L3C	A.11
1/2 of spherical lenses		L1SGA L2SA	A.4 A.6	L2SA	A.7
1/2 of cylindrical lenses		L2CA	A.8	L2CA L3CA	A.9 A.12
Bar thickness [cm]	1	L3S	A.23	–	
	2	no lens L3S	A.25 A.24		
Bar width	5.2 cm (3 bars)	no lens L3C L3S	A.22 A.21 A.20	–	
	4 cm (4 bars)	no lens L3C L3S	A.19 A.18 A.17	–	
Combined pixels (c.p.) $6.5 \times 13 \text{ mm}^2$		no lens L3S	A.13 A.15	no lens L3S	A.14 A.16
EV angle [°]	L3S	A.26	L3S	A.27	
EV depth [cm]	36	L3S	A.28	L3S	A.29
	48	L3S	A.30	–	
EV depth [cm]	35	L3S	A.31	–	
	40	L3S	–	L3S	A.32
Tilted PD plane [°] + EV depth 35 cm	10	–	–	L3S	A.33
	30	–	–	L3S	

Table A.1: Table of possible combinations of design options for the Barrel DIRC, which were not shown in Chapter 4. The opening angle of the EV of $\alpha_4 = 36^\circ$ corresponds to 4 radial rows of MCP-PMTs, and the EV opening angle of $\alpha_6 = 48^\circ$ to 6 rows.

7 – 12 mrad for the lens L3S down to 10 – 15 mrad for the lens L3C. However, the overall performance illustrated with $\sigma_0(\theta_{track})$ still meets the PID requirement. The performance of the design with the asymmetric cylindrical three-component lens without air gap and the prism EV is shown in Fig. A.12. The photon yield is around 15% lower than for the case of the lens L3S, and the SPR is about 50% worse. The overall performance cuts the red area indicating that the design with the asymmetric lens L3CA does not meet the PANDA PID requirement.

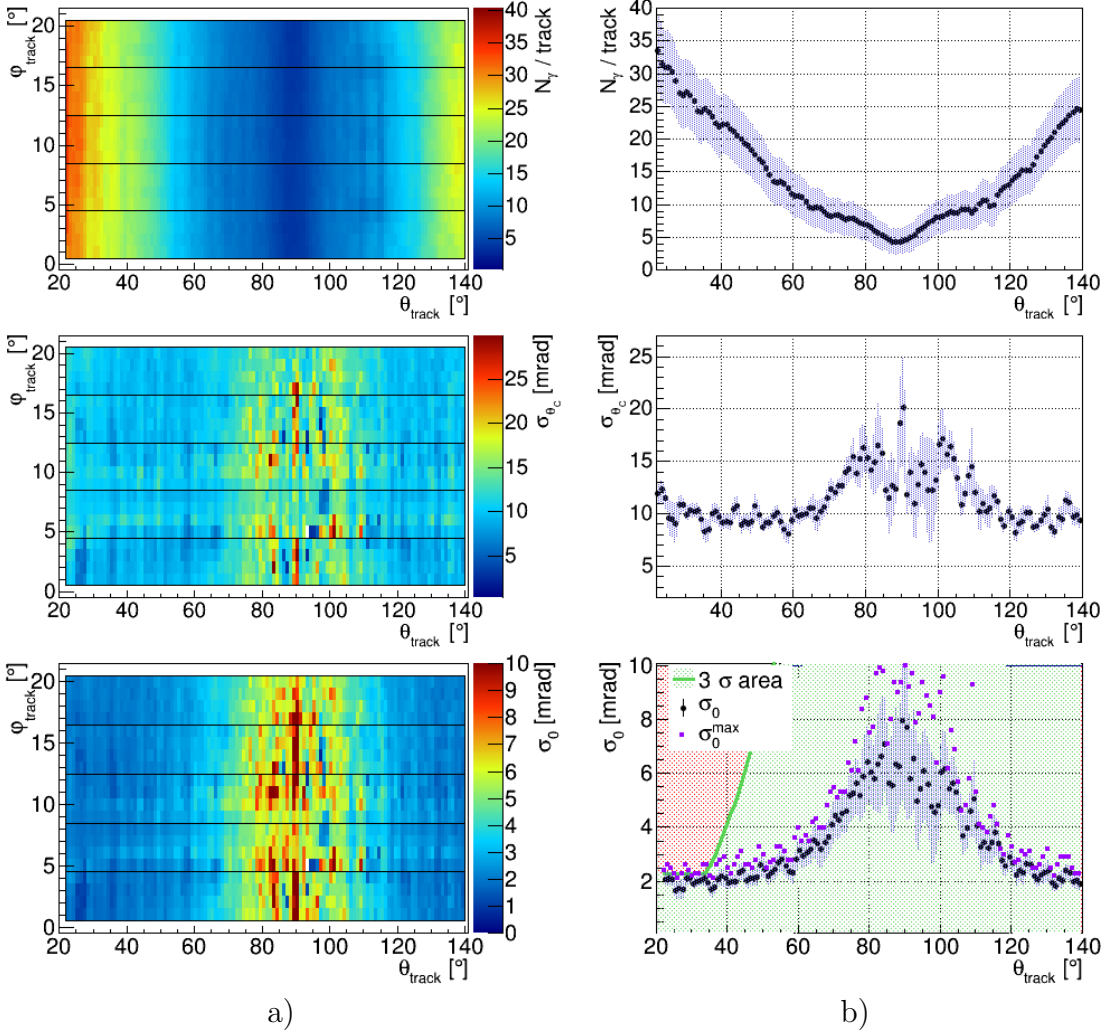


Figure A.1: Tank EV and the one-component spherical lens with an air gap (L1SG). The figures of merit: photon yield (upper row), SPR (middle row), and σ_0 (bottom row) as functions of the track polar and azimuthal angles (a) and only of the track polar angle (b). The area in the one-dimensional distribution of $\sigma_0(\theta_{\text{track}})$, where the PID requirement is fulfilled, is shaded in green. The blue uncertainty bands are described in Chapter 4.

Figure A.13 and Fig. A.14 show the figures of merit for the designs with the rectangular pixels and the tank or prism types of the EV. The performance of these designs meet the PID requirement and is almost identical with the corresponding designs with the square pixels (see Fig. 4.18 and Fig. 4.21). This means that using the square pixels in pairs almost does not influence the detector performance, while halves the number of electronic channels. The same is true for the case when the spherical three-component lens without air gap is used: the design with the lens L3S, combined pixels, and either of the EVs (shown in Fig. A.15 and A.16) performs almost the same as that with the usual square pixels (Fig. 4.30 and Fig. A.10).

Figure A.17 illustrates the performance of the design with the three-component

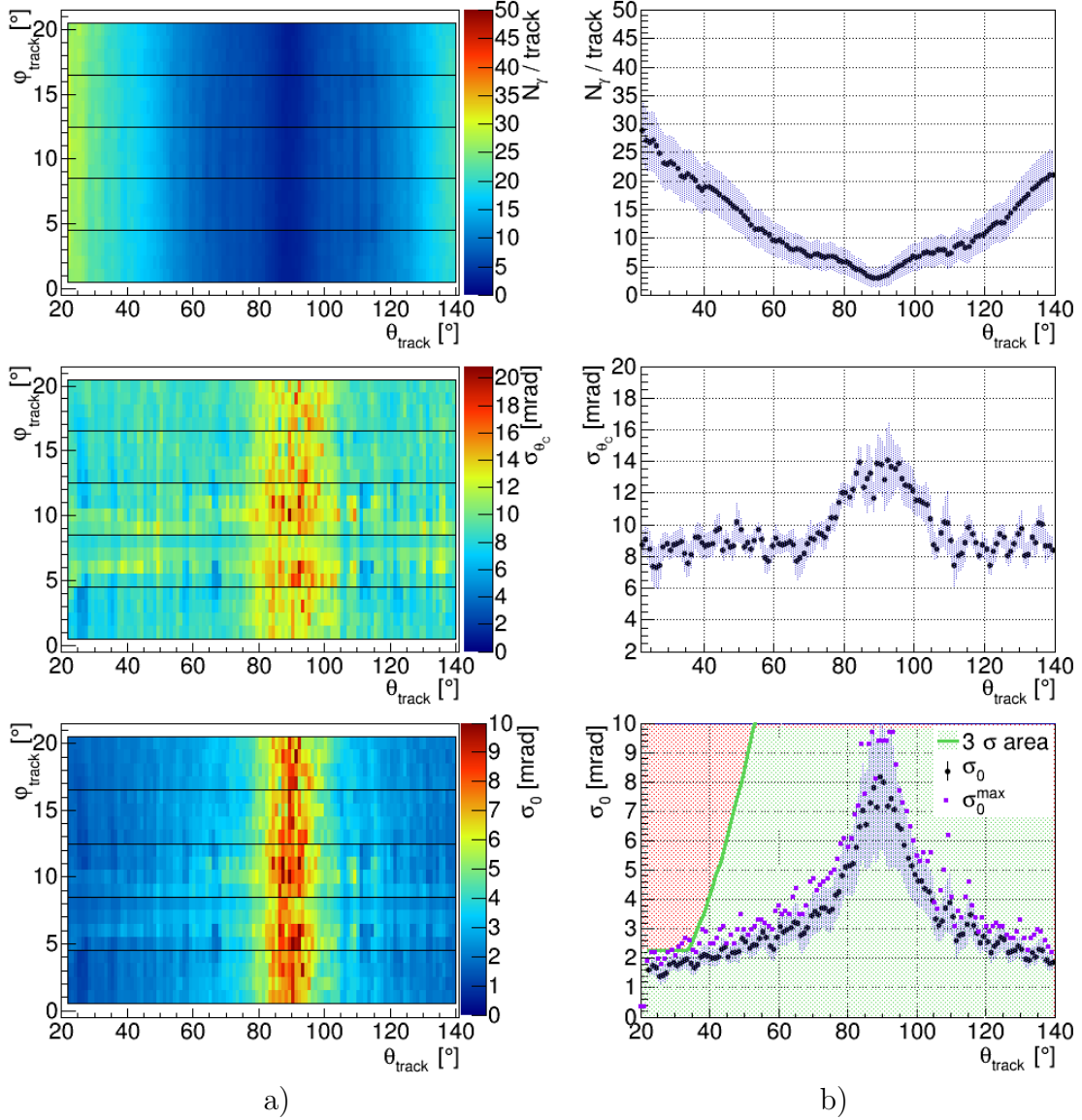


Figure A.2: Tank EV with the 2 cm thick radiators and the two-component spherical lens with an air gap (L2SG). For description of the plots see Fig. A.1.

spherical lens without air gap, the tank EV, and the four radiator bars in each flat section of the barrel. This design meets the PID requirements. Although, the same design with the cylindrical lens of the same structure L3C (see Fig. A.18) provides approximately 10% more photons per track, the SPR is about 50% worse, which results in the overall performance cutting the red area. The detector design with the tank EV, lens L3C and the 4 cm wide bars does not meet the PID requirement. Figure A.19 shows the figures of merit for the simplified design without focusing, with the tank EV, and 4 cm wide radiator bars. The plots can be compared with the figures of merit for the simplified design with the baseline radiator width (see Fig. 4.18). This design does not meet the PANDA PID requirement.

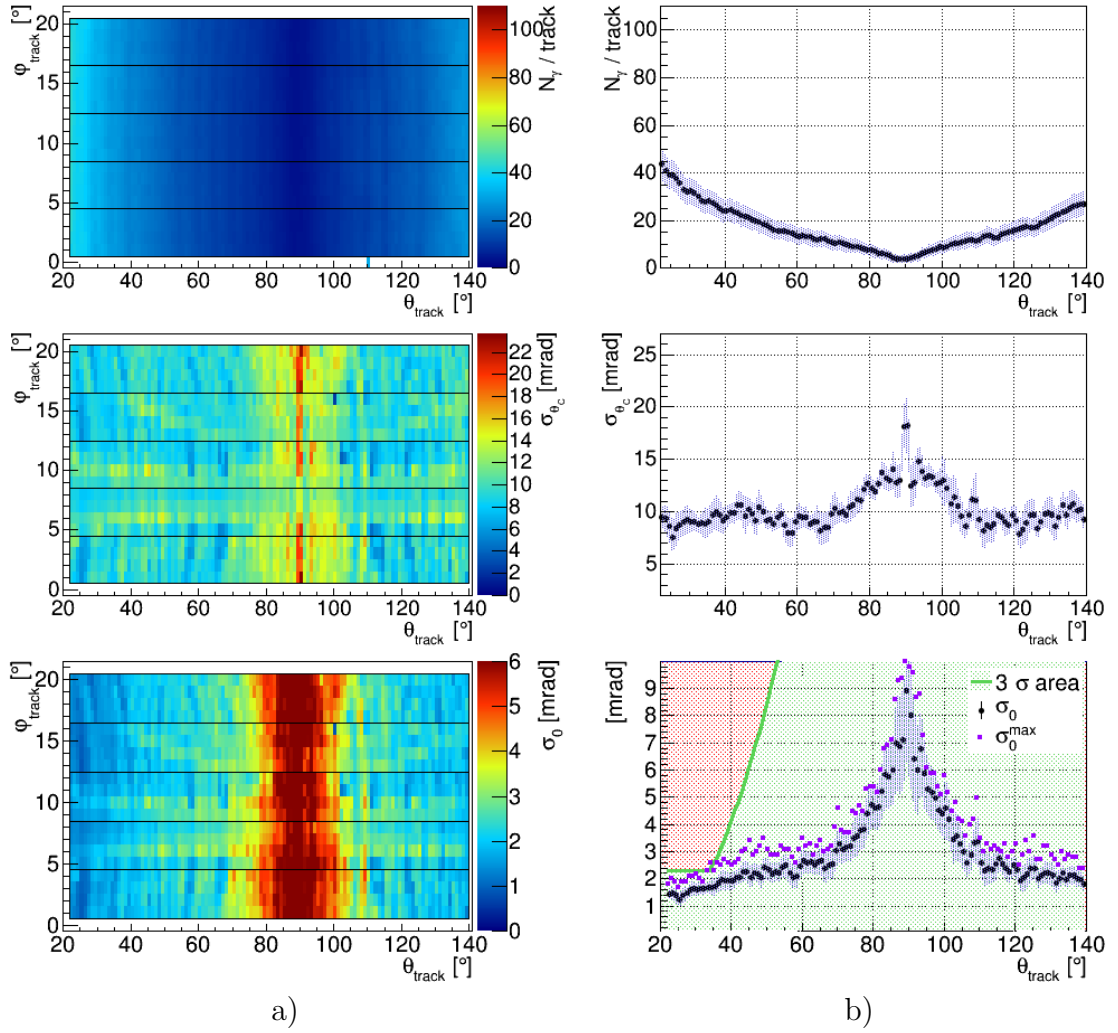


Figure A.3: Prism EV and the two-component spherical lens with an air gap (L2SG). For description of the plots see Fig. A.1.

Figure A.20 illustrates the performance of the detector design containing the tank EV, the lens L3S, and the 5.2 cm wide radiator bars, which corresponds to three radiator pieces in each flat section of the barrel. This design meets the PID requirement. The designs with the cylindrical lens L3C (Fig. A.21) and without focusing (Fig. A.22) are not acceptable.

Figure A.23 and Fig. A.24 show the performance of the design with the tank EV, lens L3S, and the radiator thickness of 1 cm and 2 cm respectively. These designs meet the PANDA PID requirement. In case when the detector geometry with the 2 cm thick radiators has no focusing, the performance is not sufficient to meet the PID requirement.

The variation of the EV opening angle does not change the detector performance visibly in case when the three-component spherical lens without air gap is used with either of the EV type. Figure A.26 and Fig. A.27 illustrate the performance of the detector designs with the tank and prism EVs, which have the opening angle of

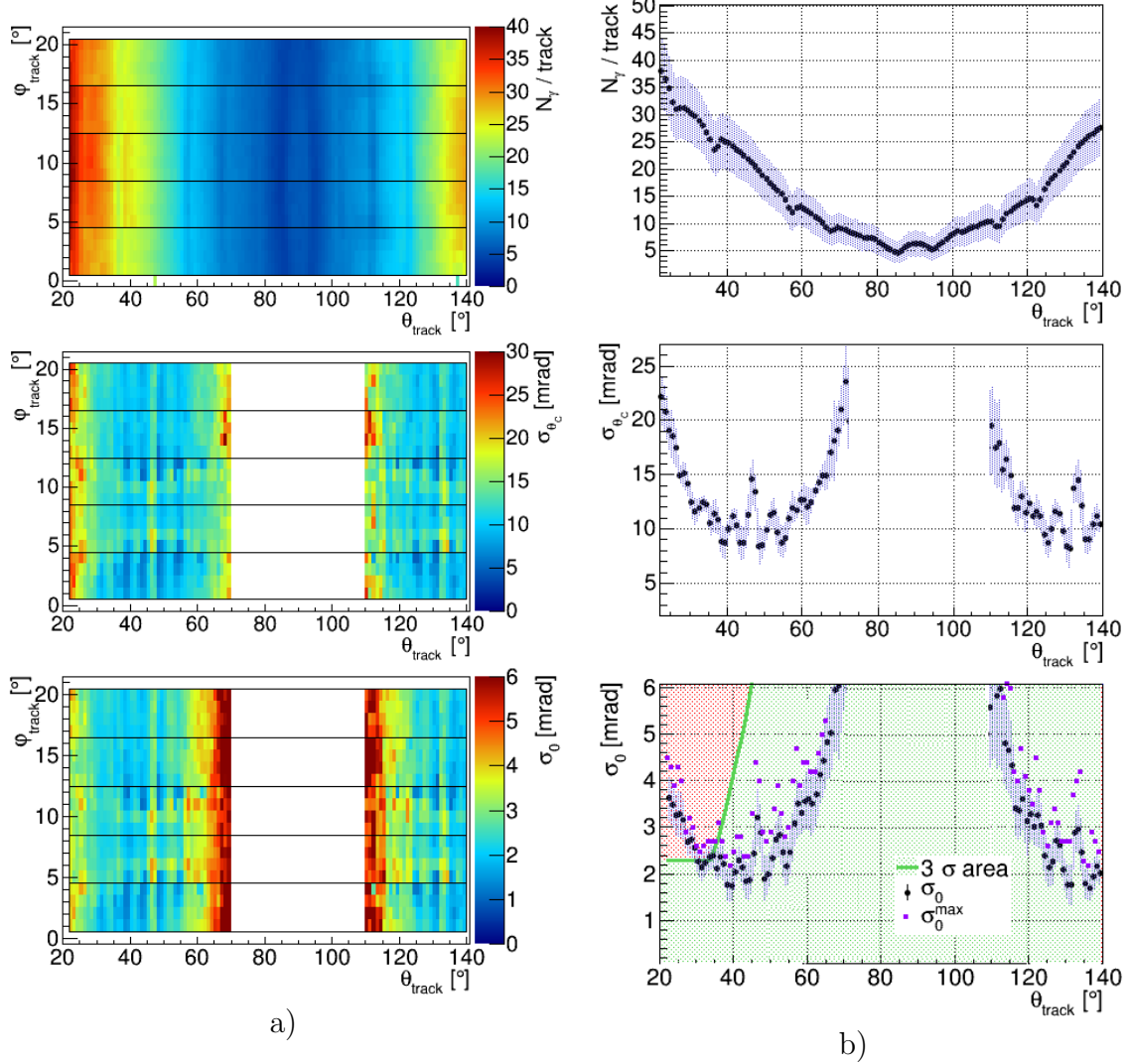


Figure A.4: Tank EV and the asymmetric one-component spherical lens with an air gap (L1SGA). For description of the plots see Fig. A.1.

$\alpha_4 = 36^\circ$, corresponding to four radial rows of photosensors. The both designs meet the PID requirement. Figure A.28 and Fig. A.29 show the figures of merit for the designs with the tank and prism types of the EV, which have the opening angle of $\alpha_6 = 42^\circ$ (corresponds to six radial rows of MCP-PMTs). These designs also meet the PID requirement.

The increased depth of the EV did not result in a visible differences of the detector performance. Thus, the designs with the tank EV, lens L3S, and the EV depth of 35 cm and 40 cm are characterized by almost identical figures of merit, which is illustrated in Fig. A.30 and Fig. A.31. Both of these designs meet the PANDA PID requirement.

Figure A.33 and Fig. A.32 show the figures of merit for the PANDA Barrel DIRC designs, which include the prism EV, lens L3S, and the tilted photodetection plane

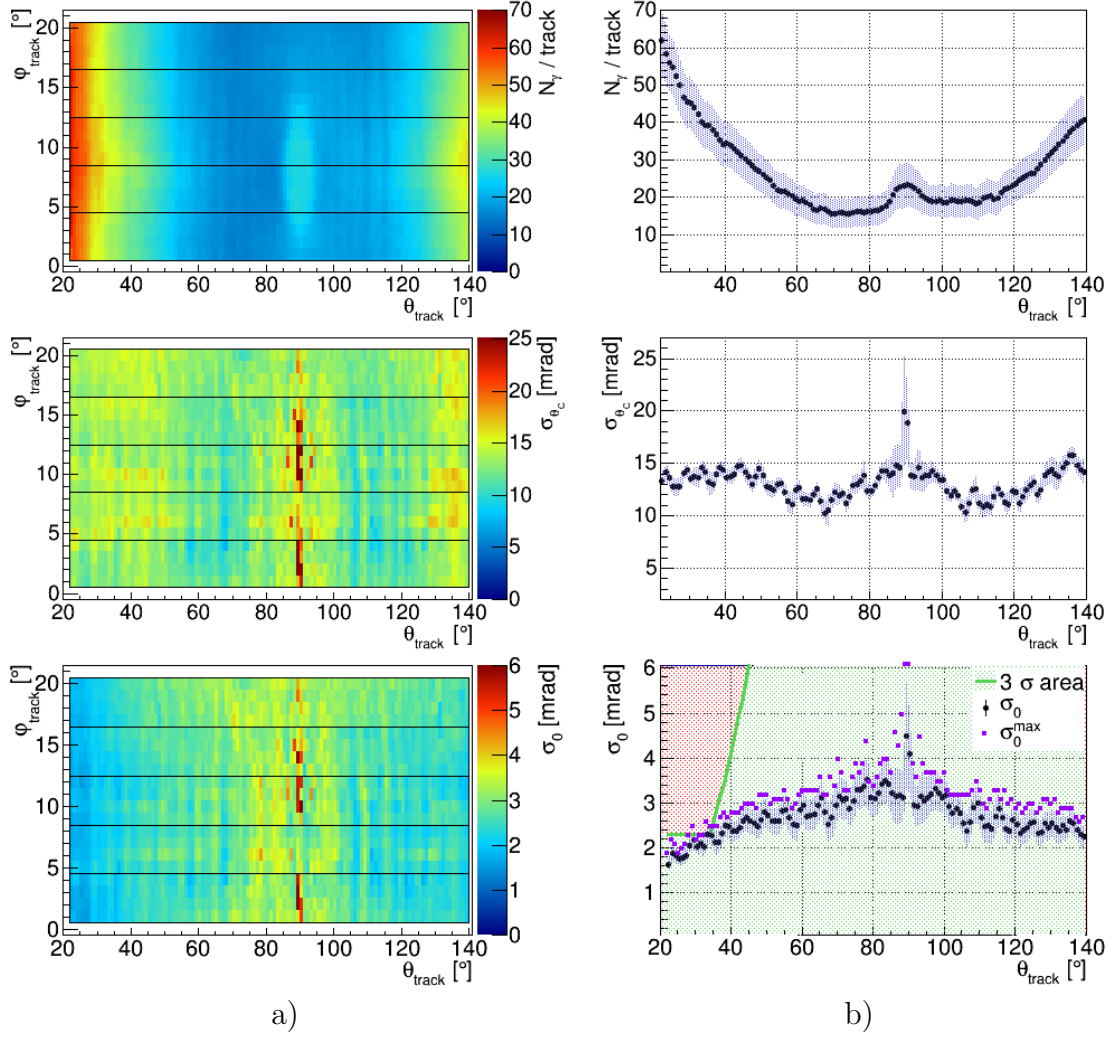


Figure A.5: Tank EV and the two-component cylindrical lens without air gap (L2C). For description of the plots see Fig. A.1.

by 30° and 10° respectively. Both design have similar performance and satisfy the PANDA PID requirements.

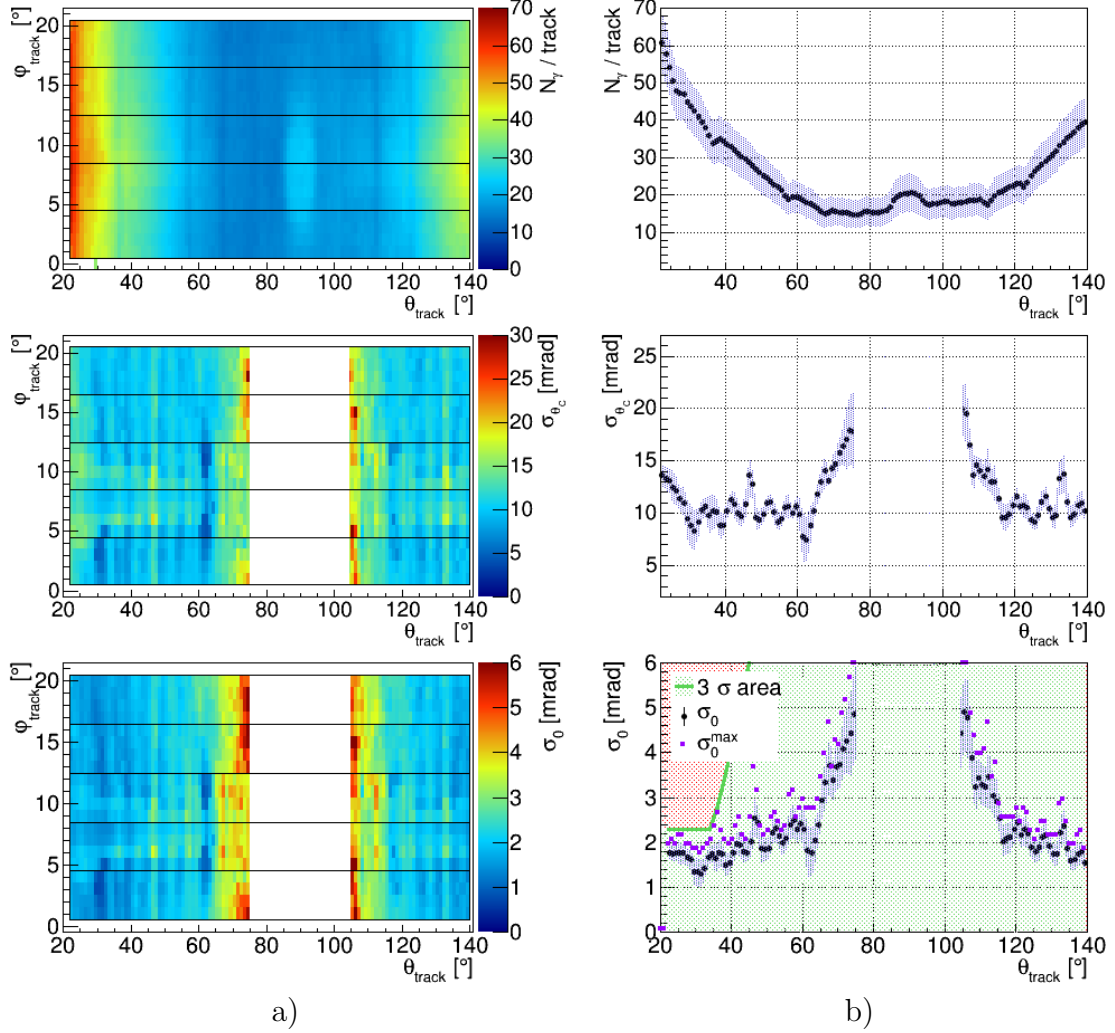


Figure A.6: Tank EV and the asymmetric spherical two-component lens without air gap (L2SA). For description of the plots see Fig. A.1.

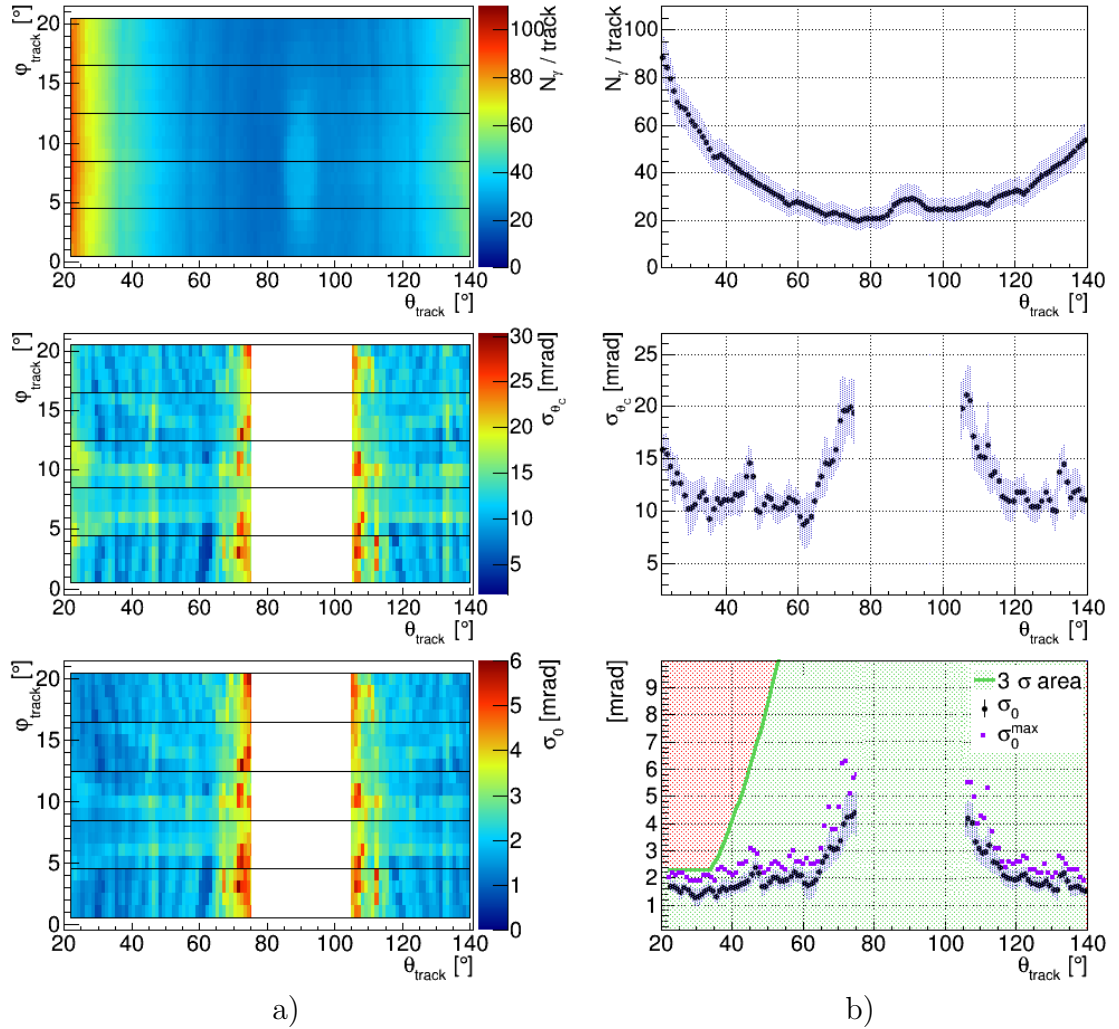


Figure A.7: Prism EV and the two-component spherical lens without air gap (L2SA). For description of the plots see Fig. A.1.

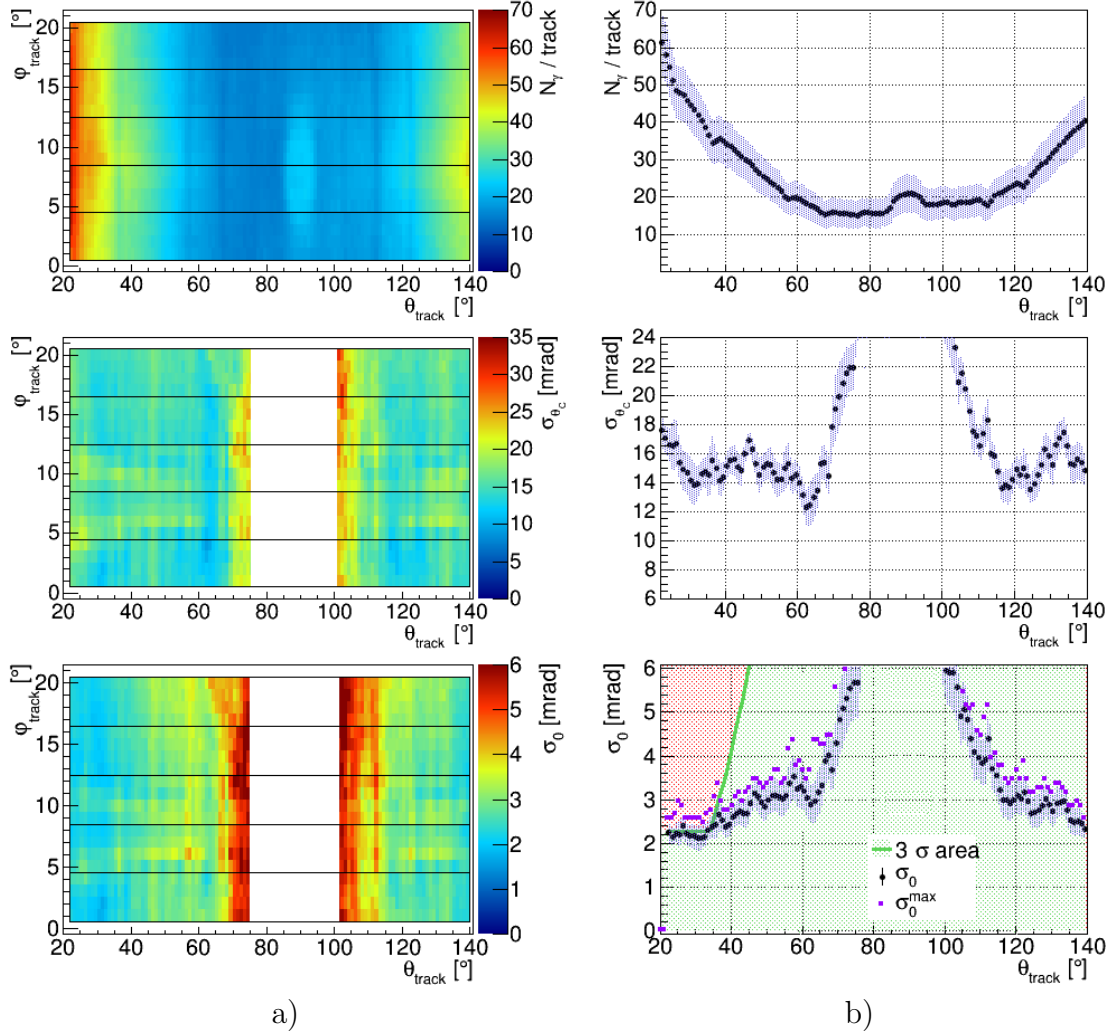


Figure A.8: Tank EV and the two-component cylindrical lens without air gap (L2CA). For description of the plots see Fig. A.1.

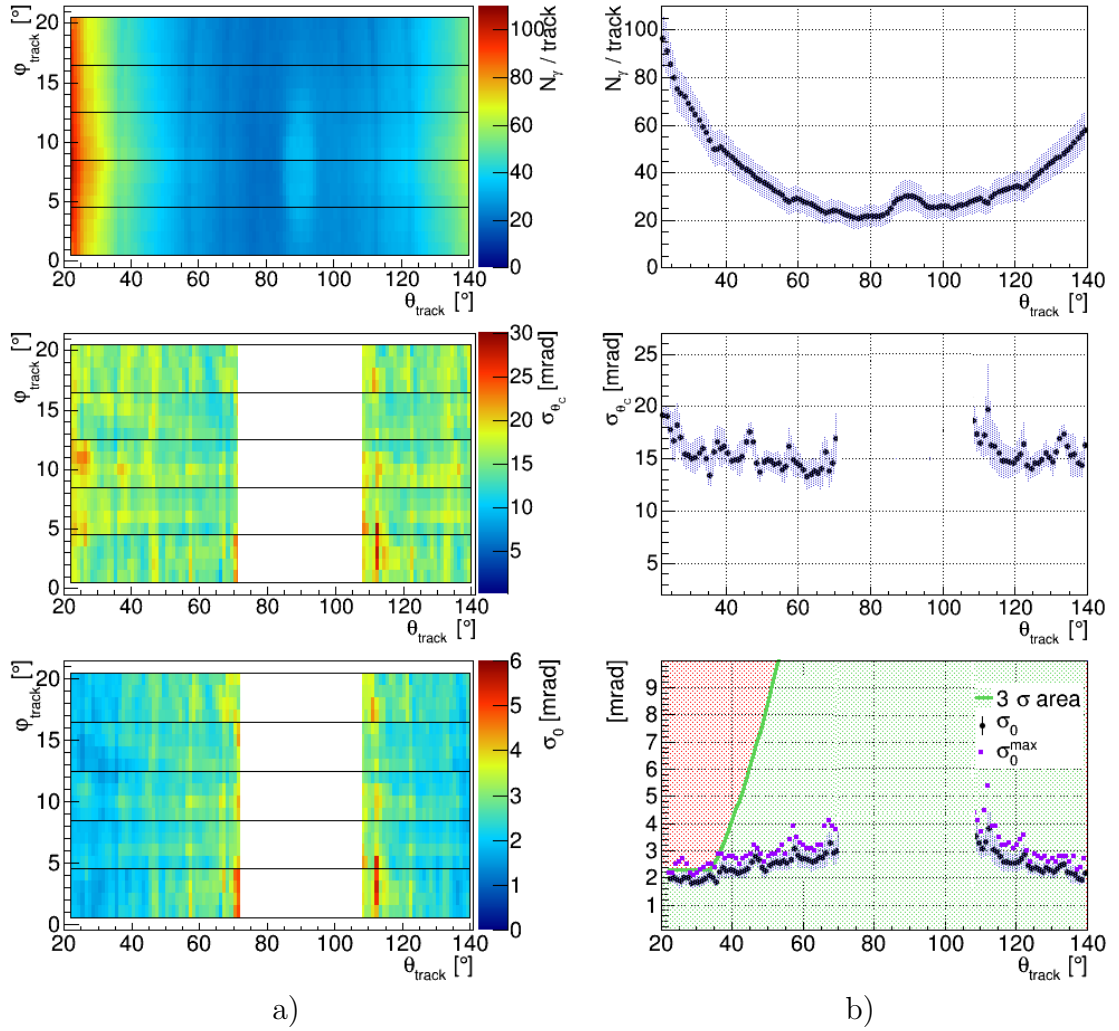


Figure A.9: Prism EV and the two-component cylindrical lens without air gap (L2CA). For description of the plots see Fig. A.1.

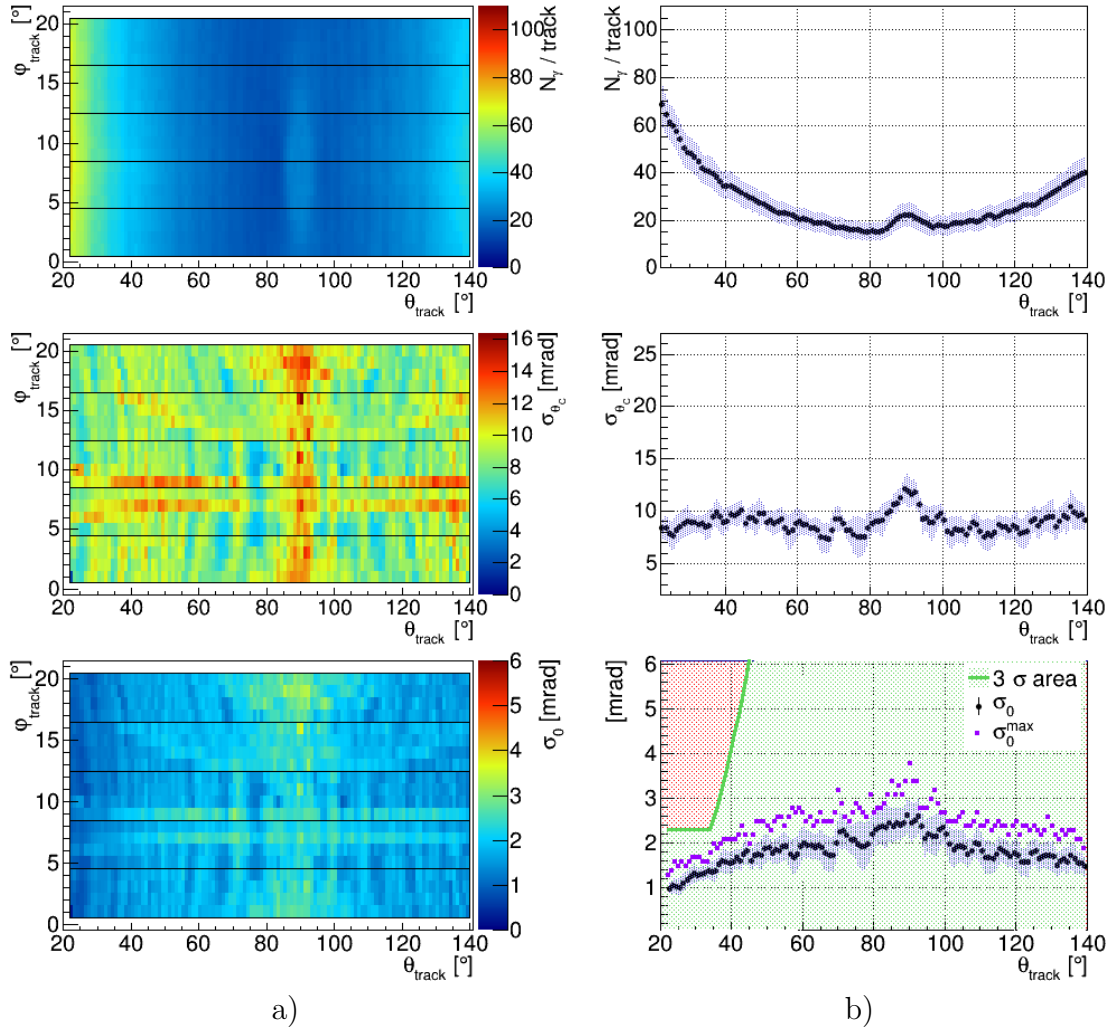


Figure A.10: Prism EV and the spherical three-component lens without air gap (L3S). For description of the plots see Fig. A.1.

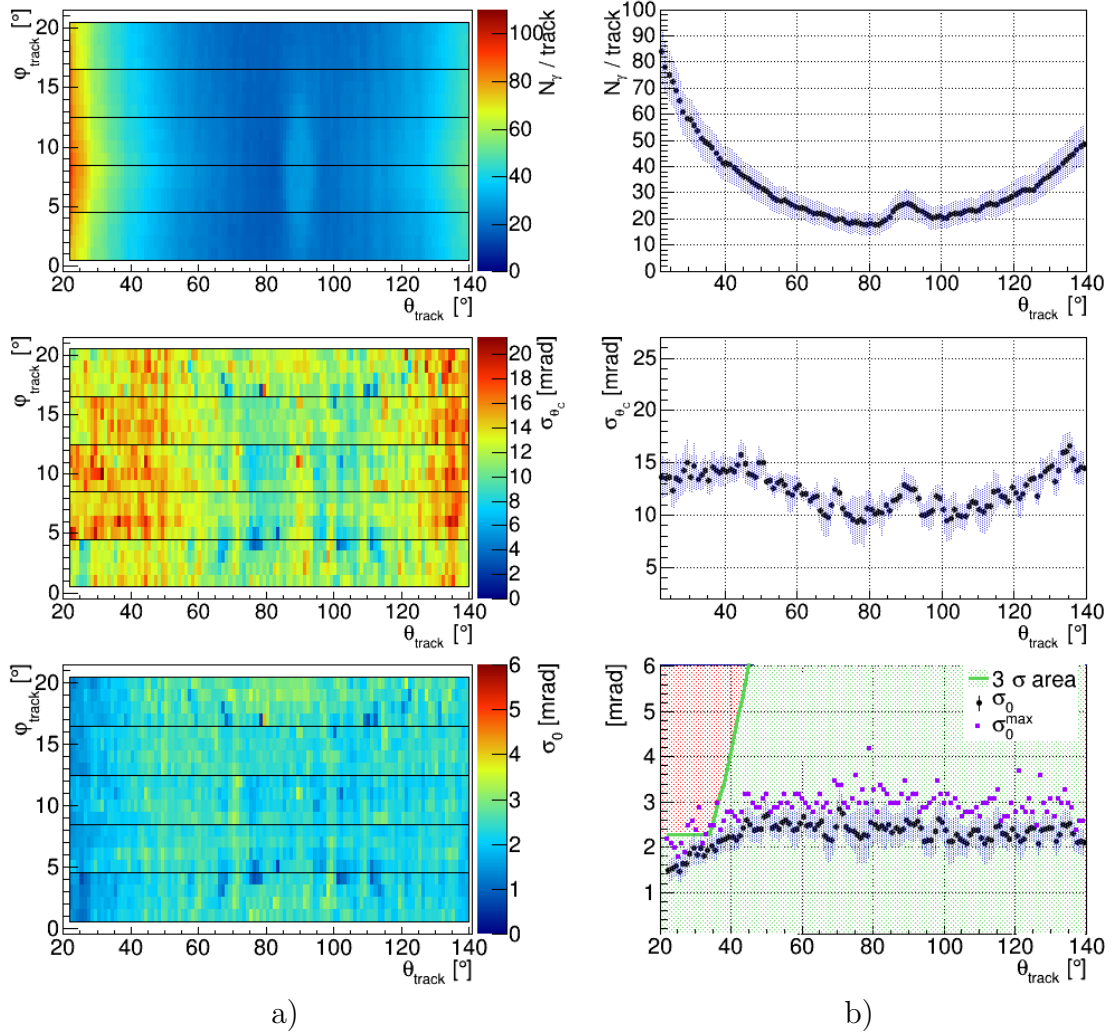


Figure A.11: Prism EV and the three-component cylindrical lens without air gap (L3C). For description of the plots see Fig. A.1.

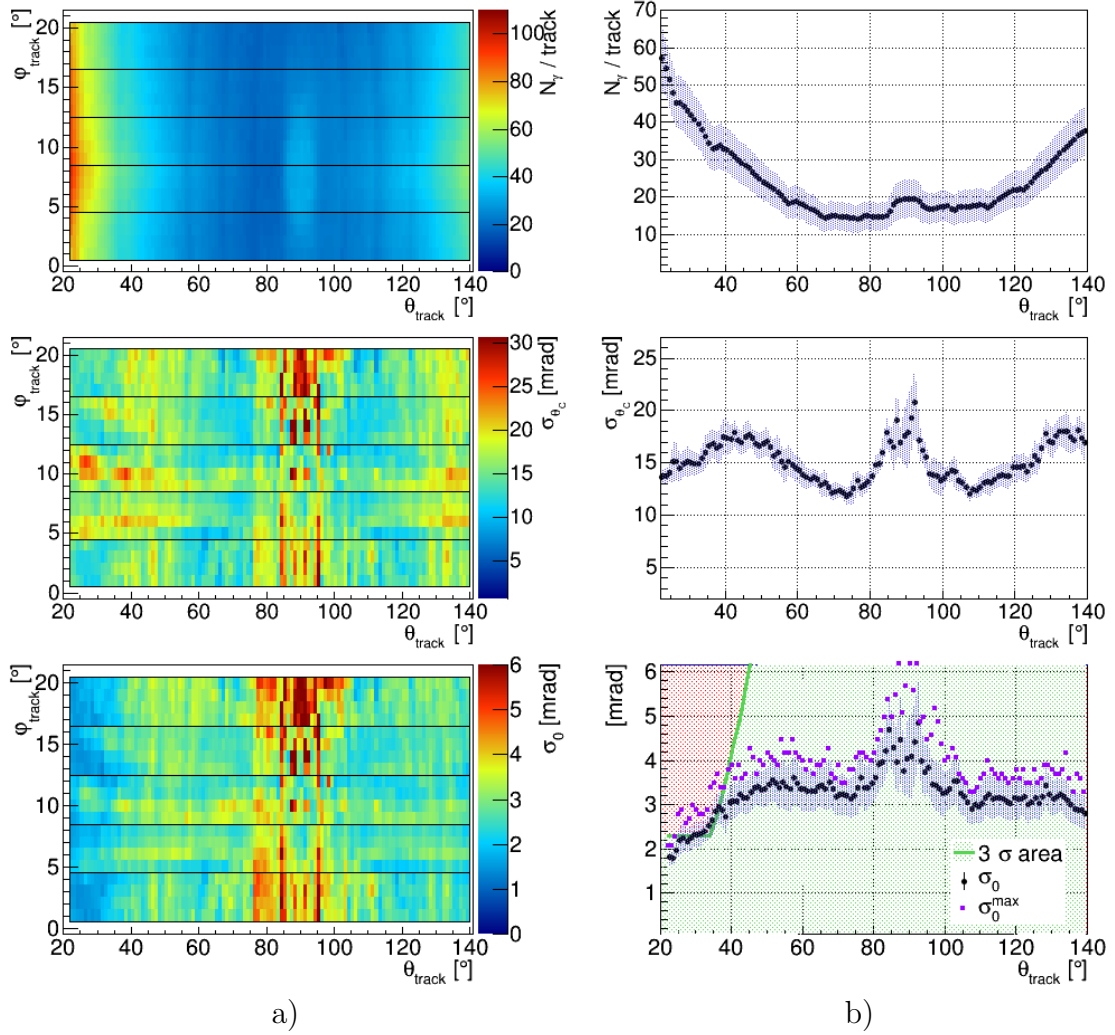


Figure A.12: Prism EV and the asymmetric three-component cylindrical lens without air gap (L3CA). For description of the plots see Fig. A.1.

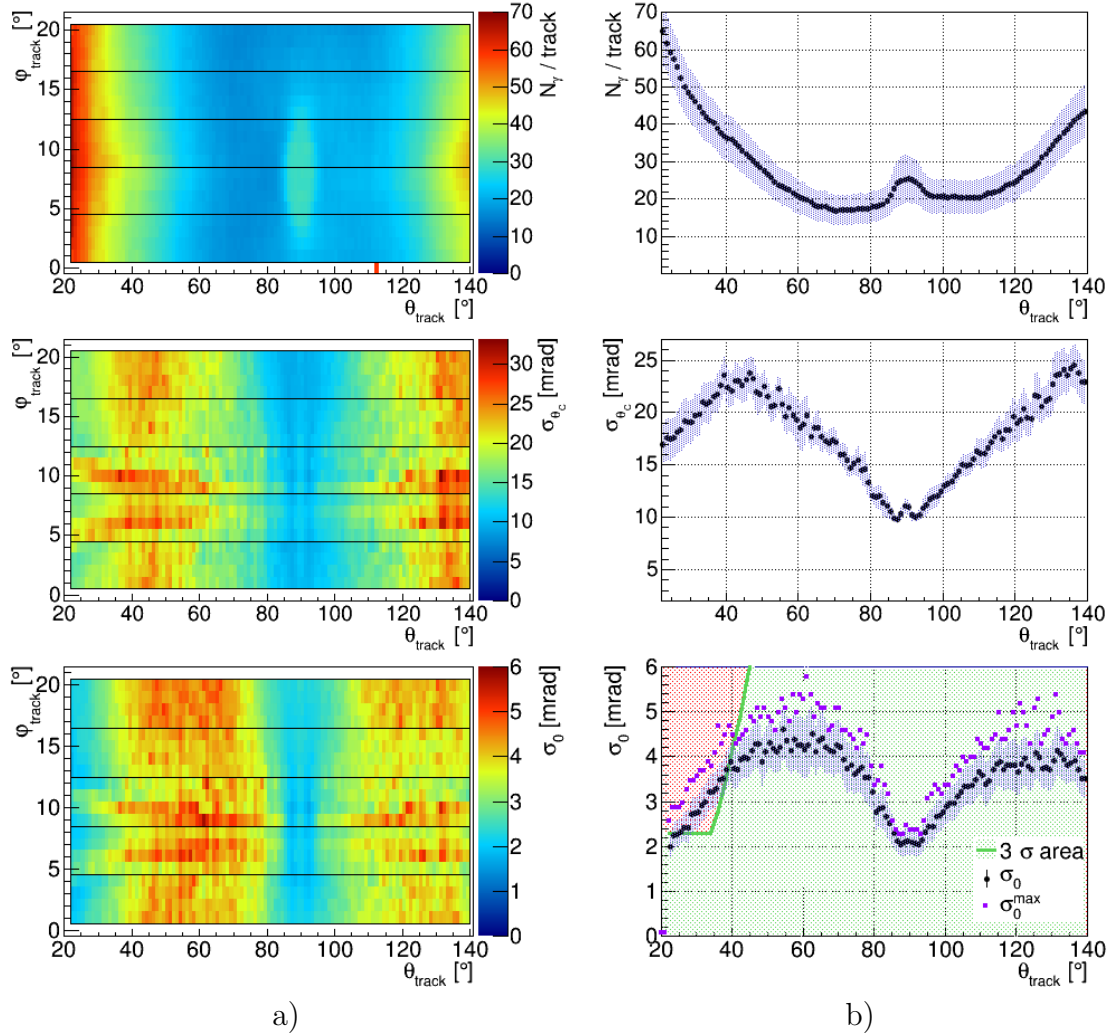


Figure A.13: Tank EV, no lens, and combined pixels. For description of the plots see Fig. A.1.

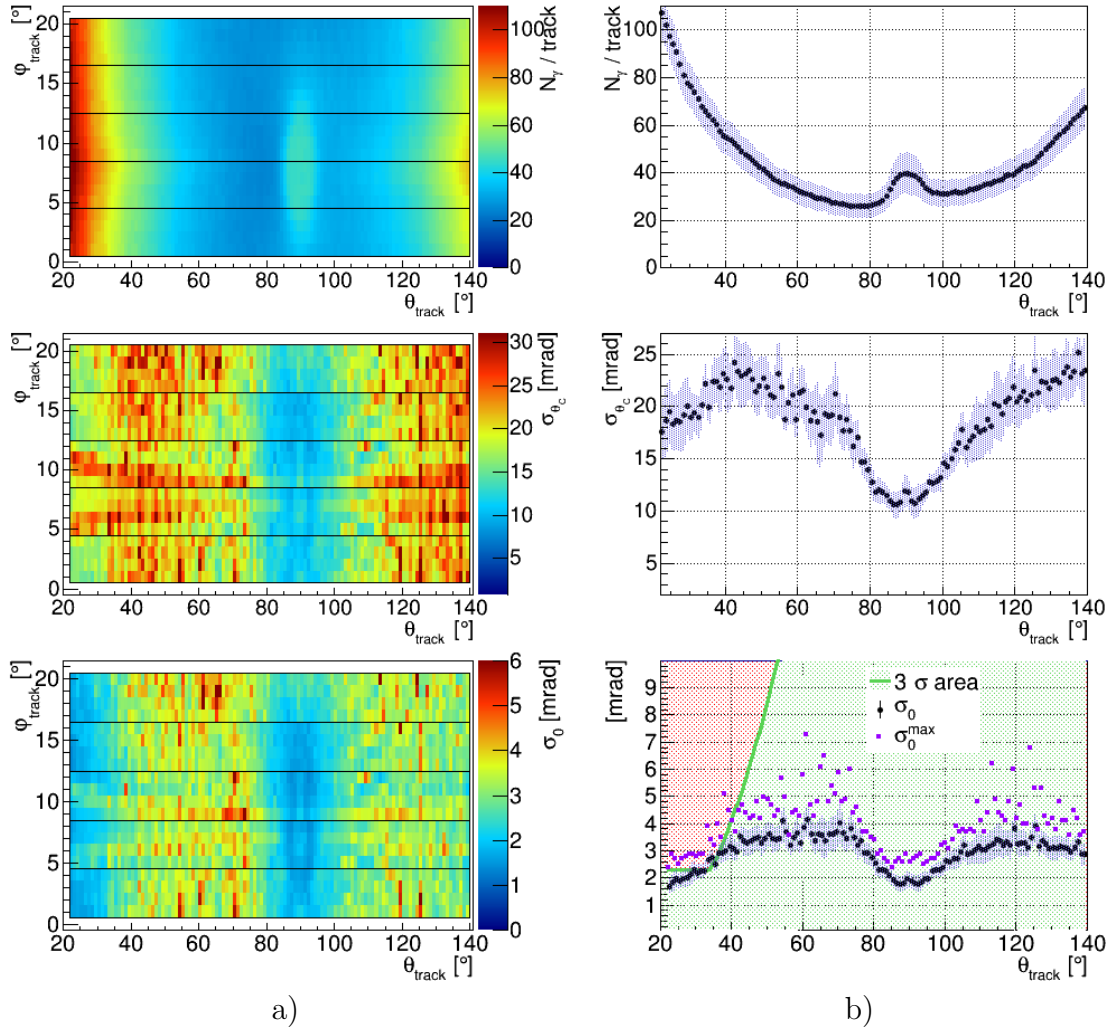


Figure A.14: Prism EV, no lens, and combined pixels. For description of the plots see Fig. A.1.

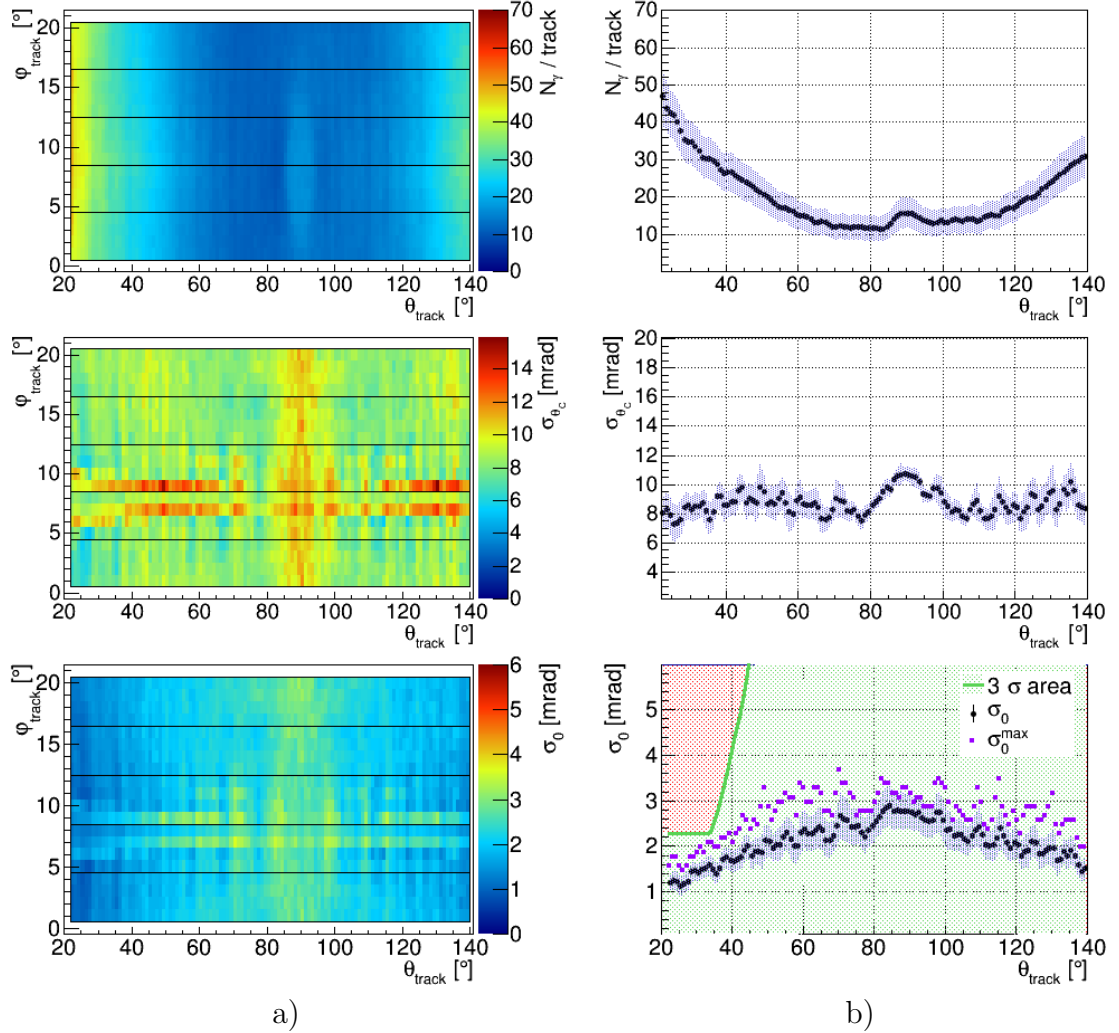


Figure A.15: Tank EV, the three-component spherical lens without air gap (L3S), and combined pixels. For description of the plots see Fig. A.1.

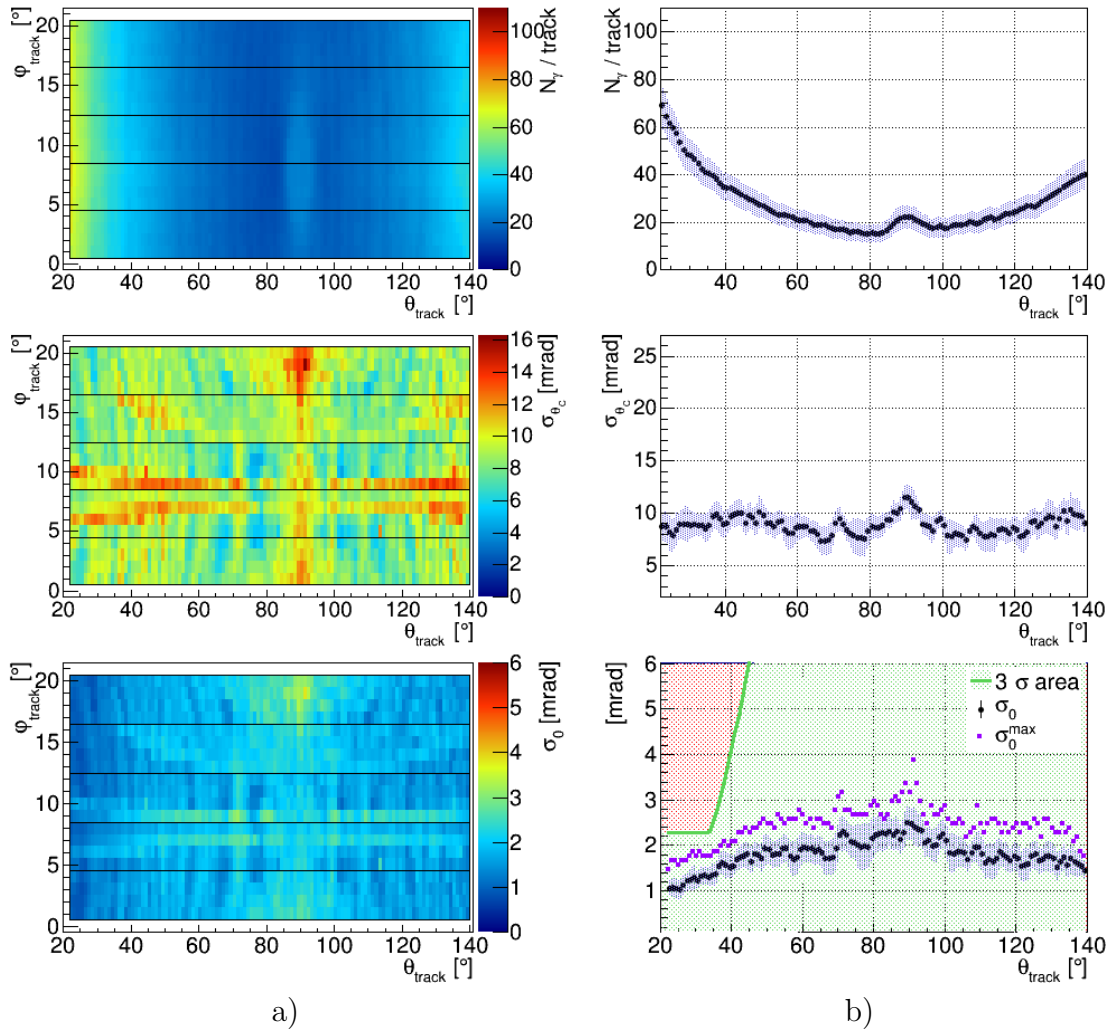


Figure A.16: Prism EV, the three-component spherical lens without air gap (L3S), and combined pixels. For description of the plots see Fig. A.1.

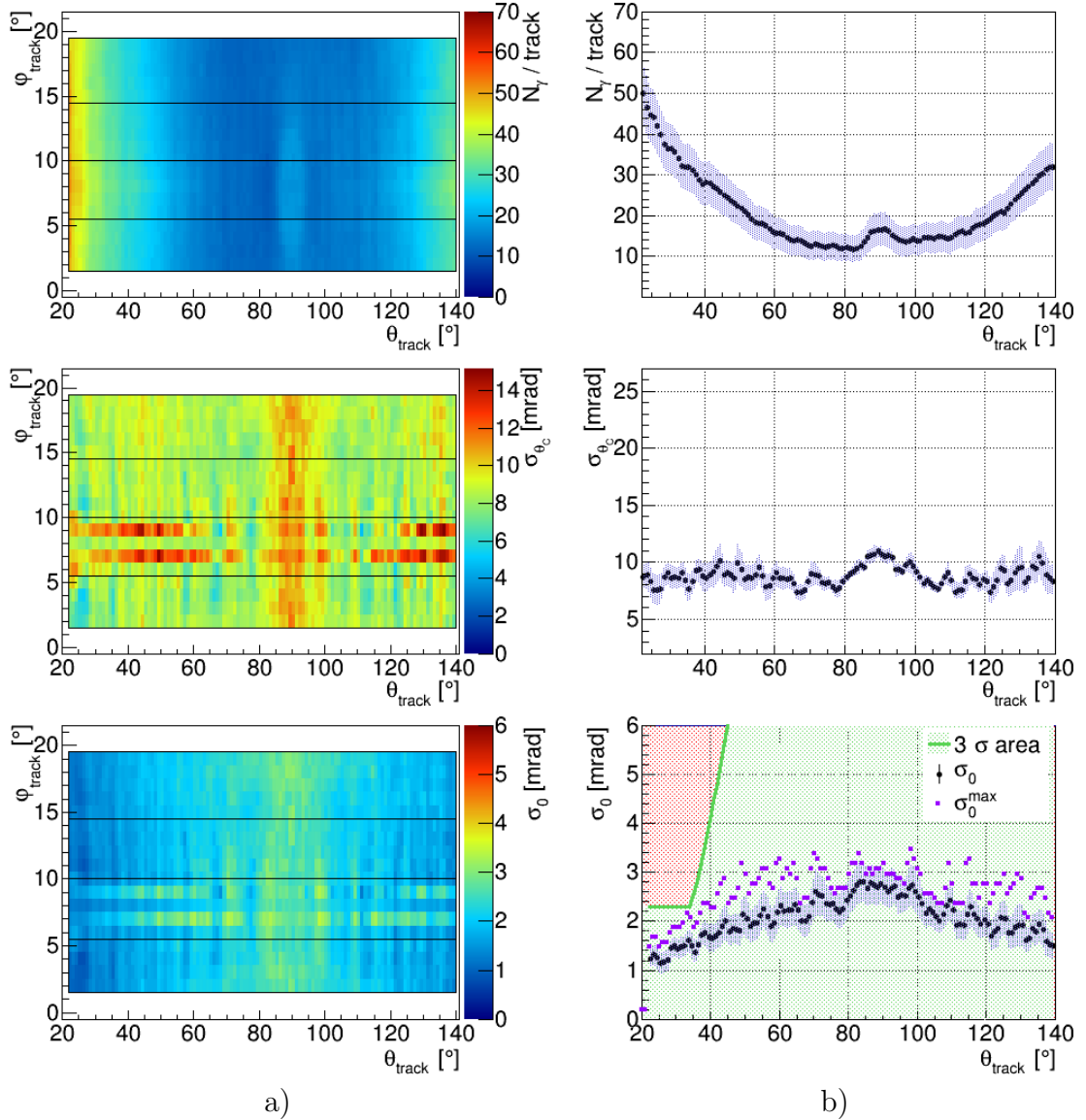


Figure A.17: Tank EV, the three-component spherical lens without air gap (L3S), the width of the radiator bars is 4 cm, corresponding to 4 radiators in each flat section of the barrel. For description of the plots see Fig. A.1.

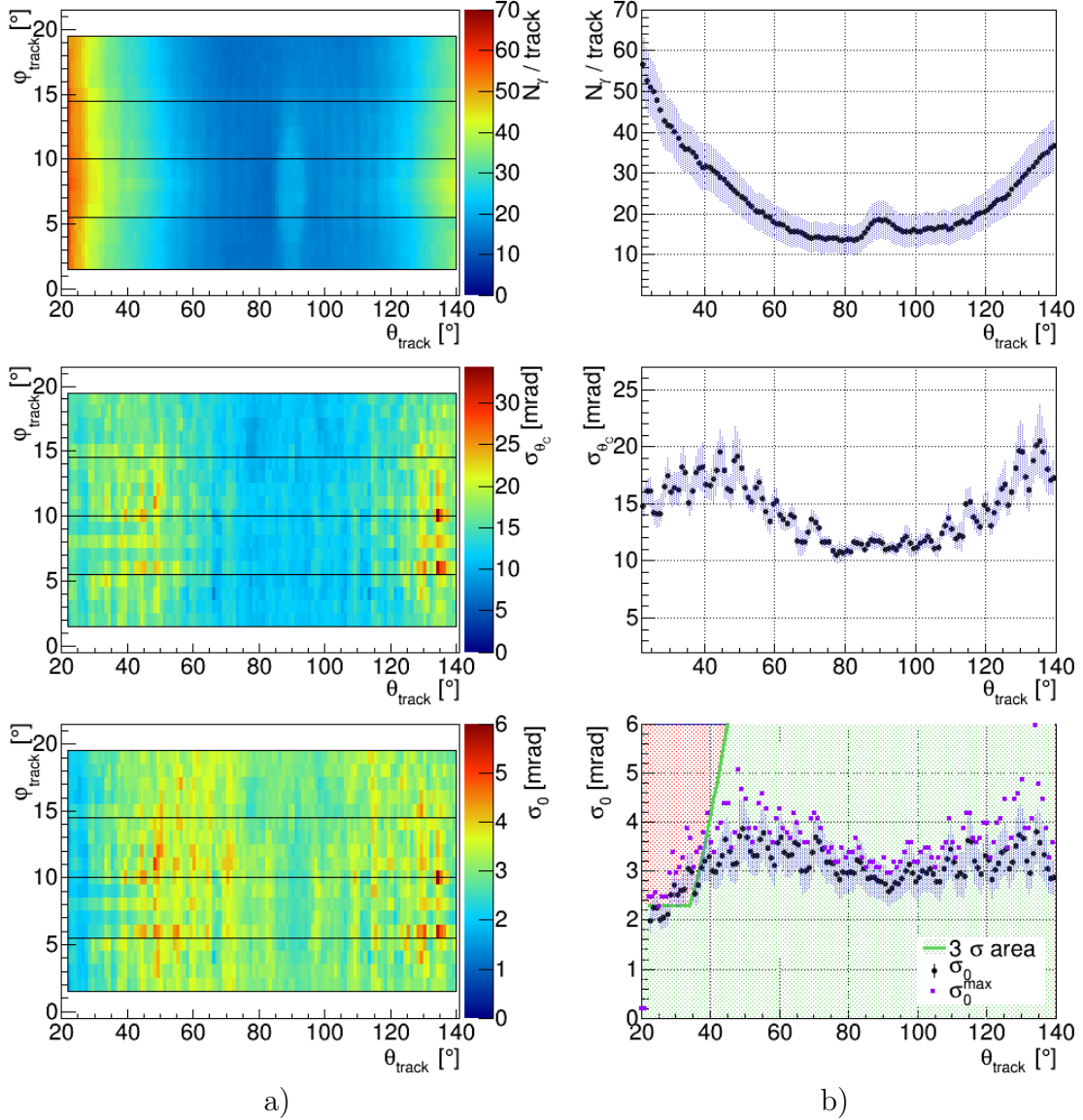


Figure A.18: Tank EV, the three-component cylindrical lens without air gap (L3C), the width of the radiator bars is 4 cm, corresponding to 4 radiators in each flat section of the barrel. For description of the plots see Fig. A.1.

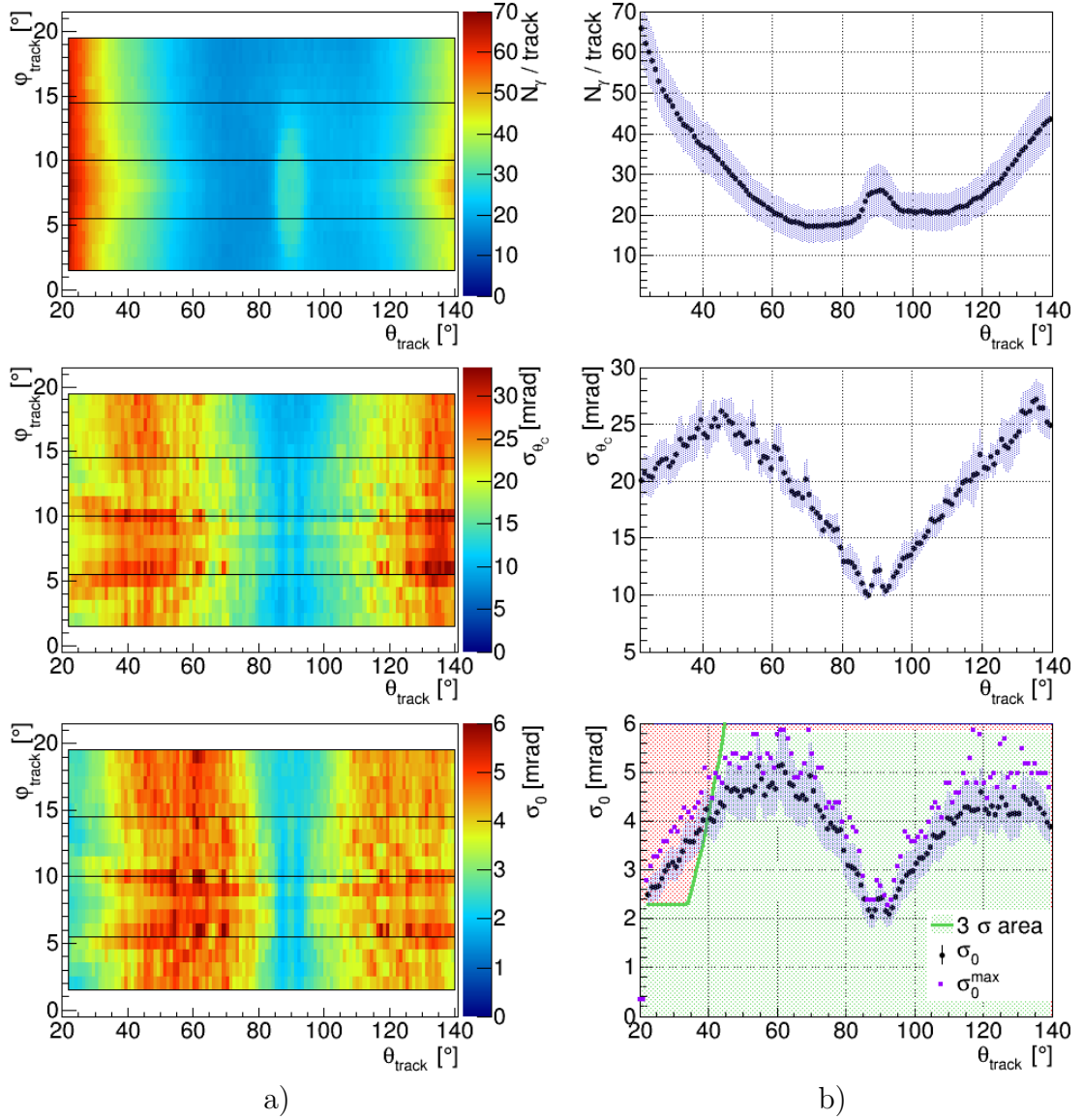


Figure A.19: Tank EV, no lens, the width of the radiator bars is 4 cm, corresponding to 4 radiators in each flat section of the barrel. For description of the plots see Fig. A.1.

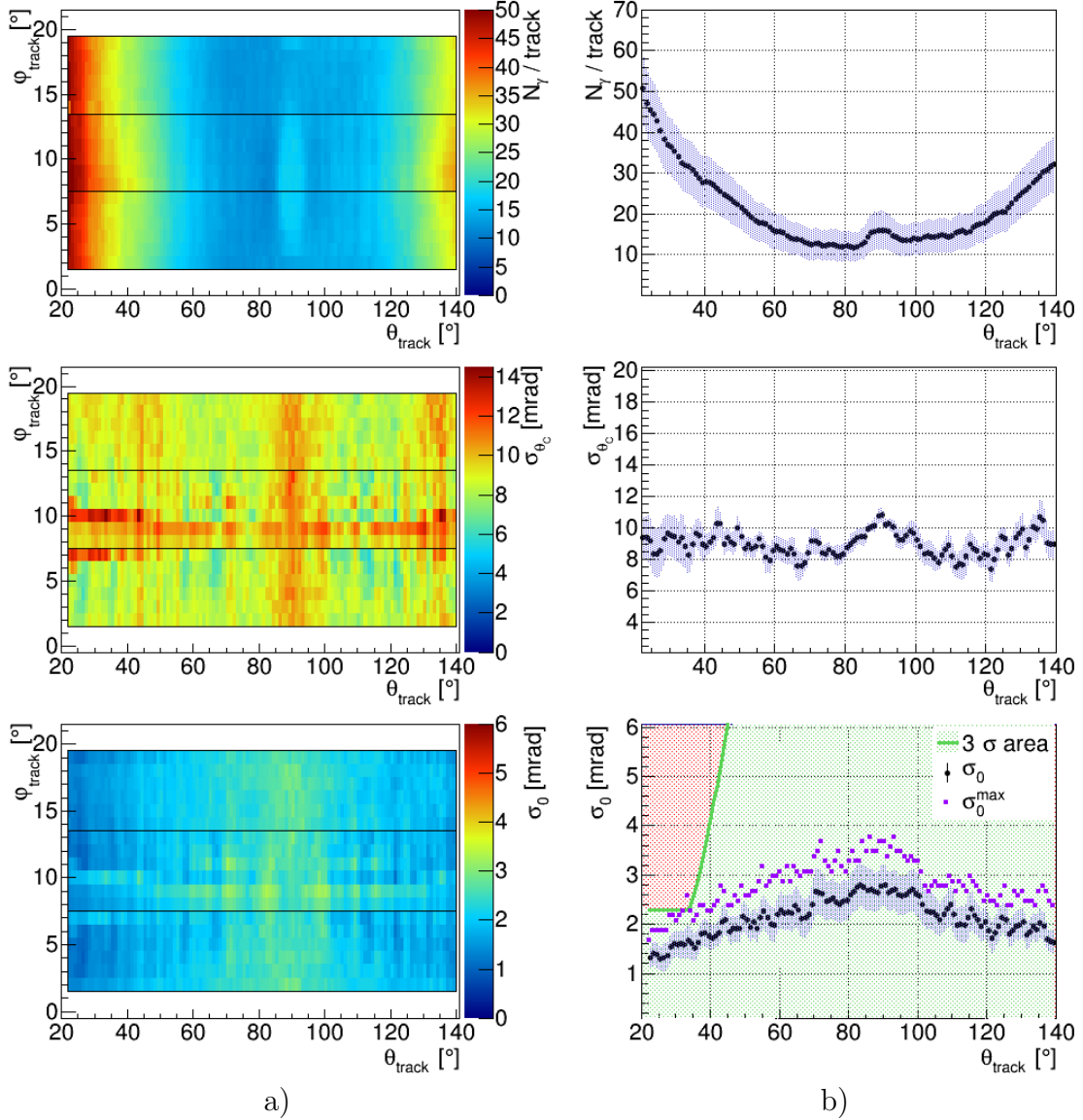


Figure A.20: Tank EV, the three-component spherical lens without air gap (L3S), the width of the radiator bars is 5.2 cm, corresponding to 3 radiators in each flat section of the barrel. For description of the plots see Fig. A.1.

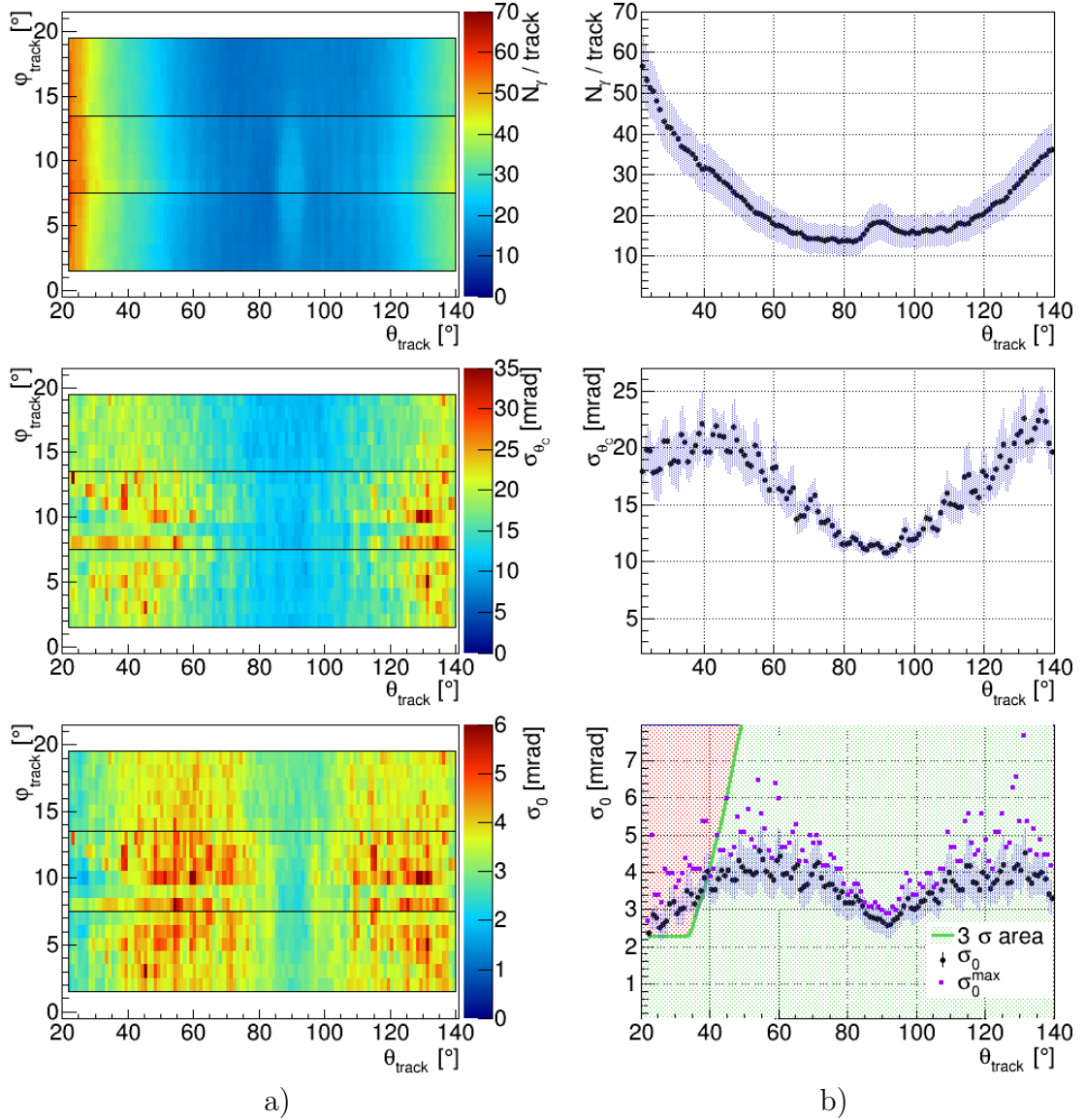


Figure A.21: Tank EV, the three-component cylindrical lens without air gap (L3C), the width of the radiator bars is 5.2 cm, corresponding to 3 radiators in each flat section of the barrel. For description of the plots see Fig. A.1.

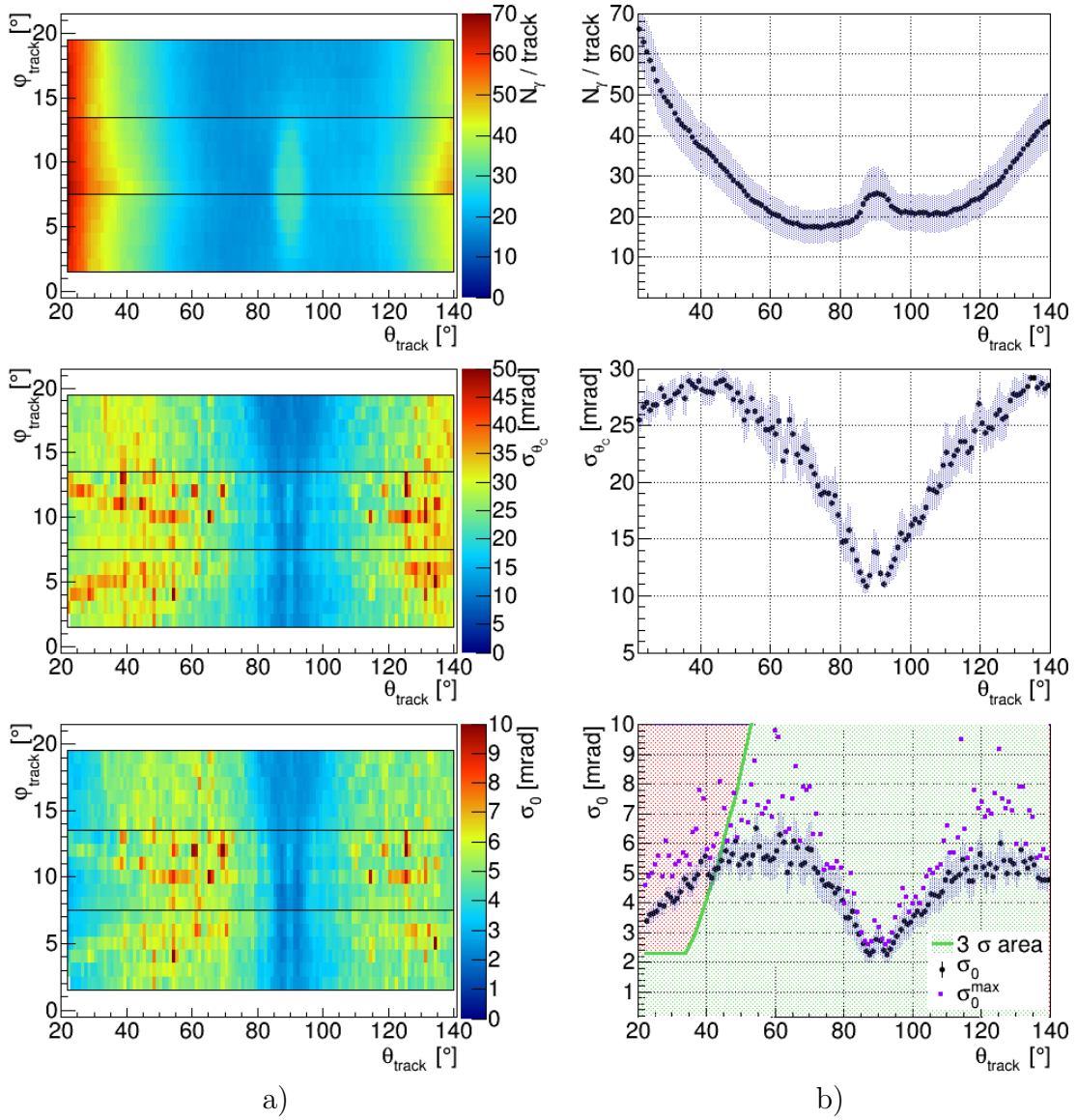


Figure A.22: Tank EV, no lens, the width of the radiator bars is 5.2 cm, corresponding to 3 radiators in each flat section of the barrel. For description of the plots see Fig. A.1.

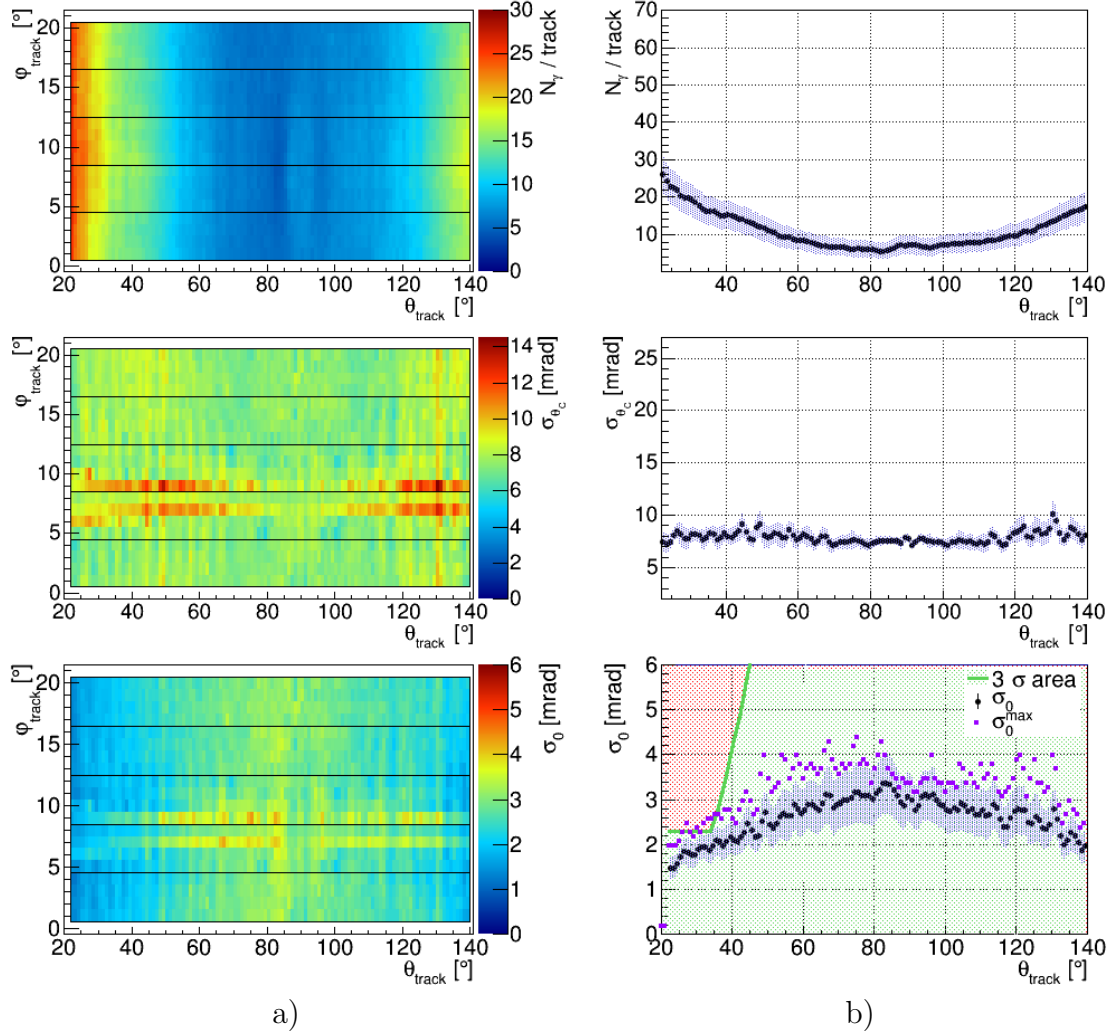


Figure A.23: Tank EV, the three-component spherical lens without air gap (L3S), the thickness of the radiator bars is 1 cm. For description of the plots see Fig. A.1.

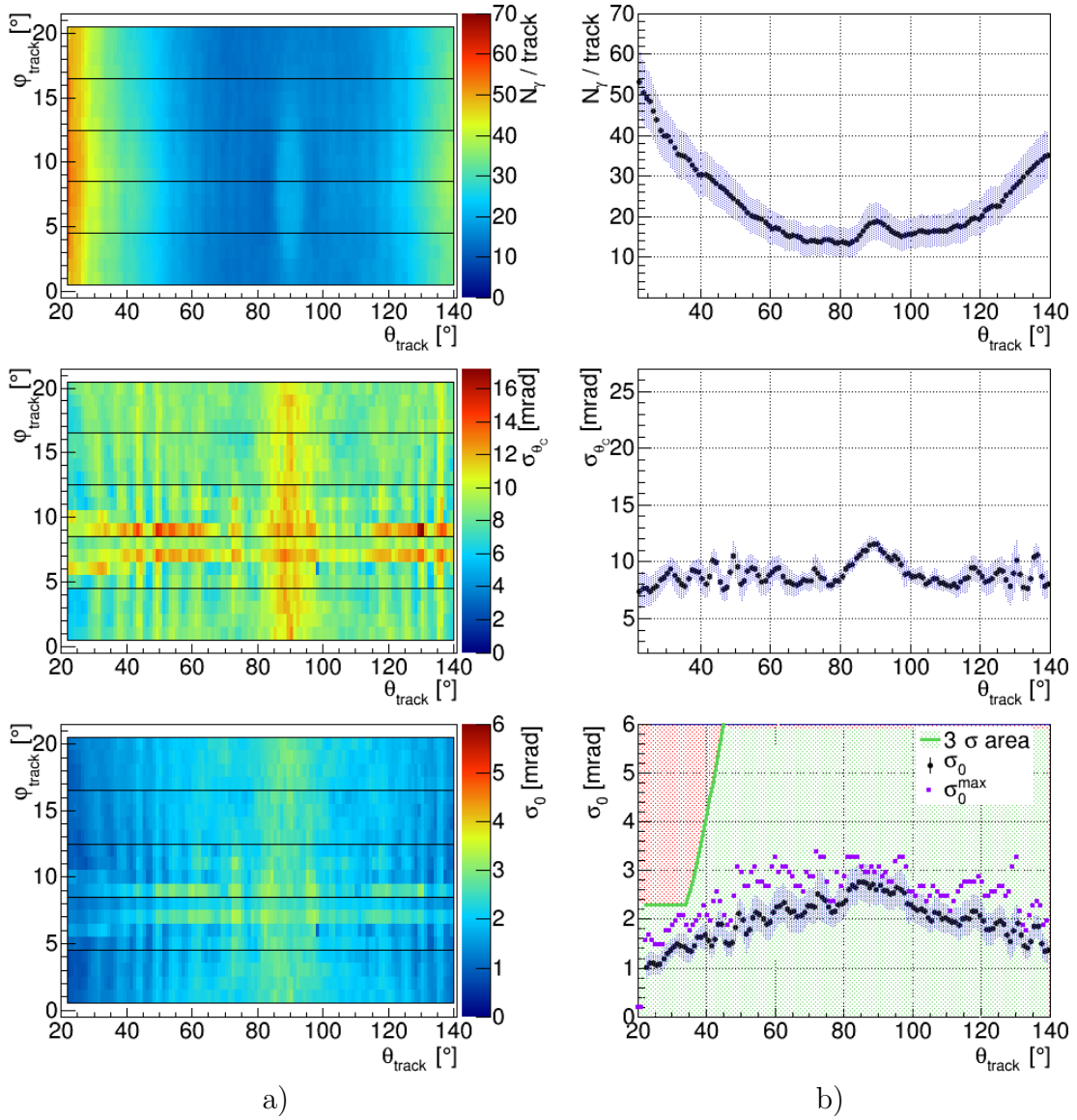


Figure A.24: Tank EV, the three-component spherical lens without air gap (L3S), the thickness of the radiator bars is 2 cm. For description of the plots see Fig. A.1.

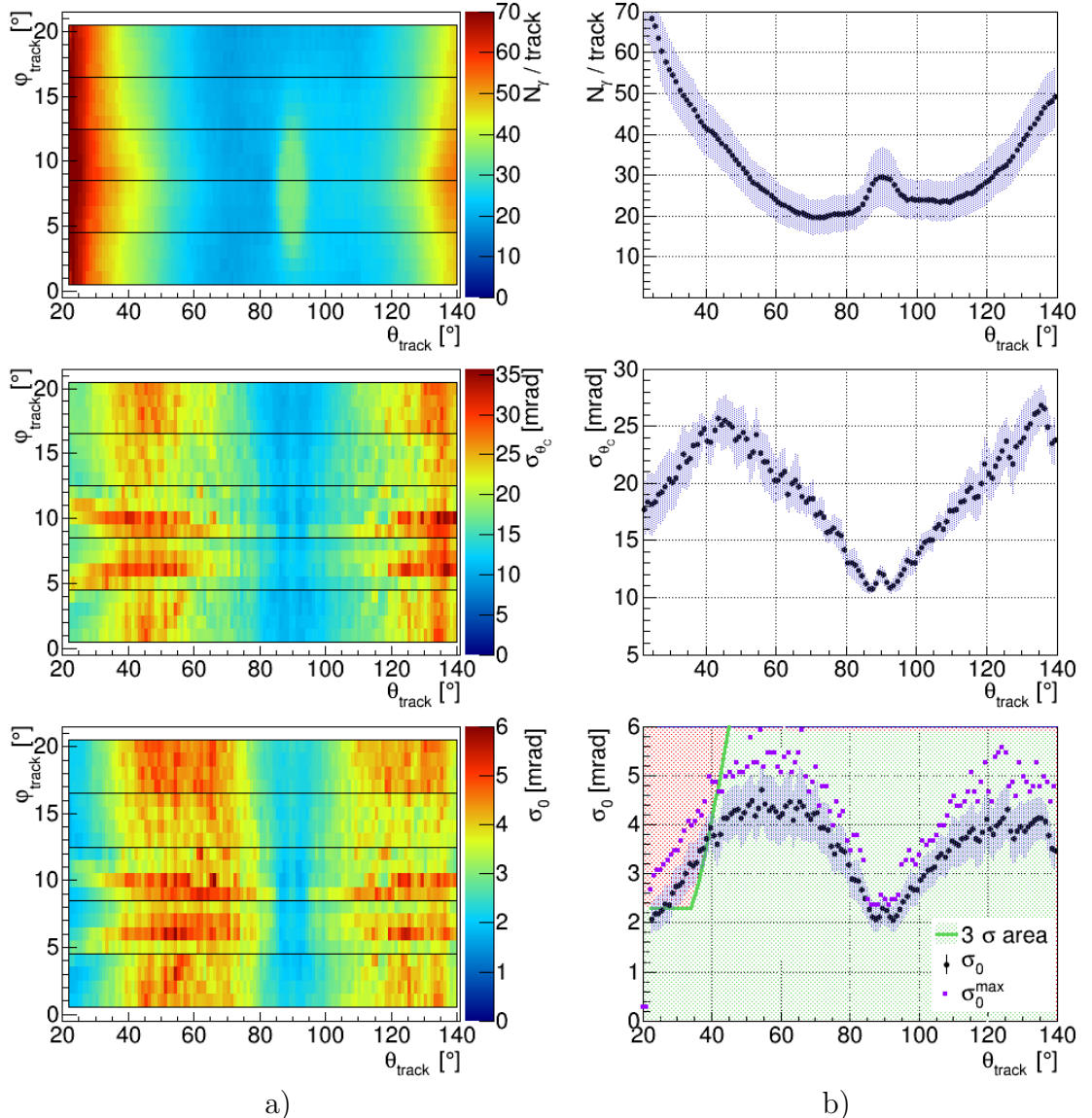


Figure A.25: Tank EV, no lens, the thickness of the radiator bars is 2 cm. For description of the plots see Fig. A.1.

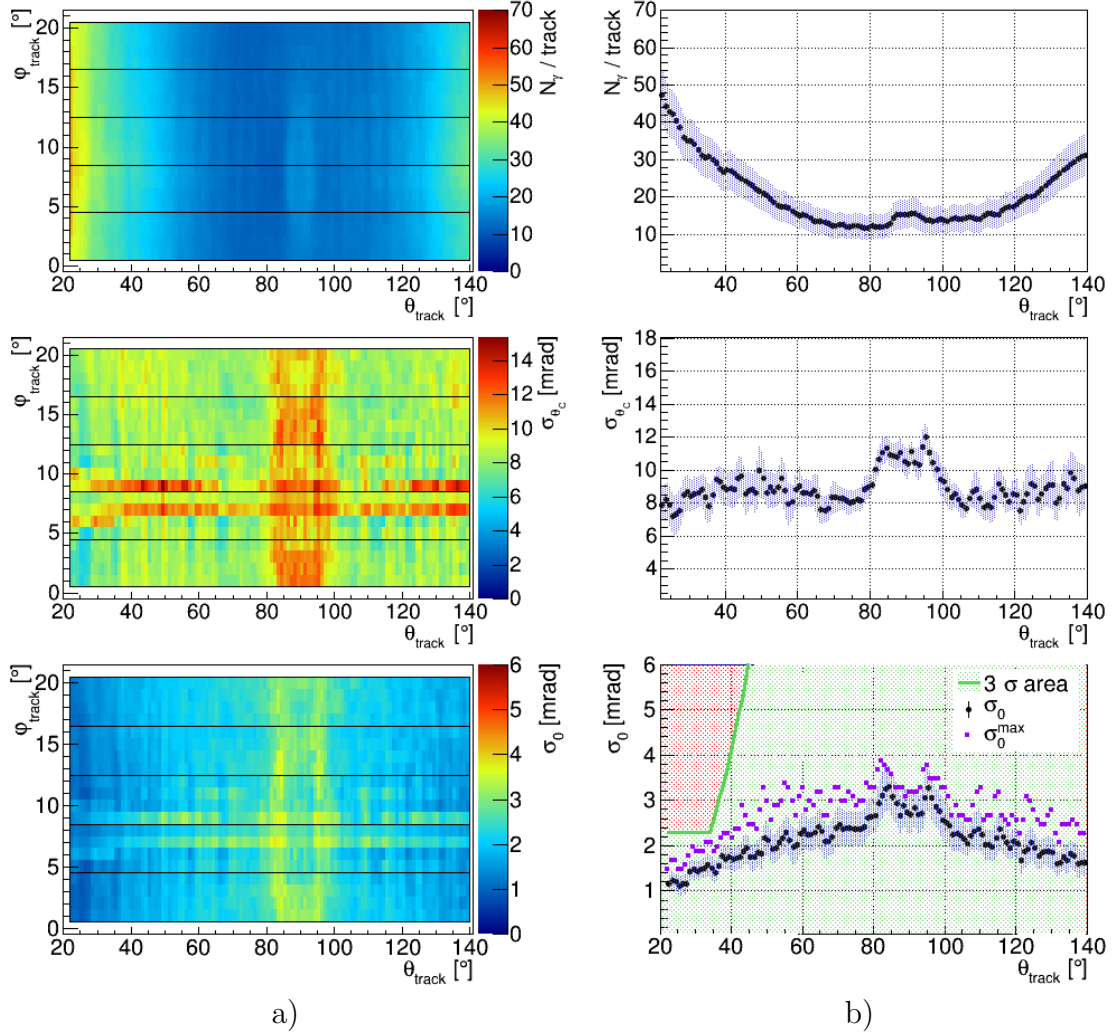


Figure A.26: Tank EV, the three-component spherical lens without air gap (L3S), and 4 radial rows of MCP-PMTs. For description of the plots see Fig. A.1.

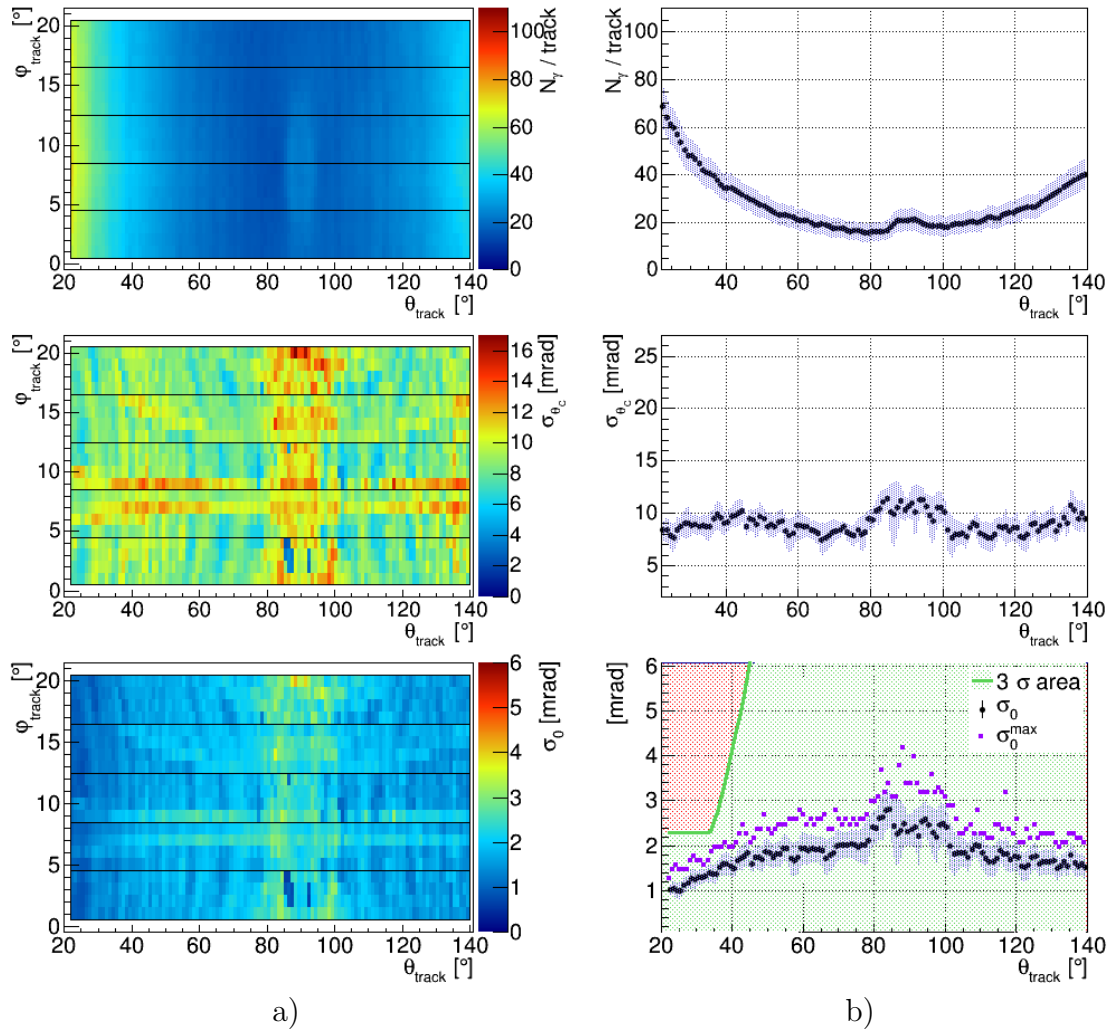


Figure A.27: Prism EV, the three-component spherical lens without air gap (L3S), and 4 radial rows of MCP-PMTs. For description of the plots see Fig. A.1.

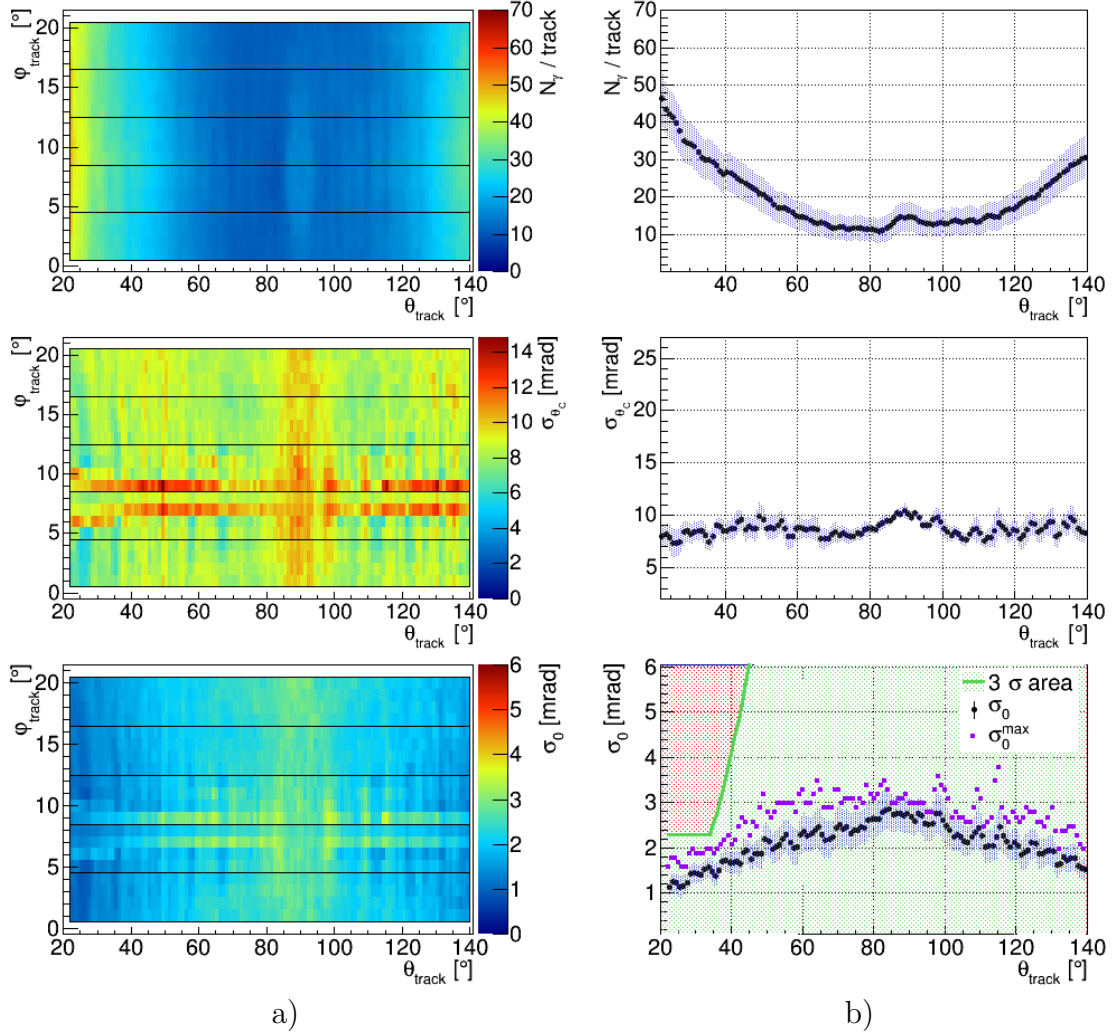


Figure A.28: Tank EV, the three-component spherical lens without air gap (L3S), and 6 radial rows of MCP-PMTs. For description of the plots see Fig. A.1.

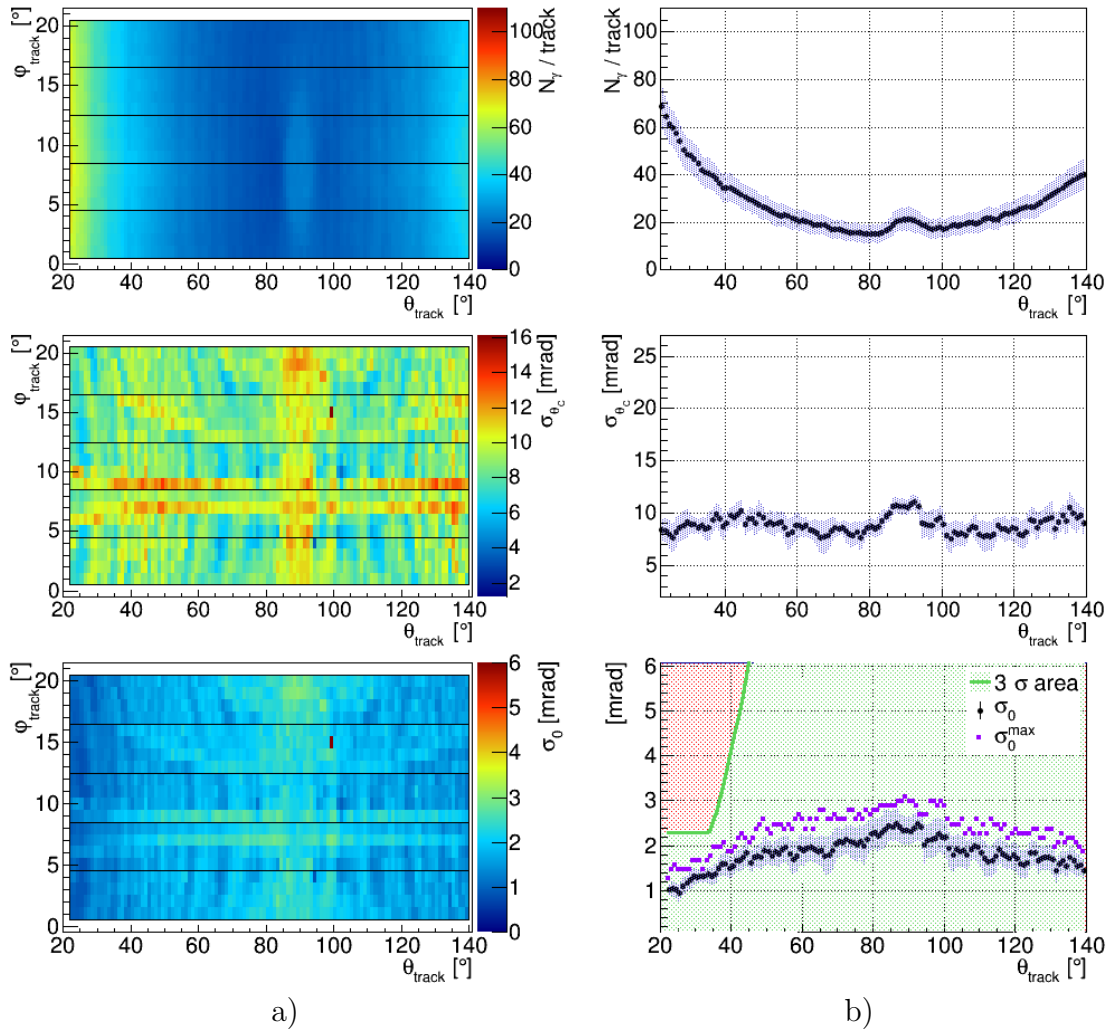


Figure A.29: Prism EV, the three-component spherical lens without air gap (L3S), and 6 radial rows of MCP-PMTs. For description of the plots see Fig. A.1.

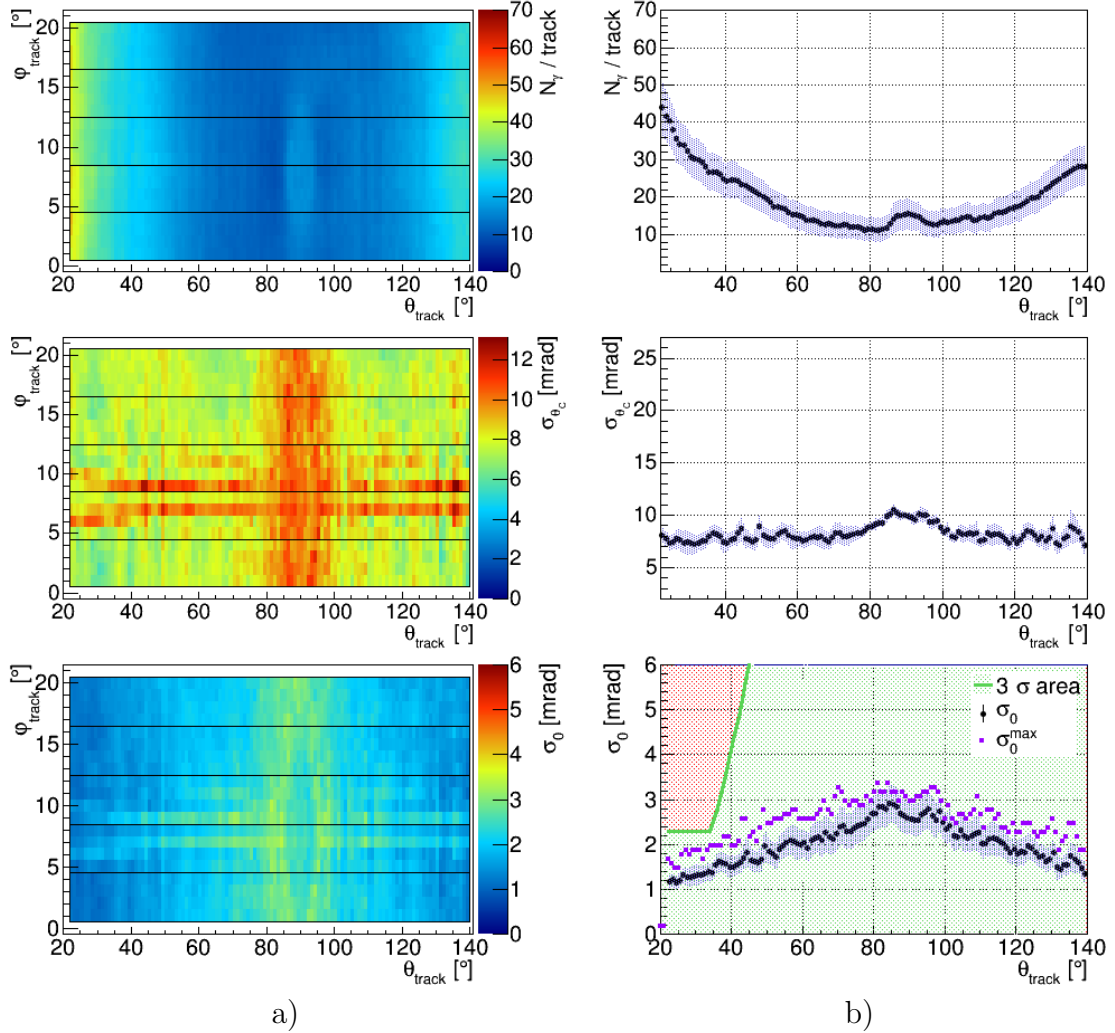


Figure A.30: Tank EV, the three-component spherical lens without air gap (L3S), and the EV depth of 35 cm. For description of the plots see Fig. A.1.

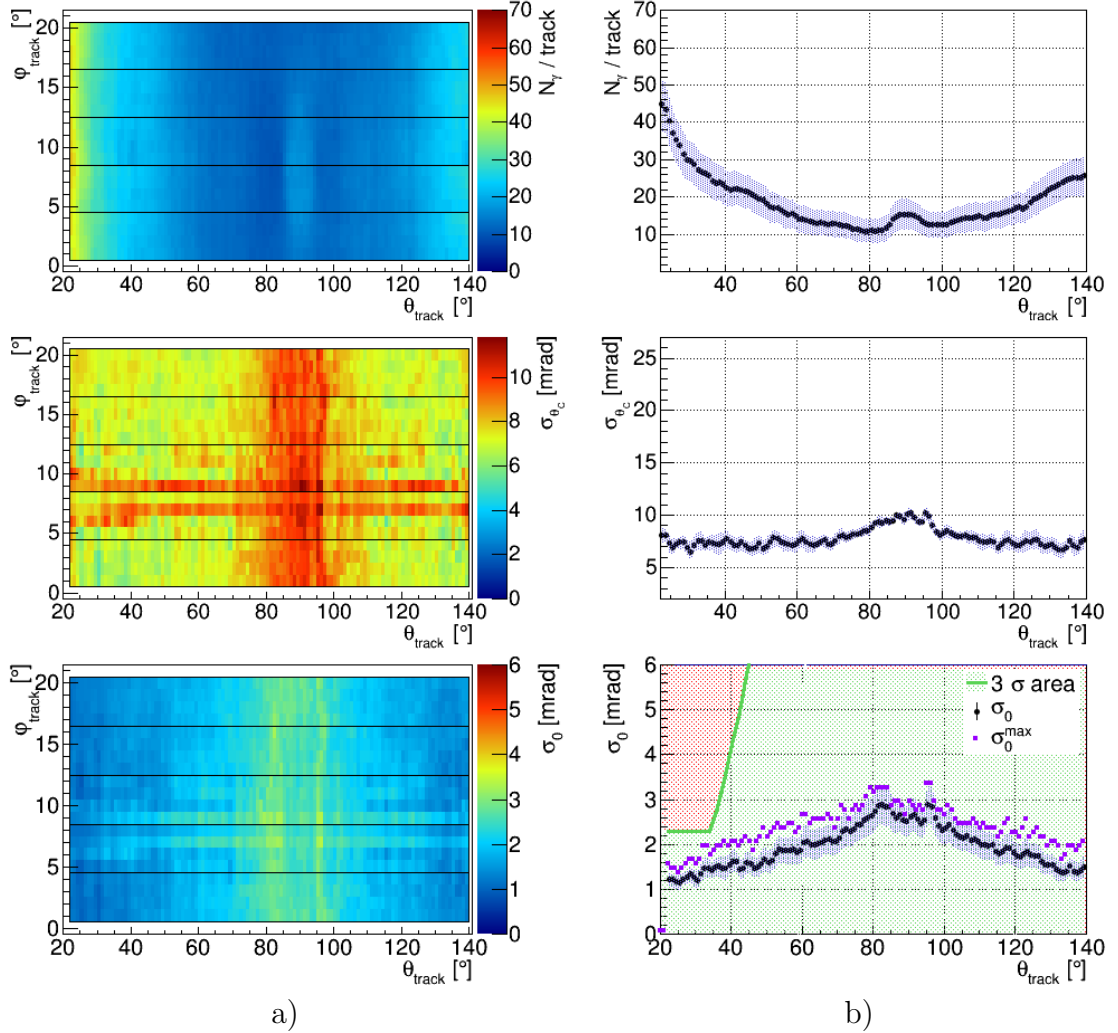


Figure A.31: Tank EV, the three-component spherical lens without air gap (L3S), and the EV depth of 40 cm. For description of the plots see Fig. A.1.

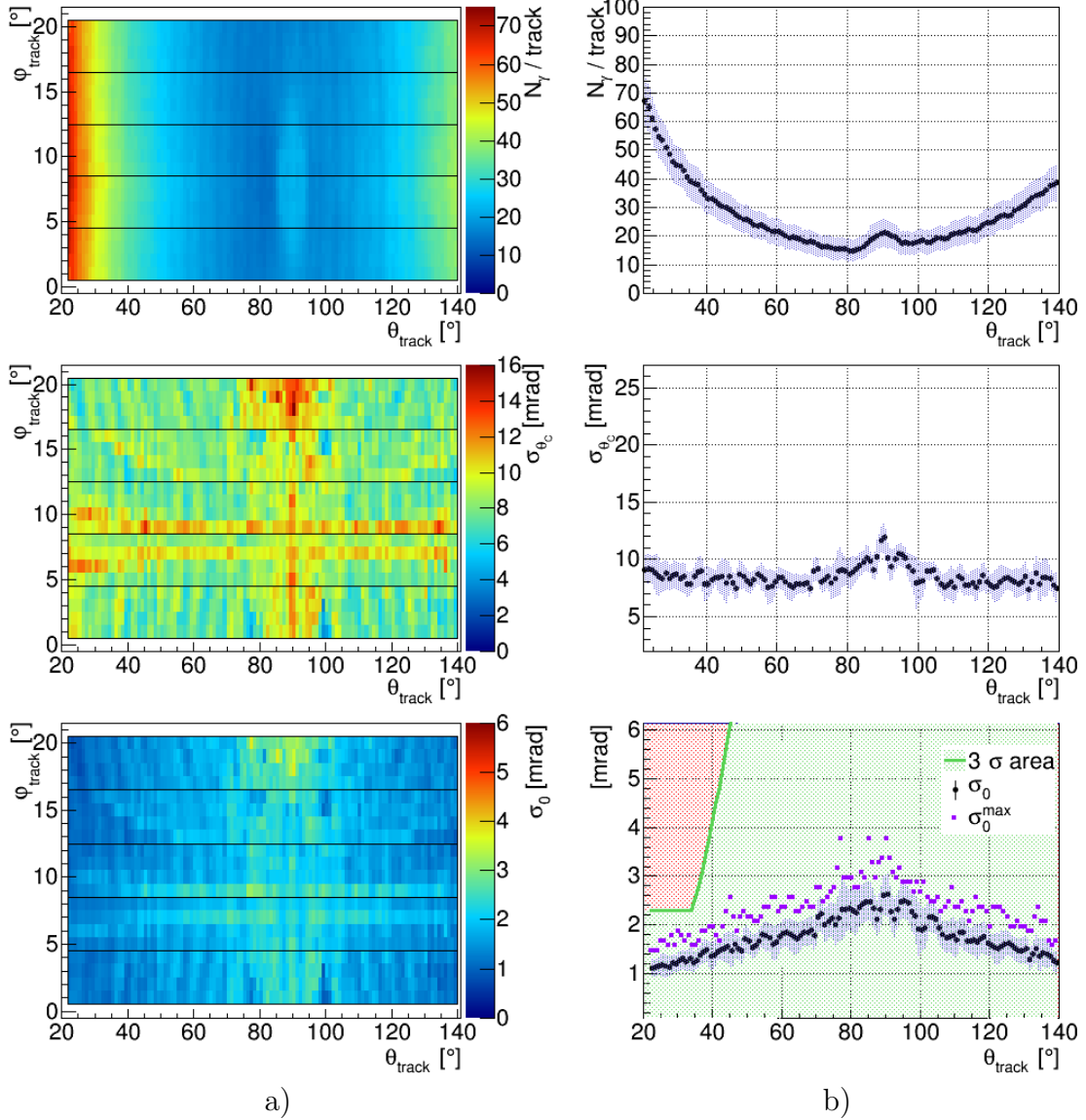


Figure A.32: Prism EV, the three-component spherical lens without air gap (L3S), the depth of the EV is 35 cm, the tilt of the photodetection plane is 10°. For description of the plots see Fig. A.1.

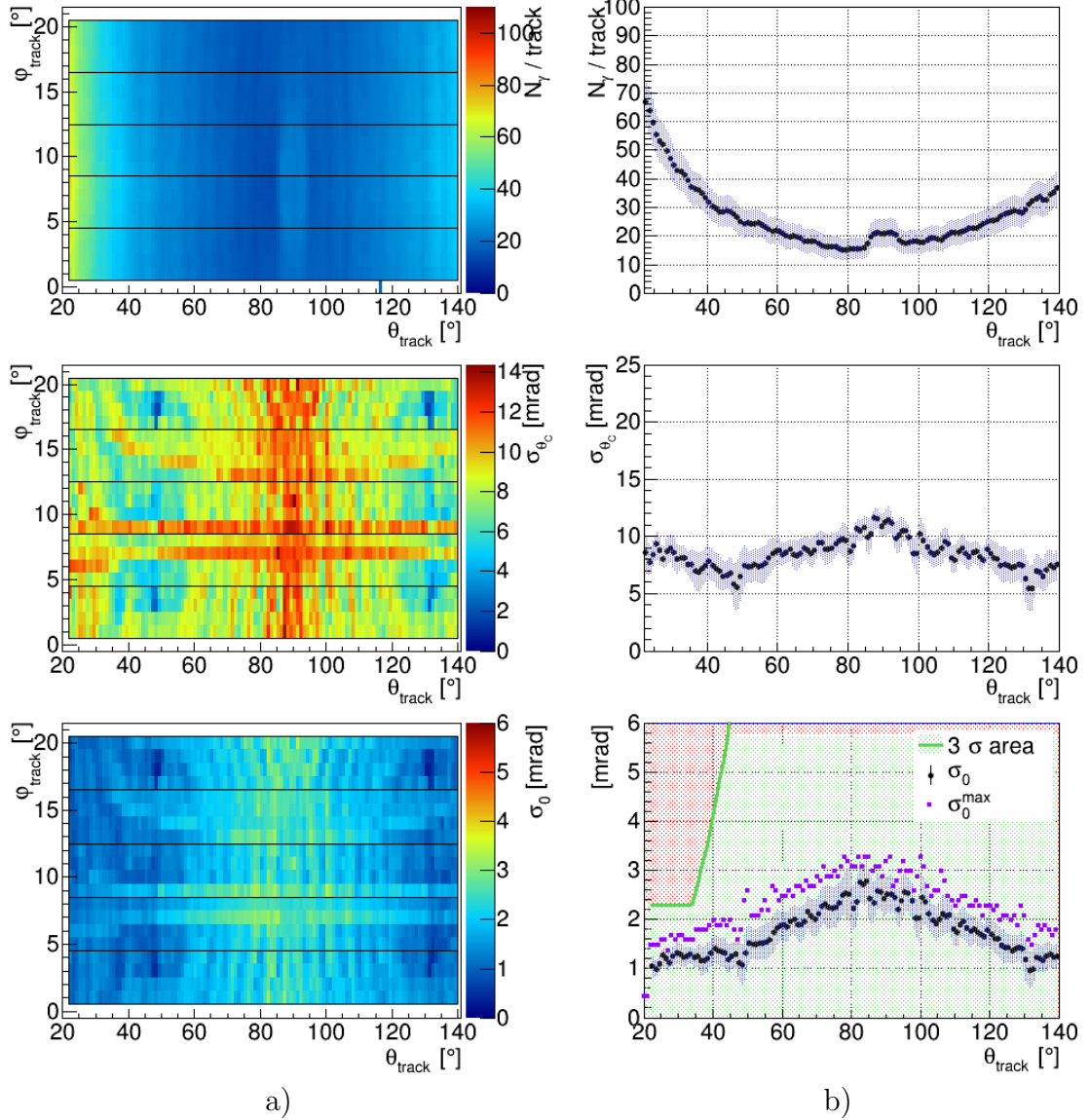


Figure A.33: Prism EV, the three-component spherical lens without air gap (L3S), the depth of the EV is 35 cm, the tilt of the photodetection plane is 30° . For description of the plots see Fig. A.1.

Legend of acronyms

CS	Coordinate System
DIRC	Detection of Internally Reflected Cherenkov light
EMC	Electromagnetic Calorimeter
EV	Expansion volume
FAIR	Facility for Antiproton and Ion Research
FDIRC	Focusing DIRC
GSI	Gesellschaft für Schwerionenforschung GmbH
HEP	High Energy Physics
HESR	High Energy Storage Ring
IP	Interaction Point
MC	Monte Carlo
MCP-PMT	Micro-Channel Plate Photomultiplier Tube
MDT	Mini Drift Tubes
MVD	Micro Vertex Detector
PANDA	AntiProton <u>AN</u> nihilation in <u>DA</u> rmstadt
PD	Photodetector
PID	Particle Identification
PMMA	Polymethylmethacrylat
PMT	Photomultiplier tube
R&D	Research and Development
RICH	Ring Imaging Cherenkov Detector
SciTil	Scintillation Tiles hodoscope

SD Standard Deviation

SPR Single photon Cherenkov angle resolution

SiPM Silicon Photomultiplier Tube

STT Straw Tubes Tracker

UV Ultra Violet

VMC Virtual Monte Carlo

Acknowledgments

I would like to express my gratitude to my supervisor Prof. Dr. Klaus Peters for accepting me as a PhD student and for his personal involvement and support. I am grateful to Prof. Dr. Wolfgang Kühn for supervising my progress and being my second referee for this thesis. I would like to thank other members of my committee, Prof. Dr. Dirk Rischke and Prof. Dr. Rene Reifarth, for their interest in my work.

I would like to express my deepest gratitude to Dr. Jochen Schwiening, who guided me throughout the PhD time and whose expertise, motivation, and patience always inspired me and pushed forward. Thank you for valuable advice and sharing personal experience. I particularly appreciate your assistance in technical writing.

I want to thank all members of the PANDA Cherenkov Group and particularly Dr. Carsten Schwarz, Dr. Klaus Götzen, and Dr. Roman Dzhugadlo, for their prompt help in various questions and many interesting discussions. Thank you for regular and thorough testing of my "side-experiments" and favourable report on them.

I am also grateful to Dr. Alexander Olshevskiy for his valuable advice during my study at the university and afterwards, and for the on-going interest in my carrier.

I would like to thank my school teacher of physics Michail Yurievich Zamyatnin, who introduced me to the world of physics and whose great personality motivated me to follow this path.

I would like to thank my family for their unceasing encouragement, attention and love. I am very grateful to my husband, who supports my endeavours.

In conclusion, I recognise that this research would not be possible without the financial assistance of Helmholtz Graduate School for Hadron and Ion Research (HGS-HIRe for FAIR) and express my gratitude to this agency.

Curriculum Vitae

Maria Patsyuk

Geboren am 5. Oktober 1985 in Alma-Ata, USSR

Ausbildung

2010 – 2015	Promotionsforschung an der GSI Helmholtzzentrum für Schwerionenforschung GmbH in Darmstadt, Deutschland Doktorand an der Johann Wolfgang Goethe-Universität in Frankfurt am Main Mitglied der Helmholtz Graduate School for Hadron and Ion Research (HGS-Hire)
2003 – 2009	Studium, Physik, Lomonosov Moskauer Staatliche Universität, Fachrichtung – Physik der Elementarteilchen Diploma Thesis: "Extraction of Gluon Distribution Function from J/ψ data in ALICE Experiment"
2003	Abitur in Gymnasium "Lyceum "Dubna" in Dubna, Russland. Gesamtnote 5.0 (von 5.0)

Akademische Lehrer

Prof. Dr. L.G. Dedenko, Prof. Dr. V.A. Aleshkevich, Prof. Dr. Saletsky A.M., Priv.-Doz. Dr. S.S. Krasilnikov, Prof. Dr. I.M. Kapitonov, Prof. Dr. D.D. Sokolov, Priv.-Doz. Dr. S.B. Kadomtsev, Priv.-Doz. A.V. Ovchinnikov, Prof. Dr. V.Y. Popov, Prof. Dr. A.N. Bogolyubov, Prof. Dr. L.S. Kuzmenkov, Prof. Dr. V.I. Denisov, Priv.-Doz. Dr. K.V. Parfenov, Priv.-Doz. Dr. I.A. Kvasnikov, Prof. Dr.

S.P. Vyatchanin, Priv.-Doz. Dr. B.S. Ishkhanov, Dr. A.G. Olshevskiy, Prof. Dr. Fursaev D.V., Prof. Dr. Sapozhnikov M.G., Prof. Dr. Akimov Yu.K., Prof. Dr. Bunyatov S.A., Dr. Teryaev O.V., Prof. Dr. Nikitin A.V., Prof. Dr. Skachkov N.B., Prof. Dr. Tsupko-Sitnikov, Acad. Prof. Dr. Kadyshevskiy V.G., Prof. Dr. Uzikov Yu.N., Dr. Naumov D.V., Prof. Dr. Peters K.

Konferenzteilnahmen

10/2014	International Conference on science and Technology for FAIR in Europe, Worms
03/2014	Frühjahrstagung der DPG, Frankfurt am Main
03/2013	Frühjahrstagung der DPG, Dresden
09/2012	XXI International Baldin Seminar on High Energy Physics Problems, Dubna (invited talk)
03/2012	Frühjahrstagung der DPG, Mainz
03/2011	Frühjahrstagung der DPG, Münster

Publikationen

2014	M. Hoek, R. Dzhugadlo, A. Gerhardt, K. Götzen, R. Hohler, G. Kalicy, H. Kumawat, D. Lehmann, B. Lewandowski, M. Patsyuk , K. Peters, G. Schepers, L. Schmitt, C. Schwarz, J. Schwiening, M. Traxler, M. Zühlsdorf, V.Kh. Dodokhov, A. Britting, W. Eyrich, A. Lehmann, F. Uhlig, M. Düren, K. Föhl, A. Harapetyan, B. Kröck, O. Merle, J. Rieke, E. Cowie, T. Keri, R. Montgomery, G. Rosner, P. Achenbach, M. Cardinali, W. Lauth, C. Sfienti, M. Thiel, P. Bühler, L. Gruber, J. Marton, K. Suzuki, <i>The PANDA Barrel DIRC detector</i> , Nucl. Instr. Meth. A 766 (2014) 9-13
------	---

2014 C. Schwarz, G. Kalicy, R. Dzhygadlo, A. Gerhardt, K. Götzen, R. Hohler, H. Kumawat, D. Lehmann, B. Lewandowski, **M. Patsyuk**, K. Peters, G. Schepers, L. Schmitt, J. Schwiening, M. Traxler, M. Zühlsdorf, V.Kh. Dodokhov, A. Britting, W. Eyrich, A. Lehmann, F. Uhlig, M. Düren, K. Föhl, A. Harapetyan, B. Kröck, O. Merle, J. Rieke, E. Cowie, T. Keri, R. Montgomery, G. Rosner, P. Achenbach, M. Cardinali, M. Hoek, W. Lauth, C. Sfienti, M. Thiel, P. Bühler, L. Gruber, J. Marton, K. Suzuki, *Prototyping the PANDA Barrel DIRC*, Nucl. Instr. Meth. A 766 (2014) 32-35

2014 R. Dzhygadlo, A. Gerhardt, K. Götzen, R. Hohler, G. Kalicy, H. Kumawat, D. Lehmann, B. Lewandowski, **M. Patsyuk**, K. Peters, G. Schepers, L. Schmitt, C. Schwarz, J. Schwiening, M. Traxler, M. Zühlsdorf, V.Kh. Dodokhov, A. Britting, W. Eyrich, A. Lehmann, F. Uhlig, M. Düren, K. Föhl, A. Harapetyan, B. Kröck, O. Merle, J. Rieke, E. Cowie, T. Keri, R. Montgomery, G. Rosner, P. Achenbach, M. Cardinali, M. Hoek, W. Lauth, C. Sfienti, M. Thiel, P. Bühler, L. Gruber, J. Marton, K. Suzuki, *Simulation and reconstruction of the PANDA Barrel DIRC*, Nucl. Instr. Meth. A 766 (2014) 263-266

2013 **M. Patsyuk**, *R & D for the PANDA Barrel DIRC*, PoS Baldin-ISHEPP-XXI(2012) 081

2012 C. Schwarz, A. Britting, P. Bühler, E. Cowie, V.Kh. Dodokhov, M. Düren, W. Eyrich, K. Föhl, L. Gruber, A. Harapetyan, M. Hoek, R. Hohler, G. Kalicy, T. Keri, P. Koch, B. Kröck, A. Lehmann, D. Lehmann, B. Lewandowski, J. Marton, O. Merle, R. Montgomery, **M. Patsyuk**, K. Peters, G. Rosner, G. Schepers, L. Schmitt, J. Schwiening, B. Seitz, C. Sfienti, K. Suzuki, F. Uhlig, A.S. Vodopianov, E. Widmann, *The Barrel DIRC of PANDA*, JINST 7 (2012) C02008

2012 PANDA Cherenkov Collaboration, G. Kalicy, H. Kumawat, J. Schwiening, R. Dzhygadlo, A. Gerhardt, R. Hohler, D. Lehmann, B. Lewandowski, **M. Patsyuk**, K. Peters, G. Schepers, L. Schmitt, C. Schwarz, M. Traxler, M. Zühlsdorf, V.Kh. Dodokhov, A.S. Vodopianov, A. Britting, W. Eyrich, A. Lehmann, F. Uhlig, M. Düren, K. Föhl, A. Harapetyan, P. Koch, B. Kröck, O. Merle, E. Cowie, T. Keri, R. Montgomery, G. Rosner, B. Seitz, P. Achenbach, M. Cardinali, M. Hoek, C. Sfienti, M. Thiel, C. Ugur, P. Bühler, L. Gruber, J. Marton, K. Suzuki, E. Widmann *Status of the PANDA Barrel DIRC*, JINST 9 (2014) C05060

Darmstadt, Mai 2015